THE CHARACTERISATION AND MODELLING OF MULTIPASS STEEL WELD HEAT-AFFECTED ZONES

By
Roger Charles Reed
Corpus Christi College
Cambridge

A dissertation submitted for the degree of
Doctor of Philosophy,
at the University of Cambridge
September 1990

THE CHARACTERISATION AND MODELLING OF MULTIPASS STEEL WELD HEAT-AFFECTED ZONES

By
Roger Charles Reed
Corpus Christi College
Cambridge

A dissertation submitted for the degree of
Doctor of Philosophy,
at the University of Cambridge
September 1990

To my parents, and sisters Alison and Katherine

"In physical science a first essential step in the direction of learning any subject is to find principles of numerical reckoning and methods for practicably measuring some quality connected with it. I often say that when you can measure what you are speaking about and express it in numbers, you know something about it; but when you cannot express it in numbers, your knowledge is of a meagre and unsatisfactory kind: it may be the beginning of knowledge, but you have scarcely in your thoughts advanced to the state of *science*, whatever the matter may be...."

Sir William Thomson, in 'Electrical Units of Measurement', a lecture given to the Institution of Civil Engineers, May 3rd, 1883.

PREFACE

R.C. Reed

30th September 1990

CONTENTS

THE CHARACTERISATION AND MODELLING OF MULTIPASS STEEL WELD HEAT-AFFECTED ZONES

Abstract

This project is concerned with the assessment and quantitative prediction of microstructure in multipass welds, with particular emphasis placed on the the heat-affected zones (HAZ's) of welded pipes fabricated from creep-resistant steels.

The pipes (of approximate composition Fe-0.5Cr-0.5Mo-0.25V-0.1C wt%, often referred to as $\frac{1}{2}$CMV) carry superheated steam from the boiler to the turbine in modern power plants. These are welded, during fabrication and repair, using the manual metal arc (MMA) process. Since the pipes are relatively thick, a large number of weld beads need to be deposited to complete the joint. For this reason, the fabrication and repair of such pipework is expensive (two men produce a single butt weld in 3 to 4 days, at a cost of £8000). The pipework is designed to operate for 30 years at 565°C, under a hoop stress of about 30 MPa. However, a significant number of failures occur before this design-life is exceeded, because local regions of microstructure become weak during service; the growth of circumferential cracks in the heat-affected zone (HAZ) (*type IV cracking*) leads to catastrophic failure of the welded joint, and is a concern of this research.

The aim of the project is twofold. Firstly, there is a desire to develop a model capable of predicting the microstructure in this kind of multipass weld. If based on the general principles of phase transformation theory, such a model would remove the need for the lengthy, and expensive experimentation which has traditionally been used to optimise such welding operations. It would also be of wide applicability in the design of all kinds of welds. For this reason, the approach adopted here has been to develop a fundamentally based model. Secondly, there is a need to characterise and assess the detailed microstructure in the heat-affected zone of such steam-pipes, in an effort to discover why type IV cracking occurs.

In chapter one of this dissertation, the background to the research is discussed in detail. In chapter two, the available theory for heat-flow in fusion welding is reviewed, and suitable (analytical) equations are chosen for use throughout this work. In chapter three, a model is developed to predict the thermal cycles experienced by each position in weld-space. The model is designed to be flexible in terms of joint geometry and welding procedure. Graphical displays illustrating the relative positions of regions which experience similar sets of weld thermal cycles are produced as output. In chapter four, empirical constants for use in elementary theory for γ-grain growth are derived, by fitting to experimental values of the γ-grain diameter in the HAZ.

In chapter five, the microstructures found in $\frac{1}{2}$CrMoV baseplate and HAZ are studied in an effort to discover why type IV cracking occurs. Particular emphasis is placed upon studying the partitioning of chemical elements between carbide phases and the ferrite matrix. This is detected using EDX spectroscopy, X-ray analysis and bulk analysis. The phenomenon of type IV cracking is rationalised in terms of the disparities between the size, distribution and volume fractions of alloy carbides, and the matrix compositions of the baseplate and the HAZ. The effect of γ-grain size is also considered.

In chapter six, a thermodynamic model is developed to describe the system Fe-C-X_1-X_2-X_3 *etc.* in the iron-rich corner of the multicomponent phase diagram. The model can cope with significant additions of Mn, Si, Ni, Cr, Mo, Cu, V, Nb, W and Co, and is capable of predicting the equilibrium and paraequilibrium phase boundaries, Gibbs free energy differences between ferrite and austenite for both nucleation and growth, and the Ae3 & Ae3′ temperatures.

This thermodynamic model is used in an attempt to model the kinetics of the reconstructive austenite to ferrite transformation in low-alloy steels in chapter seven. Detailed phase transformation theory is used to model both the nucleation and growth processes, and it has proved possible to estimate the diffusional C-curves on an isothermal TTT diagram from an input of the steel chemistry only. To do this, it proved necessary to assume that growth of allotriomorphic ferrite occurred by a paraequilibrium mechanism, rather than one involving true local equilibrium at the moving interface.

In chapter eight, some broad conclusions are drawn and suggestions for future work are made.

CHAPTER ONE
Introduction

It can be argued that our knowledge of fusion welding has, until the past fifteen years or so, been largely empirical. That is, although the technique has been used extensively as a method for joining metals, there has never been a fundamental understanding of the physical principles involved. The author suggests that this has manifested itself as an inability to predict, and so optimise the properties of fusion welds. Consequently, engineers have specified safety factors on welded structures which have been either too conservative, or wildly inaccurate. This has led to overdesigned structures, and perhaps more importantly, a number of spectacular failures.

The traditional approach to welding design has involved studying the way the weld variables (such as chemical composition, arc speed, electrode type, current and voltage) influence the physical properties (such as strength, toughness and hardness) of the fusion weld. The large number of variables associated with welding processes has made this difficult, although it should be noted that many of these are not independent. The trial welds undergo stringent mechanical testing, to determine the local optimum composition/process combination for the desired properties. This is both expensive and time-consuming.

This empirical approach is flawed, in the sense that it fails to acknowledge the primary influence on the physical properties of a metal: the size, distribution and type of microstructural phases present. Indeed, many of the problems associated with fusion welding arise because metallurgical phenomena act to weaken localised regions of microstructure; such effects can occur unexpectedly and are therefore difficult to design against in the traditional sense. It follows that the intimate relationship between the microstructure and the properties should also be recognised.

It is clear then that any programme of research that aims to study the way the properties of welds are influenced by the weld variables *without* considering the microstructure will lead to only an incomplete understanding of the problem. Therefore, this programme of research will concentrate on the prediction of weld properties *through* the metallurgy of the weld itself. In this way it is hoped to produce a general solution to the problem of the multipass weld, in the form of a computer model based upon the general principles of phase transformation, thermodynamic and heat-flow theory. Such a model would enable many of the metallurgical problems associated with fusion welding to be studied inexpensively. It would also enable the design of multipass welds to proceed in a more fundamental, and less empirical manner.

For such a computer model to be of any use, it must be possible to vary the weld metal chemistry at will. However, for the purpose of calibrating and verifying the model as it develops, it is necessary to consider particular steel compositions, hopefully without loss of generality. Therefore, within the broader framework of designing the computer model for multipass welds, this research is concerned with the characterisation and modelling of the microstructure in the creep-resistant steels used in the power generation industry, with particular emphasis on the behaviour of the heat-affected zones of the welded joints found in the steam-pipes of modern power plants.

1.1 Welded, Creep-Resistant Steels In The Power Generation Industry

The objective of welding is to achieve continuity in the load-bearing structure, so that the weld is not a source of weakness for the structure it joins. This is done by remelting some of the parent material and filling with additional compatible weld material where necessary. The size and shape of the components will influence the choice of welding process, the detailed design of the weld geometry and the manner in which the welding is carried out. Examination of some of the components in a power station steam-raising circuit gives a useful insight into the complexity of the problem, and allows the present research to be placed in context.

1.1.1 Fossil Fuel Fired, Steam Turbine Power Plants

A large proportion of the electricity produced in the United Kingdom is generated in steam turbine power plants. In a fossil fuel steam plant, the fuel is burned in a large vessel called a boiler, which encloses an assembly of pipework. The fuel ignites as it enters the boiler, and the heat of combustion is transferred to the water that is circulating in the pipework. Superheated steam leaves the boiler at approximately 565°C and is carried to the steam turbine via steam pipes. There it pushes against turbine blades that turn the shaft of a generator to create electricity. After the steam has passed through the turbine, it is condensed and re-circulated to the boiler for re-heating. This process is shown schematically in figure 1.1.

Inside the boiler the temperature rises steadily, so that the pipework has to exhibit an increasing degree of corrosion resistance. In the low temperature regions C-Mn type steel is employed, but at progressively higher temperatures $1Cr\frac{1}{2}Mo$, $2\frac{1}{4}Cr1Mo$ and finally austenitic stainless steels are necessary.

Among the largest components in the pressure circuit is the boiler drum, which is a cylindrical vessel ~60 m long, ~1.8 m outside diameter and ~150 mm wall thickness. The manufacturing sequence involves the fabrication of cylindrical sections by forming two C-Mn type steel plates into semi-circular shapes, which are butted together and welded. Several such cylinders are then butt welded to produce the desired length. In this case, the submerged arc (SA) process, which is automated, is commonly used.

In the United Kingdom, the steam-pipes which carry the superheated steam from the top of the boiler to the steam turbine are normalised & tempered $\frac{1}{2}CrMoV$ steel. Typical compositions [1] of commercial casts are tabulated in table 1.1. The pipes are of ~350 mm outside diameter and ~60 mm wall thickness (refer to figure 1.2). It is to the joining of these steam-pipes, and the behaviour of the joints during stress-relief heat-treatment and service, that the present research is addressed.

CONCENTRATION /wt%										
C	Si	S	P	Mn	Cr	Ni	Mo	V	Cu	Sn
0.105	0.19	0.021	0.023	0.48	0.41	0.10	0.53	0.22	0.07	0.01
0.105	0.14	0.024	0.036	0.47	0.35	0.11	0.50	0.24	-	-
0.13	0.28	0.038	0.018	0.53	0.34	0.10	0.53	0.24	-	-
0.12	0.30	0.035	0.020	0.55	0.42	0.06	0.54	0.25	-	-
0.10	0.17	0.018	0.026	0.61	0.44	0.08	0.41	0.26	0.07	0.01
0.105	0.15	0.030	0.028	0.50	0.40	0.11	0.52	0.24	-	-

Table 1.1: Typical compositions of $\frac{1}{2}CrMoV$ steam-pipe steel [1].

To date, these steam-pipes have been butt-welded circumferentially with $2\frac{1}{4}Cr1Mo$ electrodes, although in Germany matching $\frac{1}{2}CrMoV$ weld metal has been used. A typical weld preparation is illustrated in figure 1.2. Each weld is built up of ~15 layers, with ~10 kg of metal being deposited, as a series of stringer or woven weld beads. The arcing time, which is the time during which the weld metal is being deposited, is about 20 hours and the total working time to produce a single butt weld is 3 or 4 days [2]. The manual metal arc process (figure 1.3) is preferred for this application.

1.1.2 The Manual Metal Arc Process

This is still the most popular welding process, primarily because of the manipulative skills of welders, derived over many years of training and practice. The manual metal arc welder is able to tackle complicated joint geometries and weld preparations of limited accessibility. He provides a versatility unmatched by the automated processes, yet with experience the resulting weld can be of equally high standard. However, there is still the degree of variability attached to a manual process, and the danger of operator error.

The heat source is provided by striking an arc between an electrode and the workpiece. The voltage is low, and the current fairly high, typical values being 10–50 volts and 30–600 Amps respectively. The arc current spreads laterally, and generates a plasma jet which flows towards the plate, where a molten pool is formed. At the same time the electrode begins to melt, so that molten metal transfers across the arc and is projected into the weld pool. The processes of metal transfer and mass transport are complicated by the fact that the core wire of the electrode is coated with an extruded flux, which decomposes to give gaseous products. The principal functions of the coating are to stabilise the arc, to flux away any impurities, to form a protective gas shield, to slag over the weld and to add any metallic elements needed to adjust the final composition to that required [2].

1.1.3 The Type IV Cracking Problem

The name 'type IV cracking' comes from a German classification of weld cracking modes. The problem was first reported in Germany in 1974, in $\frac{1}{2}$CrMoV parent material welded with matching $\frac{1}{2}$CrMoV weld metal. In recent years it has also been reported in Denmark and in the United Kingdom, and according to Gooch and Kimmins [3], represents the dominant failure mechanism at times approaching 100,000 hours at the operating temperature of 565° C.

Type IV cracks in welded steam-pipe present a danger of complete severance of the joint, with the possibility of explosive failure. However, in order to understand why this is so, it is necessary to define some terms which will be used frequently in this dissertation.

Each time the welder strikes an arc between electrode and baseplate, a deposit or *pass* of molten weld metal is made. This subsequently solidifies to give what is often termed the *as-deposited fusion zone* or the *primary microstructure* of the weld. In multipass welds, however, there is a significant region of the fusion zone that becomes reheated (but not re-melted) by subsequent passes. For example, the fusion zone can experience a temperature sufficient for re-austenitisation to occur. Decomposition of this austenite can give a variety of phases, the exact amount and distribution depending on the cooling rate and chemical composition, which vary from point to point. The metallurgical and physical properties of this *re-heated fusion zone* or *secondary microstructure* can therefore differ markedly from the as-deposited material. In addition, there will exist a region in the baseplate, close to the fusion zone which, although unmelted, will also have experienced thermal cycles strong enough to have altered the properties of the baseplate. This region is often termed the *heat-affected zone* (HAZ). The relative positions of the primary microstructure, the re-heated fusion zone and the heat-affected zone are shown in figure 1.4, for the typical weld preparation of figure 1.2.

The steam-pipes are required to operate at a temperature of 565°C, and the superheated steam, under pressure, produces a hoop stress of typically 30 MPa, although there are smaller loads arising from accommodation within the pipe assembly itself. The response of structures to static loading under such temperature regimes is a process which is known as *creep*. Several creep crack growth mechanisms are known to be responsible for the failure of heavy gauge high-pressure steam pipework. Crack formation usually occurs at weld positions, either within the weld deposits (Type I and II modes of cracking) or in the region of the HAZ (Type III cracking) during stress relief treatment. These three crack modes are initiated by the interaction of impurities with microstructure, and are the common cause of repair

3

to welds in steam pipework. However, the cracks are usually detected and repaired prior to leakage. Transverse cracks like these also do not in general lead to catastrophic failure of the welded joint.

However, the heat-affected zone lies in a circumferential band on each side of the fusion zone, as can be seen from figure 1.4. It follows that the growth of circumferential cracks in the HAZ's of a multipass weld presents the danger of complete severance of the joint, possibly with explosive failure, as referred to above.

Further, the likelihood of a circumferential mode of cracking is made more probable because of the way the V-shaped weld preparation is filled. The weld beads are deposited systematically in the preparation, often side-by-side in the notch, to create a series of layers, one above another (figure 1.5). There is the additional possibility of a final *capping layer* to finish the weld. Often this involves the use of electrodes to provide larger deposition rates, and higher heat inputs.

The deposition of each bead produces an approximately radial HAZ region, and the superposition of heat pulses from successive beads leads to a complex pattern of well-defined regions, each of which will have experienced a different thermal history. The variations in thermal history lead to corresponding variations in microstructure, which can consist of complex regions of allotriomorphic ferrite, bainite and martensite. Some of these regions can be tempered or coarsened by subsequent thermal cycles, depending on the degree of overlap between beads. The general effect is to produce bands of similar microstructure which lie approximately parallel to the fusion/heat-affected zone interface. Significantly, inadequate strength or toughness in any one of these regions can therefore lead to a circumferential crack in the HAZ, either during welding, post-weld heat treatment or service.

Type IV cracks form in this way, and have been simulated [3] by pre-designed thermal creep tests (figure 1.6). Such cracks are thought to initiate somewhere in the part of the HAZ which has been only partly re-austenitised. This corresponds to a peak temperature somewhere between the Ac1 and Ac3 temperatures of the baseplate concerned. Microstructurally, the cracking occurs as uniform occurrence and linkage of creep cavities (figure 1.7), and is particularly dangerous, because it cannot be detected by routine inspection methods.

This mode of cracking has only been detected in weldments subjected to axial or bending system loading, and is thus associated with section changes, terminal welds, multiple pipe intersections and errors in setting pipe loading systems [2]. Type IV cracking would therefore seem to be a consequence of a concentration of creep strain in a region of low creep strength, the exact extent and severity of which will depend upon the thermal cycles experienced during welding, post-weld heat treatment and service.

1.2 Summary: Scope and Aim of This Work

Although algorithms for the prediction of microstructure in as-deposited region of low-alloy steel welds already exist [4,5,6], a model for multipass welds, encompassing the reheated and heat-affected zones, has yet to be designed. The general aim of the research described in this dissertation is to produce just such a model, and to couple it with the existing algorithms, so that the microstructure of multipass welds can be calculated from an input of the steel chemistry and weld variables only.

Figure 1.8 is a flow diagram representing the methodology of this work. The research begins by studying the equations available for modelling heat-flow during fusion welding. Such equations are needed in order to describe the thermal cycles which occur during welding; they depend crucially upon weld variables such as the electrode diameter, arc power and arc speed. The thermal cycles experienced during post-weld heat treatment and service must also be considered.

The 'kinetic' strength of these thermal cycles, when considered in the broader context of thermodynamic, kinetic and phase transformation theory, are directly responsible for the metallurgical phases observed in the weld. Although quantitative models capable of estimating the microstructure as a

4

function of thermal heat treatment are under development [*e.g.* 4,5,6], they often involve gross approximations, and so need to be refined. In practice, such quantitative models are difficult to formulate, because they require an intimate knowledge of kinetics as well as the laws of thermodynamics, for in fusion welding the temperature/time cycles are very rapid. In many cases, for example the reverse transformation from ferrite to austenite, suitable quantitative models do not exist as yet.

Although the welding process offers the opportunity to study interesting metallurgical phenomena, it is well to keep the problem in perspective. Fusion welding remains the most widely used method for joining structures, but it is not without its problems. The metallurgist's role here is firstly to prevent the use of designs which are flawed, or in hindsight, to discover why structures failed, so that failure will not be repeated. For this reason, it is important to be in a position to understand the limits of strength, ductility, hardness and toughness of the welded structure. Ideally, we require all the properties of the weld to be better than the structure which it holds together. The final stage of this work will then involve studying the way the microstructure influences and controls the properties of the weld. Theories for these microstructure/property relationships are incredibly immature at present.

Throughout this work, experimental data are used to calibrate and verify the computer model as it is developed. Of particular interest are the $2\frac{1}{4}$CrMo/$\frac{1}{2}$CrMoV multipass welds which are typical of those found in the steam-pipes of modern steam-generating power plants. Considerable emphasis is placed upon characterising, and modelling the evolution of microstructure in the HAZ of $\frac{1}{2}$CrMoV steels. This is of particular relevance to the problem of type IV cracking.

REFERENCES

1. K.R. Williams and B. Wilshire, Materials Science and Engineering, **47**, 151–160, (1981).
2. A.T. Price and J.A. Williams, in 'Recent Advances in Creep and Fracture of Engineering Materials and Structures', editors B. Wilshire & D.R.J. Owen, Pineridge Press, (1982).
3. D.J. Gooch and S.T. Kimmins, in the Proceedings of the Third International Conference on Creep and Fracture of Engineering Materials and Structures, Swansea, (1987).
4. H.K.D.H. Bhadeshia, L.-E. Svensson and B. Gretoft, Acta Metall., **33**, 1271–1283, (1985).
5. H.K.D.H. Bhadeshia, L.-E. Svensson and B. Gretoft, in 'Third International Conference on Welding and Performance of Pipelines', The Welding Institute, Abington, (1986).
6. H.K.D.H. Bhadeshia, L.-E. Svensson and B. Gretoft, in 'Proceedings of an International Conference on Welding Metallurgy of Structural Steels', Edited J.Y. Koo, The Metallurgical Society of the AIME, Warrendale, Pennsylvania, (1987).
7. 'Electricity: Today's Technologies, Tomorrow's Alternatives', (1987 Edition), Electric Power Research Institute, Palo Alto, California, U.S.A., (1987).
8. Metals Handbook 6, 'Welding, Brazing and Joining', ASM, (1983).
9. C.J. Middleton and B.J. Cane, Central Electricity Generating Board Report No. RD/L/N 24/77, (1977).
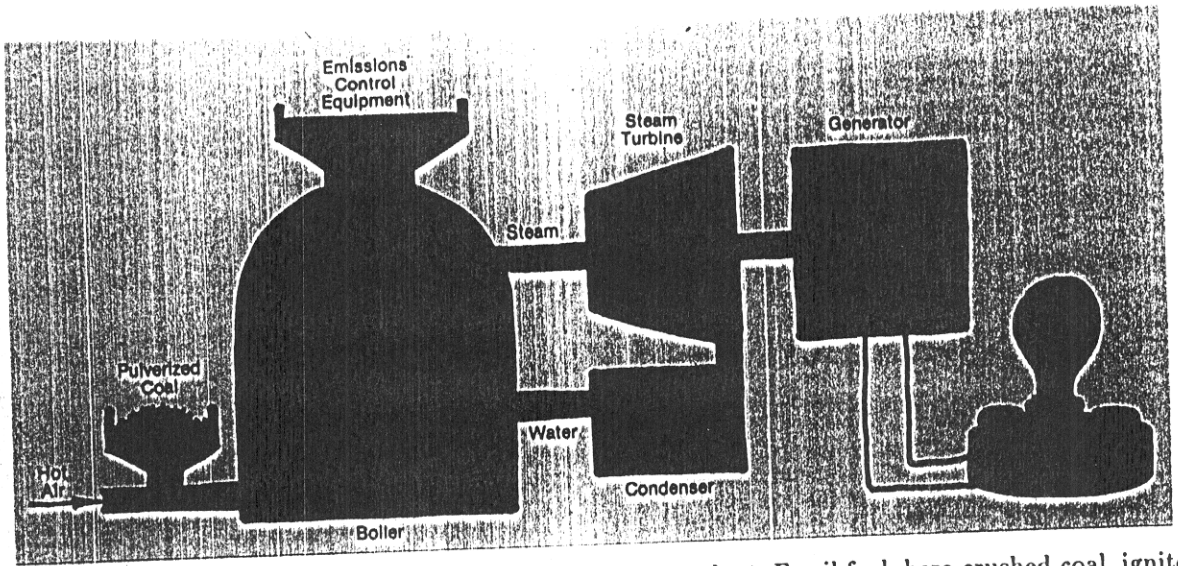
Figure 1.1: Generating electricity in the steam turbine power plant. Fossil fuel, here crushed coal, ignites as it blows into the boiler on a stream of hot air. The heat from the burning coal changes the water in the tubes into steam, and the steam turns the turbine blades that activate the generator. After [7].
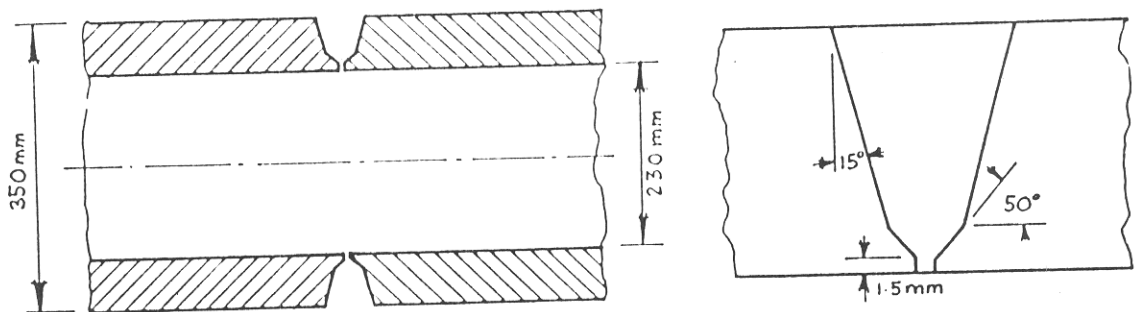
Figure 1.2: Left, the geometry of steam-pipes, used to carry superheated steam from the boiler to the steam turbine. Right, a typical weld preparation.
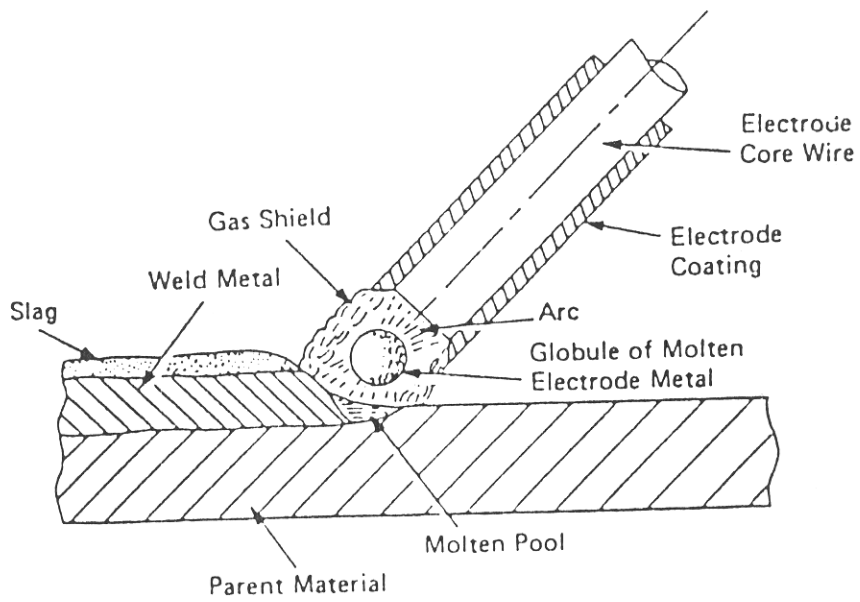
Figure 1.3: The manual metal arc process. After [8].
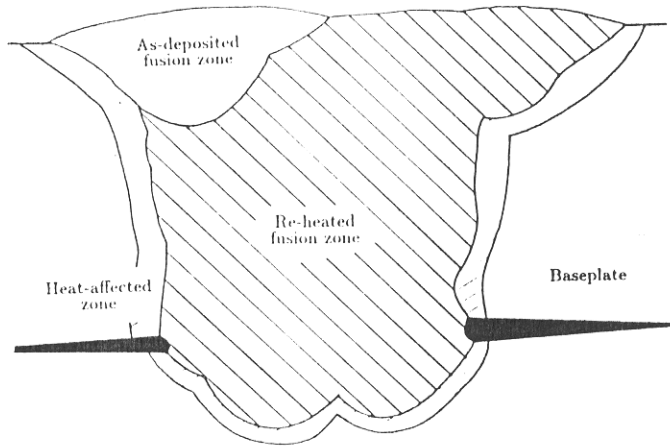
Figure 1.4: Schematic diagram of possible positions of the as-deposited weld metal, the re-heated weld metal and the heat-affected zone, in a multipass weld.
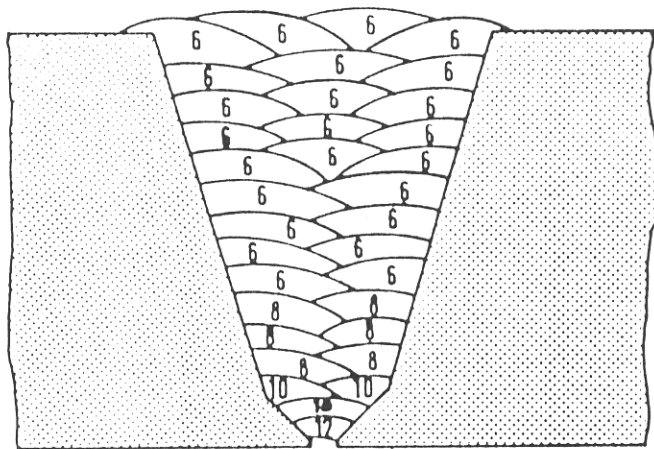
Figure 1.5: Often, the weld beads in a multipass weld are deposited in layers. After Middleton & Cane [9].
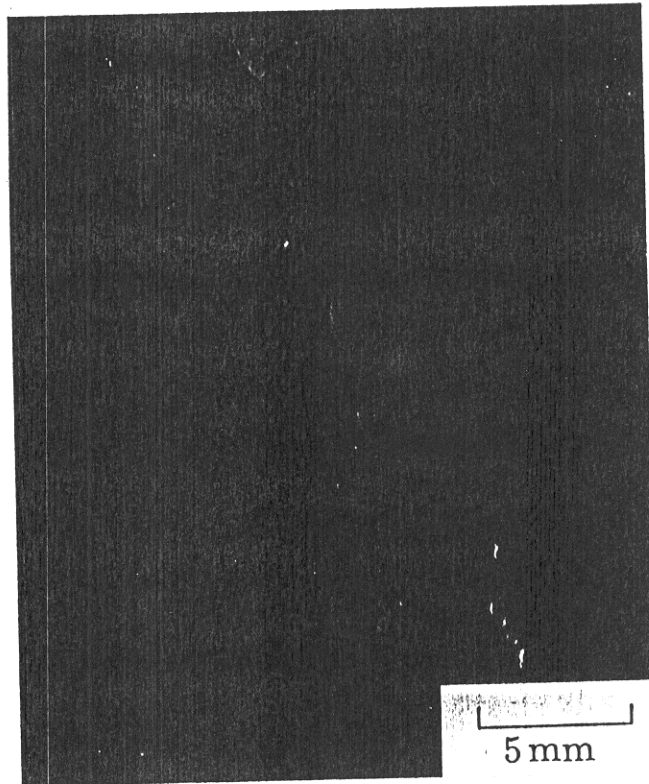
Figure 1.6: A type IV crack formed by a pre-designed thermal creep test.
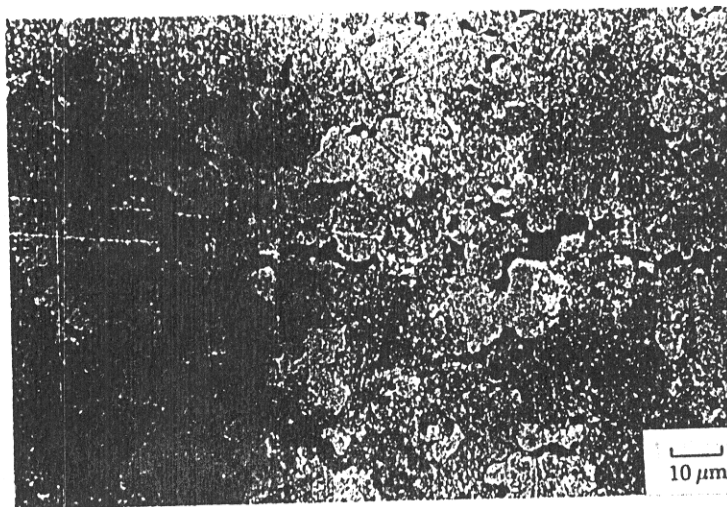
Figure 1.7: The mechanism of type IV cracks– the linkage of creep cavities.

WELD VARIABLES

↓

THERMAL CYCLES
during welding, post-weld heat treatment, and service

Kinetics, Thermodynamics
Phase Transformation Theory
↓

MICROSTRUCTURE
Volume fraction, size, distribution, morphology etc. of phases
as a function of time, position

↓

MACROSCOPIC PROPERTIES OF WELD
e.g. yield stress, hardness, toughness
as a function of time, position
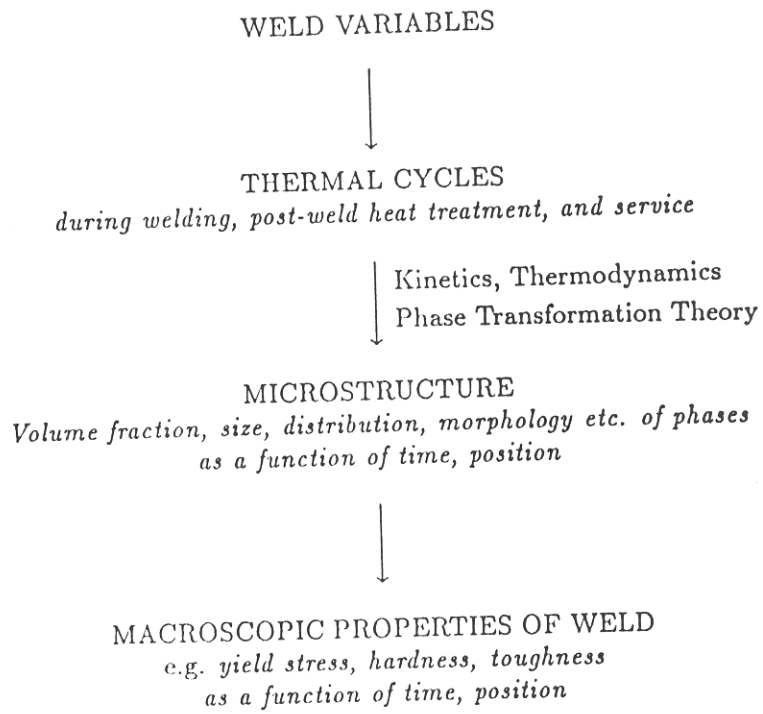
Figure 1.8: Flow diagram illustrating the proposed course of research. To understand why welded structures exhibit certain values of strength and toughness, it is necessary to study the way thermal cycles influence the metallurgical microstructure.

CHAPTER TWO
The Theory of Heat Flow In Fusion Welding

Nomenclature

a	thermal diffusivity
C_1, C_2	empirical constants in equation 2.14
d	plate thickness
I	arc current
q	effective arc power (equation 2.17)
R	distance from the heat source (equations 2.4, 2.6)
r	distance from the weld centre-line
r'	distance from the heat source (equations 2.8, 2.9)
r_b	half-width of heat source (equation 2.11)
T	instantaneous temperature
T_0	interpass temperature
t	time
t_b	time for which the source is over a particular point on the surface of the workpiece
t_p	time to reach the peak temperature
t_0	time for heat to diffuse over source half-width r_b
v	welding speed
V	arc voltage
x, y, z	coordinates fixed with respect to the workpiece
z_0	apparent distance of source above surface of work-piece
η	arc efficiency
λ	thermal conductivity
ξ	distance from the source measured along measured along x-axis (fig. 2.1)
ρc	volume heat capacity (density × specific heat capacity)

2.1 Rosenthal's Equations

Rosenthal [10,11] specified heat-flow equations that have become a source of reference for much of the work on welding that has followed. A number of assumptions were made in the original analysis, and they are summarised as follows:

- It was assumed the heat source moves along the surface of a plate with uniform speed, in a rectangular coordinate system, which moves such that its origin is always coincident with the heat source origin.
- Heat is assumed to be delivered from a point source of heat, that is, from an origin which is of infinitely small size.
- The latent heat of fusion of the weld bead, and the latent heat of any phase transformations that might occur in the weld, are ignored.
- There are no heat losses from the surface of the plate.
- The thermal properties of the weld are independent of temperature.
- The speed of the heat source, and the rate of heat input, are constant.

The time dependent solution to Laplace's equation for heat-flow in a solid material, expressed in the rectangular coordinates (x, y, z) and referred to a fixed origin in the solid has the form

$$\frac{\partial^2 T}{\partial x^2} + \frac{\partial^2 T}{\partial y^2} + \frac{\partial^2 T}{\partial z^2} = \frac{1}{a} \frac{\partial T}{\partial t}$$

(2.1

where T is the temperature, t is the time and a the thermal diffusivity. The flow of heat away from the heat source is assumed to be controlled by conduction in the solid base metal. No account is taken of heat transfer through the molten weld pool by convection.

If heat is supplied by a point source of heat moving with a constant speed $v = \partial x / \partial t$ along the x-axis, equation 2.1 may be rewritten with the source as origin. By defining the the variable $\xi = x - vt$, where ξ is the distance of the point of interest from the source measured along the x-axis, and differentiating the equation with respect to ξ, the following equation is obtained

$$\frac{\partial^2 T}{\partial \xi^2} + \frac{\partial^2 T}{\partial y^2} + \frac{\partial^2 T}{\partial z^2} = -\frac{v}{a}\frac{\partial T}{\partial \xi} + \frac{1}{a}\frac{\partial T}{\partial t} \tag{2.2}$$

The geometry and coordinate systems used for this analysis are shown in figure 2.1. Bornefeld [12] has shown that if the solid is long enough, the process is reduced to a steady state, or 'quasi-stationary' heat flow problem. This state is illustrated in figure 2.2. This means that except during the initial and final transients of the welding process, the temperature distribution *around the source* in the workpiece is *steady* with respect to the coordinate system moving with the heat source. Mathematically, this is then defined by the condition $\partial T / \partial t = 0$, so that equation 2.2 reduces to

$$\frac{\partial^2 T}{\partial \xi^2} + \frac{\partial^2 T}{\partial y^2} + \frac{\partial^2 T}{\partial z^2} = -\frac{v}{a}\frac{\partial T}{\partial \xi} \tag{2.3}$$

Equation 2.3 formed the basis of Rosenthal's analysis, which is lengthy, and need not be repeated here. His results may summarised by the following two equations, describing the heat flow in the limit of the thick plate,

$$T - T_0 = \frac{q}{2\pi\lambda R} \exp\left\{-\frac{v}{2a}(\xi + R)\right\} \tag{2.4}$$

and the thin plate,

$$T - T_0 = \frac{q}{4\pi\lambda\rho c v r'} \exp\left\{-\frac{v}{2a}(\xi + r')\right\} \tag{2.5}$$

Here T_0 is the initial plate temperature (sometimes called the interpass or preheat temperature), λ the thermal conductivity, $R^2 = \xi^2 + y^2 + z^2$, ρc the volume heat capacity, $r'^2 = \xi^2 + y^2$, d is the plate thickness and q the arc power, given by the product of the arc current, the arc voltage and the arc efficiency. These are Rosenthal's original equations, for thick and thin plates, written in the terminology used by Ion [13].

It is possible, *e.g.* Ion [13] and Rykalin *et al.* [14], to make certain approximations to Rosenthal's equations. In Ion's case, this was necessary because his work was deliberately limited to the use of a microcomputer.

2.1.1 Thick Plate Approximation

Consider first the situation in which heat is able to flow radially away from the heat source, a 3D heat flow geometry as shown in figure 2.3. Consider a fixed point in the plane $x = 0$ for convenience, in which case we have $R^2 = (-vt)^2 + y^2 + z^2$. Define the variable r as the distance of the point from the weld centre-line so that $r^2 = y^2 + z^2$, giving $R^2 = (-vt)^2 + r^2$. Ion notes that it is particularly important to appreciate that R is the distance from the point of interest to the *heat source*, a quantity that changes with time, whereas r is the radial distance from the point of interest to the *weld centre-line*, measured in the plane containing the point, and this does not change with time. Substitution of ξ and R in the exponential of equation 2.4 then yields, after simplification

$$T - T_0 = \frac{q}{2\pi\lambda R} \exp\left\{\frac{v^2 t}{2a}\left(1 - \left[1 + \left(\frac{r}{vt}\right)^2\right]^{1/2}\right)\right\} \tag{2.6}$$

12

Assuming that $r \ll v\,t$, i.e. that for the point considered the distance from the weld centre-line is large compared with the distance moved by the heat source in unit time, we may assume that $R \sim v\,t$ and also expand the square root term, using Taylor's expansion and taking the first two terms

$$\left[1 + \left(\frac{r}{v\,t}\right)^2\right]^{1/2} \simeq 1 + \frac{r^2}{2\,(v\,t)^2} \tag{2.7}$$

Substituting for R and incorporating the expansion enables equation 2.6 to be rewritten, after simplification, as

$$T - T_0 = \frac{q}{2\,\pi\,\lambda\,v\,t}\,\exp\left\{-\frac{r^2}{4\,a\,t}\right\} \tag{2.8}$$

2.1.2 Thin Plate Approximation

Consider now the situation in which heat may only disperse laterally in the plate, as shown in figure 2.3. Again consider a point in the plane $x = 0$, which gives $\xi = -v\,t$ and $r'^2 = (-v\,t)^2 + y^2$. Define r now as the lateral displacement of the point of interest from the weld centre-line, i.e. $r \equiv y$ and $r'^2 = (-v\,t)^2 + r^2$. Note the difference between r' and r (c.f. R and r in the thick plate case). Treatment of the exponential part of equation 2.5 in the same manner as above yields

$$T - T_0 = \frac{q}{(4\,\pi\,\lambda\,\rho\,c\,v\,r')^{1/2}\,d}\,\exp\left\{-\frac{r^2}{4\,a\,t}\right\} \tag{2.8}$$

Substitution for r' in equation 2.8 gives

$$T - T_0 = \frac{q}{(4\,\pi\,\lambda\,\rho\,c\,t)^{1/2}\,v\,d}\,\exp\left\{-\frac{r^2}{4\,a\,t}\right\} \tag{2.9}$$

2.2 Refinements to Rosenthal's Equations

Christensen *et al.* [15], Kou [16], Ashby & Easterling [17] and Clark [1] have all noted that because of the unrealistic assumptions, the Rosenthal equations cannot be used to predict accurately the heat flow and solidification behaviour in the weld pool. It should be appreciated that if the weld pool is to be modelled successfully, factors such as convective mixing, the impact of fused droplets, magnetic forces, latent heat of fusion, surface heat losses and the finite size of the heat source should be considered. Consequently, many investigators have tried to take these factors into account, by modifying mathematically the equations that Rosenthal presented.

2.2.1 Replacement of the Point Source by a Circular Disc Source

One of the problems with the Rosenthal analysis is that it predicts a singularity at the weld centre-line. This means that on this line, the predicted temperature reaches infinity, a direct consequence of the assumption that heat is injected instantaneously from a point source. This problem may be partially overcome if the point source is replaced by a circular disc source, of radius r_b. If the speed of the beam is high, it can be treated as a line source, of finite width in the y direction, but infinitessimally thin in the x direction. For this case, Rykalin *et al.* [14] have presented an analytical solution for the temperature field $T\{y, z, t\}$ in the thick plate case

$$T - T_0 = \frac{q/v}{2\,\pi\,\lambda\,[t\,(t + t_0)]^{1/2}}\,\exp\left\{-\frac{1}{4\,a}\left(\frac{z^2}{t} + \frac{y^2}{(t + t_0)}\right)\right\} \tag{2.11}$$

where

$$t_0 = \frac{r_b^2}{4\,a} \tag{2.11}$$

13

Equation 2.11 is an obvious modification of equation 2.7, spreading the heat source in the y direction. The parameter t_0 is the time taken for the heat to diffuse over the source half-width r_b. Far from the heat source where $z^2 + y^2 \gg r_b^2$ and when $t \gg t_0$, equation 2.11 reduces to the result for a point source. However, this equation, like that for the point source, leads to infinite temperatures (and thus melting) at the surface where the arc energy impinges. This is again due to the 'high speed' (line source) assumption which means that a finite energy is injected into the solid at $t = 0$.

Ashby & Easterling [17] modified Rykalin's equation to take account of the width of the heat source in the travel direction. To do this, they noted that, if the source has radius r_b, then energy is injected at a given point on the surface of the weld centre-line over a time

$$t_b = \frac{2 \, r_b}{v} \tag{2.11c}$$

Heat diffuses inwards during this injection time, draining heat away from the surface, thereby limiting the surface temperature to a finite value. Ashby & Easterling allowed for this by replacing the real source in the plane $z = 0$ by an apparent source in the plane $z = z_0$ above the surface, so that

$$T - T_0 = \frac{q/v}{2 \, \pi \, \lambda \, [t \, (t + t_0)]^{1/2}} \exp \left\{ -\frac{1}{4 \, a} \left(\frac{(z + z_0)^2}{t} + \frac{y^2}{(t + t_0)} \right) \right\} \tag{2.12a}$$

where, as before

$$t_0 = \frac{r_b^2}{4 \, a} \tag{2.12b}$$

By considering a stationary Gaussian beam of average intensity $q/\pi r_b^2$, applied for a time t_b, they determined

$$z_0^2 = \left[\frac{r_b}{e} \left(\frac{\pi \, a \, r_b}{v} \right)^{1/2} \right] \tag{2.12c}$$

provided $t \gg t_0$, which will be the case if the heat flow is 'quasi-stationary'. The geometry is shown in figure 2.4 and figure 2.5. These equations for heat flow were combined with kinetic models to predict the near-surface structure and hardness of plain carbon hypo-eutectoid steels, after laser treatment.

The work has since been extended by Li, Easterling & Ashby [18] to hyper-eutectoid steels, and by Shercliff & Ashby [19] to the prediction of case-depth in laser-surface treatments. Although this work applies the equations to the applications of lasers, the same equations will be applicable in any welding process where the 'high speed' (line source) approximation is no longer valid. For example, the equations were used by Ion *et al.* [20] to develop diagrams of microstructure and hardness for HAZ's in fusion welds.

2.2.2 *The Temperature-Dependence of Properties and Finite Element Analysis*

The above equations represent analytical solutions to the problem of heat-flow in welds. Provided the assumptions are satisfied, these solutions can be exact; however in most welding situations the assumptions hold to only varying degrees, so the solutions are usually in error.

In the past fifteen years or so, the increasing availability of fast computational facilities has encouraged the modelling of the arc physics and the fluid mechanics of the weld pool. The solutions are achieved by applying the laws of conservation of momentum and energy. Recent research has focussed upon modelling the convection in the weld pool, which is driven by a combination of surface tension, electromagnetic and buoyancy forces [21]. Such models assume that the current density and thermal efficiency of the arc, as well as the temperature-dependent properties such as viscosity, surface tension, specific heat, thermal conductivity & diffusivity (figure 2.6) are known. This temperature-dependency in particular, greatly complicates the solution for the temperature field, and numerical techniques such as finite-element analysis become necessary. The work of Kou [16] is a good example.

It is interesting to note that in just the same way that recent analytical solutions have focussed upon distributing the arc power over a finite area, the distribution of the heating effect of the arc is often the critical decision in finite element analyses. As in the case of the analytical solutions, the point or line sources predict infinite temperatures at the source and are quite wrong near the source. Pavelic et al. [22] proposed a circular disc with a Gaussian distribution of flux. Anderson [23] used a constant flux over the weld pool. Goldak et al. [24] distributed the power density with a Gaussian distribution in a double ellipsoid model of the weld pool. Later they generalised this to arbitrary distribution functions for the power density over the interior of the weld pool and an arbitrary distribution of flux over the surface [25,26]. As Goldak [27] points out, it is partly true that the solution needs to be known before the solution can be calculated.

In summary, there can be no doubt that the temperature field in and near the weld pool is most rigorously modelled using finite element analyses [27] . However, such models for the physics of the welding arc are immature [28], and until software for weld pools becomes available, simpler models will be used by metallurgists to compute the temperature field. Of these, the analytic model of Ashby & Easterling [17] remains the easiest to work with.

2.3 Heat Flow in the Molten Weld Pool

It has already been noted that it is not correct to apply Rosenthal's equations to the thermal cycles in the weld pool. In this region, heat is transferred by convective mixing rather than by conduction. The electromagnetic forces and the momentum associated with the arc also cause magnetic and physical stirring, so that the temperature gradients will not settle down until the arc has passed.

However, it seems likely that the cooling rate in the fusion zone will not vary significantly with position. The fact that the microstructure in this zone is observed to be homogeneous is good evidence for this. Bhadeshia et al. [29] started with this assumption in their model for the development of microstructure in low alloy weld deposits. They noted that the cooling rate in the fusion zone has been described by [30]

$$\frac{dT}{dt} = -\frac{2\pi\lambda}{q/v}(T - T_0)^2 \tag{2.13}$$

where the equation has been written in the terminology used here.

Equation 2.13 can be rationalised in terms of the Rosenthal equations. The equation refers to the *cooling rate beyond the peak of the thermal cycle*. Consider figure 2.7, which represents graphically the approximation to the Rosenthal equation (equation 2.4) in the thick plate case. Beyond the peak of the cycle, the temperature quickly tends to

$$T - T_0 = \frac{q}{2\pi\lambda v t} \tag{2.14}$$

from which it is easy to arrive at equation 2.13 by differentiation.

Bhadeshia et al. obtained cooling curves from the fusion zone of experimental welds by harpooning Pt/Pt-Rh thermocouples into the centre of the weld pool, immediately after the passage of the welding arc. They found equation 2.13 inadequate in representing the experimental data produced. The following empirical equation,

$$\frac{dT}{dt} = -C_1(T - T_0)^{C_2} \tag{2.15}$$

where C_1 and C_2 are constants, was used to describe the cooling curve over the temperature range of interest (800–500 °C). They determined a value of 1.63 for C_2 for their set of experimental data.

2.4 Discussion Relating to Rosenthal's Equations

Assuming the equations developed by Ashby & Easterling [17] (equation 2.12) represent the best easily accessible solution to the problem of heat flow in fusion welding, these equations are now analysed in order to discover the influence of the weld variables upon which they depend. In the calculations which follow, and in the rest of this work, we assume $\lambda = 41 \, \text{Jm}^{-1}\text{s}^{-1}\text{K}^{-1}$ and $a = 9.1 \times 10^{-6} \, \text{m}^2\text{s}^{-1}$ [17]. In both cases these properties are assumed to be temperature independent.

2.4.1 Temperature–Time Profiles

The parameter which influences the temperature–time profile observed by an element under the surface of a plate most predominately is the *heat input* (J/m). It is usual to define

$$\text{heat input} = q/v \tag{2.16}$$

where v is the travel speed of the arc, and q is the arc power, given by

$$q = \eta \, I \, V \tag{2.17}$$

Here, I is the arc current, V the arc voltage and η an arc efficiency factor, which will vary from process to process. In the calculations which follow, and throughout this work, we assume $\eta = 0.75$ which is reasonable for the MMA process [31].

Large values of heat input will lead to large weld pools, and isotherms which penetrate deeply. Clearly, it would be wrong to consider merely the arc power, since large values of arc power can be compensated by large welding speeds. This point is illustrated by figure 2.8.

Close to the weld centre-line, the peak temperature of the thermal cycle is very large, but the cooling rate is very rapid, because of the large heat sink nearby. Further from the centre-line, the peak temperature is not so great, and the cooling rate not so rapid (figure 2.9).

2.4.2 Temperature–Distance Profiles

The form of the temperature distribution field given by equation 2.12 has already been illustrated by figure 2.2. Note that the intense heat source and the very effective heat sink of the plate result in extremely steep temperature gradients, particularly during heating. This is because the movement of the arc results in the isotherms 'piling up' ahead of the leading edge, due to the fact that the speed of the arc is considerably greater than the speed of thermal diffusivity in the workpiece.

The temperature–distance profile below the surface of the plate is important in determining the shape of the isotherms in the heat-affected zone, and the shape of the weld pool. This profile will be a function of time, and figure 2.10 illustrates such a profile, 3 seconds after the arc has passed, for the weld variables shown. If preheat is applied, the equations predict an effective numerical increase in the value of each isotherm, but do not influence the effective shape or range.

2.4.3 The Peak Temperature

For every pass in a multirun weld, there will be a peak temperature associated with each point in the weld material. This temperature will be the most important factor in determining the nature and extent of the phase transformations in the HAZ. It is therefore necessary to determine the peak temperature as a function of the weld variables which determine the heat flow.

This can be done by differentiating an expression for temperature with respect to time, and determining the time at which the peak temperature occurs, by setting $\partial T / \partial t = 0$. For equation 2.12, this yields

$$2at_p(2t_p + t_0)(t_p + t_0) = t_p^2 y^2 + (z + z_0)^2 (t_p + t_0)^2 \tag{2.18}$$

where t_p will be commonly referred to as the *peak time*. Equation 2.18 is a polynomial of the third degree in t_p. It can be shown that two of the three roots will be imaginary, leaving the third root unambiguously as the peak time, from which the peak temperature may be determined using equation 2.12.

Figure 2.11 shows the peak temperature variation below the surface of a plate. The weld variables are typical of the manual metal arc process.

REFERENCES

10. D. Rosenthal, Welding Journal Research Supplement, **20**, 220s–234s, (1941).
11. D. Rosenthal, Trans. ASME, **68**, 849–866, (1946).
12. H. Bornefeld, Technische Zentralblatt für Praktische Metalbearbeitung, **43**, 14–18, (1933).
13. J.C. Ion, Ph.D. Thesis, University of Luleå, Sweden, (1984).
14. N. Rykalin, A. Uglov and A. Kokova, 'Laser Machining and Welding', Chapter 3, Pergamon Press, Oxford, (1978).
15. N. Christensen, V. de L. Davies and K. Gjermundsen, British Welding Journal, **12**, 54–75, (1965).
16. S. Kou, Metall. Trans., **12A**, 2025–2030, (1978).
17. M.F. Ashby and K.E. Easterling, Acta Metall., **32**, 1935–1948, (1984).
18. W.-B. Li, K.E. Easterling and M.F. Ashby, Acta Metall., **34**, 1533–1543, (1986).
19. H.L. Shercliff and M.F. Ashby, Cambridge University Engineering Department Report CUED/C-Mat./TR134, (1986).
20. J.C. Ion, K.E. Easterling and M.F. Ashby, Acta Metall., **32**, 1949–1962, (1984).
21. J. Szekely, in 'Recent Trends in Welding Science and Technology', 3–11, Edited S.A. David & J.M. Vitek, ASM International, (1990).
22. V. Pavelic, R. Tanbakuchi, O.A. Uyehara and P.S.Myers, Welding Journal Research Supplement, **48**, 295s–305s, (1969).
23. B.A.B. Anderson, Trans. ASME, **100**, 356–362, (1978).
24. J.A. Goldak, A. Chakravarti and M.J. Bibby, Trans. AIME, **15B**, 299–305, (1984).
25. J.A. Goldak, M.J. Bibby, J. Moore, R. House and B. Patel, Trans. AIME, **17B**, 587–600, (1986).
26. J.A. Goldak, M. McDill, A. Oddy, R. House, X. Chi and M.J. Bibby, in 'Proceedings of an International Conference on Trends in Welding Technology', Edited S.A. David, ASM International, (1986).
27. J.A. Goldak, in 'Recent Trends in Welding Science and Technology', 71–82, Edited S.A. David & J.M. Vitek, ASM International, (1990).
28. J.F. Lancaster, The Physics of Welding, 2nd Edition, Pergamon Press, (1986).
29. H.K.D.H. Bhadeshia, L.-E. Svensson and B. Gretoft, Acta Metall., **33**, 1271–1283, (1985).
30. Welding Handbook, p.79, 7th Edition, 1, American Welding Society, (1981).
31. K.E. Easterling, 'Introduction to the Physical Metallurgy of Welding', Butterworths Press, (1983).
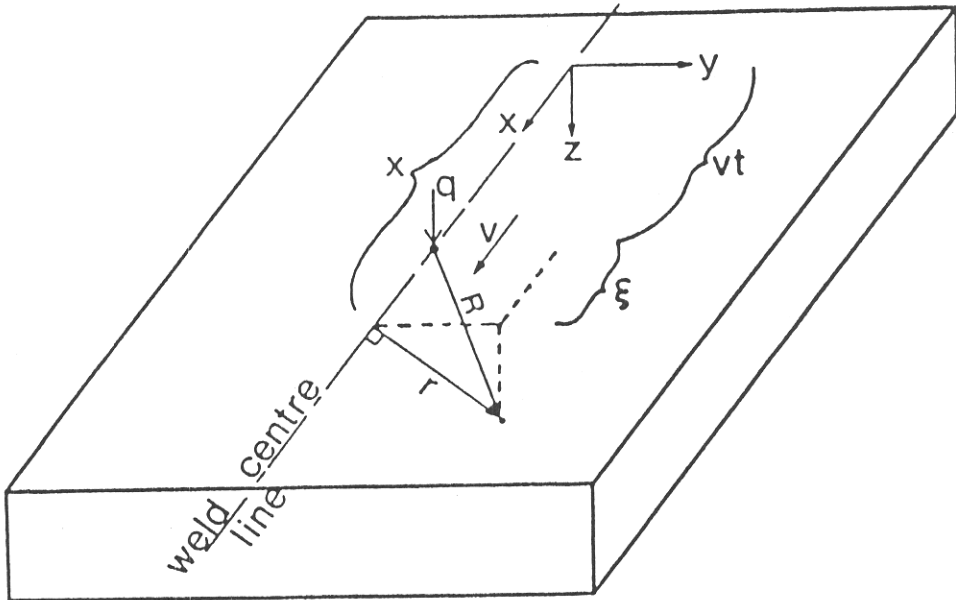
Figure 2.1: Geometry and coordinate systems used for the analysis of the Rosenthal equations. After Ion [13].

$$T_0 = 298\,\text{K}$$
$$q = 1500\,\text{J/s}$$
$$v = 4\,\text{mm/s}$$
$$r_b = 2\,\text{mm}$$
$$z = 5\,\text{mm}$$

Peak Temperature: 718.3 K
Dimensions of Plot: 80 mm × 100 mm ($\equiv$ 20 seconds)
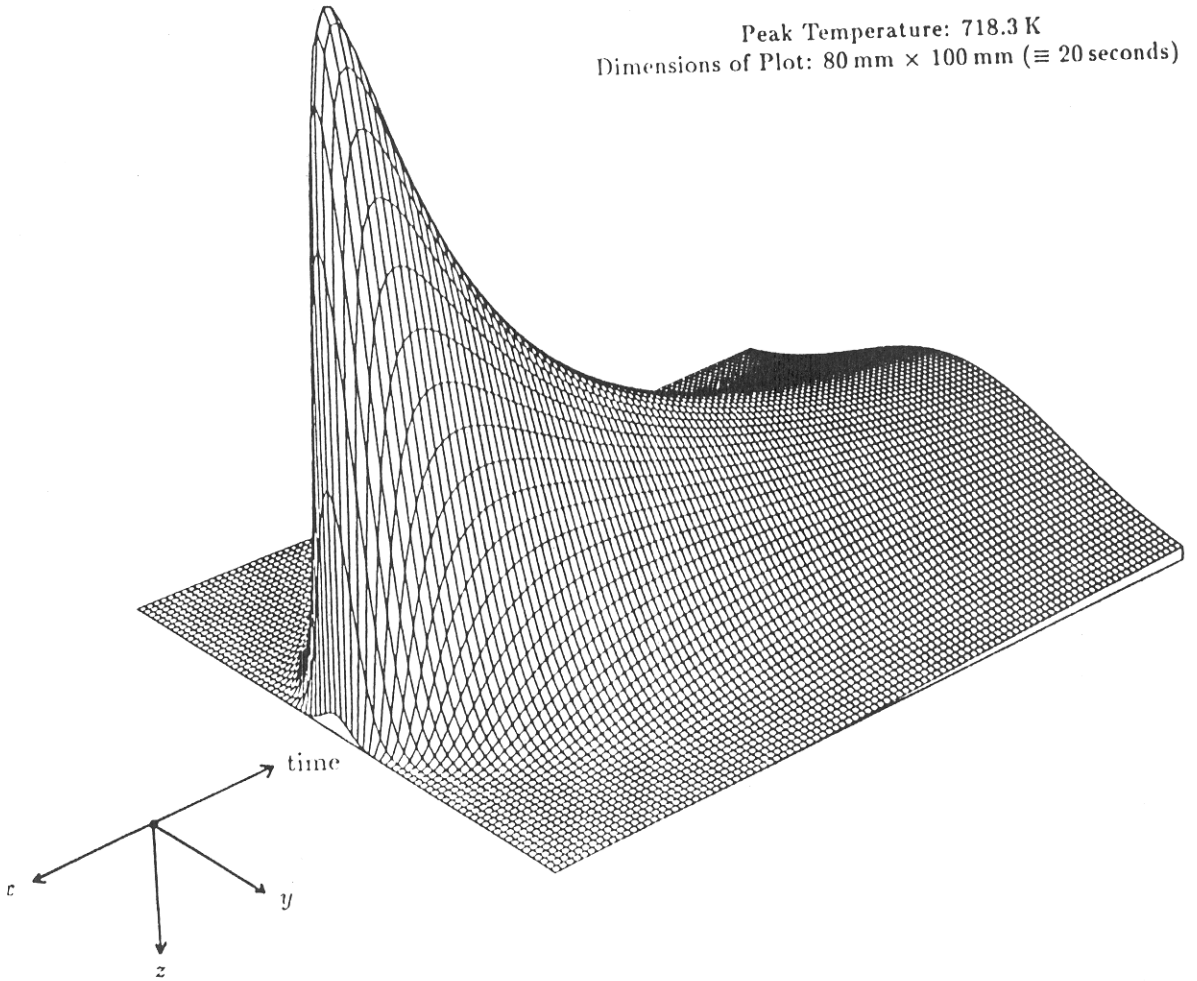
Figure 2.2: Illustrating the 'quasi-stationary' nature of the heat flow problem. The temperature distribution around the heat source is steady with respect to the coordinate system moving with the heat source, initial and final transients excepted.
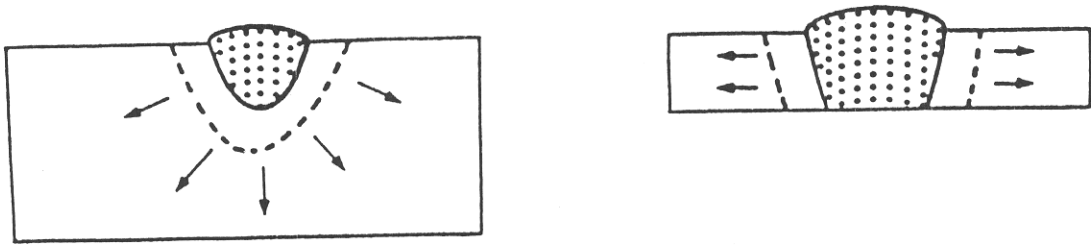
Figure 2.3: Illustrating 3D (left) and 2D (right) heat flow likely to be observed in thick and thin plates respectively. After Ion [13].
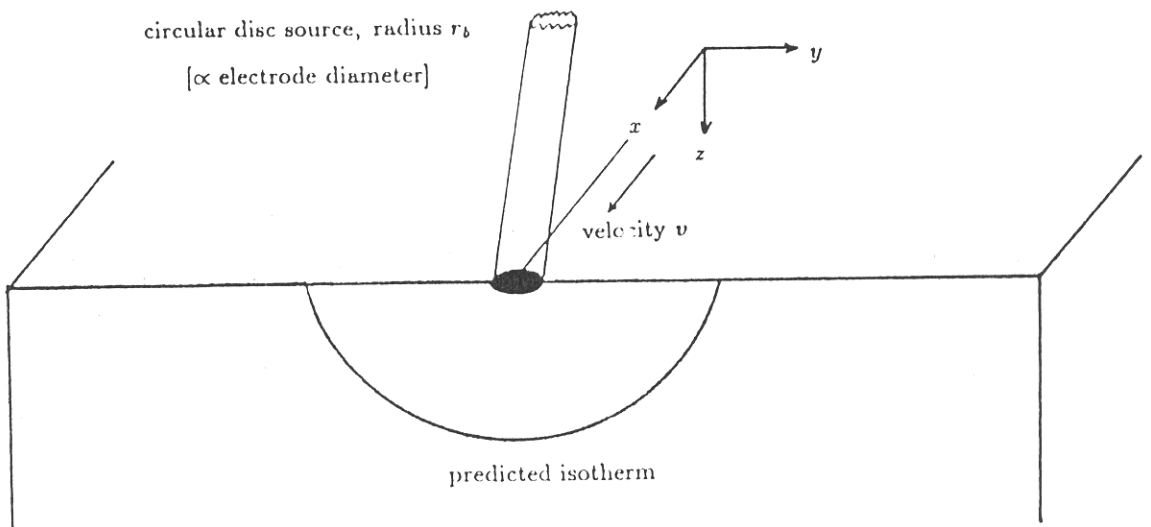
Figure 2.4: The circular disc source travels across the surface of the plate at uniform speed.
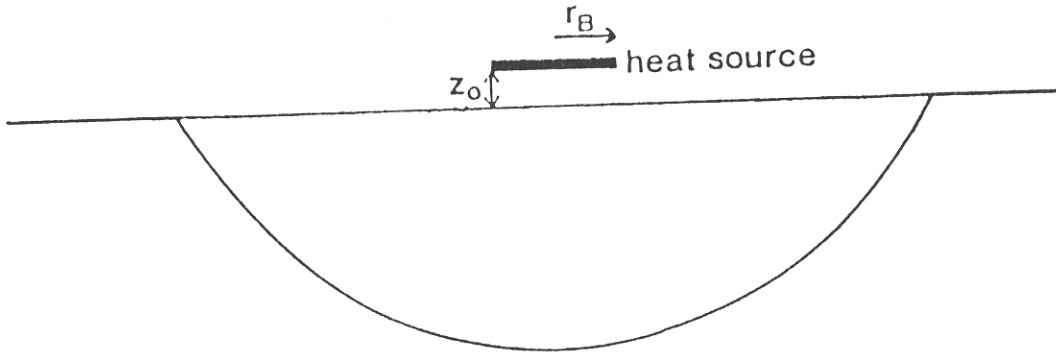
Figure 2.5: The terms r_b and z_0 as defined by Ashby & Easterling [17]. After Ion [13].
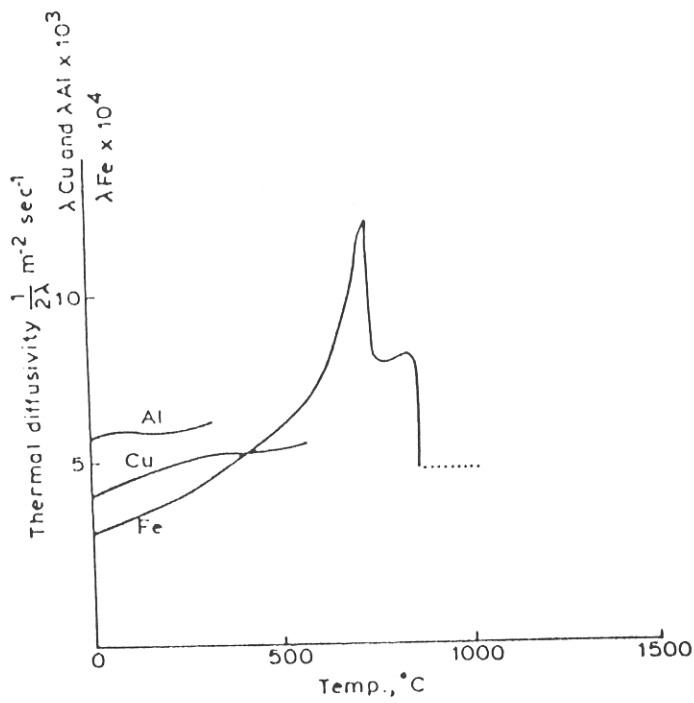
Figure 2.6: The variation of the thermal diffusivity of iron, aluminium and copper with temperature. After Easterling [31].

21
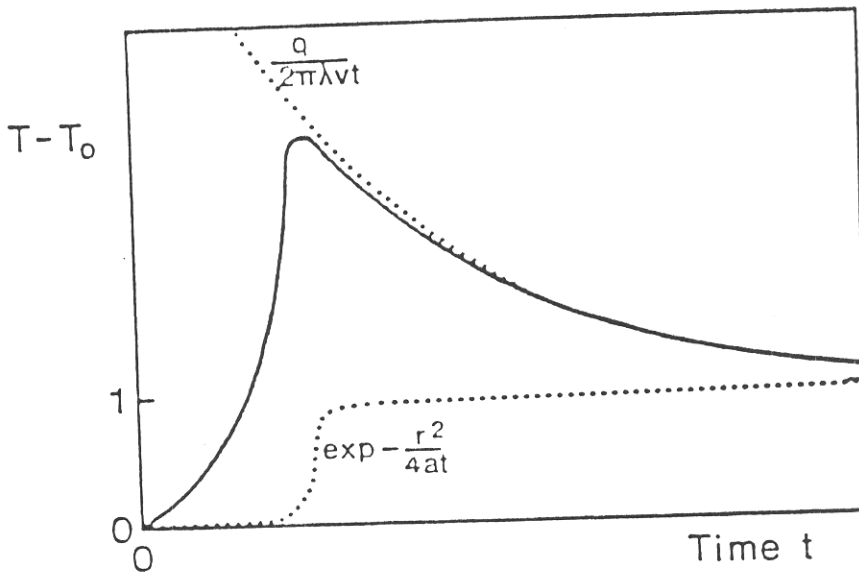
Figure 2.7: The approximation to the temperature-time variation in the case of the thick plate. The expression (equation 2.4) can be represented by the product of the two terms shown, to one of which the expression tends after the peak temperature has been reached. After Ion [13].
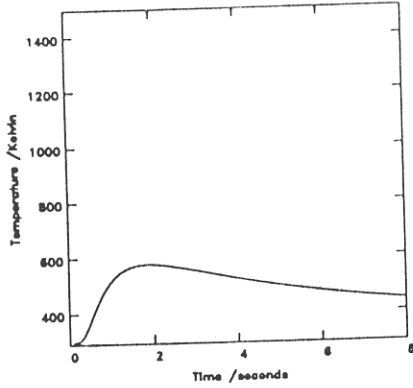
$T_0 = 298$ K
$q = 1500$ J/s
$v = 4$ mm/s
$r_b = 2$ mm
$y = 5$ mm
$z = 5$ mm

Peak Temperature = 576.3 K
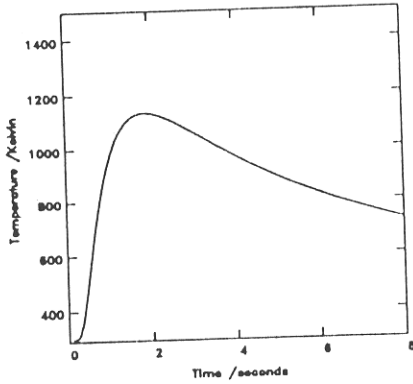
$T_0 = 298$ K
$q = 4500$ J/s
$v = 4$ mm/s
$r_b = 2$ mm
$y = 5$ mm
$z = 5$ mm

Peak Temperature = 1132.9 K
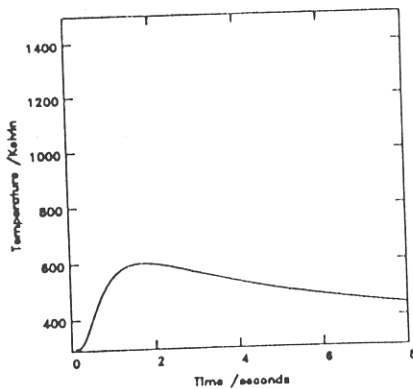
$T_0 = 298$ K
$q = 4500$ J/s
$v = 12$ mm/s
$r_b = 2$ mm
$y = 5$ mm
$z = 5$ mm

Peak Temperature = 599.0 K

Figure 2.8: Showing that the *heat input* controls the thermal cycle for a given point in the heat-affected zone. Top, the cooling curve for $q = 1500$ J s^{-1}, $v = 4$ mm s^{-1}. Middle, same conditions, but q increased to 4500 J s^{-1}. Bottom, almost complete compensation by increasing v to 12 mm s^{-1}.
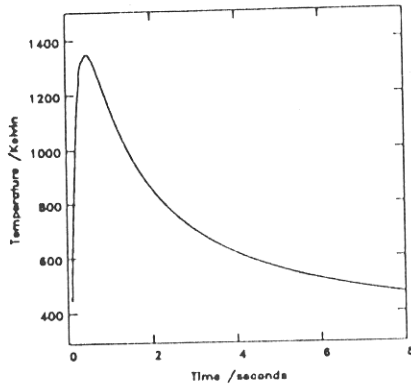
$T_0 = 298\,\mathrm{K}$

$q = 1500\,\mathrm{J/s}$

$v = 4\,\mathrm{mm/s}$

$r_b = 2\,\mathrm{mm}$

$y = 2\,\mathrm{mm}$

$z = 2\,\mathrm{mm}$

Peak Temperature $= 1349.4\,\mathrm{K}$
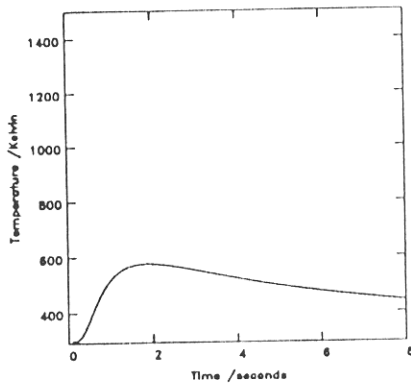
$T_0 = 298\,\mathrm{K}$

$q = 1500\,\mathrm{J/s}$

$v = 4\,\mathrm{mm/s}$

$r_b = 2\,\mathrm{mm}$

$y = 5\,\mathrm{mm}$

$z = 5\,\mathrm{mm}$

Peak Temperature $= 576.3\,\mathrm{K}$

Figure 2.9: Comparing the temperature–time profiles as a function of position. Near the centre-line, the peak temperature is large, and the cooling rate high. Further from the centre-line, the peak temperature is not so great, and the cooling rate not so rapid.

$$T_0 = 298\,\mathrm{K}$$
$$q = 1500\,\mathrm{J/s}$$
$$v = 4\,\mathrm{mm/s}$$
$$r_b = 2\,\mathrm{mm}$$
$$t = 3\,\mathrm{s}$$

Dimensions of Plot: $50\,\mathrm{mm} \times 25\,\mathrm{mm}$
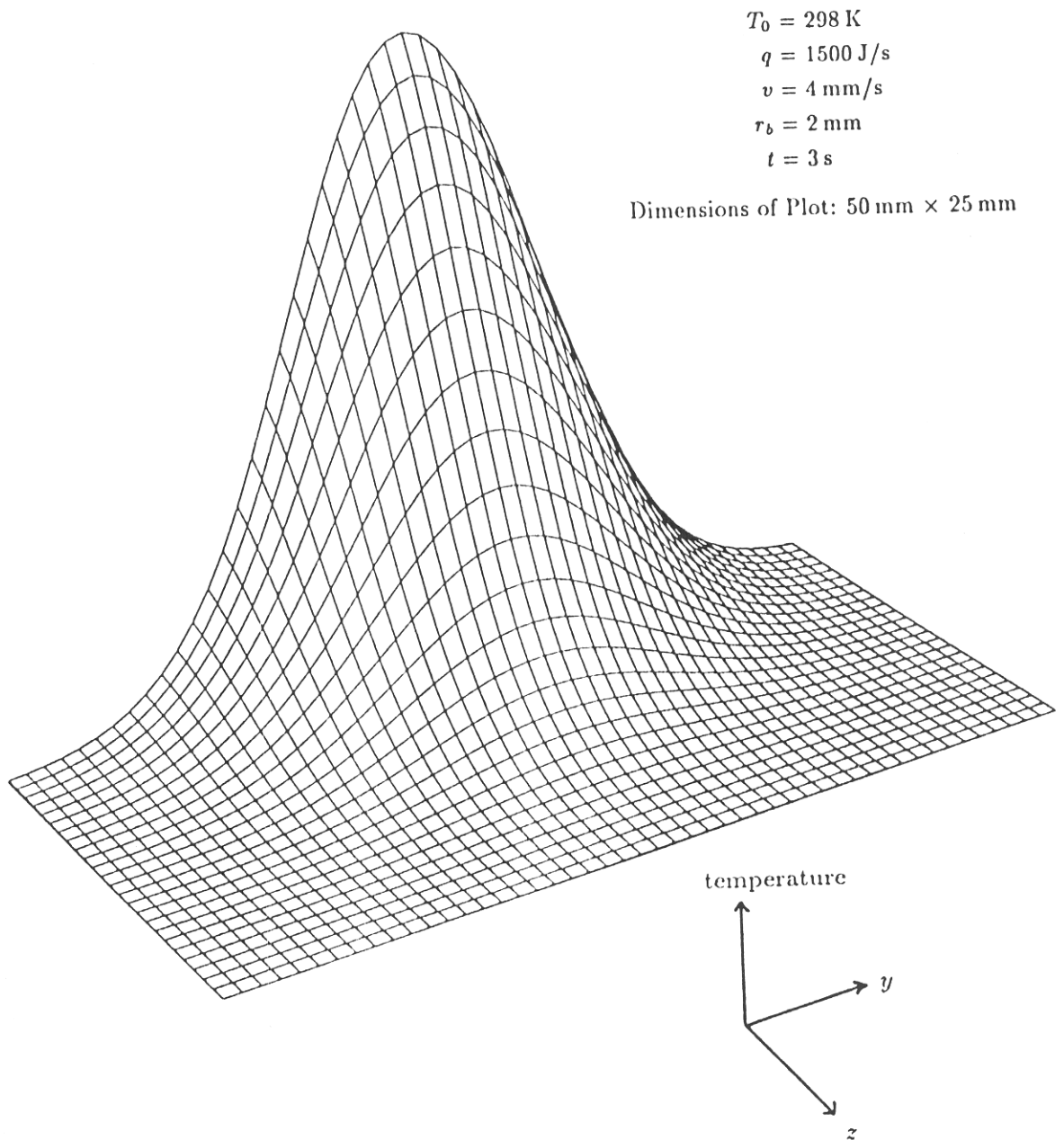
Figure 2.10: The temperature–distance profile below the surface of a plate, 3 seconds after the arc has passed. The welding conditions shown are typical of the manual metal arc process.
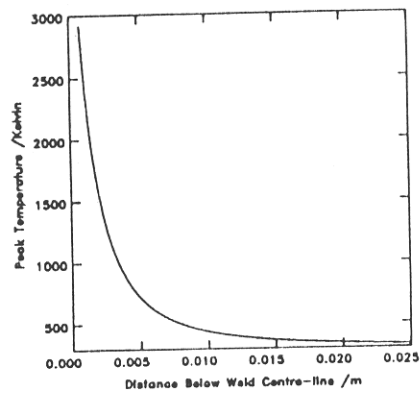
$T_0 = 298\,\mathrm{K}$
$q = 1500\,\mathrm{J/s}$
$v = 4\,\mathrm{mm/s}$
$r_b = 2\,\mathrm{mm}$
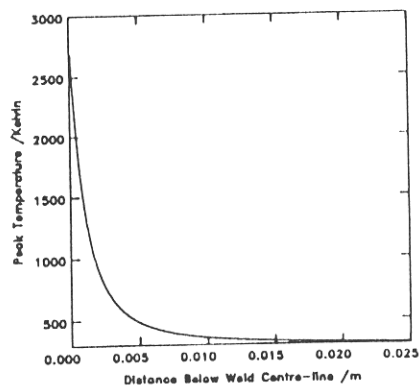
$T_0 = 298\,\mathrm{K}$
$q = 1500\,\mathrm{J/s}$
$v = 10\,\mathrm{mm/s}$
$r_b = 2\,\mathrm{mm}$

Figure 2.11: Peak temperature–distance profiles below the surface of a plate. Top, $q = 1500\,\mathrm{J\,s^{-1}}$, $v = 4\,\mathrm{mm\,s^{-1}}$. Bottom, $q = 1500\,\mathrm{J\,s^{-1}}$, $v = 10\,\mathrm{mm\,s^{-1}}$.

CHAPTER THREE
A Model For Multipass Steel Welds

Nomenclature

A_1	weld bead reinforcement area (figure 3.2)
A_2	cross-section of baseplate melted by arc (figure 3.2)
Ac3	temperature at which $\alpha \rightarrow \gamma$ transformation is complete, on heating
Ae3	equilibrium $\gamma/(\gamma + \alpha)$ temperature
Ac1	temperature at which $\alpha \rightarrow \gamma$ transformation begins, on heating
Ae1	equilibrium $\alpha/(\gamma + \alpha)$ temperature
a	width of single bead-on-plate weld (figure 3.2)
b	weld bead spacing (equation 3.7)
d	diameter of electrode
h	height of single bead-on-plate weld (figure 3.2)
I	arc current
K	constant in equation 3.8
L	latent heat of melting per unit volume
p	penetration of single bead-on-plate weld (figure 3.2)
q	effective arc power (equation 2.17)
q^*	effective arc power, after latent heat correction (equation 3.5)
r_b	radius of circular disc heat source
R_1	reaustenitisation distance, defined as the distance between solidus and Ac3 isotherms, measured beneath the weld centre-line.
R_2	reinforcement height
T_{gc}	γ-grain coarsening temperature
T_s	solidus temperature
T_t	tempering temperature
v	welding speed
Δ	% weld bead overlap
θ	angle used to define shape of A_1 (figure 3.2)
ρ	density of electrode (equation 3.8)

3.1 Introduction

Despite the fact that the welding process is a sophisticated as well as a crucial operation, the practice of fusion welding has, until the past ten years or so, not been amenable to theoretical modelling. Welding metallurgists have relied upon their knowledge and experience accumulated through lengthy, and often expensive experimentation, summarised in tables, charts and databases. Such empiricism has proved immensely successful and has led to codes of practice which have been adopted throughout the world.

However, the approach is often less than satisfactory in a number of senses. Firstly, many of the problems associated with fusion welding arise because metallurgical phenomena act to weaken localised regions of microstructure; solidification cracking, 'type IV' cracking and hydrogen-induced cracking are good examples. The empirical approach to welding design, which involves the production of a large number of trial welds with associated mechanical testing, fails to recognise the intimate relationship between microstructure and properties. Often, the approach is expensive and time consuming too. Secondly, even when the microstructure is studied, the inability to *predict* the microstructure of welds in a fundamental way means that structure/property relationships are difficult to establish on a genera

27

basis, with each study being restricted in application to the particular set of circumstances considered. Extrapolation between alloy systems and different sets of welding variables can be dangerous. Thirdly, without the ability to predict the microstructure and properties in a quite general way, it is difficult to be certain whether existing welding procedures have been optimised. The development of welding consumables and design of new geometries is restricted, and it is quite possible that potentially novel welding designs are missed.

Part of the reason for the empirical, rather than theoretical, approach is that the process of welding is exceedingly complex. The number of process and metallurgical variables is large, and the nature of the weld thermal cycle is such that very rapid heating and cooling rates can occur. Thus, to be able to predict the microstructure with any accuracy, it is necessary to understand the *kinetics* of the phase transformations involved, since only minimal time is available for equilibrium to be attained.

Recent research [4,5,6] has been based soundly upon the principles of phase transformation theory and as a consequence it is now possible to estimate the volume fractions of phases present in the as-deposited weld metal (the primary microstructure). Typically, this consists of a mixture of one or more of the phases allotriomorphic ferrite, Widmanstätten ferrite, acicular ferrite, martensite, retained austenite or degenerate pearlite, contained within the columnar prior austenite grains of the solidification structure. For multipass welds, or the heat-affected zone, there remains no satisfactory model. Some attempts have been made (*e.g.* [32,33]) but these are largely empirical in form, and do not make any quantitative predictions concerning the volume fractions of phases in the reheated fusion zone, or the heat-affected zone, because they do not take account of the phase transformation theory which is at the heart of the problem. The absence of such a model is significant because, as figure 1.4 indicates, it is not the primary microstructure which controls the mechanical properties of multipass welds, rather the secondary microstructure and/or the heat-affected zone (HAZ). The work described here represents a first attempt at designing such a model.

3.2 The Single Bead-on-Plate Weld

The starting point for the prediction of both fusion zone and heat-affected zone properties is a rigorous analysis of the *single bead-on-plate weld*. This involves the deposition of a single pass of metal on the surface of a plate. The flow of heat from the arc causes each point in the baseplate to experience a thermal cycle, the kinetic strength of which depends upon the distance from the heat source, for a given set of weld variables. In low-alloy steels, it is possible to identify Ac1, Ac3 and the solidus isotherms in the heat-affected zone (which in this case lies in the baseplate). The region between the Ac3 and solidus isotherms is completely reaustenitised, whereas that between Ac3 and Ac1 isotherms only partially transforms to austenite during heating, and all regions heated to temperatures less than Ac1 are tempered (figure 3.1).

The use of the word *weld* in this context is therefore unfortunate, because no joining is involved. Nonetheless this kind of deposit has relevance to, for example, the hardfacing process, where a hard, wear resistant layer is deposited by a MMA, TIG or laser-cladding technique. As figure 3.2 shows, the size and shape of the weld is highly dependent upon the weld variables; it is only after understanding these effects that the more complicated problem of multipass welds can be tackled. In the calculations which follow, it is shown that the single bead-on-plate weld can be described satisfactorily using analytical heat-flow equations [17] coupled with a knowledge of the rate at which the weld metal is deposited.

3.2.1 Calculation of Weld Bead Reinforcement

The volume of material deposited per unit length of weld (measured along the welding line) corresponds to the area A_1 in figure 3.3; it is generally referred to as the *weld bead reinforcement*. Its magnitude, which determines the number of weld beads required to fill a particular weld geometry, is

given by

$$\text{Area } A_1 = \frac{\pi \text{ electrode diameter}^2}{4} \times \text{recovery} \times \frac{\text{feed speed}}{\text{welding speed}} \qquad (3.1)$$

for the case of MMA welding. The welding speed is the speed at which the arc traverses the baseplate, and the feed speed refers to the rate of consumption of the wire which is being melted. In the case of MMA welding, this is the electrode itself. A recovery term must be incorporated, because the amount of material deposited differs from the amount of *electrode* melted per unit time. This occurs because the electrodes are covered with a flux containing elements and compounds which contribute to the chemistry of the weld pool; this permits the composition of the weld deposit to be modified.

In order to test equation 3.1, values of A_1 were calculated from the values of electrode diameter, welding speed and feed speed measured by Clark [34]. This work is one of the best available sources of data for the MMA single bead-on-plate weld, and one in which the weld bead dimensions have been carefully measured. Values [35] of the recovery term, for the Suprex B electrodes employed, are listed in Appendix 3.1. The calculated values of A_1 compare reasonably with the measured values (figure 3.4).

3.2.2 Calculation of Weld Bead Reinforcement Shape

A weld bead width and height follow from the definition of the reinforcement area A_1 (figure 3.3). The weld bead height h refers to a perpendicular height *above* the undisturbed baseplate, and the weld bead width a refers to the width measured *along* the undisturbed baseplate.

In order to estimate a and h, we make the common assumption (*e.g.* [32]) that the reinforcement area is bounded by a circular arc which subtends an angle of 2θ beneath the surface of the plate, so that it takes the shape of a spherical cap on the surface of the baseplate. The angle θ is then the 'contact angle' by analogy with a droplet lying on a sheet of glass. With this spherical cap geometry, a and h are related to θ through the equations

$$a = \left[\frac{4A_1}{\theta/\sin^2\theta - \cos\theta/\sin\theta} \right]^{1/2} \qquad (3.2)$$

and

$$h = \left[\frac{A_1}{\theta - \sin\theta\cos\theta} \right]^{1/2} (1 - \cos\theta) \qquad (3.3)$$

and the angle θ is dependent upon the ratio a/h only, and is independent of the exact magnitude of A_1:

$$\theta = \sin^{-1} \left\{ \frac{4a/h}{4 + (a/h)^2} \right\} \qquad (3.4)$$

The angle θ can influence the properties of multipass welds. For example, a large value of θ results in a rather tall or 'crowned' [36] weld bead. Thus a welder is likely to deposit a greater number of beads per layer, so that the 'average reinforcement height' (the distance between weld layers) is larger.

In order to test out the assumptions inherent in this geometry, equations 3.1, 3.2 & 3.3 were used to calculate values of a and h for various values of θ. The values of θ which gave the best agreement between measured and calculated values of a and h (determined by the gradient of the best-fit line being equal to unity) were 50.9° and 62.9° respectively. An average value of 56.9° was then used to calculate values of a and h which were then compared with the experimental values (figures 3.5 & 3.6). The analysis shows that it is reasonable to assume that the weld metal which contributes to reinforcement during MMA welding adopts a spherical cap geometry in cross-section.

3.2.3 Use of Heat-Flow Equations for Weld Isotherms

In the previous chapter of this dissertation, the equations due to Ashby & Easterling [17] were chosen as the best analytical solution to the problem of the moving heat source. The equations extend

the power intensity of the heat source over a finite area, so that, the temperature predicted at the weld centre-line no longer rises to infinity. In principle, such equations can be used to calculate the positions of the weld bead isotherms.

However, it is necessary to study the effect of extending the heat source. In Ashby & Easterling's original reference, they state that the radius of the circular disc source is likely to be proportional to the radius of the electrode itself. It is therefore appropriate to determine a suitable value for the constant of proportionality relating these two quantities:

$$\text{Radius of Circular Disc Source } r_b = \text{Proportionality Factor} \times \text{Electrode Radius} \qquad (3.5)$$

In the calculations which follow, estimated equilibrium melting and Ae3 temperatures (1520°C and 850°C respectively) were used to define the solidus and Ac3 isotherms for the mild steel baseplate used in Clark's work. As discussed by Ashby & Easterling [17] a significant part of the arc energy is absorbed as latent heat of fusion, and as such is temporarily unavailable to melt more material. The power q^* available to raise the temperature of the remaining solid is then

$$q^* = q - vLA_2 \qquad (3.6)$$

where q is the effective arc power (given by equation 2.17), v is the welding speed, L the latent heat of melting per unit volume (taken as 2.1×10^9 Jm^{-3} [17]), and A_2 is the cross-sectional area of baseplate which is melted. Unlike Ashby & Easterling [17], this correction is applied to the calculation of the solidus *and* the other temperature contours. This ensures that the temperature field produced by the equations is self-consistent. The method involves finding the value of q^* which, when used in place of q in equations 2.12 & 2.18, satisfies equation 3.6. Since A_2 is a function of q^*, this equation must be solved iteratively. Figures 3.7 & 3.8 illustrate the effect of extending the heat source, for typical weld variables. As the proportionality factor in equation 3.5 is increased, so that the arc power density is lowered, both the weld bead width and the penetration decrease.

In an effort to find the best-fit value of this parameter, values between 1.0 & 2.0 were used to determine a, p and the reaustenitisation distance R_1, defined as the between the Ac3 and solidus isotherms, measured beneath the weld centre-line. The weld bead height h also follows, since the reinforcement area A_1 can be calculated from equation 3.1. It was found that a value of 1.6 for the aforementioned proportionality factor described the experimental data satisfactorily. The results of the statistical analysis are presented in table 3.1. The calculated values of width and penetration are compared with the observed values, in figures 3.9 & 3.10.

	Correlation Coefficient	Regression Coefficient
Weld Bead Width a	0.89	1.02
Weld Bead Penetration p	0.67	1.03
Weld Bead Reaustenitisation Distance R_1	0.79	1.19
Weld Bead Height h	0.68	0.86
Weld Bead Reinforcement Area A_1	0.93	1.07

Table 3.1: Results of statistical analysis on single bead-on-plate welds. Data is from Clark [34]. The diameter of the circular disc source is taken as 1.6 times that of the appropriate electrode diameter.

The heat-flow equations overpredict Clark's experimental values of the reaustenitisation distance by approximately 19%, and it was found that the magnitude of this overprediction was unchanged for all values of the proportionality factor considered. The overprediction of the reaustenitisation distance can be attributed to the fact that reaustenitisation is unlikely to occur at the equilibrium Ae3 temperature. This is due to the very rapid heating rates (typically $\sim$500°C s^{-1}) caused by the passage of the arc, and because the time available for transformation to austenite during the weld thermal cycle is exceedingly

short. Both these factors act to raise the effective transformation temperature. The analysis was repeated for values of Ac3 temperatures lying above 850°C and it was found that with Ac3 equal to 910°C the regression coefficient for the calculation for the reaustenitisation distance was unity.

The above analysis indicates that the heat-flow equations predict the positions of the solidus and the Ac3 isotherm to a satisfactory degree. In view of the inherent difficulty in quantifying manual processes, and the variability associated with the arc itself, these equations represent a useful approximation to the problem of heat-flow in thick-plate (3D) welding, at least for the MMA process. In welding processes such as the submerged arc process, where the heat input is generally higher, the fusion boundary can be non-gaussian in shape. In that case, there is evidence for a two stage melting process [37] in which the passage of the powerful arc causes the 'digging' of a 'weld finger' and the superheating of the molten metal creates a secondary melting process which causes a characteristic 'weld crater'. It should be noted that the equations considered here are not capable of predicting non-gaussian fusion profiles.

3.2.4 Summary

The size and shape of the single bead-on-plate weld, and the temperature field below the fusion isotherm, can be computed from the heat-flow equations, together with a knowledge of the volume of metal deposited per unit length of weld. This volume is simply related to the electrode diameter, the feed speed of the electrode, the arc speed and a recovery term. The methodology for such a computation is as follows:

- Calculate the solidus, Ac3 and Ac1 isotherms using the heat-flow equations. The equilibrium melting, Ae3 and Ae1 temperatures can be assumed in the absence of better estimates. This yields the weld bead width and penetration.
- Calculate the volume of metal deposited per unit length of weld. This corresponds to the cross-sectional area of the weld bead.
- Assume this reinforcement area adopts the shape of a spherical cap on the surface of the plate. Calculate the height of the weld bead above the original baseplate.

3.3 Multipass Welds

In multipass welds, the gap between the components to be joined is filled using a sequence of weld passes, each of which fills only a part of the weld gap. The metal deposited is therefore influenced significantly by the additional thermal cycles induced by the deposition of subsequent passes. Only the final pass to be deposited can then be expected to exhibit a true primary microstructure. The remaining regions of the welds may have undergone transient temperature rises high enough to cause partial or complete reverse transformation to austenite, which on subsequent cooling retransforms to ferrite, but not necessarily to the same microstructure as the primary regions. The regions which do not experience peak temperatures high enough to cause reversion to austenite, are tempered to an extent which is dependent on factors such as the starting microstructure and alloy chemistry.

In order to model multipass welds, consider first a sequence of weld beads deposited side-by-side in a single layer on a plate. The spacing between weld beads determines the number of weld beads deposited within the layer, and the % overlap Δ between weld beads can be defined through the equation [32]

$$b = a \left(\frac{100 - \Delta}{100} \right) \tag{3.7}$$

where b is the weld bead spacing. The configuration is illustrated in Figures 3.11a & 3.12a. It is again possible to identify the isotherms in the HAZ, but this time for simplicity the overlapping of isotherms from adjacent beads is ignored. The effect of deposition is such as to raise the surface of the workpiece although in practice this is no longer flat, it is nevertheless possible to define [32] a *reinforcement heigh*

31

R_2 which corresponds to the "average" distance by which the height of the workpiece is raised. A multipass weld can be considered as a sequence of these layers, one above the last (figures 3.11b & 3.12b).

The above discussion illustrates that the microstructure (and hence the properties) of multipass welds is dependent upon the degree to which adjacent weld beads and layers overlap. There will, in general, be large variations in the microstructure as a function of position. In a later part of this work, emphasis is placed upon designing a weld in which such variations are eliminated. One condition for this is that all regions of as-deposited metal become reaustenitised by the deposition of subsequent passes. As figures 3.11 and 3.12 show, in the simplified case of the spacing of weld beads being uniform, and assuming the new weld beads are placed directly over the centre-lines of the beads in the original layer, the condition for the heat input associated with the deposition of the second layer to completely reaustenitise the metal deposited in the first layer, is given by $R_1 \geq R_2$, where R_1 is the reaustenitisation distance defined earlier. In practice, the spacing between weld beads in a multipass weld tends to be non-uniform. The weld beads in any given layer are not deposited exactly above those in the previous layer, and after the deposition of the first layer the workpiece surface is no longer flat, but adopts the contours of the individual beads. This can be partly a consequence of the human error associated with the manual component of the welding processes. However, there is also the physical constraint that an integral number of beads must be deposited in any layer of the weld, the space available being determined by the weld geometry. In these circumstances, it is possible for unreaustenitised regions to exist even though the condition $R_1 > R_2$ is not violated. Therefore, a more general criterion which must be met if a fully reaustenitised weld is to be approached is that the ratio R_1/R_2 be maximised.

3.4 Classification Scheme For Multipass Weldments

The considerable amount of microstructural work which has been carried out for multipass welds has suffered from the lack of a scheme by which to characterise the various microstructures. Such a scheme is particularly necessary when the isotherms from neighbouring weld passes lie very close to each other, so that the microstructure changes over distances as small as 200 μm. A scheme is now introduced, and it forms the basis for the methodology of the computer model.

Consider a series of weld thermal cycles, as depicted in figure 3.13. These have been calculated [17] for weld variables typical of the manual metal arc process. It should be noted that it is the *peak* of the thermal cycle which describes the essence of the kinetic effect; for example, there is an obvious correlation between the peak temperature and the cooling rate past any chosen temperature. This has given rise to the idea that a set of weld thermal cycles can be divided broadly into a number of categories. Thermal cycles which then fall into the same category, should be expected to have a similar microstructural effect.

There remains the question of choosing critical values of the peak temperatures, to distinguish the various categories of thermal cycles. These peak temperatures should have physical significance in terms of the microstructure. To provide maximum flexibility, the temperatures chosen, and used throughout this work are:

T_s solidus temperature

T_{gc} γ-grain coarsening temperature

Ac3 temperature at which $\alpha \rightarrow \gamma$ reaction is complete, on heating.

Ac1 temperature at which $\alpha \rightarrow \gamma$ reaction begins, on heating.

T_t tempering temperature, < Ac1.

The temperature at which γ-grain growth accelerates due to the dissolution of pinning carbides or nitrides is referred to as T_{gc}; it lies between Ac3 and T_s, and even in the absence of a well-defined abnormal γ-grain growth temperature, may be used to define the positions where γ-grains have grown to

a particular ('large') size. In a similar way, T_t defines a temperature (below Ac1) above which tempering occurs to a significant degree.

It could be used to define a thermal cycle strong enough to recrystallise the microstructure, or to coarsen carbides such as cementite, or otherwise. Events in regions where the temperature does not exceed T_t are considered not to have a significant effect on the microstructure and properties. A thermal cycle is then denoted by one of the letters $A \rightarrow F$, the particular letter being dependent upon the magnitude of the peak temperature. Table 3.2 illustrates the notation.

NOTATION	EXPLANATION		
A		Peak Temp. $>$	T_s
B	$T_s >$	Peak Temp. $>$	T_{gc}
C	$T_{gc} >$	Peak Temp. $>$	Ac3
D	Ac3 $>$	Peak Temp. $>$	Ac1
E	Ac1 $>$	Peak Temp. $>$	T_t
F	$T_t >$	Peak Temp.	

Table 3.2: Division and notation of weld thermal cycles dependent upon the peak temperature.

A series of sequential weld thermal cycles (e.g. A, C, D & F, in that order) experienced by one point in weld-space can then be represented by a series of letters (e.g. ACDF in this case). The computer model uses this notation to describe the temperature fields.

3.5 The Model

Since this work is a part of a project whose aim it is to provide a facility for modelling the complete microstructure of multipass welds and their heat-affected zones, the method used is designed to be flexible in terms of joint geometry, welding procedures and alloy chemistry, with the penalty that the computing times involved can become rather large. The methodology of the program involves superimposing a square mesh of size 100 μm by 100 μm upon the entire joint and parent plate, the dimensions and shape of which are specified by the user. Throughout the computation, each element in the mesh is then associated with one component of a multidimensional matrix; while the program is running, the matrix is filled with as much information as is necessary to determine the required output. Specifically, the thermal cycles associated with each element are recorded, as the beads are deposited, until the weld gap is filled. The matrix approach has the advantage that it is a relatively easy matter to determine quantitatively the volume fraction of all regions (either within the fusion zone or the parent plate or the entire assembly) which have experienced a specified sequence of thermal treatments.

The program first computes the data associated with the single bead-on-plate weld, using the method prescribed, and uses this as a "building block" for the multipass weld. The variables required are therefore the interpass temperature, the electrode recovery, arc current, arc voltage, electrode diameter, welding speed and wire feed speed; these values, together with the arc efficiency, thermal diffusivity, thermal conductivity (refer to chapter two) and latent heat of melting allow the weld thermal cycles to be calculated using equation 2.12.

To build up the multipass weld, the user must choose one of two options. The first involves specifying the number of beads deposited in each layer; the program then assumes that these beads are to be spaced evenly within that layer. The other option requires the user to specify the weld bead overlap Δ [7]; the program then attempts to accommodate this value. However, some beads cannot be deposited at the the same distance apart because it is necessary to deposit an integral number of beads within each layer, and in those cases, the program fits an uneven spacing in the central region of the weld. In all cases, weld beads are deposited at the very end of each layer, next to the near-vertical face of the plate being welded. Once a layer of beads has been deposited, the program computes the amount of material deposited in that layer, followed by reinforcement height [7]. The next layer of beads is then deposited at this 'average' height above the previous layer.

Using the above methodology it is possible to locate the positions of the weld centre-lines for each of the weld passes, for any required geometry. Figure 3.14 illustrates schematically the locations of the weld centre-lines computed for the experimental weld examined later in this work.

In applying the analytical solution for the temperature field around each of the weld centre-lines, it is necessary to make certain approximations when weld beads are deposited at the end of each layer, next to the near-vertical face (figure 3.15). In this case, the distances ab & bc are assumed to be equal to half the weld bead width, $a/2$ and be & bd are set equal to the weld bead penetration p. This is done by dividing the HAZ into three regions abe, bde & bcd. For the region abe the z & y co-ordinates in equation 2.12 are assumed to lie along be & ba respectively. For bcd z & y are assumed to lie along bd & bc respectively. For bde, y in equation 2.12 is set equal to zero, and z is assumed to be equal to the distance from point b. The area abc is set equal to the area A_1 (calculated using equation 3.1) and the arc ac is assumed to be circular, such that the centre of the circle lies on the bisector of the angle ebd.

Within each weld layer, the fusion profiles are assumed to be superimposed (figure 3.16) and thus the model does not properly take into account the remelting of the weld metal from adjacent weld beads. Indeed, it is not easy to see how this effect could be incorporated into such a model. However, since a large proportion of the weld metal above OO′ is remelted by the deposition of the subsequent layer of weld beads, the inaccuracy incurred is considered to be small. To calculate the thermal cycles experienced by the adjacent weld metal lying above OO′, the z & y co-ordinates in equation 2.12 are assumed to lie along e′b′ & e′a′ respectively.

To create images of the multipass welds, a colour is assigned to each element in weld-space, chosen such that each colour is associated with a particular set of weld thermal cycles. Figure 3.17 tabulates the sets of weld thermal cycles, together with the associated colours chosen; this scheme is adopted throughout this work.

3.6 Calculations: The Effect of the Weld Variables

In order to test the validity of the model developed, an attempt is now made to compare the predictions of the model with experimental observations. In the calculations which follow, we assume a range of values for the interpass temperature, arc current, arc voltage, electrode diameter and arc travel speed; these are tabulated in table 6.3. In addition, values for the recovery of the electrodes are taken from appendix 3.1, and the weld bead overlap is held constant at 35%. The values of the weld variables in table 3.3 span the ranges measured experimentally by Clark [34].

VARIABLE	VALUES EMPLOYED
Interpass Temperature	20 °C, 100 °C, 200 °C, 250 °C
Arc Current	75 A, 100 A, 150 A, 200 A, 250 A
Arc Voltage	24.0 V
Electrode Diameter	2.5 mm, 3.25 mm, 4 mm, 5 mm, 6 mm
Welding Speed	2.0 mm s^{-1}, 4.0 mm s^{-1}, 6.0 mm s^{-1}, 8.0 mm s^{-1}, 10.0 mm s^{-1}

Table 3.3: The weld variables used in the theoretical analysis.

An effort was made to reduce the number of weld variables necessary for the calculations; Clark [34] noted that the wire feed speed varies linearly with the arc current, through the equation

$$\text{Wire Feed Speed} = \frac{4KI}{\pi \rho d^2} \tag{3.8}$$

where $K = 2.5 \, \text{mg A}^{-1} \text{s}^{-1}$ [34], I is the arc current, d is the electrode diameter and ρ is the density of the electrode, taken here as $7800 \, \text{kg m}^{-3}$. In all the calculations which follow in this section, the feed speed has been calculated using equation 3.8.

The weld geometry chosen for these calculations is that of the experimental weld examined in chapter five of this dissertation; the details of the weld preparation appear in figure 5.2, and the chemical

composition of the baseplate in table 5.2. Thus the temperatures T_s, T_{gc}, Ac3, Ac1 & T_t remain as undefined input parameters. Since in practice the chemical composition of the baseplate differs from that of the weld metal, these temperatures should in theory be defined for the fusion zone as well as the HAZ. However for simplicity we assume here one set of temperatures for the entire weldment, chosen so as to apply to the $\frac{1}{2}$CrMoV steel baseplate. The temperature T_s has been estimated as 1516°C using a thermodynamic method [38]. The Ac3 & Ac1 temperatures are taken as 960°C and 860°C respectively; it will be seen in chapter five of this dissertation that these values are reasonable for $\frac{1}{2}$CrMoV steel. The temperatures T_{gc} and T_t are set equal to 1500 K and 750 K respectively. The choice of these temperatures is, in the context of this work, somewhat arbitrary.

3.6.1 The Electrode Diameter

An increase in electrode diameter at constant arc current, arc voltage, arc speed and interpass temperature must result in the weld gap being filled with a greater number of weld beads, since the feed speed of the electrode and hence the weld bead reinforcement area is decreased (equation 3.18). However, since the effective arc power remains constant, (with the effective power density decreasing, since the cross-sectional area of the electrode increases) the temperature field beneath the weld centre-line is expected to change only slightly.

Figure 3.18 illustrates the computed effect of the electrode diameter on the volume fraction of unreaustenitised weld metal, volume fraction of reaustenitised weld metal (large γ-grain size), volume fraction & cross-sectional area of reaustenitised HAZ (large γ-grain size) and the volume fraction & cross-sectional area of partially reaustenitised HAZ. The graphs are plotted for the range of arc travel speeds considered, for an arc current of 200 A and an interpass temperature of 20°C. Figures 3.19 & 3.20 are representative of the graphical output from the model.

The model predicts that the effect of increasing the electrode diameter from 2.5 mm to 6 mm is to cause a ~10% reduction in the volume fraction of unreaustenitised weld metal. It is these regions which maintain the columnar grain structure typical of the as-deposited weld metal. A large fraction of the remaining unreaustenitised weld metal lies in the final weld layer.

This result is contrary to that found by Evans [39] (figure 3.21); he reports that an increase in electrode diameter led to an increase in the percentage amount of unrefined weld metal, with a decrease in the percentage amount of recrystallisation in the bulk of the deposit. However, in this work the arc voltage, welding speed and particularly the arc current were not held constant (when the electrode diameter was increased from 3.25 mm to 6 mm the arc current increased from 125 A to 280 A). Therefore, it was not just the effect of the electrode diameter which Evans was studying.

The model predicts that the volume fraction of weld metal with a large γ-grain size remains at ~20%, and is almost independent of electrode diameter. This effect occurs because, as discussed above, the temperature field below the weld centre-line remains almost unchanged, whilst the number of beads deposited depends strongly on the electrode diameter. For the same reason the volume fractions & cross-sectional areas of reaustenitised HAZ (large γ-grain size) and partially reaustenitised HAZ remain unchanged.

An increase in the welding speed decreases the heat input, resulting in a smaller weld bead reinforcement area and hence a greater number of weld beads in the multipass weld. However, the temperature field beneath the weld centre-line also changes, and both effects must be taken into account when rationalising the effect of the welding speed. Thus the computer model is invaluable in this respect. The model predicts that an increase in welding speed has the effect of decreasing the fraction of unreaustenitised weld metal and of increasing the volume fraction of reaustenitised weld metal (large γ-grain size). The cross-sectional areas of reaustenitised HAZ (large γ-grain size) and partially reaustenitised HAZ decrease, since the HAZ as a whole gets smaller. However, when these areas are expressed as a fraction

of the HAZ as a whole, the fractions do not depend strongly upon the welding speed. These results indicate that it is the effect on the temperature field, rather than the change in weld bead reinforcement height, which is important in determining the volume fractions, when the welding speed is altered.

Finally it should be noted that the effect of electrode diameter can easily be masked, because larger gauge electrodes are usually associated with larger arc currents. The effect of arc current is considered next.

3.6.2 Welding Current

For constant electrode diameter, arc voltage, welding speed and interpass temperature, an increase in arc current increases the feed speed of the electrode, resulting in a larger weld bead reinforcement area and hence fewer beads in the multipass weld. However, the temperature field beneath the weld centre-line also changes, and once again both effects need to be considered.

Figure 3.22 illustrates the computed effect of arc current on the volume fraction of unreaustenitised weld metal, volume fraction of reaustenitised weld metal (large γ-grain size), volume fraction & cross-sectional area of reaustenitised HAZ (large γ-grain size) and the volume fraction & cross-sectional area of reaustenitised HAZ. The graphs are plotted for the range of arc travel speeds considered, for an electrode diameter of 3.25 mm and an interpass temperature of 20°C. Figure 3.23 is representative of the graphical output from the model.

The model predicts that an increase in arc current is associated with an increase in volume fraction of unreaustenitised (columnar) weld metal. At the same time, the volume fraction of reaustenitised weld metal (large γ-grain size) tends to decrease slightly. These results occur because the increase in reaustenitisation distance is offset by the fact that fewer weld beads are deposited in the weld.

The model predicts that increasing the arc current has the effect of increasing the cross-sectional area of reaustenitised HAZ (large γ-grain size) and partially reaustenitised HAZ. When expressed as a fraction of the HAZ as a whole, the volume fraction of reaustenitised HAZ (large γ-grain size) tends to decrease slightly, and the volume fraction of partially reaustenitised material is almost constant.

The effect of welding speed at constant arc current is as described in subsection 3.6.1. An increase in welding speed has an effect almost equivalent to a decrease in arc current, since it is the *ratio* of the effective arc power to welding speed which is important in determining the temperature field.

In a study of the effect of heat input on the microstructure and properties of multipass weld deposits, Evans [40] altered the heat input by changing the welding speed at constant arc current. It was found that the amount of columnar weld metal remaining in the bulk of the deposit varied unsystematically with heat input (figure 3.24). However, in this work only a few (between 1 and 4) weld beads were deposited per layer and hence it is unlikely that the weld bead overlap Δ was maintained at a constant value. Thus, to quote Evans, the 'degree of recrystallisation differed dependent upon the number of beads per layer'.

3.6.3 The Interpass Temperature

An examination of equation 2.12 shows that an increase in interpass temperature at constant arc current, arc voltage, welding speed and electrode diameter has the effect of increasing the temperature at any point in the weld assembly, by the same magnitude. Therefore the effect is such as to extend the weld isotherms to greater distances from the weld centre-line. The weld bead width, penetration and reaustenitisation distance increase, although the weld bead reinforcement area remains unchanged, because the interpass temperature has little effect on the arc characteristics.

Figure 3.25 illustrates the computed effect of interpass temperature on the volume fraction of unreaustenitised weld metal, volume fraction of reaustenitised weld metal (large γ-grain size), volume fraction & cross-sectional area of reaustenitised HAZ (large γ-grain size) and the volume fraction &

cross-sectional area of partially reaustenitised HAZ. The graphs are plotted for the range of arc travel speeds considered, for an electrode diameter of 4 mm and an arc current of 200 A. Figure 3.26 is representative of the graphical output from the model.

The model predicts that an increase in interpass temperature reduces the volume fraction of unreaustenitised weld metal. The volume fraction of reaustenitised weld metal (large γ-grain size) increases, until the interpass temperature becomes so high that this region becomes reaustenitised again, but this time to a small γ-grain size; at this point, the volume fraction starts to decrease.

With increasing interpass temperature, the model predicts that the volume fraction of reaustenitised HAZ (large γ-grain size) and the volume fraction of partially reaustenitised HAZ both decrease. When the corresponding cross-sectional areas are considered, the area of partially reaustenitised HAZ increases, but significantly the area of reaustenitised HAZ (large γ-grain size) decreases still, even though the physical size of the HAZ increases.

The results predicted by the model can be rationalised on the grounds that an increase in interpass temperature increases the distance of the isotherms from the weld centre-line. The interpass temperature has little effect on the arc characteristics, so that the feed speed and hence the number of weld beads deposited in the weld remains unchanged.

In a study of the effect of interpass temperature on the microstructure and properties of multipass welds, Evans [41] found that the width of the recrystallized zones increased, and this tended to eliminate the columnar bands from the bulk of the deposit (figure 3.27). Thus, in this case, the computer model confirms Evans' experimental observations.

The effect of welding speed at constant interpass temperature is as described in subsections *3.6.1 & 3.6.2*.

3.7 Calculations: Complete Reaustenitisation

3.7.1 Introduction

Given that each region of a multipass weld is likely to have experienced a different thermal history, the weld microstructure is expected to be inhomogeneous on a scale related to the dimensions of each weld pass, and on the detailed welding conditions (*e.g.* the heat input). This should necessarily lead to variations in mechanical properties, a feature which is most obviously reflected in the hardness profiles of such welds. There are indications that welds which are not mechanically homogeneous are susceptible to undesirable scatter in toughness [42,43,44], scatter which prevents the achievement of optimum properties and presents difficulties in engineering design. This phenomenon is well established in wrought steels where the microstructure may consist of a mixture of martensite and bainite, in which case the scatter in toughness is observed to be larger than in the corresponding uniform microstructures consisting of just martensite or bainite [45,46].

It can therefore be argued that it is desirable to produce mechanically homogeneous welds although it is difficult to see how this can be achieved for *multipass* welds. One possibility is to anneal the final weld to such an extent that the differences in strength between the variety of microstructures are reduced. Unfortunately, this has the obvious disadvantage that the general level of strength should also drop. The strength may be reduced to a level where only solid solution strengthening and the intrinsic strength of pure iron are the main contributors to strength, whereas the microstructural contribution (*e.g.* grain boundary and dislocation strengthening) is minimal by comparison.

This is in conflict with the increasing industrial demand for exceptionally high-strength, tough steel welds, particularly for use in the manufacture of submarines. There have been many attempts in the past to produce high-strength welds, but there is usually a penalty to be paid as far as toughness is concerned. Progress has been made in designing alloys which give an unusual primary weld microstructure which is essentially an approximately equal mixture of acicular ferrite and low carbon martensite [47]. Strength

37

levels greater than 700 MPa can then be achieved. Whether these welds have reached their optimum level of toughness remains to be demonstrated, since in the multipass condition, they are to some extent mechanically inhomogeneous.

3.7.2 The Concept

It has been suggested that with these new range of alloys, it should be possible to design a multipass weld that has at all positions, a microstructure which differs little from the as-deposited microstructure. To achieve this, requires the simultaneous fulfilment of three main conditions. The first of these is that the Ae3 temperature should be as low as is practicable, so that the effect of depositing a new layer is to reaustenitise as much of the adjacent underlying layer as possible. The second condition requires the hardenability of the alloy concerned to be high enough to lead to the retransformation of the reformed austenite to a microstructure resembling the as-deposited regions, *i.e.* into the required mixture of just acicular ferrite and martensite. The low Ae3 temperature also ensures that regions which do not reaustenitise are tempered to a lower peak temperature, thereby ensuring a lower loss in microstructural strength. The third condition requires that the alloy concerned should have a high tempering resistance.

3.7.3 Possible Solutions

There are at least two ways that in which this problem can be tackled. A first approach involves the addition of those alloying elements to the welding consumable, which reduce the temperature at which austenite transforms to ferrite. The distance between the solidus isotherm and the Ac3 isotherm will then be larger. Nickel, manganese, chromium and copper all have the effect of lowering the Ae3 temperature in steels, but it is necessary to consider carefully which additions might be the most appropriate; for example, the use of too much nickel or manganese can lead to increased segregation during solidification [48]. Similarly, carbon cannot be used in high concentrations if toughness and resistance to tempering is to be maintained.

A second approach involves controlling the rate at which the welding electrode (*i.e.* filler wire) is consumed. The requirement that the ratio R_1/R_2 be maximised can also be achieved by minimising the ratio of the rate at which the filler wire is consumed (the *feed speed*) to the heat input. This has the effect of extending the isotherms to deeper positions below the fusion boundary. For processes such as submerged arc (SA), or tungsten inert gas (TIG) welding, it is possible to adjust the feed speed independently of the heat input. This is because the electrode itself is not consumed. However, in other processes such as manual metal-arc (MMA) welding, the filler wire itself acts as the source of heat, so that, as already noted, the feed speed and the heat input are no longer independent.

To summarise, the extent of material reaustenitised by the deposition of a new bead is likely to be maximised if a significant fraction of the arc power enters the workpiece, rather than being used in melting the filler material. These qualitative predictions are tested in the work presented below.

3.7.4 Application of Model

The program outlined above, together with the quantities deduced from the analysis of experimental data, have been applied to a multipass weld, typical of those deposited in the power generation industry. This weld is examined in detail in chapter five of this dissertation; the essential weld variables needed for the modelling are listed in tables 5.1 and 5.2. An optical micrograph of a transverse section of the weld appears in figure 5.2.

The melting and Ae3 temperatures of the weld metal were estimated as 1516°C [38] and, using the model described in chapter six of this dissertation, 867°C. However, for the modelling it is necessary to know the Ac3 temperature. In the absence of this data, a series of temperatures was assumed in the modelling (50°C intervals between 817 and 1017°C). This approach has the additional advantage of

38

allowing the effect of altering the Ac3 & Ac1 transformation temperatures to be studied. In all cases the Ac1 temperature was assumed to lie 100°C below Ac3.

Figure 3.28 illustrates the computed effect of Ac3 & Ac1 temperatures on the volume fraction of unreaustenitised weld metal, volume fraction of reaustenitised weld metal (large γ-grain size), volume fraction & cross-sectional area of reaustenitised HAZ (large γ-grain size) and the volume fraction & cross-sectional area of partially reaustenitised HAZ. Figure 3.29 is representative of the graphical output from the model.

As the Ac3 temperature is depressed, the volume fraction of unreaustenitised weld metal is decreased. The match between the experimental weld and the computed output, assuming that the etching contrast in the macrograph presented in figure 5.2 can be related directly to the temperature fields predicted by the computer, appeared to occur at an Ac3 temperature of 100 to 150° C above the calculated Ae3 temperature of the weld metal. This difference is considered to be reasonable given the high heating rates associated with the process. This result confirms the qualitative prediction [47,49] that the amount of reaustenitised material should increase as the Ac3 temperature is reduced; it further demonstrates that the relationship between the volume fraction of reaustenitised metal and the Ac3 temperature is non-linear, with diminishing returns as the alloying element concentration is increased.

The modelling also predicts that with decreasing Ac3/Ac1 temperatures, the volume fraction of reaustenitised weld metal (large γ-grain size) decreases, as does the volume fraction and area of reaustenitised HAZ (large γ-grain size). The volume fraction and area of partially reaustenitised HAZ increases with decreasing Ac3/Ac1 temperatures. These results follow from the fact that the heat-flow calculations and hence the temperature fields are identical for each of the above calculations. The volume fractions follow from a choice of the temperatures T_s, T_{gc}, Ac3, Ac1 and T_t.

There is, however, the other proposed way in which it is possible to design a completely reaustenitised weld. This involved designing a consumable in which the amount of metal deposited per pass is low, but the heat input is kept high. In order to test this proposition, the modelling has been repeated, but this time the feed speed is decreased steadily from the measured value of $3.60 \, \mathrm{mm \, s^{-1}}$, to $2.06 \, \mathrm{mm \, s^{-1}}$ All other variables are held constant, with the weld bead overlap remaining at 35%.

Figure 3.30 illustrates the computed effect of the feed speed on the volume fraction of unreaustenitised weld metal, volume fraction of reaustenitised weld metal (large γ-grain size), volume fraction & cross-sectional area of reaustenitised HAZ (large γ-grain size) and the volume fraction & cross-sectional area of partially reaustenitised HAZ. Figure 3.31 is representative of the graphical output from the model.

A smaller volume fraction of unreaustenitised weld metal is observed at low feed speeds, again confirming the prediction discussed earlier. In addition, the model predicts that with increasing feed speed the volume fraction of reaustenitised weld metal (large γ-grain size) increases, as does the volume fraction and area of reaustenitised HAZ (large γ-grain size). This result occurs because the heat-flow into the workpiece and HAZ remains is independent of the feed speed in these calculations. As a consequence, it is unsurprising that the volume fraction and area of partially reaustenitised HAZ remains constant.

3.7.5 Summary

The idea that by suitable alloying, multipass welds may be designed in which the deposition of weld metal onto a previously deposited layer causes the latter to almost completely reaustenitise has been confirmed theoretically using this model. The results provide a basis for much further work towards the design of multipass weld deposits which are microstructurally and mechanically homogeneous.

Given that the basic concept of almost complete reaustenitisation has now been established theoretically, future work towards the design of mechanically homogeneous multipass welds will focus on ensuring that the reaustenitised regions transform back to a microstructure of acicular ferrite and low

carbon martensite (*i.e.* similar to the primary regions). It is also vital to ensure that third layer effects can be minimised, so that any tempering beneath the reaustenitised regions has a minimal effect on mechanical properties of those regions. This in turn requires alloys designed for tempering resistance.

3.8 Summary and Conclusions

A computer model capable of mapping the thermal cycles in multipass welds has been designed. The methodology involves first calculating the size and shape of the single bead-on-plate weld. The isotherms beneath the weld centre-line are calculated using Ashby & Easterling's [17] analytical solution for the problem of heat-flow into a thick plate. The volume of weld metal deposited per unit length of weld, *i.e.* the reinforcement area, is then assumed to adopt the shape of a spherical cap on the surface of the plate. Good agreement with experimental data has been demonstrated.

For multipass welds, the model calculates the positions of the weld centre-lines within the weld gap, either from an input of the number of beads per layer, or from a input of the percentage overlap between weld beads. The weld beads are then deposited one by one, *i.e.* the heat-flow equations are applied and the weld metal is deposited. It is necessary to make certain geometrical approximations at the end of each layer, and in addition, the model does not properly take into account the remelting of weld beads.

The variables required as input are therefore the weld preparation geometry, the interpass temperature, the electrode diameter, arc current, arc voltage, welding speed, feed speed of the filler wire and the electrode recovery. The feed speed is proportional to the arc current, and can therefore be estimated, provided the proportionality constant is known. Similarly, the electrode recovery is a function of electrode diameter only, and values are documented by the electrode manufacturers. Finally, five temperatures need to be chosen; these serve to divide the weld thermal cycles into six categories, dependent upon the highest temperature reached during the thermal cycle. Thermal cycles which fall into the same category are expected to have a similar microstructural effect.

The model has been used to investigate the effect of electrode diameter, arc current, welding speed, interpass temperature and Ac3/Ac1 temperatures on the volume fractions of regions which experience similar sets of thermal cycles. The predictions with respect to the volume fraction of unreaustenitised (columnar) weld metal were considered in detail. In the case of electrode diameter, arc current and welding speed the results are not entirely in agreement with the experimental data examined, but possible explanations for the discrepancies have been offered. In the case of the interpass temperature, the model predicts that the volume fraction of columnar (unreaustenitised) weld metal decreases with increasing interpass temperature, as has been observed in practice.

The heat-flow model described in this chapter forms the basis of much further work towards the ultimate goal of predicting the microstructure of multipass welds from an input of the weld variables and alloy chemistry only. Ultimately it needs to be coupled with the sort of thermodynamic/kinetic model developed in chapters six & seven of this dissertation, and the sort of phase transformation theory which has been used successfully [4,5,6] to predict the microstructure in the as-deposited regions of low-alloy steel welds.

REFERENCES

32. P.J. Alberry and W.K.C. Jones, Metals Technology, 9, 419–426, (1982).

33. P.J. Alberry, in 'Computer Technology in Welding', Paper 2, The Welding Institute, (1986).

34. J.N. Clark, Materials Science and Technology, 1, 1069–1098, (1985).

35. P. Wilkins, BOC Murex Ltd, Private Communication, (1987).

36. C.E.C. Rense, G.R. Edwards and H.R. Frost, Journal of Materials for Energy Systems, 5, 149–159, (1983).

37. J.A. Barlow, Welding Institute Research Bulletin, 23, 177–180, (1982).

38. A.A.B. Sugden and H.K.D.H. Bhadeshia, Materials Science and Technology, **5**, 977–984, (1989).

39. G.M. Evans, Welding Review, **1**, (2), 4–8, (1982).

40. G.M. Evans, Welding Journal, **61**, (4), 125s–132s, (1982).

41. G.M. Evans, Welding Review, **1**, (1), 14–20, (1982).

42. J.H. Tweed and J.F. Knott, Metal Science, **17**, 45–54, (1983).

43. J.H. Tweed and J.F. Knott, Acta Metall., **35**, 1401–1414, (1987).

44. A.A.B. Sugden and H.K.D.H. Bhadeshia, in 'Recent Trends in Welding Science and Technology', 745–748, Edited S.A. David & J.M. Vitek, ASM International, (1990).

45. P. Bowen, S.G. Druce and J.F. Knott, Acta Metall., **34**, 1121–1131, (1986).

46. D.J. Neville and J.F. Knott, J. Mech. Phys. Solids, **34**, 243–291, (1986).

47. L.-E. Svensson and H.K.D.H. Bhadeshia, in 'Weld Quality and the Role of Computers', published by Pergamon Press for the IIW, 71–78, (1988).

48. B. Gretoft, H.K.D.H. Bhadeshia and L.-E. Svensson, Acta Stereologica, **5**, 365–371, (1986).

49. L.-E. Svensson, B. Gretoft, A.A.B. Sugden and H.K.D.H. Bhadeshia, in the Proceedings of the Second International Conference on Computer Technology in Welding, The Welding Institute, Cambridge, Paper 24, (1988).

Appendix 3.1

ELECTRODE DIAMETER /mm	RECOVERY /%
2.5	123
3.25	121
4.0	119
5.0	117
6.0	115

Values of the recovery term as a function of electrode diameter for Murex Suprex B electrodes [35].

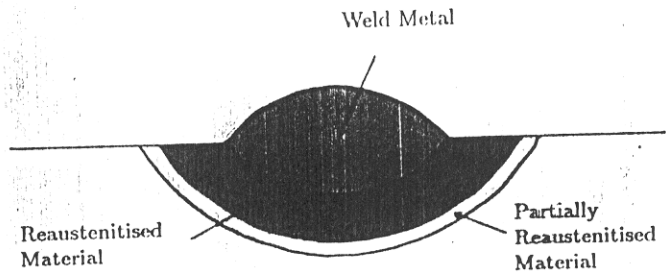Figure 3.1: Schematic illustration of the single bead-on-plate weld.

a)
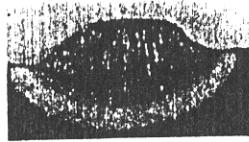
Heat Input 0.395 kJ/mm, Arc Speed 3.30 mm/s
Electrode Diameter 2.5 mm

b)
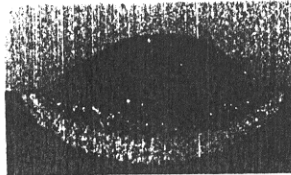
Heat Input 0.528 kJ/mm, Arc Speed 3.23 mm/s
Electrode Diameter 3.25 mm

c)
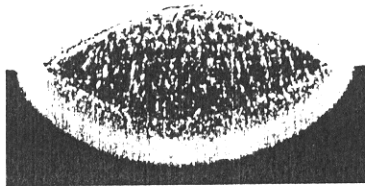
Heat Input 0.757 kJ/mm, Arc Speed 3.01 mm/s
Electrode Diameter 4.0 mm

d)
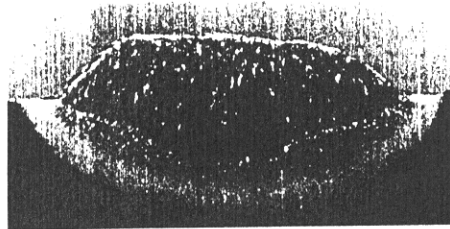
Heat Input 1.163 kJ/mm, Arc Speed 2.91 mm/s
Electrode Diameter 5.0 mm

1 cm
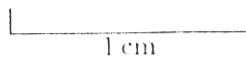
Figure 3.2: Examples of the single bead-on-plate weld. The weld bead dimensions are functions of the weld variables, such as heat input, welding speed and electrode diameter.
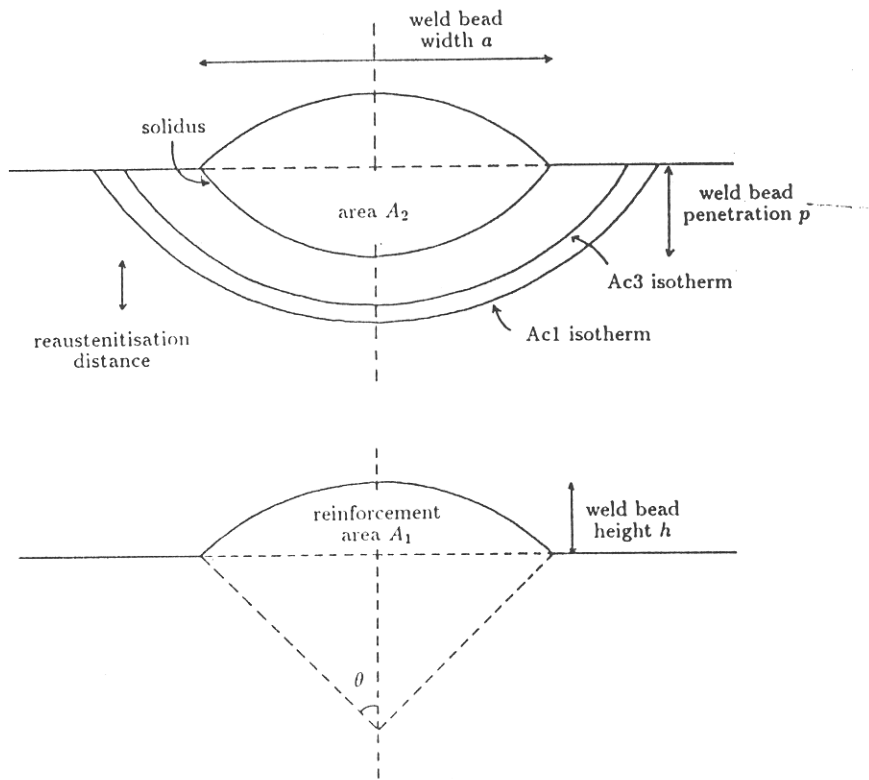
Figure 3.3: Top, definitions of the terms used in this work. Bottom, the spherical cap geometry which leads to equations 3.2, 3.3, & 3.4.
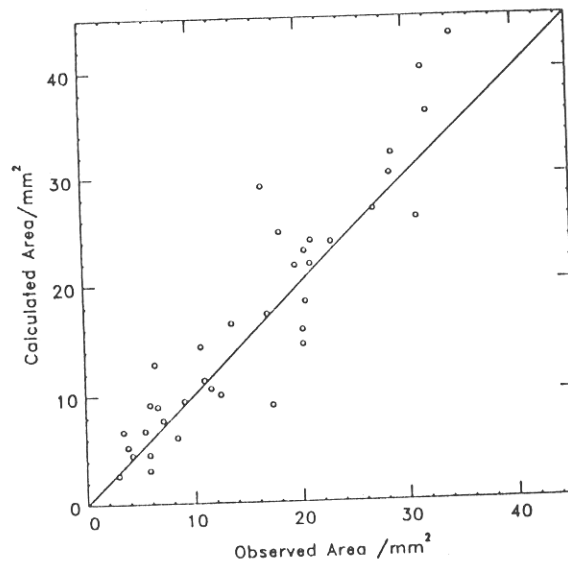
Figure 3.4: A comparison of values of the weld bead reinforcement area calculated using equation 3.1 and the values observed. The best fit line through the origin has a gradient of 1.07. The correlation coefficient is 0.93.
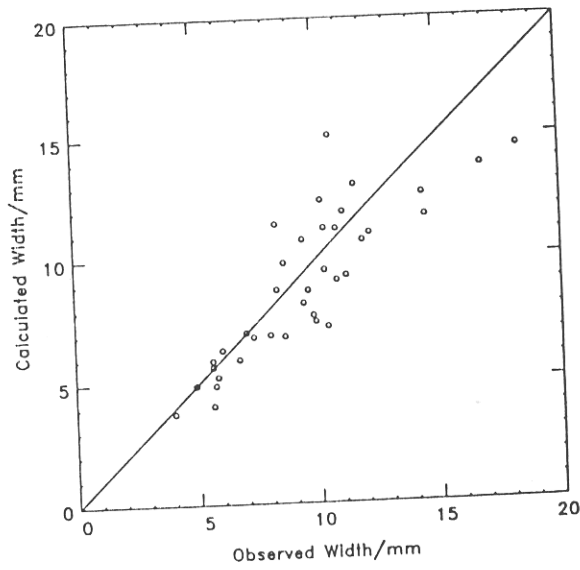
Figure 3.5: Comparison of observed single bead-on-plate width with values calculated assuming spherical cap geometry. The straight line has a gradient of unity. Regression coefficient=0.93, correlation coefficient=0.85.
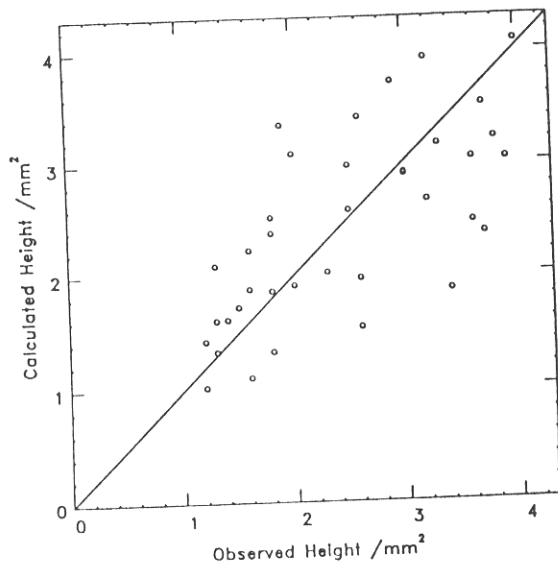
Figure 3.6: Comparison of observed single bead-on-plate height with values calculated assuming spherical cap geometry. The straight line has a gradient of unity. Regression coefficient=0.95, correlation coefficient=0.69.
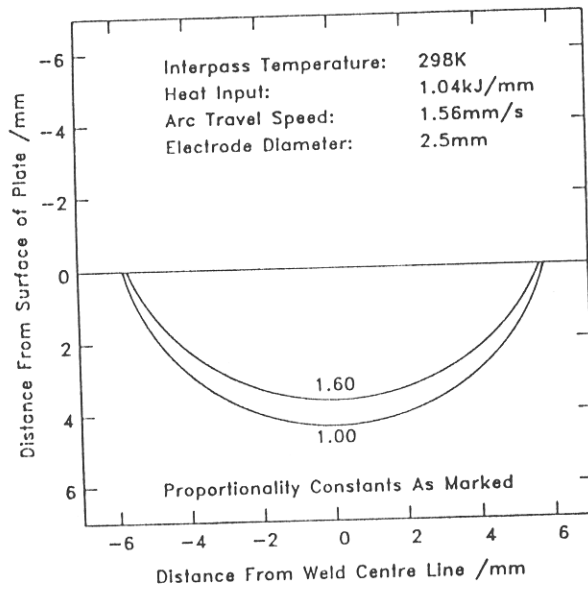
Figure 3.7: Illustrating the effect of varying the proportionality constant in equation 3.4, on the predicted fusion profile.
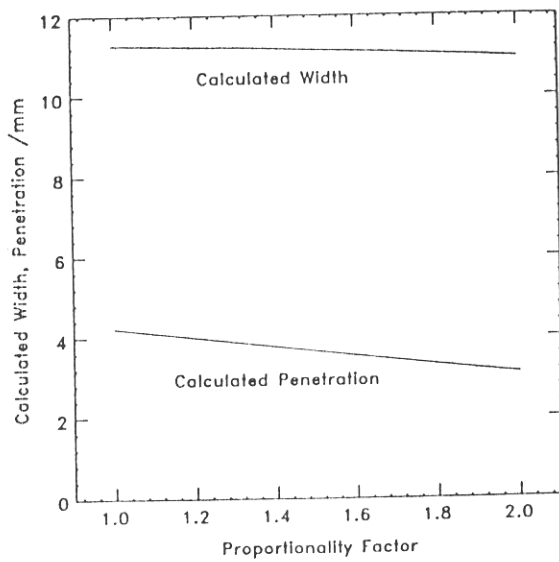
Figure 3.8: Illustrating the effect of extending the heat source. As the arc power is spread, both the weld bead width and penetration decrease.
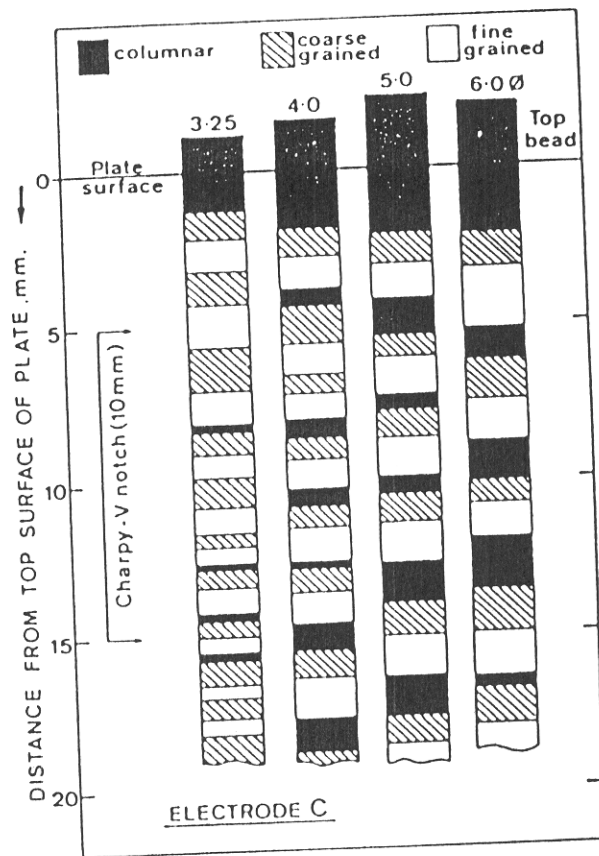
Figure 3.21: Zone distribution along the vertical centre-line of a low-alloy Fe-Mn-C multipass steel welds, as a function of electrode diameter. Note that the volume fraction of unreaustenitised (columnar) weld metal appears to increase with increasing electrode diameter. This work suggests that this occurs because the arc current is not constant. After Evans [39].
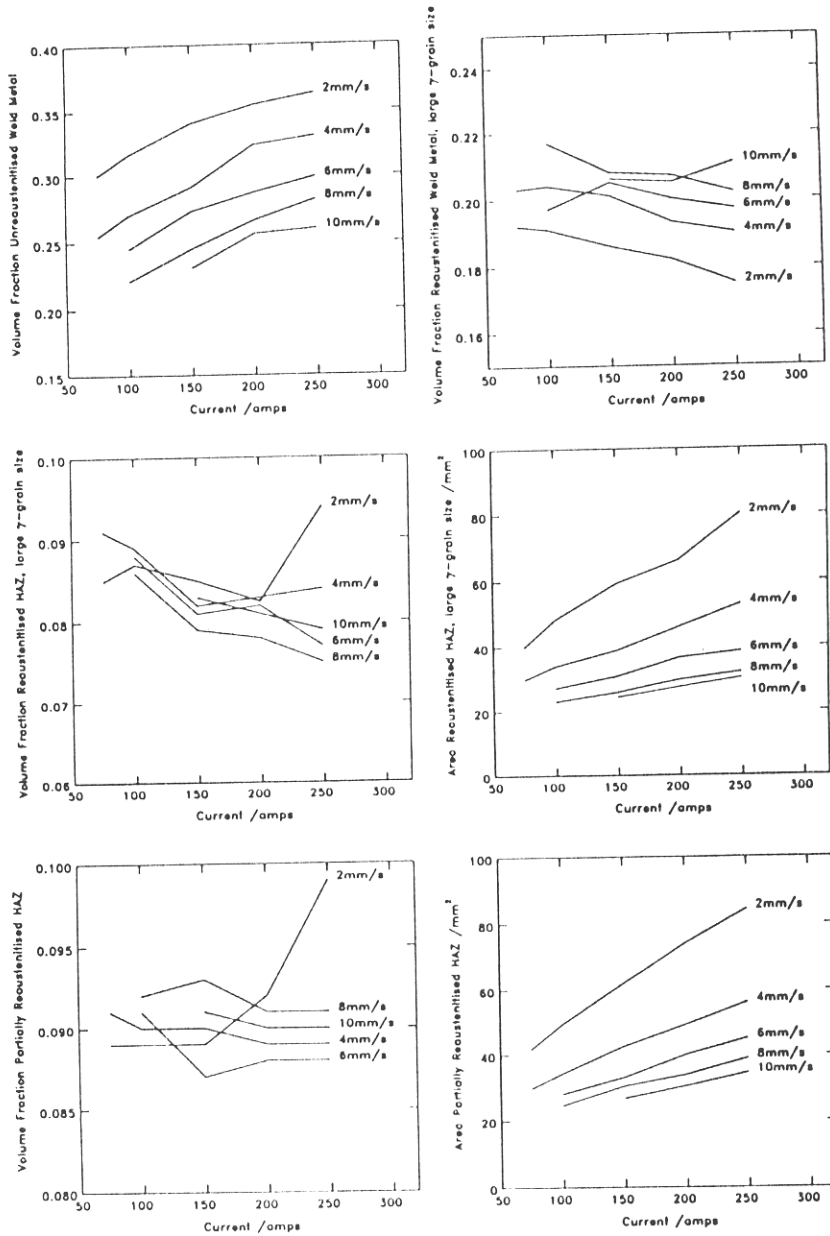
Figure 3.22: Computed effect of arc current on the volume fractions of regions in the multipass weld. The electrode diameter is 3.25 mm and the interpass temperature is 20°C.
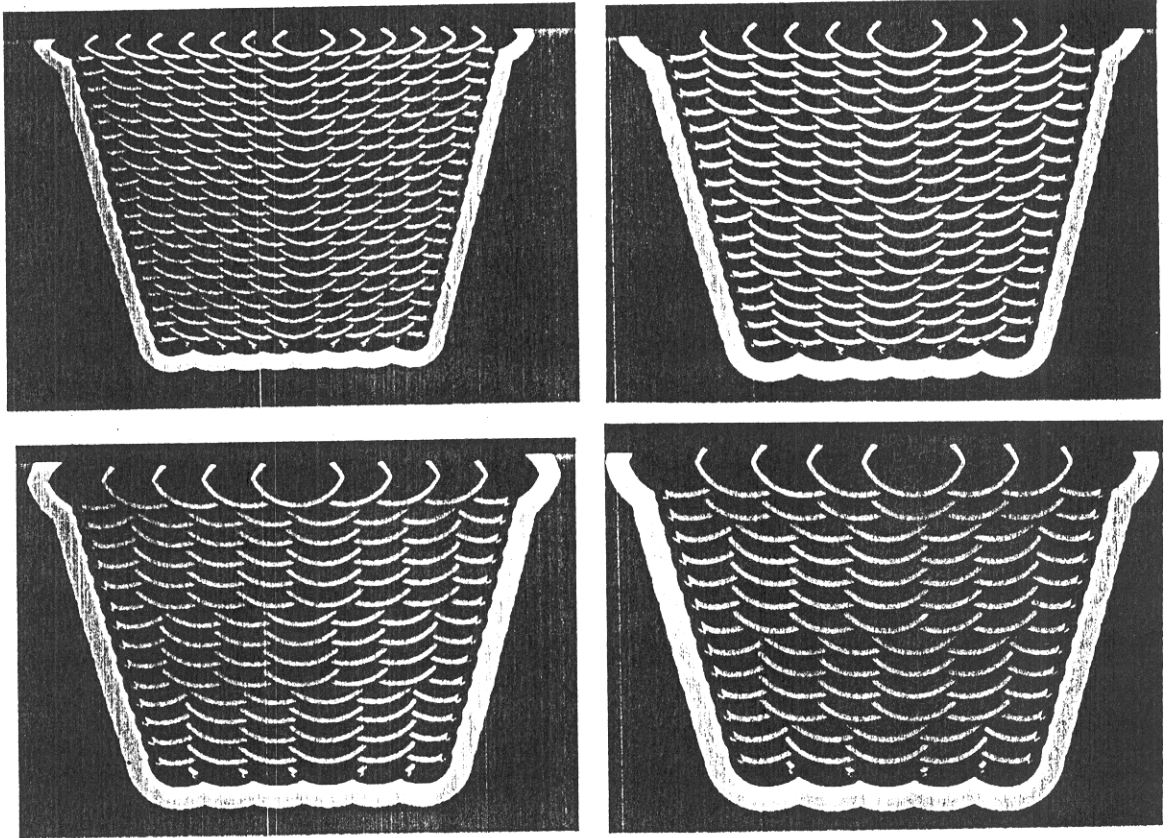
Figure 3.23: Illustrating the effect of arc current, for an electrode diameter of 3.25 mm, an interpass temperature of 20°C and a welding speed of $6\,\mathrm{mm\,s^{-1}}$. Top left, 100 A, top right, 150 A, bottom left, 200 A and bottom right, 250 A.
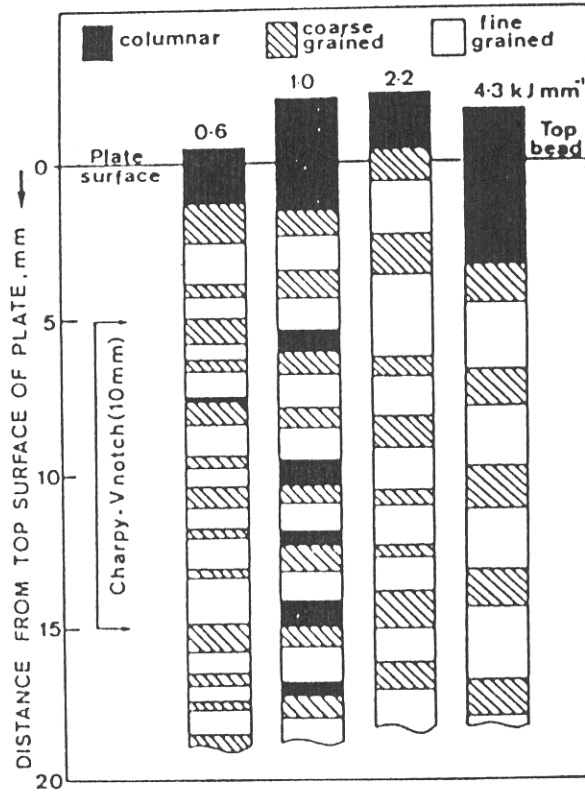
Figure 3.24: Zone distribution along the vertical centre-line of a low-alloy Fe-Mn-C multipass steel welds, as a function of welding speed, at constant arc power. From the left, $6.18\,\mathrm{mm\,s^{-1}}$, $3.58\,\mathrm{mm\,s^{-1}}$, $1.66\,\mathrm{mm\,s^{-1}}$ and $0.87\,\mathrm{mm\,s^{-1}}$. Note that the volume fraction of unreaustenitised (columnar) weld metal appears to vary unsystematically with increasing electrode diameter. It is suggested that this occurs because only a few beads are deposited per layer, so that the weld bead overlap Δ is unlikely to remain constant. After Evans [40].
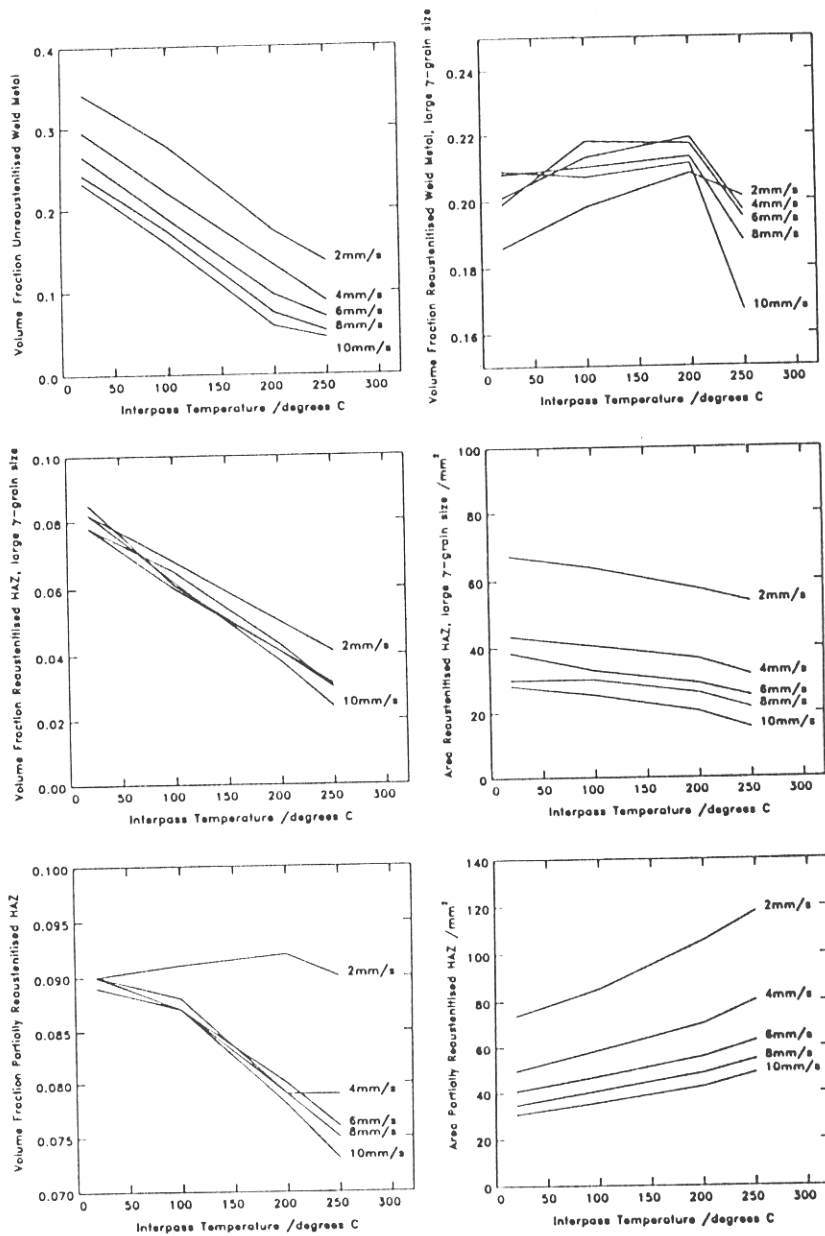
Figure 3.25: Computed effect of interpass temperature on the volume fractions of regions in the multipass weld. The electrode diameter is 4 mm and the arc current is 200 A.
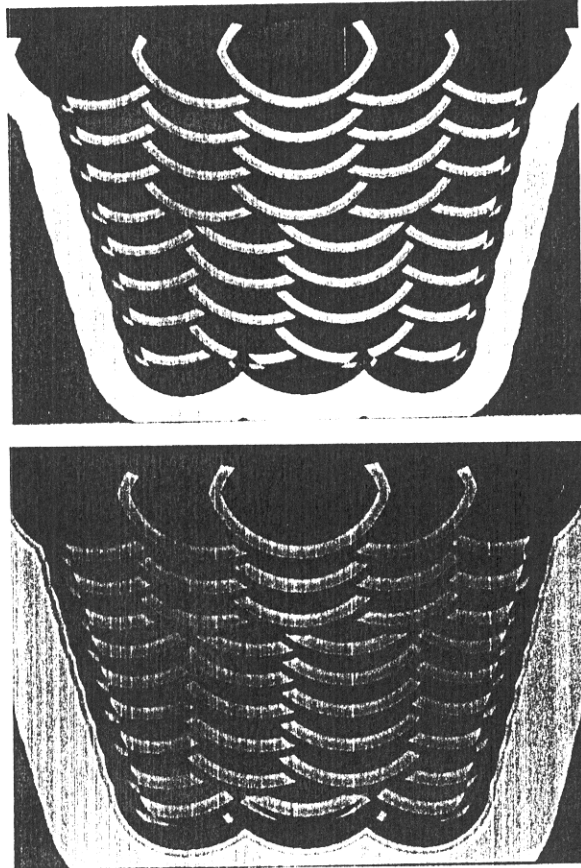
Figure 3.26: Graphical representation of the effect of interpass temperature, for an electrode diameter of 4 mm, an arc current of 200 A and a welding speed of 6 mm s^{-1}. Top, 20°C and bottom 250°C.
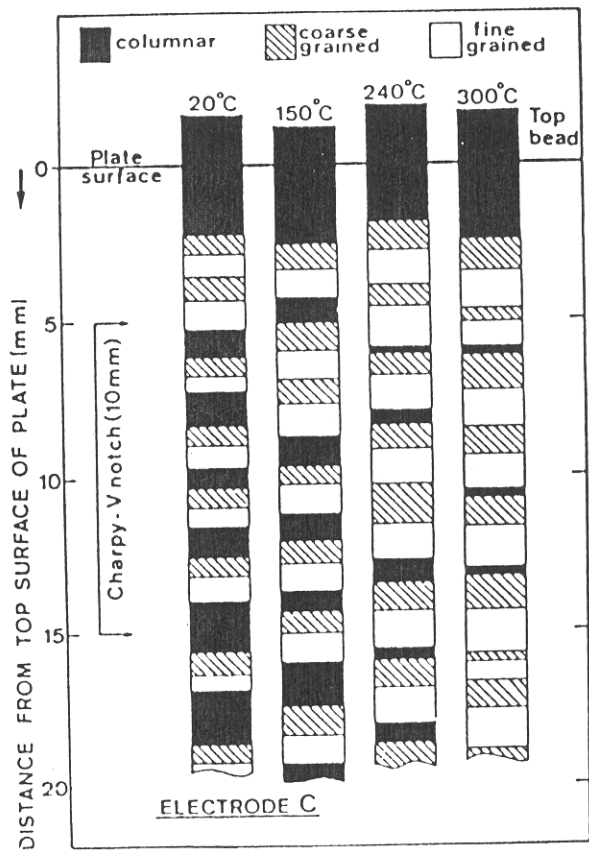
Figure 3.27: Zone distribution along the vertical centre-line of a low-alloy Fe-Mn-C multipass steel welds, as a function of interpass temperature, all other variables held constant. Note that the volume fraction of unreausteniitised (columnar) weld metal decreases with increasing interpass temperature. After Evans [41].
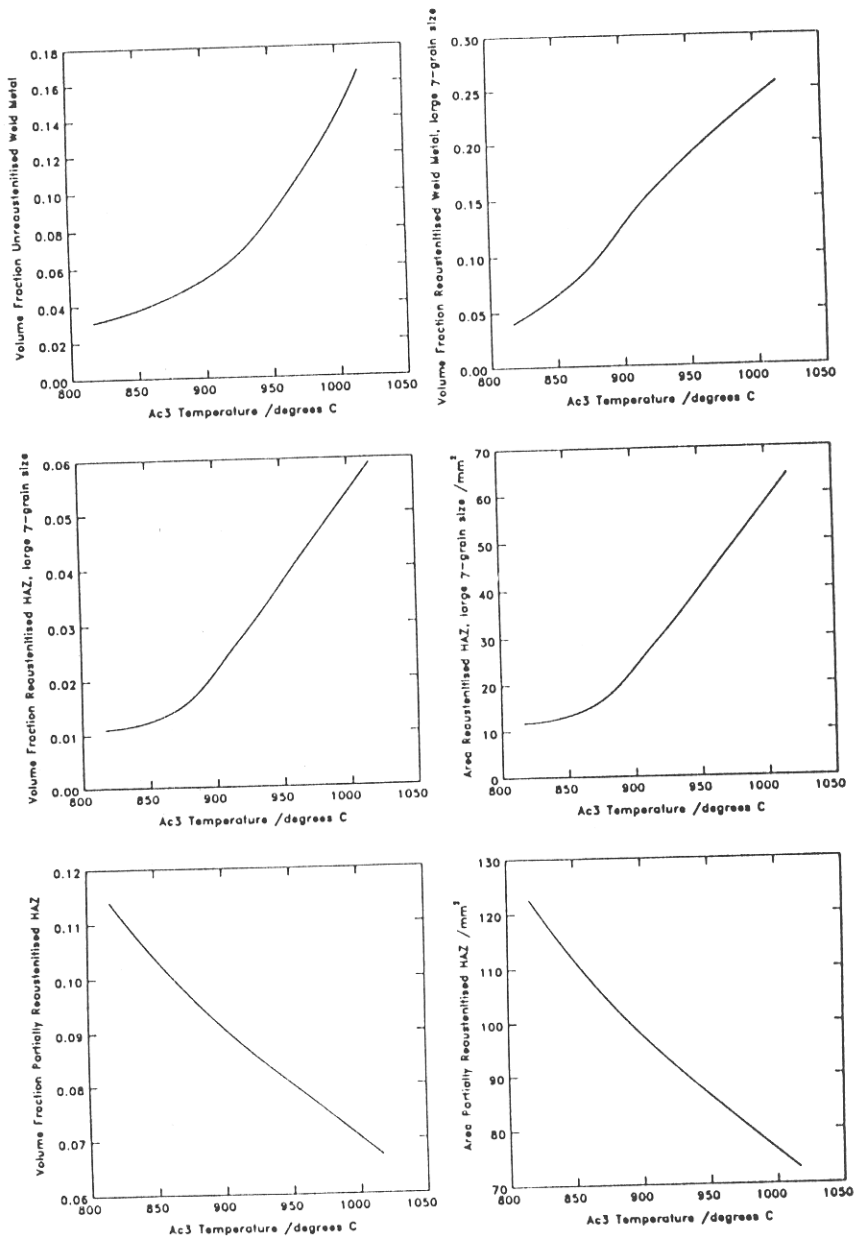
Figure 3.28: Computed effect of Ac3 & Ac1 temperatures on the volume fractions of regions in the experimental multipass weld modelled.
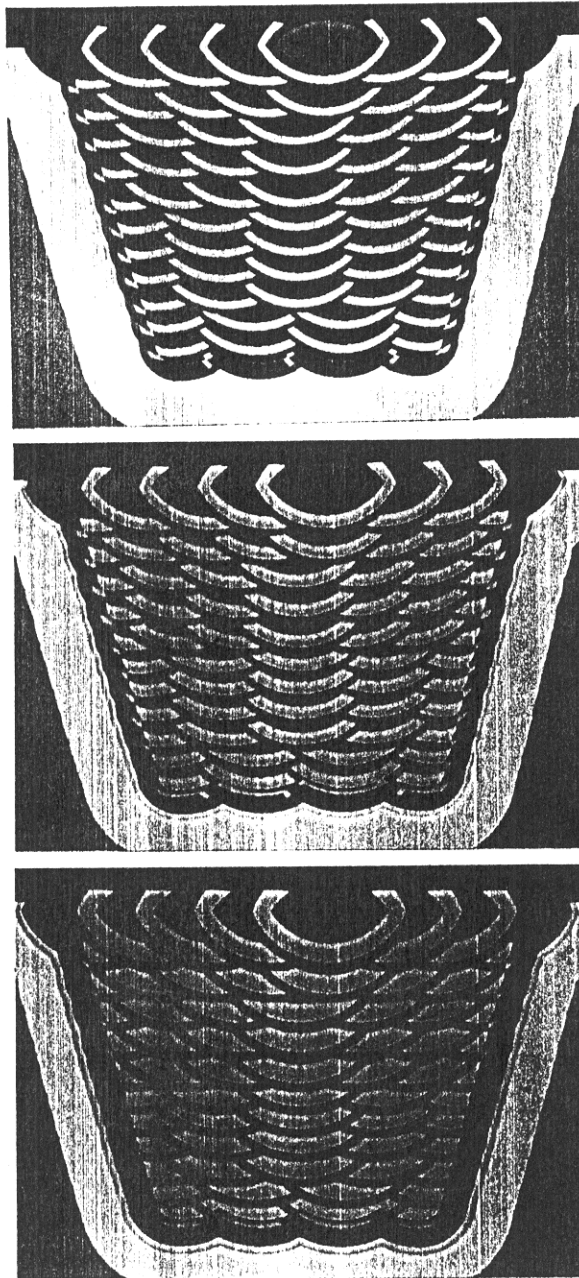
Figure 3.29: Graphical representation of the effect of Ac3 & Ac1 temperatures. Top, Ac3 = 817°C and Ac1 = 717°C. Middle, Ac3 = 917°C and Ac1 = 817°C. Bottom, Ac3 = 1017°C and Ac1 = 917°C.
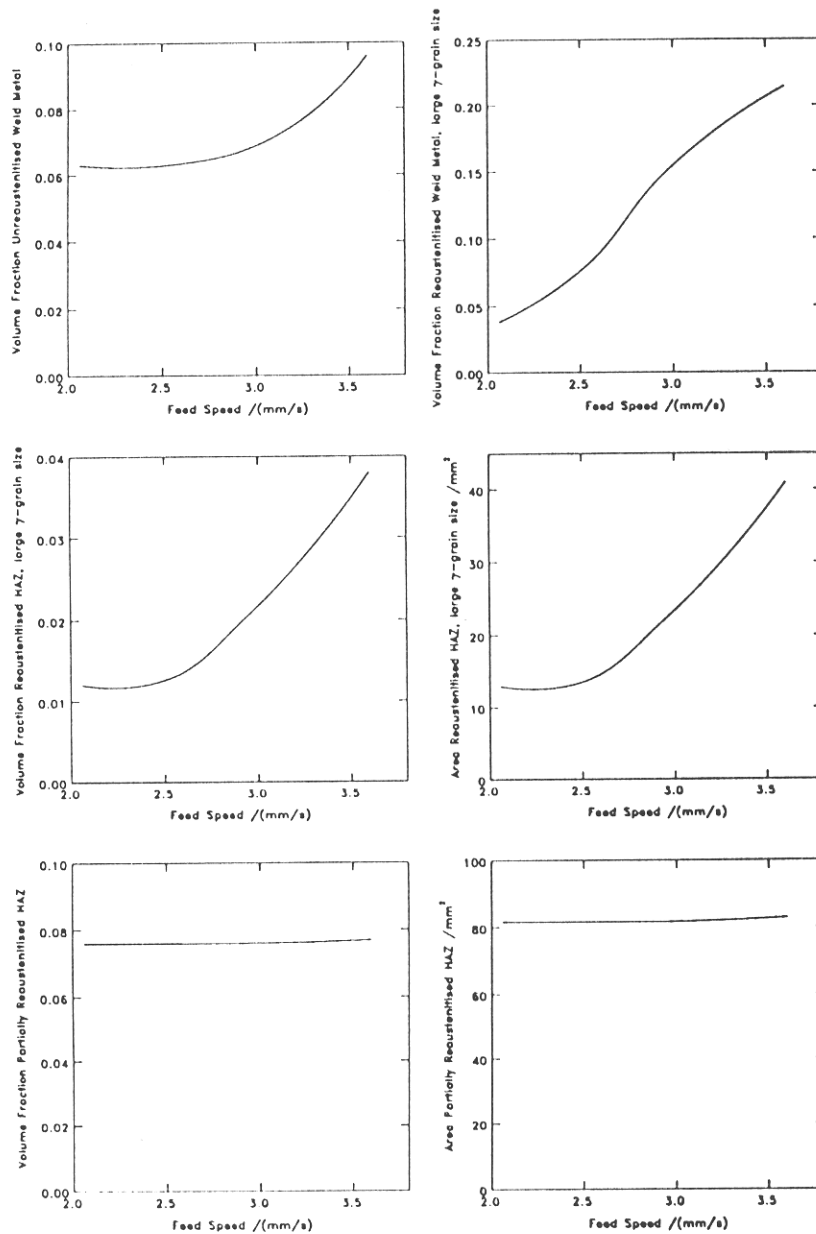
Figure 3.30: Computed effect of feed speed on the volume fractions of regions in the experimental multipass weld modelled.
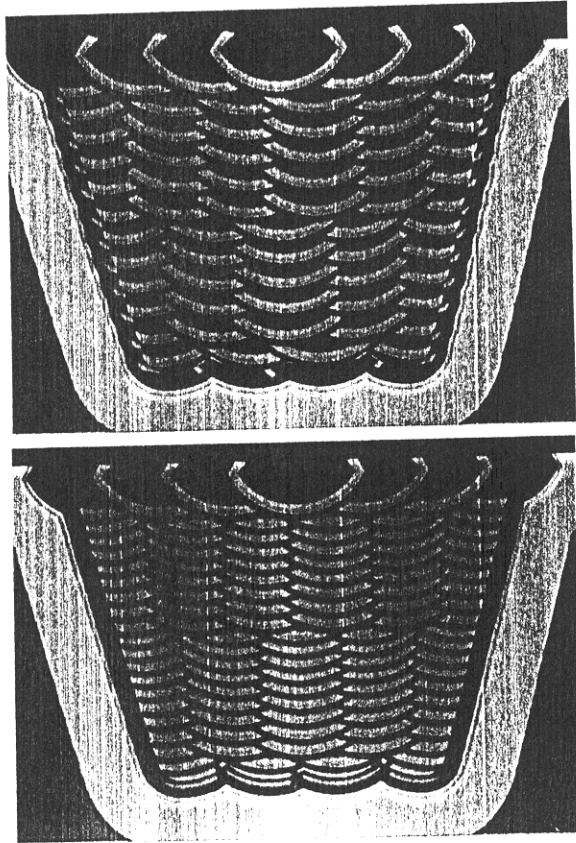
Figure 3.31: Graphical representation of the effect of feed speed. Top, $3.60 \, \mathrm{mm\,s^{-1}}$. Bottom, $2.06 \, \mathrm{mm\,s^{-1}}$.

CHAPTER FOUR
A Study of The Kinetics of Austenite Grain Growth

Nomenclature

$\overline{D}_0$	mean austenite grain diameter at start of grain growth
$\overline{D}$	mean austenite grain diameter
I	kinetic strength of weld thermal cycle
K	kinetic constant (equation 4.4)
K'	pre-exponential term (equation 4.4)
L	length of line; used in lineal analysis
$\overline{L/\lambda}$	mean linear intercept
n	grain growth exponent
Q	activation energy for grain boundary growth
R	universal gas constant
T	absolute temperature
T_p	peak temperature of weld thermal cycle
t	time
t_p	time at which peak temperature of weld thermal cycle occurs
λ	number of grain boundaries intercepted by line of length L

4.1 Introduction

The austenite grain size needs to be known in order to treat the kinetics of subsequent transformation during cooling [e.g. 50]. In low-alloy steels, the effect of a general heat treatment on the austenite grain distribution is usually studied [e.g. 51,52] by heating specimens into the γ-phase field and then quenching to martensite or bainite, so that vestiges of the γ-grain boundary structure are retained. The use of etchants and wetting agents allows the prior austenite grain boundaries to be delineated, and lineal analysis can be used to determine the mean austenite grain size. A variety of subsequent tempering treatments (e.g. 10 minutes at ~315°C [50], intercritical heat treatments at 810°C [51]) have been used to reveal these boundaries more clearly.

4.2 Experimental

4.2.1 Austenite Grain Boundary Grooving

The procedure described above is well established. However, a difficulty arises when austenite decomposes to allotriomorphic ferrite, because this reaction product completely destroys the prior austenite grain boundaries; this occurs because it grows into *both* of the adjoining γ-grains.

Here an alternative method is adopted which relies upon the formation of thermal grooves on the surface of a polished, plane section during austenitisation [52]. The grooves correspond to the intersections of the γ-boundaries with the free surface, and are a result of preferential evaporation, due to a need to balance the surface tensions at the free surface. Specimens of approximate size 1 cm × 1 cm × 3 mm were ground and polished in the usual way, before being sealed within quartz capsules under a partial pressure of argon. The specimens were heat-treated at temperatures between 1050°C and 1250°C for time-periods between 5 minutes and 5 hours. The specimens, still encapsulated, were cooled to room temperature in air, before optical examination.

4.2.2 Results

Best results were obtained when specimens and quartz tubes were thoroughly clean; in practice this meant polishing both sides of the specimens to a 1 μm finish. Despite these precautions, several specimens were ruined due to oxidation of the polished surfaces. Figure 4.1a illustrates the formation of the austenite grain boundary grooves on the plane polished surface; the surface tilts which can also be seen in this figure are due to the decomposition of austenite to bainite on cooling.

It is necessary to confirm that the grooves correspond to the intersection of austenite grain boundaries with the free surface. To do this, the specimens were photographed before and after a subsequent light polish and etch treatment, and photographs compared. Figures 4.1a, b &c illustrate that the grooves correspond to austenite grain boundaries; the Nomarski interference technique is used to differentiate between the surface relief caused by the bainite reaction.

In order to quantify austenite grain growth, the mean γ-grain sizes were obtained by first finding *mean linear intercepts* on the thermally grooved surfaces. This technique involves drawing a line of length L across the surface, counting the number λ of intercepts with grain boundaries crossed, and calculating L/λ. This process is repeated with the line drawn at random orientations, and finally the mean value of L/λ is calculated. This value is termed the *mean linear intercept*. To convert this to a value of the mean grain diameter $\overline{D}$, it is necessary to make an assumption about the shape of the austenite grains. In this work, we assume a slightly distorted form [54] of the regular tetrakaidecahedron, so that [55]

$$\overline{D} = 1.74\overline{L/\lambda} \tag{4.1}$$

The results obtained in this way are tabulated in table 4.1; also tabulated are the standard deviations in the measured values of $\overline{L/\lambda}$.

TEMPERATURE /°C	MEAN GRAIN DIAMETER /microns					
	5 mins	10 mins	30 mins	1 hour	3 hours	5 hours
1050	22.1 ± 2.3	23.3 ± 7.3	30.8 ± 5.2	-	50.6 ± 8.4	67.9 ± 9.9
1100	62.8 ± 12.4	72.0 ± 17.6	-	122.0 ± 22.8	145.3 ± 28.4	189.0 ± 36.7
1150	94.6 ± 16.9	-	142.5 ± 31.5	-	190.9 ± 27.7	230.6 ± 48.2
1200	159.6 ± 35.1	201.7 ± 42.8	248.8 ± 67.5	258.6 ± 61.4	245.0 ± 54.1	290.1 ± 66.3
1250	244.8 ± 53.2	297.4 ± 62.5	296.7 ± 52.2	314.4 ± 44.2	357.9 ± 58.1	447.4 ± 86.0

Table 4.1: Mean austenite grain diameter (in microns) calculated using the mean linear intercept method, on thermally grooved plane polished sections.

Consistent with previous observations [56], it was found that the grooves take a finite time to be set up, and that they become more pronounced with increasing time and temperature. These observations mean that the thermal grooving technique is unsuitable for γ-grain size determination at low temperatures and/or low reaustenitisation times.

4.2.3 Discussion

In a classic paper of 1952, Burke and Turnbull [57] assumed normal grain growth to occur by atom transport across the boundary under a pressure due to surface curvature, to arrive at the expression

$$\overline{D}^n - \overline{D}_0^n = Kt \tag{4.2}$$

where $\overline{D}$ is the mean grain size a time t, $\overline{D}_0$ is the initial mean grain size, K is a kinetic constant associated with the grain boundary mobility and n is a parameter often referred to as the *grain growth exponent*. Burke and Turnbull showed that subject to a number of assumptions $n = 2$, and hence deduced a parabolic relationship for grain growth kinetics.

Since the parabolic law for grain growth kinetics was deduced, a considerable amount of experimentation has been carried out to extract values of the grain growth exponent n. Experimentally n is found

usually to have a magnitude greater than 2 [58], and there has been a tendency to associate different values of n with different factors controlling grain growth (see for example [59]). Such factors include the size & distribution of pores, extent of solid second phases (particle pinning), level of dopants & their segregation (solute drag) and texture.

4.2.4 Interpretation of Results

The difficulty with interpreting the data as it stands is that each of the specimens takes a finite time to heat up to the isothermal temperature, so that, the time for grain growth cannot be measured from the time that the specimens were placed in the furnace.

To surmount this difficulty, Alberry *et al.* [51] considered the grain growth increment $(\overline{D}_1 - \overline{D}_2)$ which occurs during a period $(t_1 - t_2)$, where the grain sizes $\overline{D}_1$ and $\overline{D}_2$ are measured at times t_1 and t_2 respectively. A relationship of the form

$$\overline{D}_1^n - \overline{D}_2^n = K\,(t_1 - t_2) \tag{4.3}$$

is assumed, and n varied in order to obtain best fit, as judged by considering the correlation coefficient of the data around the best fit line determined by the method of least squares, and passing through the origin. The gradient of this best fit line represents a value for the constant K.

An identical procedure is adopted here; it yielded values for n of 2.484, 2.551 & 2.480 at 1250°C, 1150°C and 1100°C respectively; unfortunately for the 1200°C and 1050°C data the correlation coefficient did not reach a maximum when n was varied between 1 and 5. It is reasonable to suppose that the scatter in the data at these temperatures is responsible for this. However, in view of the reasonable agreement attained for the data at other temperatures, we assume an average value of 2.51 for n at these temperatures. Figure 4.2 illustrates the level of agreement attained in this manner.

Next, for $n = 2.51$ best-fit lines were recalculated to yield values of the kinetic constant K as a function of temperature. Assuming an Arrhenius type of relationship, we have

$$K = K' \exp\left\{-\frac{Q}{RT}\right\} \tag{4.4}$$

where Q represents an activation energy for grain boundary migration, K' is a constant, R is the universal gas constant and T the absolute temperature. The values of K obtained above were used to determine K' and Q by plotting a graph of $\ln\{K\}$ vs. $1/T$, (figure 4.3) and finding the best fit line, to yield $Q = (3.3 \pm 0.8) \times 10^5 \mathrm{J\,mol^{-1}}$ and $K' = 5 \times 10^{13 \pm 3}\,\mu m^{2.51} s^{-1}$. The errors quoted for Q and K' are standard errors in the gradient and intercept of the best fit line through the data points in figure 4.3. The large uncertainty K' arises because its value has been determined by extrapolation outside of the regime of the data points.

Figures 4.4 & 4.5 illustrate the level of agreement between experiment and theory assuming the values of n, K' and Q derived. For an alloy of similar composition Alberry *et al.* [51] found $n = 2.73 \pm 0.5$, $Q = (4.60 \pm 0.33) \times 10^5 \mathrm{J\,mol^{-1}}$ and $K' = (5.4 \pm 0.6) \times 10^{12}\, mm^{2.73}$, equivalent to $K' = (8.4 \pm 0.9) \times 10^{20}\,\mu m^{2.73}$.

4.3 Application to the Welding Process

4.3.1 The Kinetic Strength of the Weld Thermal Cycle

Despite the complicating nature of the arc welding process, successful attempts have been made to rationalise the development of the HAZ γ-grain distribution following particle dissolution in terms of elementary kinetic models for grain growth [13,20,51]. In these studies the theoretical approach was based on the idea of integrating equation 4.2 over the weld thermal cycle, assuming that the temperature

dependence of the grain boundary mobility term is adequately described by equation 4.4. Ion *et al.* [20] wrote

$$\overline{D}^n - \overline{D}_0^n = K' I \tag{4.5}$$

where I, given by

$$I = \int_0^\infty \exp\left\{-\frac{Q}{RT\{t\}}\right\} dt \tag{4.6}$$

is referred to as the 'kinetic strength', reflecting the number of diffusive jumps which take place during the thermal cycle.

Equation 4.6 is not quite correct, since austenite grain growth can only begin when the temperature reaches Ac3, and grain growth ceases at the temperature at which austenite decomposes, *i.e.* at Ar3, B_s or M_s. If these two temperatures occur at times t_1 and t_2 respectively during the heating and cooling regimes of the thermal cycle, a more correct term for the kinetic strength is

$$I = \int_{t_1}^{t_2} \exp\left\{-\frac{Q}{RT\{t\}}\right\} dt \tag{4.7}$$

Ion's justification for using equation 4.6 was that it is the *peak* of the thermal cycle which is responsible for the kinetic changes; here, diffusion is fastest. By approximating the peak of the temperature cycle to a parabola, and using the 3D heat flow equations due to Ashby & Easterling [17] he was able to show

$$I \simeq \left(\frac{2\pi R T_p}{Q}\right)^{\frac{1}{2}} t_p \exp\left\{-\frac{Q}{RT_p}\right\} \tag{4.8}$$

for the thick plate case, using a Taylor expansion around the peak temperature T_p at the peak time t_p.

Equations of the form of 4.5 & 4.7 were used originally by Alberry *et al.* [51] in their study of austenite grain growth in $\frac{1}{2}$CrMoV steel. In this steel, they assumed that austenite was stable beyond 950°C on heating, and to 550°C on cooling, for the weld thermal cycle in their work. They summed, rather than integrated the weld thermal cycle to arrive at an expression

$$\overline{D}^n = \sum_{t_{950}}^{t'_{550}} K' \exp\left\{\frac{Q}{RT\{t\}}\right\} \Delta t \tag{4.9}$$

for $\overline{D}$, the mean γ-grain size.

4.3.2 Calculation of the Austenite Grain Size in the HAZ

In the calculations which follow, data [51] for the prior austenite grain diameter as a function of heat input are used in order to test equations 4.5 & 4.7, and the chosen values of n, K' & Q. It is assumed that austenite grain growth begins at an Ac3 temperature of 950°C, (when D_0 is assumed to be 10 μm) and stops at a bainite start temperature of 630°C. It will be seen in chapter five of this dissertation that these assumptions are reasonable.

There is an additional problem in applying such equations to the HAZ. Strictly, each position in the HAZ has a unique thermal cycle associated with it, so that the isotherms themselves have no physical width, because the temperature is different everywhere at any given time. Therefore, particularly near to the fusion boundary, where the austenite grains are large, the computed thermal cycle varies considerably across each grain. For the purposes of modelling, we must therefore assume that some 'average' thermal cycle is responsible for grain growth. Alberry *et al.* [51] assumed that the austenite grain diameter measured close to the fusion boundary, corresponded to the 1465°C isotherm, a temperature 60–70°C lower than the melting temperature. The same assumption is adopted here.

Effective Arc Power /J s^{-1}	Welding Speed /mm s^{-1}	Electrode Diameter /mm	Observed Grain Size at 1465°C isotherm /μm	Calculated* Grain Size at 1465°C isotherm /μm	Calculated** Grain Size at 1465°C isotherm /μm
1800	2.5	3.25	91	23, 16–37	269, 110–655
2306	2.5	4.0	130	26, 17–42	299, 123–727
3075	2.5	5.0	146	29, 18–46	327, 134–797
4425	2.5	6.0	177	33, 21–53	374, 153–911

Table 4.2: Values of the prior austenite grain size developed in the HAZ as a function of weld variables [51], and associated computed values. An interpass temperature of 298 K is assumed.
* assuming $n = 2.5$, $Q = (3.3 \pm 0.8) \times 10^5\,\mathrm{J\,mol^{-1}}$ and $K' = 5 \times 10^{13 \pm 3}\,\mu\mathrm{m}^{2.5}\mathrm{s}^{-1}$
** assuming $n = 2.73$, $Q = (4.60 \pm 0.33) \times 10^5\,\mathrm{J\,mol^{-1}}$ and $K' = (5.4 \pm 0.6) \times 10^{12}\,\mathrm{mm}^{2.73}\mathrm{s}^{-1}$

The calculations were performed using the values of n, K' & Q found here, and again with the values found by Alberry et al. [51]. These values, together with the experimental data are tabulated in table 4.2.

It is clear that equations 4.5 & 4.7, together with the constants derived, grossly underpredict the austenite grain size. The model in its present state is therefore unsatisfactory.

In order to obtain better fit with this HAZ data, values of $\overline{D}$ have been calculated as a function of n, K' & Q, for values of n between 1.0 & 3.0, values of Q between 300,000 & 500,000 J mol^{-1} and K' between 1×10^{12} & $1 \times 10^{16}\,\mu\mathrm{m}^n\mathrm{s}^{-1}$. For each set of values, the best-fit line through the observed and calculated data points was determined by the method of least squares, and the correlation & regression coefficients computed. The results of this statistical analysis are tabulated in table 4.3.

Q /J mol^{-1}	K' /μm^{n}s^{-1}	n	Correlation Coefficient	Regression Coefficient
300,000	0.1D+16	2.7	0.979	1.022
300,000	0.4D+16	3.0	0.980	0.985
310,000	0.2D+16	2.7	0.979	1.016
310,000	0.3D+16	2.8	0.980	0.983
310,000	0.5D+16	2.9	0.980	0.988
310,000	0.9D+16	3.0	0.980	1.019
320,000	0.8D+15	2.4	0.978	0.963
320,000	0.9D+15	2.4	0.978	1.012
320,000	0.4D+16	2.7	0.979	1.010
320,000	0.7D+16	2.8	0.980	1.032
330,000	0.2D+14	1.5	0.972	1.007
330,000	0.5D+14	1.7	0.974	0.956
330,000	0.9D+14	1.8	0.975	1.005
330,000	0.4D+15	2.1	0.977	1.001
330,000	0.7D+15	2.2	0.978	1.029
330,000	0.1D+16	2.3	0.978	0.967
330,000	0.3D+16	2.5	0.979	1.010
330,000	0.5D+16	2.6	0.979	1.015
330,000	0.7D+16	2.7	0.980	0.956
340,000	0.4D+16	2.4	0.979	1.044
350,000	0.7D+16	2.4	0.979	0.981
350,000	0.8D+16	2.4	0.979	1.038
360,000	0.6D+16	2.2	0.978	1.042
360,000	0.9D+16	2.3	0.979	0.999
370,000	0.4D+16	2.0	0.977	0.988
370,000	0.7D+16	2.1	0.978	1.017
380,000	0.3D+16	1.8	0.976	0.989
380,000	0.5D+16	1.9	0.977	0.995
390,000	0.4D+16	1.7	0.975	1.037
390,000	0.6D+16	1.8	0.976	0.982
400,000	0.8D+16	1.7	0.975	1.030
410,000	0.6D+16	1.5	0.973	1.042
410,000	0.9D+16	1.6	0.975	0.979
420,000	0.4D+16	1.3	0.971	0.973
420,000	0.7D+16	1.4	0.972	1.011
430,000	0.8D+16	1.3	0.971	0.965
440,000	0.6D+16	1.1	0.967	0.986
450,000	0.7D+16	1.0	0.965	0.956

Table 4.3: Typical output from the statistical analysis.

The results indicate that a range of values of n, K' and Q are suitable for describing the austenite grain diameters observed in the HAZ; the values of K' found here are typically 2-3 orders of magnitude

larger than that found from the thermal grooving experiments.

For consistency with these experiments, the values chosen are $n = 2.5$ & $Q = 3.3 \times 10^5 \, \text{Jmol}^{-1}$, as before, but now $K' = 3 \times 10^{15} \, \mu\text{m}^{2.5}\text{s}^{-1}$. Figure 4.6 compares the observed and calculated values of $\overline{D}$.

4.3.3 Thermal Pinning

As already noted, the severe temperature gradients which are common in weld deposits might influence the austenite grain distribution. In the heat-affected zone or the reheated fusion zone it is not uncommon for a drop in temperature of 30–50° C to occur over a distance of ~100 μm, depending upon the heat input. This means that grain growth can be physically restricted by the narrow width of the HAZ isotherms. Alberry et al. [51] referred to this phenomenon as *thermal pinning*, although there was no attempt to explain the effect quantitatively. Strictly, in the presence of *any* temperature gradient, the use of equations such as 4.5 & 4.7 to describe grain size distributions must be incorrect, because in reality the kinetic strength varies across each grain.

The limiting case for the rate of change of γ-grain size with distance occurs when the calculated γ-grain size changes over a distance equal to that γ-grain size. Mathematically, this is equivalent to the condition that

$$\left| \frac{\partial \overline{D}}{\partial r} \right| < 1 \qquad (4.10)$$

where r refers to a distance in an arbitrary direction. Equation 4.10 represents mathematically the condition for thermal pinning.

For the 5 mm electrode at an effective heat input of 0.6 kJ mm^{-1}, $\partial \overline{D}/\partial r$ approaches -0.4 at the fusion boundary (figure 4.7). In this case at least, thermal pinning is likely to occur, if at all, in the vicinity of the fusion boundary.

Figure 4.7 also illustrates the error introduced by using equation 4.7 rather than 4.6; the approximation underestimates I by typically 15%, although near the Ac1 isotherm the error vanishes. Equation 4.6 is adopted throughout this work.

4.4 Summary

Austenite grain growth in $\frac{1}{2}$CrMoV steel was studied by monitoring the movement of the thermal grooves developed on the surface of a plane, polished section during heat treatment under a partial pressure of argon. These grooves correspond to the intersection of the austenite grain boundaries with the polished surface.

The austenite grain growth observed in this way was quantified in terms of theory for normal grain growth. Empirical constants were derived from the experimental data.

When these equations were applied to grain growth in the HAZ, the austenite grain size was underpredicted; other available empirical constants still failed to predict the austenite grain distribution with any accuracy. These constants were re-derived for the case of austenite grain growth in the HAZ.

It was noted that the austenite grain distribution might be influenced by the severe temperature gradients in the HAZ; calculations here show that such 'thermal pinning' is likely to occur only in the vicinity of the fusion boundary.

REFERENCES

50. W.F. Lange, M.E. Enomoto and H.I. Aaronson, Metall. Trans., 20A, 427–440, (1988).

51. P.J. Alberry, B. Chew and W.K.C. Jones, Metals Technology, 4, 317–325, (1977).

52. R. Millsop, in 'Hardenability Concepts with Applications to Steel' (Edited D.V. Doane and J.S. Kirkaldy), TMS-AIME, Warrendale, Pa., 316–333, (1978).

53. N.E. Hannerz and F. de Kazinczy, J.I.S.I., 208, 475–481, (1970).

54. R.E. Williams, Science, 161, 276–277, (1968).

55. A.W. Thompson, Metallography, 5, 366–369, (1972).

56. S.A. Hackney and G.C. Ojard, Scripta Metall., 22, 1731–1735, (1988).

57. J.E. Burke and D. Turnbull, Progress in Metal Physics, 3, 220–292, (1952).

58. J.W. Martin and R.D. Doherty, 'Stability of Microstructure in Metallic Systems', p.228, Cambridge University Press, (1976).

59. H.V. Atkinson, Acta Metall., 36, 469–491, (1988).
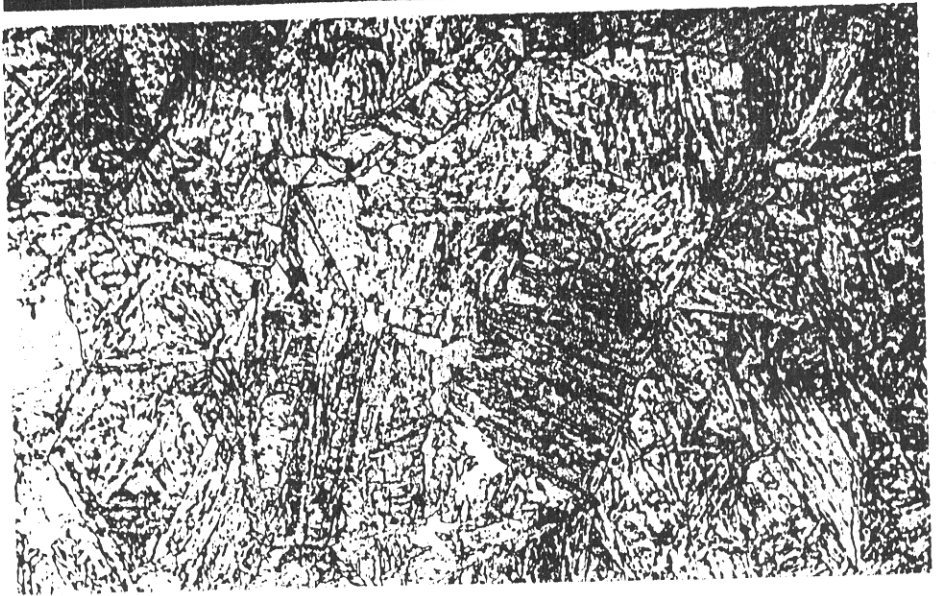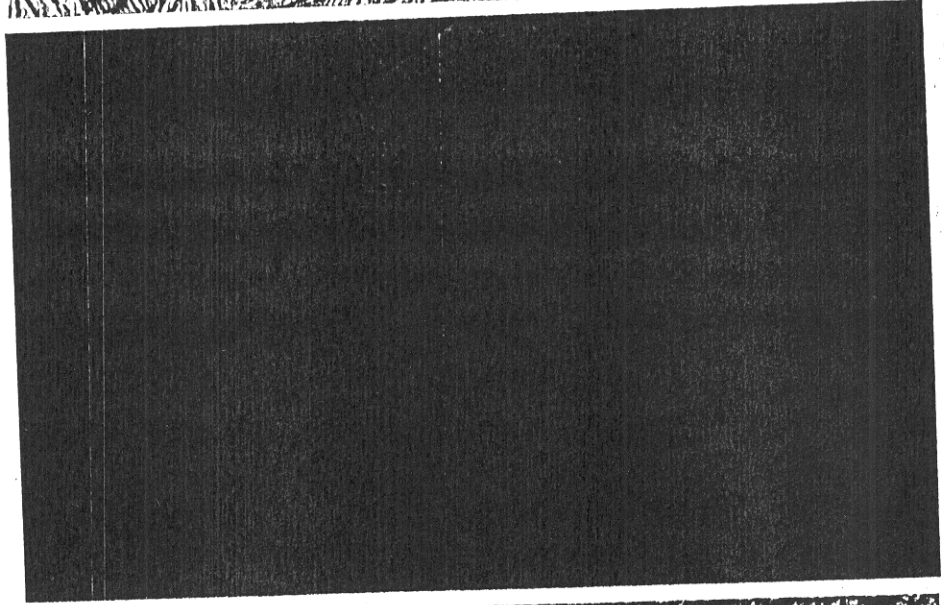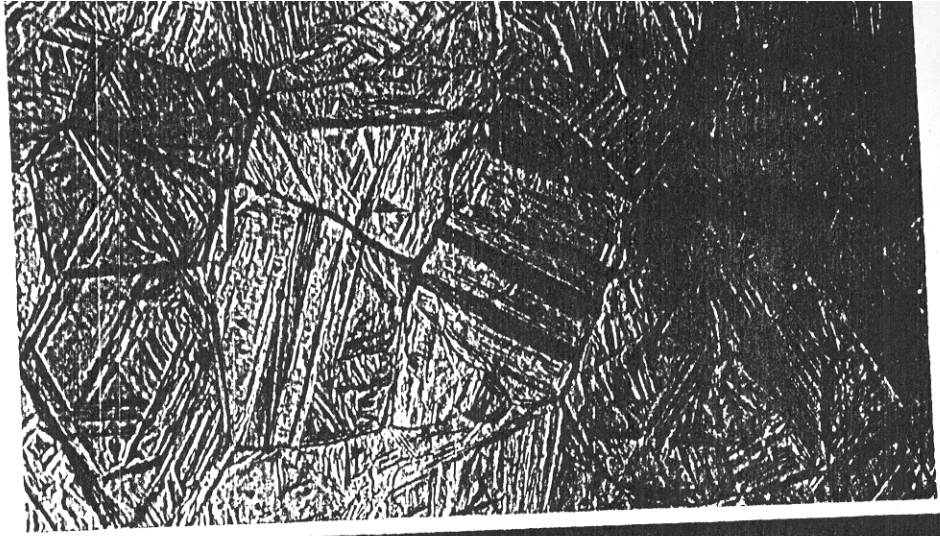
100 µm

Figure 4.1: a) Top, optical micrograph illustrating the thermal grooves developed on a plane polished service, (3 hours at 1200°C); b) Middle, Nomarski interference micrograph; c) Bottom, the same field of view after conventional polishing and etching in 2% nital.

75
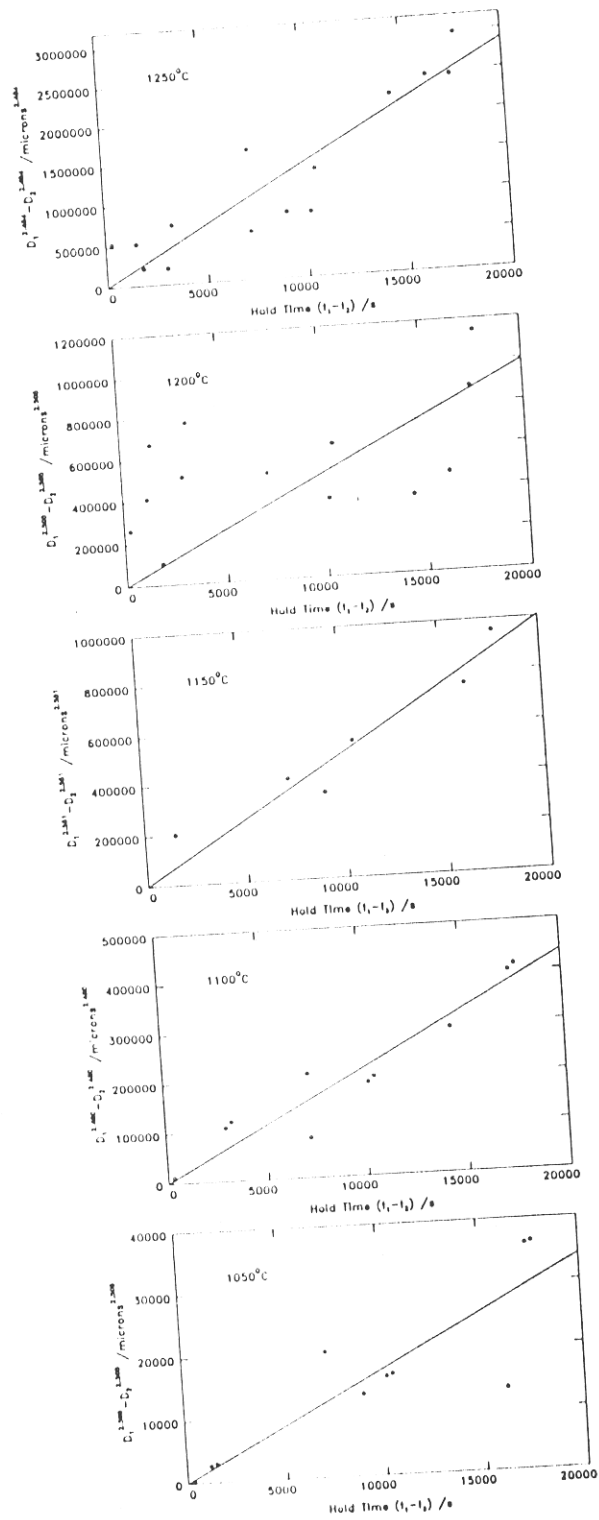
Figure 4.2: The level of agreement attained in the analysis for the grain growth exponent n.
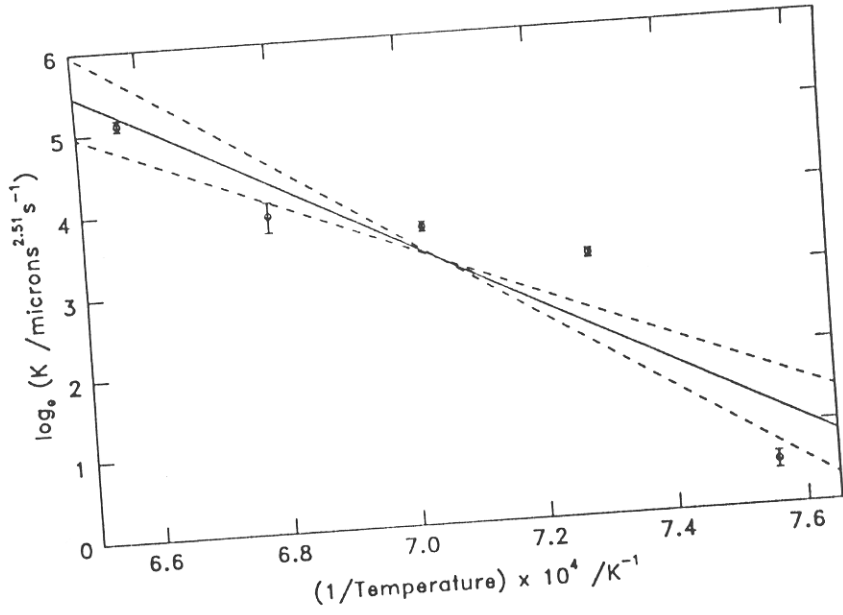
Figure 4.3: Determination of the activation energy for grain boundary growth. The kinetic constant K is assumed to obey an Arrhenius type relationship.
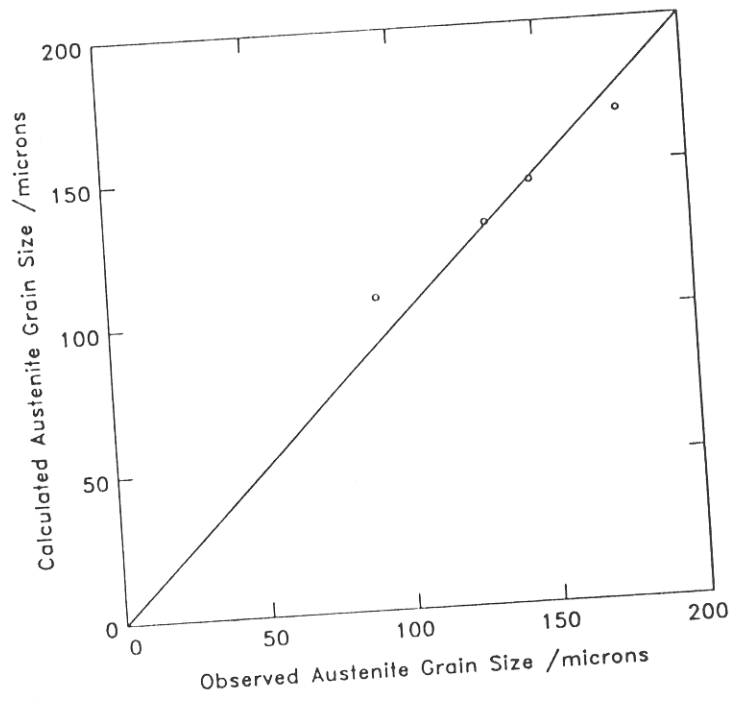
Figure 4.6: Comparison of observed and calculated austenite grain diameters near the fusion boundary in the HAZ of $\frac{1}{2}$CrMoV steel.
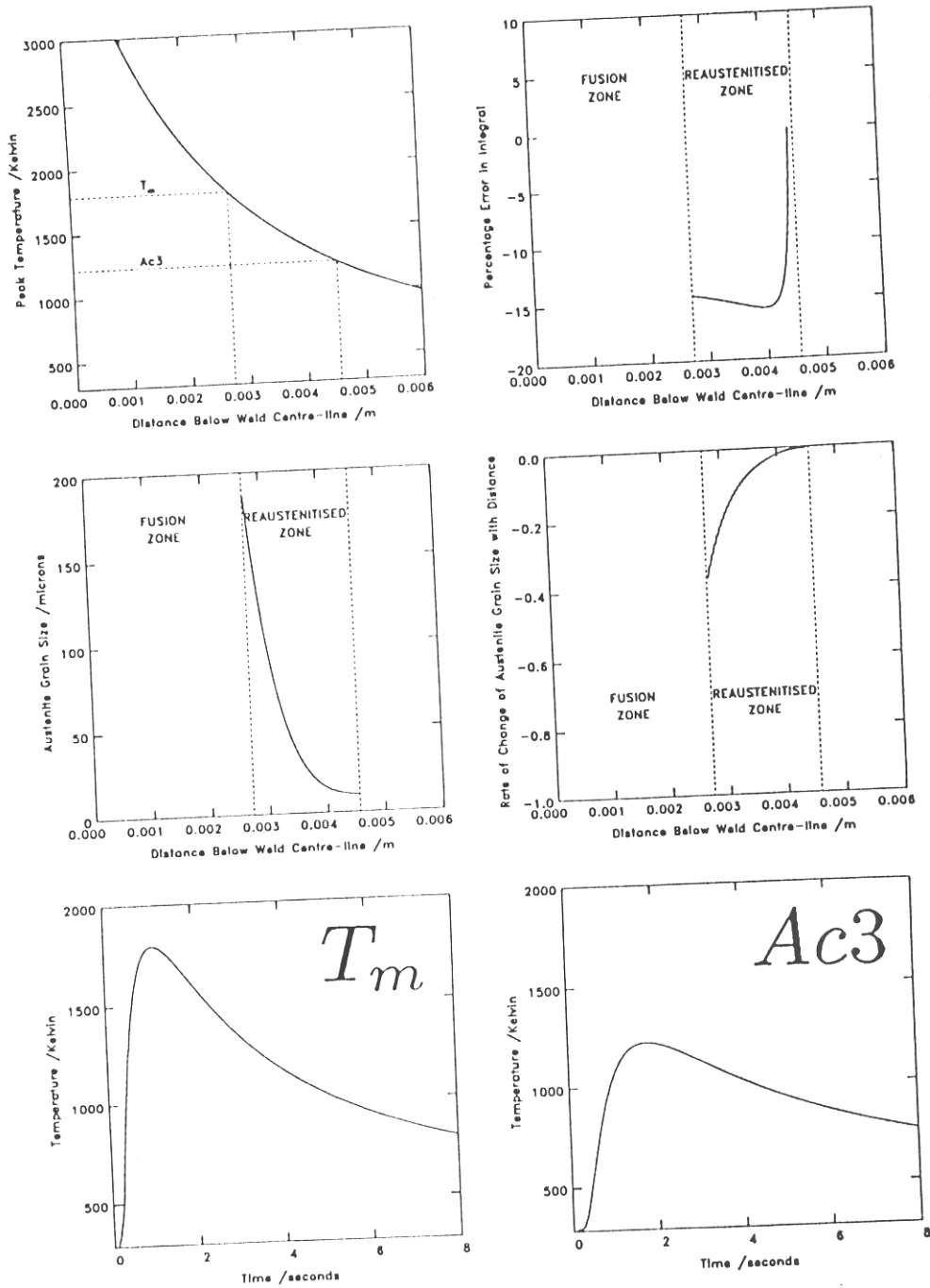
Figure 4.7: Calculations for a 5 mm electrode at a heat input of 0.6 kJmol^{-1}. Top left, the peak temperature of the thermal cycle as a function of distance below the weld centre-line. Middle left, the austenite grain diameter in the reaustenitised zone. Top right, comparison of the evaluation of the integral I with equations 4.6 & 4.7. Middle right, the rate of change of austenite grain diameter with distance. Bottom left & right, calculated temperature-time profiles at the fusion, and Ac3 isotherms respectively.

CHAPTER FIVE
The Characterisation and Modelling of
Low-Alloy 0.5CrMoV Steel Weld Heat-Affected Zones

5.1 Introduction

In modern steam-generating power plants, low-alloy $\frac{1}{2}$CrMoV steel is used almost exclusively for the main piping which carries superheated steam from the boiler to the turbine, where electricity is generated. The steam-pipes are typically of 75 mm thickness, with an inside bore of 225 mm, and are required to operate at temperatures in the vicinity of 565°C for the design life of the power station (∼30 years). During fabrication and repair, the pipes are welded together with $2\frac{1}{4}$CrMo weld metal, using the manual-metal-arc (MMA) process. Because the pipes are constrained, the as-welded residual stresses can approach the magnitude of the yield stress, and so it is normal practice to stress-relieve the welds at 690–720°C for 3 hours prior to service. During service itself, the superheated steam generates stresses within the pipes; the hoop stress can typically reach 30 MPa [2], although these stresses vary due to accommodation within the pipe assembly, variations in the wall thickness, and changes in steam pressure.

The growth of cavities and cracks in such steam-pipes necessitate a great number of repairs, and present a hazard to the integrity and safety of the power plant. For service exposure times of less than 5 years, the major concerns have been [60] the occurrence of transverse weld metal cracking [61], and circumferential HAZ ('stress-relief') cracking adjacent to the fusion boundary [62]. However, for service times greater than 10 years, repeated cracking has been observed [63] parallel to the circumferential joint in the partially reaustenitised region of the HAZ, next to the parent metal; it is particularly predominant near shaped components, and because of its circumferential nature, it can lead ultimately to catastrophic failure of the pipe. This mode of failure has been termed 'type IV cracking' and is now considered the major end-of-life failure mechanism in such components [60]. The incidence of type IV cracking is especially unexpected since the longitudinal stress in the pipe is approximately only half that of the circumferential hoop stress. It demonstrates that the limits of load bearing capacity can be inadvertently exceeded in operation, due to the effects of construction.

Since the parent plate and heat-affected zone possess the same chemical composition, the poorer creep properties of the HAZ (which the occurrence of type IV cracking infers) must arise because the HAZ microstructure differs from that found in the baseplate. Creep resistant $\frac{1}{2}$CrMoV steel attains its most favourable properties in the normalised and tempered condition, but this condition is changed locally by the thermal cycles associated with the welding operation. It is thus evident that the effect of stress-relief heat treatment is insufficient to restore the HAZ to the creep strength and ductility levels of the baseplate.

In this work, the microstructures found in $\frac{1}{2}$CrMoV baseplate and HAZ are studied in an effort to discover why type IV cracking occurs. Particular emphasis is placed upon studying the partitioning of chemical elements between carbide phases and the ferrite matrix. This is detected using a variety of methods: EDX spectroscopy, X-ray analysis and bulk analysis.

VARIABLE	VALUE
Interpass Temperature	250 °C
Recovery	113.7 %
Heat Input (Efficiency=0.75)	$0.987 \, \mathrm{kJ \, mm^{-1}}$
Arc Current	231 A
Arc Voltage	22.0 V
Electrode Diameter	5 mm
Welding Speed	$3.76 \, \mathrm{mm \, s^{-1}}$
Wire Burn-Off Rate	$3.20 \, \mathrm{mm \, s^{-1}}$

Table 5.1: The weld variables recorded for the multipass weld studied in this work.

5.2 Experimental Details

An experimental weld was designed in a manner considered to be typical of welds deposited in the power generation industry. The multipass weld consists of 69 weld beads deposited in 12 layers; the $2\frac{1}{4}$CrMo weld metal was deposited using a manual metal-arc technique in a V-notch weld geometry of $\frac{1}{2}$CrMoV steel. Suprex B electrodes of 5 mm diameter were employed; these gave an effective heat input of $0.987 \, \mathrm{kJ \, mm^{-1}}$ (assuming an arc efficiency of 0.75) at an interpass temperature of 250°C. All of the essential weld variables are presented in table 5.1, and the geometry of the weld preparation is shown in figure 5.1.

The baseplate (and hence the HAZ) of the multipass weld is referred to throughout this work as Steel A. Unless stated otherwise, both baseplate and HAZ are examined in the as-welded state. The HAZ is also examined after the standard stress-relief heat-treatment of 3 hours at 700°C. Two other $\frac{1}{2}$CrMoV steels were examined. Steel B is ex-service material (~35,000 hours at 565°C) which was been subsequently re-normalised & tempered (1 hour at 965 ± 10°C, air cool; 3 hours at 700 ± 10°C, air cool). Steel C is ex-service material (~8,000 hours at 565°C) which was subsequently re-normalised & tempered in the same way; this material is also used in the service-aged condition. The heat treatment given to steels B & C was designed to reproduce the microstructure of the steels when they enter service. The chemical compositions of steels A, B and C, determined using spectroscopic analyses, are tabulated in table 5.2.

REF.	CONCENTRATION /wt%											
	C	Cr	Mo	V	Si	Mn	Ni	Cu	Nb	Ti	S	P
A	0.13	0.41	0.58	0.25	0.23	0.50	0.25	0.17	0.002	0.001	0.005	0.033
B	0.13	0.44	0.60	0.23	0.20	0.60	0.19	0.17	0.002	0.001	0.038	0.014
C	0.13	0.44	0.59	0.23	0.20	0.59	0.19	0.17	0.002	0.001	0.034	0.015

Table 5.2: The compositions of materials used in this study.

5.3 Optical Microscopy

A section of the weld was cut, such that the surface itself was normal to the welding direction. This transverse section was ground, polished and etched in 2% nital. A macrograph of the prepared surface is shown in figure 5.2. Optical microscopy was used to confirm the number of weld beads deposited in each of the 12 layers, although the relative positions of the beads were recorded during welding.

The HAZ from near the root of the weld, and that from the vicinity of the vertical face of the fusion boundary were examined in detail. Figure 5.3 is a composite optical micrograph of the HAZ from the root of the weld. The region is due to the deposition of two adjacent beads; the manner in which the isotherms have overlapped is revealed by the metallographic technique. Figure 5.4 is a similar micrograph of the HAZ near the vertical face of the weld.

5.4 Comparison With Computer Model

In chapter three of this dissertation, a computer model capable of mapping the spatial distribution of the temperature fields in multipass welds was designed. This model is now used to help interpret the

has been used to confirm that figure 5.9 is the correct interpretation of figure 5.4. A range of microstructures similar to those from the root HAZ were observed.

5.6 Transmission Electron Microscopy

The baseplate and HAZ of the experimental weld were characterised using transmission electron microscopy (TEM). Both thin foil and carbon replica specimens were examined in a Philips 400T TEM operated at 120kV.

5.6.1 Carbon Replicas

Carbon replica specimens were prepared by deposition of an amorphous layer of carbon onto a specimen which had been prepared first for optical examination in the usual way. The specimens were first electrolytically etched (5 volts positive) in a mixture of 2% concentrated hydrochloric acid in methanol, before being thoroughly washed in ethanol. The carbon replicas were finally floated off by careful immersion in distilled water, and examined on copper grids.

The use of carbon replica specimens enables an area as large as $7\,mm^2$ to be examined in a single specimen, thus offering an advantage over thin foils, when the microstructure varies with position as considerably as it does in the HAZ. The technique used here involved first observing the carbon replica in an optical microscope, to locate a particular area for study; that area could then be examined in the TEM since the copper grid acts as a marker for the area of interest.

Figure 5.19 is a TEM micrograph of a carbon replica of the baseplate of the multipass weld. The microstructure consists of spheroidised nodules of pearlite separated by large regions of ferrite. Within the ferrite, a fine dispersion of vanadium carbide particles is found.

Figures 5.20a & b, 5.21a & b and 5.22a & b are optical, and TEM micrographs respectively of a carbon replica specimen extracted from the root HAZ. Figure 5.20 illustrates the coarse structure next to the fusion boundary (thermal cycles **FBE** or **FBF**). Figure 5.21 is taken from the area next to the fusion boundary which has been partially reaustenitised (thermal cycles **BDF**) where a large amount of carbide is associated with the prior austenite grain boundary. Finally figure 5.22 is taken from the partially reaustenitised area (thermal cycles **FCE** or **FCF**); a duplex microstructure of regions of coarse carbide separated from regions of finer coarsened carbide.

In all cases electron diffraction and EDX analysis indicated that the coarse needle-like carbides are cementite; also present are a number of smaller vanadium carbide particles, although it is noticable that such particles are rather coarser than in the baseplate. Consistent with previous observations [64,65] molybdenum carbide was found associated with vanadium carbide (figure 5.23).

5.6.2 Thin Foils

There is a difficulty in preparing TEM foils when the microstructure is variable, as in the HAZ. This was overcome in this work by the using the following procedure (figure 5.24). Firstly, thin strips of metal (of thickness $\sim$0.3 mm) were slit from the HAZ using a diamond wheel, such that the plane of each strip lay parallel to the fusion boundary. Each strip was then prepared for optical examination in the usual way, so that areas of interest could be located. Discs of diameter 3 mm were then punched from the sheet, and thinned to a thickness of 50 μm by mechanically grinding away the unprepared side. The discs were electropolished in a solution of 5% perchloric acid/25% glycerol in ethanol, at an applied voltage of 55 volts and a temperature of $-10°C$.

Figures 5.25 & 5.26 are thin foil micrographs of spheroidised pearlite nodules found in the baseplate of the multipass weld. Electron diffraction (figure 5.27) revealed an orientation relationship between cementite and ferrite near to the Pitsch [66] orientation relationship.† The vanadium carbide particles

---

† $<3\bar{1}1>_\alpha$ 2.6° from $(100)_{Fe_3C}$, $<131>_\alpha$ 2.6° from $(010)_{Fe_3C}$, $<\overline{2}15>_\alpha \parallel (001)_{Fe_3C}$

were identified (figure 5.28) by tilting the foil to a $<001>_\alpha$ zone axis; this revealed that the carbides exhibit an orientation relationship with ferrite consistent with the Baker-Nutting [67] orientation relationship.‡ Such carbides precipitate at the moving α/γ boundary by a mechanism which is termed *interphase precipitation*; it yields rows of fine carbides which are closely spaced.

Figure 5.29 is a thin foil micrograph of the region near to the fusion boundary (thermal cycles FBE or FBF), showing nucleation of upper bainite at a prior austenite grain boundary. The hardenability of this steel is insufficient to stabilise the residual austenite associated with the bainite reaction, and consequently such austenite breaks down to a ferrite/cementite aggregate (figure 5.30). A consequence of this is that ferrite is continuous throughout a bainite sheaf (and the orientation relationship is almost constant). However, adjacent sheaves were observed to be twin-related (figure 5.31).

Figure 5.32 illustrates that further from the fusion boundary (thermal cycles FCE or FCF) the microstructure is still upper bainite, with the sub-units separated by ferrite/cementite aggregate as before.

Thin foil microscopy of the partially reaustenitised region revealed the presence of twinned plates of martensite within the regions where transformation to austenite had taken place (figure 5.33). It is believed that this occurs because these areas become enriched in carbon during reaustenitisation, with a resultant increase in hardenability.

In all regions that had transformed to austenite, it was noted that the volume fraction of vanadium carbide was considerably smaller than in the baseplate.

5.7 Energy Dispersive X-Ray Analysis of Microphases

In the power generation industry, where creep-resistant steels operate at temperatures as high as 565°C, it is necessary to know the amount of creep life remaining, *i.e.* the *remanent life* of a particular component, so that power plants can operate both economically and within the required safety limits. The problem of remanent life is complicated by the fact that the creep strength of such steels is a strong function of temperature; for example a rise in temperature of 10°C is associated with a 50% reduction in creep-life [68]. Even if a time-temperature history is known for such components, it is then not easy to extract from it an estimate for the remanent life.

For this reason, the study of the way in which the chemical compositions of the carbide phases change during service life has assumed prominence in recent years, because such compositions, monitored using non-destructive microanalytical techniques, can be used as a built-in recorder for the time-temperature history experienced by the steel.

Therefore considerable attention has been paid to monitoring the compositions of carbide phases, with particular emphasis on microanalysis. Microanalysis can be accomplished in the TEM, with an accuracy within ±5-10%, using energy dispersive X-ray analysis (EDX). The electron beam in a standard TEM can be condensed down to ~5 nm in diameter, which with beam interaction within the foil, gives a spreading of typically ~25 nm for a 100 nm thick iron based foil. Strictly the magnitude of the spreading depends upon the density of the material, the foil thickness as well as the electron accelerating voltage. The area sampled in conventional TEM mode is therefore ~500 nm², and can only be reduced by preparing thinner foils. The beam diameter can be reduced by the use of the scanning transmission electron microscope (STEM) mode, so that the area sampled is reduced to ~50 nm²; however, STEM suffers from poorer image resolution and lower count rates, which require long counting times for comparable statistical accuracy. Beam drift during sampling is then often a problem.

The microanalysis reported here was performed exclusively upon carbon replica specimens, so that any signal from the matrix was entirely removed. Trial comparisons of EDX performed in conven-

---

‡ $<001>_\alpha \parallel <001>_{V_8C_7}$, $<100>_\alpha \parallel <110>_{V_8C_7}$

tional TEM and STEM modes yielded essentially identical results, so that the greater count rate of the conventional mode meant that it was eventually adopted.

A Link series 860 EDX attachment to the Philips 400T was employed throughout. The preset live time was typically between 100 and 300 seconds, with the system operated with dead time not greater than 25%.

5.7.1 Results

Microanalysis was performed on bainitic cementite extracted from the HAZ (both before and after subsequent stress-relief heat treatment), pearlitic cementite from the baseplate of the multipass weld, and the pearlitic cementite extracted from the service-aged material C. The results are presented table 5.3, and figure 5.34 illustrates typical data. It is found that the pearlitic cementite has a composition which is considerably enriched with respect to Cr, Mo and Mn. This observation in itself does not necessarily imply, but is consistent with, equilibrium partitioning of substitutional solutes during the growth of pearlite by a reconstructive mechanism.

On the other hand, the concentration of alloying elements in the bainitic HAZ cementite is significantly lower, and only slightly in excess of the overall mean composition of the steel. Thus it seems likely that such cementite has formed by a mechanism which involves no partitioning of substitutional elements; this evidence in itself does not confirm a displacive reaction mechanism, since it is possible for cementite to grow from carbon-enriched residual austenite by a reconstructive mechanism at a rate controlled by the diffusion of substitutional solutes ahead of the cementite/ferrite/austenite interface. The slight enrichment observed with respect to all substitutional elements could occur during subsequent weld thermal cycles, the kinetic strength of which can be sufficient to permit such redistribution.

During stress-relief heat treatment (3 hours at 700°C) Cr, Mo, V and Mn partition to the bainitic cementite, in an effort to attain equilibrium between the ferrite and cementite. The HAZ cementite then has approximately the composition of the cementite in the baseplate.

The microanalysis results of the vanadium carbide particles present in the baseplate and HAZ are also presented in table 5.3, and figure 5.35. The results are somewhat inconclusive, since with molybdenum carbide nucleating on, or from, vanadium carbide, the microanalysis results represent averages over the particles as a whole. However, it was evident that the concentration of Mo in the vanadium carbide particles present in the fully reaustenitised region of the HAZ is small. This is likely to reflect the coarsening/dissolving and reprecipitation of vanadium carbide which occurs for strong weld thermal cycles.

Finally it should be noted that the accuracy to which the compositions in table 5.3 are presented cannot be justified, except to ensure consistency.

REF.	CONCENTRATION /wt%							
	Fe	Cr	Mo	V	Ni	Si	Mn	S
Fe$_3$C in Baseplate of Multipass Weld	85.017	4.902	3.673	2.003	0.137	0.225	3.861	0.183
Fe$_3$C in HAZ of Multipass Weld	95.432	0.837	1.264	0.845	0.424	0.347	0.605	0.246
Fe$_3$C in HAZ, after stress-relief	83.123	6.970	2.836	2.007	0.294	0.155	4.274	0.340
Fe$_3$C in Material C Service Aged	87.398	2.400	4.599	1.398	0.108	0.107	3.829	0.160
Fe$_3$C in Material C Service Aged + Heat Treatment	92.106	0.893	2.165	1.791	0.149	0.140	2.396	0.359
V$_8$C$_7$/Mo$_2$C in Baseplate of Multipass Weld	0.891	2.780	24.343	67.746	0.128	0.403	1.211	2.499
V$_8$C$_7$/Mo$_2$C in HAZ of Multipass Weld	3.032	1.548	12.495	79.258	0.204	2.023	0.242	1.198

Table 5.3: The mean composition of microphases determined using EDX microanalysis in the TEM.

5.8 Bulk Extraction of Particulate Phases

In order to aid the identification of finer non-metallic phases, an attempt was made to isolate them using an electrolytic extraction method. The method is essentially that described by Andrews and Hughes

[69], and was used more recently by Stuart & Ridley [70], Leitnaker *et al.* [71] and Pilling & Ridley [72]. Extraction allows the possibility of obtaining quantitative lattice parameter and volume fraction data using X-ray techniques [73]. In addition, a direct measurement of the mass of the extracted residue gives an overall estimate of the mass of the minor phases relative to that of the matrix. Chemical analysis of the solution resulting from the anodic extraction, and of the extract itself, using standard analytical techniques, can be used to determine the way in which the elements partition between the matrix and the extract. The results can be correlated with the TEM and EDX results on carbon replica specimens.

Accurately weighed specimens of the steels A, B & C (size $5 \times 2 \times \frac{1}{2}$ cm) were anodically corroded at 1.5 V using a platinum cathode in an aqueous solution of 5%HCl. Two successive extractions are carried out for each steel, at constant voltage. As previously observed [69,71], the precipitates tended to adhere to the specimen, and were removed by ultrasonic vibration in ethanol. They were separated from the supernate by centrifuging, washed in ethanol, centrifuged again, dried in a vacuum desiccator, and weighed. Possible errors are therefore due to loss of precipitate through dissolution or inadequate centrifuging, and inadequate cleaning of glassware or precipitate.

Typical masses of extracts are $\sim$0.05 g. When expressed as a percentage of the original specimen volume, the masses extracted from each of the two specimens are within 0.2% of each other (refer to table 5.4).

REF.	ORIGIN	WEIGHT % EXTRACTED	
A1	Baseplate of Multipass Weld	2.6	2.6
A2	HAZ of Multipass Weld	2.0	2.2
A3	HAZ, after stress-relief	3.4	3.6
B	Ex-Service Material: As-received	2.7	2.6
C1	Ex-Service Material: As-received	3.1	2.9
C2	Ex-Service Material: Heat-Treated	2.4	2.5

Table 5.4: Bulk-Extraction of carbides.

The mass fraction of cementite at ferrite/cementite equilibrium can be crudely estimated from the binary Fe-C phase diagram, although strictly multicomponent phase diagrams are appropriate. Assuming a carbon content of zero in ferrite, 6.67 wt% in Fe_3C and with a mean alloy carbon content of 0.13 wt%, the mass fraction of cementite is then 0.13/6.67 or 1.95%. If the density of Fe_3C is taken as 7.67 g cm^{-3} [70] and that of carbon-free ferrite as 7.87 g cm^{-3}, this value can be converted to a volume fraction of 0.020 or 2.0%. Thus it is likely that an appreciable fraction of the mass extracted in these experiments corresponds to phases other than cementite.

5.8.1 Chemical Analysis of Solutions Resulting from Extraction

During anodic extraction the matrix steadily dissolves in the HCl electrolyte. Analysis of the chemical composition of this electrolyte allows an estimation of chemical composition of the matrix itself. The technique of Inductively Coupled Plasma-Optical Emission Spectrometry (ICP-OES) is used here. Briefly, this involves pumping the solution through an atomiser via a spray chamber into an argon plasma. Here the ions emit emit light which passes into a spectrometer, where it is measured by photomultipliers at the wavelengths characteristic of the elements. Before analysis it is usual to calibrate the instrument using standard solutions.

The results are tabulated in table 5.5, where the compositions are expressed in at%. It is notable that the concentrations of molybdenum, and particularly vanadium are considerably higher in the matrix of the as-welded HAZ than in that of the baseplate. After stress-relief heat treatment, the concentrations of vanadium is almost restored to that found in the baseplate, due to the reprecipitation of vanaium

carbide. The same effect occurs with molybdenum, although after stress-relief the concentration is still somewhat short of that found in the baseplate. These trends are consistent with the earlier TEM observations that V_8C_7 & Mo_2C are almost entirely absent in the as-welded HAZ.

REF.	ORIGIN	CONCENTRATION /at%						
		Fe	Cr	Mo	V	Ni	Si	Mn
A1	Baseplate of Multipass Weld	98.48	0.315	0.253	0.026	0.232	0.301	0.392
"	"	98.47	0.329	0.253	0.033	0.233	0.299	0.387
A2	HAZ of Multipass Weld	96.71	0.367	0.367	0.126	0.277	0.330	1.819
"	"	97.41	0.374	0.367	0.136	0.221	0.334	1.158
A3	HAZ, after stress-relief	98.68	0.316	0.286	0.041	0.197	0.103	0.377
"	"	98.59	0.363	0.294	0.028	0.220	0.113	0.396
B	Ex-Service Material: As-received	98.50	0.354	0.272	0.029	0.173	0.259	0.408
"	"	98.51	0.361	0.284	0.023	0.171	0.245	0.407
C1	Ex-Service Material: As-received	98.55	0.352	0.265	0.012	0.164	0.240	0.412
"	"	98.55	0.353	0.251	0.016	0.171	0.246	0.410
C2	Ex-Service Material: Heat-Treated	98.49	0.356	0.260	0.027	0.168	0.284	0.411
"	"	98.50	0.341	0.250	0.030	0.179	0.285	0.412

Table 5.5: The compositions of the electrolyte after bulk extraction, as determined by plasma-optical emission spectroscopy.

5.9 X-Ray Analysis of Extracted Phases

5.9.1 Method

All the extracted samples were mixed with an accurately weighed amount of CeO_2, so that the proportion in the sample was exactly 25.0% by mass. The mixture was then thoroughly shaken. Prior to X-ray analysis, (CuKα radiation) the samples were mixed with ethanol to make a paste which was smeared onto a single-crystal wafer of silicon which serves as the substrate for the sample, and is so orientated that no silicon lines are detected. A Siemens D500 diffractometer was used to scan between $30°$ and $65°$ 2θ at a step size of $0.004°$ 2θ, with a 1 second duration per step, so that each run took ~146 mins.

5.9.2 Theory

The expression for the intensity diffracted by a single-phase powder specimen in a diffractometer is [74]:

$$I = \left(\frac{I_0 A \lambda^3}{32\pi r}\right) \left[\left(\frac{\mu_0}{4\pi}\right)^2 \frac{e^4}{m^2}\right] \left(\frac{1}{v^2}\right) \left[F^2 p \left(\frac{1+\cos^2 2\theta}{\sin^2 \theta \cos \theta}\right)\right] \left(\frac{\exp\{-2M\}}{2\mu}\right) \quad (5.1)$$

where I is the integrated intensity per unit length of diffraction line, I_0 is the intensity of the incident beam, A is the cross-sectional area of the exposed region of the sample, λ is the wavelength of the incident beam, r is the radius of the diffraction circle, μ_0 is the magnetic permeability of free space, e is the charge on the electron, m is the mass of the electron, v is the volume of the unit cell, F is the structure factor, p is the multiplicity factor, θ is the Bragg angle, μ is the linear absorption coefficient and $\exp\{-2M\}$ is the temperature factor. The temperature factor corrects for thermal agitation of the atoms on the crystal lattice. The term M is difficult to determine accurately, but can be estimated, at least for cubic crystal structures [74].

As it stands, this expression is not in a form suitable for the analysis of a mixture of phases. However, when I_α is measured relative to the intensity of a reference line in the mixture, i.e. an internal standard it is not necessary to know many of the constants in the above expression. Thus, for a reference consisting of CeO_2, we have

$$\frac{I_\alpha}{I_{CeO_2}} = \frac{R_\alpha c_\alpha}{R_{CeO_2} c_{CeO_2}} \quad (5.2)$$

where

$$R_\alpha = \left(\frac{1}{v^2}\right) \left[F^2 p \left(\frac{1+\cos^2 2\theta}{\sin^2 \theta \cos \theta}\right)\right] (\exp\{-2M\}) \quad (5.3)$$

and c_α and c_{CeO_2} are the volume fractions of alpha and cerium oxide respectively.

Siemens DIFFRAC 500 software was used to locate the positions, and to calculate the integrated intensities associated with the diffraction peaks. The software subtracts the background radiation, eliminates the contribution from $CuK\alpha_2$ (assuming a $K\alpha_1/K\alpha_2$ intensity ratio of 2.0) and finds the peak locations as second derivative minima.

There are errors introduced in the measured values of the d-spacings, due to misalignment of the diffractometer, absorbtion in the specimen, displacement of the specimen from the diffractometer axis, and vertical divergence of the incident beam [74]. No single extrapolation function is completely satisfactory for correcting for these errors. However, the d-spacings of the internal standard are known to a high degree of accuracy.[1] Therefore, a polynomial function has been applied to correct the discrepancies.

5.9.3 Results

Figure 5.36 shows a diffractometer trace for extract from specimen B. The four CeO_2 peaks, together with peaks due to cementite (Fe_3C, θ)[2] are indicated as markers whose heights are scaled to the intensities reported on the appropriate JCPDS card.

Most of the observed diffraction peaks are due to cementite, but there are others which cannot be attributed to this phase. Figure 5.37 shows the same data with the markers due to vanadium carbide (V_8C_7, cubic, diamond structure, $a = 8.334$Å)[3] and molybdenum carbide (Mo_2C, hexagonal, $a = 3.012$Å, $c = 4.735$Å)[4]. It is evident that V_8C_7 is present in the sample, although the peaks occur at a rather somewhat lower 2θ value. This is consistent with partitioning of molydenum into V_8C_7 causing an increase in the lattice parameter, as observed in the EDX spectroscopy reported earlier. The absence of the {101} Mo_2C reflexion, which is normally very intense, is a good indication that this carbide is not present in significant quantities. The {200} manganese sulphide[5] and {420} & {422} $M_{23}C_6$[6] peaks were also detected.

Figure 5.38 compares the diffractometer traces for samples A1 & A2 (multipass weld baseplate and as-welded HAZ). The V_8C_7 peak at $2\theta \sim 62.5°$ is significantly weaker for the as-welded HAZ sample.

Figure 5.39 compares the diffractometer traces for samples C1 and C2 (service material as received, and after solution heat-treatment). Here it is evident that the shape of the V_8C_7 peak is altered during service life. It is possible that this is due to formation of Mo_2C on, or from V_8C_7, as observed in the TEM.

Corrected d-spacings, as well as the integrated intensities of diffraction peaks which do not overlap, are presented in table 5.6.

5.9.4 Cementite Lattice Parameters

The determination of the d-spacings of several Fe_3C planes with high precision enables the calculation of the room temperature lattice parameters for this phase. Since Fe_3C is orthorhombic, the d-spacing for a plane hkl is given by the expression

$$\frac{1}{d_{hkl}^2} = \frac{h^2}{a^2} + \frac{k^2}{b^2} + \frac{l^2}{c^2} \tag{5.4}$$

where a, b and c are the lattice parameters. The measured d-spacings (table 5.6) were fitted to this expression using a non-linear least-squares procedure, to arrive at estimates for a, b and c (table 5.7).

---

[1] Joint Committee for Powder Diffraction Studies (JCPDS) reference 34–394
[2] JCPDS reference 35–772
[3] JCPDS 35–786
[4] JCPDS 35–787
[5] JCPDS 6–518
[6] JCPDS 25–405

PHASE	hkl	INTERPLANAR SPACING d /Å					INTEGRATED INTENSITY				
		A1	A2	B	C1	C2	A1	A2	B	C1	C2
CeO_2	{200}	2.7056	2.7057	2.7054	2.7056	2.7056	7850	2967	2072	5138	5091
MnS	{200}	–	–	2.6114	2.6136	2.6117	–	–	1194	1477	1599
$M_{23}C_6$	{420}	2.3572	–	2.3557	2.3582	2.3567	1220	–	1005	1809	1244
Fe_3C	{200}	2.2641	2.2613	2.2644	2.2634	2.2641	1881	2928	1761	1742	1904
Fe_3C	{120}	2.2165	2.2157	2.2170	2.2169	2.2168	1354	1696	1227	1185	1416
$M_{23}C_6$	{422}	–	–	2.1513	2.1513	2.1506	–	–	755	1129	1100
Fe_3C	{022}	2.0284	2.0312	2.0293	2.0292	2.0295	17841	8099	12671	12697	10140
Fe_3C	{103}	2.0147	2.0157	2.0154	2.0150	2.0152	9710	14299	18685	9847	11237
Fe_3C	{211}	1.9776	1.9767	1.9777	1.9777	1.9776	4024	6206	4687	3926	4556
CeO_2	{220}	1.9134	1.9133	1.9136	1.9135	1.9134	16221	5702	4708	10667	11545
Fe_3C	{113}	1.8732	1.8723	1.8737	1.8734	1.8735	2643	4317	6337	3192	4263
Fe_3C	{122}	1.8528	1.8525	1.8530	1.8529	1.8531	3266	5577	5939	4849	6827
Fe_3C	{212}	1.7632	1.7613	1.7637	1.7640	1.7638	1671	2327	2056	1895	1772
Fe_3C	{220}	1.6852	1.6857	1.6852	1.6862	1.6854	1605	1701	2702	1584	1963
CeO_2	{311}	1.6318	1.6319	1.6316	1.6317	1.6318	14251	5288	4244	9833	10490
Fe_3C	{130}	1.5871	1.5886	1.5871	1.5875	1.5874	1330	1734	1386	1463	1476
CeO_2	{222}	1.5622	1.5621	–	1.5623	1.5622	2495	590	–	878	1792
V_8C_7	{440}	1.4847	1.4837	1.4837	1.4813	1.4874	5555	2905	6943	7007	3224

Table 5.6: d-spacings and integrated intensities observed using powder diffractometry.

REF.	a /Å	b /Å	c /Å
A1	4.523 ± 0.005	5.081 ± 0.004	6.753 ± 0.008
A2	4.517 ± 0.004	5.086 ± 0.004	6.753 ± 0.007
B	4.523 ± 0.005	5.081 ± 0.004	6.756 ± 0.008
C1	4.524 ± 0.004	5.082 ± 0.004	6.754 ± 0.007
C2	4.523 ± 0.005	5.082 ± 0.004	6.756 ± 0.008

Table 5.7: Lattice parameters (with standard errors) calculated for cementite.

5.9.5 Discussion and Possible Application to the Remanent Life Problem

The calculated cementite lattice parameters are in reasonable agreement with values previously reported [75,76,77]. The values for cementite from samples A1, B, C1 & C2 are consistent with each other; this is unsurprising since microanalysis has shown that the chemical compositions of cementite in these steels are very similar. However, cementite extracted from the HAZ shows values of a and b which are some way from those found for the other samples. This might be explained by the fact that this cementite is known to have a significantly different composition. Since the monitoring of cementite composition is of great relevance to the problem of remanent life estimation, it is suggested that future work be carried out to test whether the bulk extraction/X-ray technique is sensitive to changes in cementite composition. With significantly longer X-ray run-times, it is likely that the standard error in the calculated lattice parameters could be reduced, so that the technique is then more sensitive.

5.9.6 Estimation of Volume Fraction of Cementite

The unit cell of cementite contains 12 iron and 4 carbon atoms, and if the orthogonal unit cell axes are chosen so as to be consistent with the space group $Pbnm$, the equivalent points are:

$$\pm(x, y, z), \pm(x, y, \tfrac{1}{2} - z), \pm(\tfrac{1}{2} - x, \tfrac{1}{2} + y, z), \pm(\tfrac{1}{2} - x, \tfrac{1}{2} + y, \tfrac{1}{2} - z)$$

The symmetry elements on the lattice give rise to the special positions:

$$\pm(u, v, \tfrac{1}{4}), \pm(\tfrac{1}{2} - u, \tfrac{1}{2} + v, \tfrac{1}{4})$$

In 1940, Lipson and Petch [75] used X-ray powder-diffraction data to locate the carbon atoms, and to refine the positions of the iron atoms. The Lipson-Petch structure has since been confirmed, and according to the review by Yakel [78], the most accurate determination to date [77] gives

$$8 \text{ Fe at } x = 0.3374, y = 0.1816, z = 0.0666;$$

90

$$4 \text{ Fe at } u = 0.8402, v = 0.0367;$$
$$4 \text{ C at } u = 0.444, v = 0.877.$$

The effect of Mn, Cr, Mo & V partitioning to cementite is taken into account by using the concentrations calculated using the carbon replica EDX spectroscopy (table 5.3), through the expression

$$f_{av} = x_{Fe}f_{Fe} + x_{Mn}f_{Mn} + x_{Cr}f_{Cr} + x_{Mo}f_{Mo} + x_{V}f_{V} \qquad (5.5)$$

where f_{av} represents the average atomic scattering factor of cation sites, the f's are elemental atomic scattering scattering factors, and the x's are mole fractions of elements on cation sites, The f's in turn are strong functions of $\sin\theta/\lambda$, and are tabulated in many standard X-ray text-books [e.g. 74]. This information, together with a knowledge of the positions of the atoms, allows the structure factor of a general plane hkl to be calculated using standard methods. Cerium oxide is isostructural with fluorite, so that the structure factors of this phase can also be calculated.

Following Lipson and Petch [75] the temperature factor for cementite in equation 5.3 is evaluated according to the empirical equation

$$\exp\left\{-2M\right\}_{Fe_3C} = \exp\left\{-3\sin^2\theta\right\} \qquad (5.6)$$

where θ is the Bragg angle. Calculation of the temperature factor for cerium oxide is difficult, since an expression for M in equation 5.3 for this phase does not appear to be available. Hence, in the following calculations we make the assumption

$$\exp\left\{-2M\right\}_{CeO_2} = 1 \qquad (5.7)$$

Lastly, a CeO_2 mass fraction of 0.250 in the sample is assumed to correspond to a volume fraction of 0.262 in equation 5.2, assuming a stoichiometric density of 7.22 g cm^{-3} for CeO_2, and assuming the rest of the powder to have a density of 7.67 g cm^{-3} [70] (that of cementite).

Thus the volume fraction of cementite in the powder specimens can be estimated from equation 5.3. In all cases the expected linear relationship between the integrated intensity and the R-factor was confirmed (see for example figure 5.40). The ratio of the gradients of these two plots yields a ratio for c_{Fe_3C}/c_{CeO_2} (equation 5.2) from which c_{Fe_3C} can be calculated (table 5.8).

REF.	VOLUME FRACTION c_{Fe_3C}
Fe_3C in Baseplate of Multipass Weld	0.80
Fe_3C in HAZ of Multipass Weld	3.50
Fe_3C in Material C Service Aged	1.35
Fe_3C in Material C Service Aged + Heat Treated	1.61

Table 5.8: Volume fractions of Fe_3C calculated using powder diffractometry.

In some cases the cementite volume fractions calculated in this manner turn out to be greater than unity. It is probable that this is because a temperature factor for CeO_2 has not been included (the temperature factor for CeO_2 in equation 5.3 will always be less than unity).

Nevertheless, the results can be interpreted in a qualitative manner. Since the mass of carbide extracted from the HAZ is smaller than that extracted from the baseplate, and the X-ray analysis indicates that a far greater proportion of the carbide in the HAZ is cementite, it seems reasonable to conclude that the disparity can be explained by the near-absence of vanadium carbide in the HAZ. This conclusion is supported by the chemical analyses of the bulk extraction electrolytes.

5.10 Study of Reaction Kinetics Using Dilatometry

Dilatometry remains one of the most powerful techniques for following the kinetics of phase transformations as they happen. It relies upon the fact that in nearly all phase transformations, the change in crystal structure is manifested as a change in the volume of the specimen; thus, measurement of the specimen dimensions as a function of temperature and time represents a record of the phase transformations undergone.

The more difficult problem is then to relate the values of the instantaneous length change to the volume fractions of the phases present. This conversion is not at all trivial; most obviously, it is necessary to have a physical model for the phase transformations which occur. Where direct measurement of the volume fractions of phases is difficult (as in the bainite or martensite reactions) the lattice parameters of the phases must be known, as a function of temperature, to a high degree of accuracy. This necessity arises because it is the *differences* in phase densities which lead to changes in dimensions. In these cases measurement of the volume fractions of phases using dilatometry can only be considered as indirect.

In this work a dilatometer of the quartz rod type is used to measure the length of cylindrical specimens (3 mm diameter and $\sim$1.5 cm in length) as a function of temperature and time. A radio-frequency (RF) induction coil of near zero thermal mass, complemented by a facility to allow helium gas to be injected to remove heat, accomplishes the very rapid temperature changes (up to $250°C\,s^{-1}$ on heating, $\Delta t_{8/5} = 6$-10 s on cooling) necessary for this work.

The temperature is monitored continuously via a Pt/Pt-10%Rh thermocouple spot-welded to the centre of the specimen. The whole arrangement is sealed under a vacuum of better than 10^{-3} atmospheres during operation. Finally the system is interfaced to a microcomputer to permit continuous collection, and later analysis, of the data.

5.10.1 Continuous Heating/Cooling

Dilatometrical specimens of sample C2 were heated/cooled continuously between ambient temperature and 1250°C at various linear rates using a Data Trak programmer attached to the dilatometer. The heating/cooling rates chosen, were respectively, 1.64, 40, 240 and $1400°C\,min^{-1}$. It was found that the desired cooling rates were not maintained over the entire temperature range, particularly for the highest cooling rates asked of the machine; this effect occurs because the vacuum surrounding the specimen is incapable of removing heat from the specimen at a fast enough rate without the use of helium as a quenching medium. However, both temperature and time (as well as relative length change) are monitored during the heating/cooling cycle, so that a complete record of the thermal history of the specimen is known. This enables values of $\Delta t_{8/5}$ to be calculated (table 5.9); the results indicate that the lowest value of $\Delta t_{8/5}$ which can be achieved without the use of helium gas as a quenching medium, is $\sim$120 s.

DESIRED COOLING RATE /$°C\,min^{-1}$	COOLING TIME $\Delta t_{8/5}$ /s
1.64	11000
40	450
240	120
1400	120

Table 5.9: The values of $\Delta t_{8/5}$ observed during continuous cooling experiments.

Figure 5.41 shows graphs of relative length change vs. temperature for each of the experiments. The local gradient of these plots gives the *instantaneous* expansion coefficient; as discussed below this need not necessarily be constant with temperature, but to a good approximation can be taken to be, over small temperature ranges. Linear expansion coefficients were calculated for the ranges 20–600 & 950–1200°C on heating, and 1200–850 & 700–400°C on cooling. The results of the analyses are presented in table 5.10. In each analysis, the correlation coefficient was typically $\sim$0.995, and the standard error in

the expansion coefficient $\sim 3 \times 10^{-8}$ or $\sim 0.1\%$, indicating that the assumption of linearity is a reasonable one. There is some scatter in the values of the expansion coefficients, perhaps due to temperature inhomogeneities within the specimens (which will be most significant, if at all, at higher heating rates).

TEMPERATURE RANGE	EXPANSION COEFFICIENT /°C			
	$1.64°C \, min^{-1}$	$40°C \, min^{-1}$	$240°C \, min^{-1}$	$1400°C \, min^{-1}$
20–600°C	1.276×10^{-5}	1.297×10^{-5}	1.328×10^{-5}	1.237×10^{-5}
950–1200°C	1.660×10^{-5}	1.745×10^{-5}	1.909×10^{-5}	1.750×10^{-5}
1200–850°C	2.192×10^{-5}	2.089×10^{-5}	2.101×10^{-5}	2.016×10^{-5}
700–400°C	1.438×10^{-5}	–	–	–

Table 5.10: Expansion coefficients measured for steel C, in the temperature ranges indicated, for different heating and cooling rates.

5.10.2 Discussion

The determination of thermal expansivities should be carried out under conditions of very slow heating and cooling, to allow time for equilibration of temperature gradients within the specimen. How-ever, in the multiphase steels which are under consideration here, particular care needs to be taken in the interpretation of the dilatometric curves, because there is the obvious additional complication of cementite and alloy carbides dissolving or precipitating during continuous heating or cooling. For example, Darbyshire and Barford [79,80] have shown that precipitation sequences during the tempering of martensitic or bainitic structures lead to changes in density; cementite precipitation is associated with a contraction, while the nucleation of vanadium or molybdenum carbide from a ferrite/cementite mixture leads to a marked expansion. On the basis of Darbyshire and Barford's data, the contraction $\Delta l/l$ which would be measured (relative to a fully tempered specimen) when a slightly autotempered Fe-0.14C (wt%) martensite is tempered at 500°C, is $\sim 3 \times 10^{-4}$, assuming the very slow heating employed led to complete cementite precipitation. The expansion when cementite transforms to vanadium carbide in a ferrite matrix at 650°C in a Fe-0.12C-0.5V (wt%) steel would be of the same order of magnitude. The density changes which are likely to occur during alloy carbide precipitation from, or dissolution in, austenite remain unknown, but there is no reason to believe that they are insignificant.

The complications which arise due to the presence of carbide phases do not preclude the use of dilatometry as a technique for the study of the kinetics of the ferrite to austenite ($\alpha \rightarrow \gamma$) and austenite to ferrite ($\gamma \rightarrow \alpha$) transformations, provided adequate care is taken. This is because whilst the difference between the density of carbide and the density of either ferrite or austenite is comparable to that between ferrite and austenite, the volume fractions of cementite and alloy carbides, in low-alloy steels at least, are very small.

5.10.3 Estimation of Allotriomorphic Ferrite Start/Finish, and Bainite Start Temperatures

The fact that the expansion coefficient of both ferrite and austenite is, over small temperature ranges, linear to a good approximation, allows the start and finish of the $\alpha \rightarrow \gamma$ and the $\gamma \rightarrow \alpha$ reactions to be detected as the first and last deviations from linearity in a plot of relative length change vs. temperature. This means that dynamic transformation temperatures are best determined by an examination of the gradients of such plots.

The raw data collected from the dilatometer showed noise fluctuations which meant that differen-tiation of the graphs in figure 5.41 proved useless without some kind of smoothing being carried out. The universally accepted method for the smoothing of many kinds of data which are subject to random fluctuations, is to replace each point with a weighted average of itself and its neighbours. Thus, in this work, a polynomial function of degree p is fitted to the set of $2m + 1$ data points lying symmetrically around x_i, the data point under consideration; this polynomial is then evaluated at x_i. In a set of n data points, this process is possible for $n - 2m$ of the data points. The variables which must be optimised

93

for the process are then the degree of the polynomial p, and m, which determines the number of data points used for smoothing.

The value chosen for p was 2, since at most, the second differential of the relative length vs. temperature plot needed to be considered. In practice, the value of p controls the ease with which the smoothed data can accommodate sharp changes in gradient. It was found that the value of m determined the degree of smoothing performed. If a small value of m resulted in only very small amounts of smoothing; if m was too large, then detail in the raw data began to be lost. In general, it is therefore likely that the optimum value of m depends upon the rate of data collection during the experiment. For the experiments described here, a value of 30 for m performed the degree of smoothing required.

The dynamic transformation temperatures were estimated from the raw data presented in figure 5.41, after smoothing. As figures 5.42 & 5.43 show, this was most easily done using the plot of the first differential of the relative length against temperature. The values obtained in this way are tabulated in table 5.11.

5.10.4 Confirmation of Microstructures Using Optical and Transmission Electron Microscopy

Very slow cooling ($\Delta t_{8/5} = 11000$ s) resulted in austenite decomposing at $\sim 850°$C. This is in broad agreement with calculated values of $867°$C for Ae3, and $855°$C for Ae3' (chapter six). Optical microscopy (figure 5.44) showed clearly that the transformation product is a mixture of allotriomorphic ferrite and pearlite. Thin foil electron microscopy revealed (figures 5.45 & 5.46) the presence of fine rows of carbides which would have precipitated at the moving α/γ boundary (interphase precipitation). Tilting the foil to a $<100>_\alpha$ zone axis again revealed that the carbides exhibit an orientation relationship with ferrite consistent with the Baker-Nutting orientation relationship. These carbides are therefore, as before, V_8C_7. More rapid cooling ($\Delta t_{8/5} = 450$ s) resulted in a mixed transformation product, of allotriomorphic ferrite and upper bainite (figures 5.47). At the highest cooling rate ($\Delta t_{8/5} = 120$ s) the decomposition product was found to be fully bainitic (figure 5.48).

HEATING RATE /°C min⁻¹	COOLING TIME $\Delta t_{8/5}$ /s	Ac1 /°C	Ac3 /°C	Ar1 /°C	Ar3 /°C	Bₛ /°C
1.64	11000	705	960	~700	830	-
40	450	720	940	-	795	~630
240	120	710	950	-	-	630
1400	120	740	960	-	-	630

Table 5.11: Dynamic transformation temperatures observed during heating/cooling using dilatometry.

5.11 Discussion

The creep strength, ductility and rupture life of a ferritic creep-resistant steel is dependent upon the chemical composition as well as the purity of the alloy concerned. As a further complication, the thermal cycles experienced during normalising, stress-relief heat-treatment and service can differ, resulting in variations in microstructure, and hence creep performance.

Of these variations in microstructure, it is often considered [81,82] that it is the nature of dispersed carbide phases such as V_8C_7 and Mo_2C which is the most important factor in influencing the creep behaviour of ferritic steels. For example, in a study of 1CrMoV steel castings, Buchi et al. [83] observed that the highest creep strengths were associated with microstructures consisting of a uniformily dispersed precipitate of fine vanadium carbide platelets in a matrix of irregularly shaped ferrite grains. The poor-est creep properties were associated with specimens exhibiting coarse irregularly distributed vanadium carbide particles in a polygonal ferrite matrix. It should be noted however, that the role of such carbide

microstructures in figures 5.3 & 5.4. The computer model requires an input of the weld variables (as given in table 5.1), as well as details of the weld geometry (taken from figure 5.1). Values of the T_s, T_{gc}, Ac3, Ac1 and T_t temperatures are the last inputs required.

Figures 5.5, 5.6 & 5.7 show output generated for initial 'guess' values of T_s, T_{gc}, Ac3, Ac1 and T_t. These are 1547°C, 1227°C, 917°C, 867°C and 477°C respectively. A comparison of figures 5.3 & 5.4 and figures 5.6 & 5.7 reveals that there is a correlation between the temperature fields in the HAZ, as calculated by the model, and the contrast developed on the specimen during etching. This, in itself, is not a particularly surprising result, since it is the weld thermal cycles which induce the microstructure, and it is local variations in microstructure which lead to preferential attack by the etchant. However, the broad agreement observed is encouraging, and it permits the correlation of the temperature fields predicted by the computer model, with the microstructure observed in the HAZ, using optical microscopy at a higher magnification than before.

Figures 5.8 & 5.9 are interpretations of figures 5.3 & 5.4, on the basis of the graphical output from the computer model.

5.5 Further Optical Microscopy

Optical microscopy was used to correlate the microstructure with the predictions from the heat-flow modelling described above.

5.5.1 Baseplate of Multipass Weld

Figure 5.10 shows an optical micrograph of the baseplate. The microstructure is a mixture of ferrite/~5% pearlite. Transmission electron microscopy was used to identify the finer phases; the details will be discussed later but it is sufficient here to note that the microstructure consists of spheroidised nodules of pearlite within a matrix of ferrite; the latter contains a fine dispersion of vanadium carbide particles.

5.5.2 HAZ from Root of Multipass Weld

The advantage of examining samples from this region is that the overlap of the adjacent beads is slight, making the interpretation of the microstructural regions easier.

The way in which the weld thermal cycle alters the microstructure of the baseplate is dependent upon the distance from the fusion boundary. Near the fusion boundary, a rather coarse bainitic structure is found (figure 5.11), characterised by large prior austenite grains (~50 μm). In terms of the notation introduced above, the set of weld thermal cycles which produce this microstructure is **FBE** or **FBF**. Further from the fusion boundary, the prior austenite grains are rather smaller (~10 μm), and the microstructure is again bainitic (figure 5.12, thermal cycles **FCE** or **FCF**). Figures 5.13 & 5.14 show typical microstructures yet further from the fusion boundary; here the baseplate is only partially reaustenitised (thermal cycles **FDE** or **FDF**).

Due to the deposition of further weld beads, each point in the HAZ will experience further thermal cycles, (A→F) the strength of each cycle again being dependent upon the distance from the heat-source. Figures 5.15, 5.16, 5.17 & 5.18 show the microstructures, due to sets of weld thermal cycles **BBF, BCF, BDF** and **CDF**. It is notable that reaustenitisation occurs preferentially at the prior γ-grain boundaries. From this observation it can be inferred that retained austenite is absent (TEM observations presented later confirm this) since the presence of retained austenite removes the need for austenite nucleation. High energy boundaries are the nucleation sites, in the absence of retained austenite.

5.5.3 HAZ from Vertical Face of Multipass Weld

The isotherms which create the HAZ associated with the near vertical face of the weld are more closely overlapped, making the microstructure more difficult to interpret. However, optical microscopy

in promoting creep resistance has not been fully explained. Baker and Nutting [84] suggested that they have an effect on the passage of dislocations at higher temperatures, which results in the stiffening of grains, so that deformation is then more difficult.

All substitutional alloying element additions, as well as specifically the secondary hardening elements such as vanadium and molybdenum, impart a degree of solid solution strengthening so that alloys, in general, are expected to have higher creep strengths than metals [81]. Myers [85] has studied the effect of variations in vanadium concentration in $\frac{1}{2}$CrMoV steels. It was found that susceptibility to HAZ stress-relief cracking increased with increasing vanadium content, with resistance improving significantly below 0.27wt%. This was attributed to vanadium strengthening the matrix thereby limiting any deformation during stress-relief to regions near grain boundaries. Myers conjectured that other elements such as nickel, manganese, chromium and molybdenum are likely to have similar effects.

Thus intercrystalline failure (into which category the phenomenon of type IV cracking falls) occurs [86] when the relative strength of the body of the crystal exceeds that of the grain boundary by a critical amount. Thus, strengthening of the matrix relative to the grain boundaries may lead to intercrystalline fracture and low ductility [81].

In pure metals and single phase solid solutions creep resistance is thought to increase with increasing grain size, since grain boundaries are a source of weakness in creep. There has been a tendency to assume that ferritic steels also behave in this way [81], but Glen & Murray [87] have shown that, compared with other factors, grain size has a negligible effect on the creep resistance of such alloys [81].

5.12 Type IV Cracking

The above discussion, together with the experimental data gathered in this work, suggest that the following could be contributory factors in weakening $\frac{1}{2}$CrMoV heat-affected zones:

- The austenite grain size is a minimum at the position of type IV failure, and increases with distance towards the fusion boundary. The austenite grain size at the type IV position is considerably smaller than in the baseplate. It is the austenite grain size which is likely to control the creep properties of the HAZ, since the reaustenitised regions there are bainitic, and bainitic sub-units are separated by low-angle boundaries. The sizes of bainite sheaves and sub-units are unlikely to be important.

- The experimental evidence suggests that the size, distribution and volume fraction of alloy carbides in the HAZ, specifically vanadium and molybdenum carbides, are different from those in the baseplate. In the baseplate, a fine dispersion of vanadium carbide forms co-operatively with allotriomorphic ferrite (interphase precipitation), by the decomposition of austenite, during slow cooling of the thick section pipe. On the other hand the HAZ consists entirely of upper bainite, and the alloy carbides re-precipitate during stress-relief heat-treatment. The size, distribution and volume fraction of these carbides therefore depend upon the kinetics of re-precipitation and coarsening.

- The concentrations of carbide forming elements (such as vanadium and molybdenum) in the ferrite matrices reflect the volume fractions of carbides present. For example, the concentrations of molybdenum in the ferrite matrix of the baseplate of the experimental weld examined was 15% lower than in the matrix of the HAZ.

It is recognised that of the three factors isolated, only the first could explain why it is the partially reaustenitised/fully reaustenitised boundary (i.e. the type IV region) which is weak, rather than the HAZ as a whole. However, it is quite possible that the second and third factors apply locally to the type IV region, and thus contribute to the effect.

95

5.13 Summary

The baseplate and as-welded HAZ of a $2\frac{1}{4}$CrMo/$\frac{1}{2}$CrMoV multipass weld has been characterised using optical and transmission electron microscopy. The heat-flow model developed in chapter three has been used to characterise the spatial distribution of regions in the HAZ which have experienced similar sets of weld thermal cycles.

The microstructure of the $\frac{1}{2}$CrMoV baseplate consisted of a mixture of ferrite and spheroidised pearlite, the former being associated with a fine dispersion of vanadium carbide precipitates which had grown by interphase precipitation. EDX microanalysis revealed that the cementite within the pearlite had considerable amounts of Cr, Mo, V & Mn associated with it; such observations are consistent with partitioning of these elements to cementite during growth by a reconstructive mechanism.

Thin foil microscopy of the as-welded HAZ revealed that the fully reaustenitised regions consist of upper bainite. The hardenability of the steel is low enough for the residual austenite associated with such bainite to decompose to a mixture of ferrite and cementite. In the partially reaustenitised regions twinned martensite was found, perhaps because partitioning of carbon into these regions during austenite growth is associated with a local increase in hardenability. Use of the EDX technique on carbon replica specimens showed that the composition of cementite associated with the as-welded HAZ is near the overall composition of the steel itself.

Stress-relief heat treatment resulted in the precipitation of vanadium carbide in the HAZ, as detected by bulk analysis of the ferrite matrix. Chromium, molybdenum, vanadium and manganese partition to the partition to the bainitic cementite, in an effort to attain equilibrium. The HAZ then had approximately the composition of the cementite in the baseplate.

X-ray analysis of cementite extracted from the baseplate, and the as-welded HAZ appeared to be sensitive enough to detect the disparity in composition of the cementite associated with the as-welded HAZ. It therefore seems that the use of this technique to monitor changes in cementite concentration during long term tempering of such creep-resistant steels should be investigated, in view of the implications with regard to the problem of remanent life.

Finally, an attempt has been made to rationalise the susceptibility of $\frac{1}{2}$CrMoV HAZ's to type IV cracking, i.e. to intergranular failure in creep at the partially reaustenitised/fully reaustenitised boundary. The effect of γ-grain size was considered. The disparities between the size, distribution and volume fractions of alloy carbides, and matrix compositions in the baseplate and the HAZ were also noted.

REFERENCES

60. D.J. Gooch and S.T. Kimmins, in the 'Proceedings of the Third International Conference on Creep and Fracture of Engineering Materials and Structures', Swansea, (1987).

61. D.J. Gooch and B.L. King, in the 'Proceedings of the Second International Conference on Pipe-welding', The Welding Institute, Cambridge, 223–232, (1980).

62. J. Myers, Metals Technology, **5**, 391–396, (1978).

63. H.J. Schuller, Allianz Power, **22**, (1975).

64. M.C. Murphy and G.D. Branch, J.I.S.I., 207, 1347–1364, (1969).

65. M.J. Collins, Metals Technology, 8, 325–326, (1978).

66. W. Pitsch, Acta Metall., 10, 79–80, (1962), (errata p.906)

67. R.G. Baker and J. Nutting, I.S.I. Special Report No. 64, 1–22, (1959).

68. B.J. Cane and R.D. Townsend, Report TPRD/L/2674/N84, Central Electricity Research Laboratories, Leatherhead, (1984).

69. K.W. Andrews and H. Hughes, Iron & Steel, 30, 43–50, (1958).

70. H. Stuart and N. Ridley, J.I.S.I., **204**, 711–717, (1966).

71. J.M. Leitnaker, R.L. Klueh and W.R. Laing, Metall. Trans., **6A**, 1949–1955, (1975).

72. J. Pilling and N. Ridley, Metall. Trans., **13A**, 557–563, (1982).

73. J.E. Spruiell and R.E. Gehlbach, Trans. Am. Nucl. Soc. 15, **2**, 769–770, (1972).

74. B.D. Cullity, Elements of X-Ray Diffraction, Second Edition, 352–358, Addison-Wesley Publishing Co., Reading, Massachusetts, U.S.A., (1978).

75. H. Lipson and N.J. Petch, J.I.S.I., **142**, 95–103, (1940).

76. W. Hume-Rothery and P.W. Reynolds, J.I.S.I., **145**, 143–151, (1942).

77. E.J. Fasiska and G.A. Jeffrey, Acta Crystallograph., **20A**, 463–468, (1965).

78. H.L. Yakel, International Metallurgical Reviews, 30, No.1, (1985).

79. J.M. Darbyshire and J. Barford, Central Electricity Research Laboratories Report RD/L/R 1408, (1968).

80. J.M. Darbyshire and S.D. Knight, Central Electricity Research Laboratories Report RD/L/N 29/77, (1977).

81. J.H. Woodhead and A.G. Quarrell, J.I.S.I., **203**, 605–620, (1965).

81. M.C. Murphy and G.D. Branch, J.I.S.I., **209**, 546–561, (1971).

83. G.J.P. Buchi, J.H.R. Page and M.P. Sidey, J.I.S.I., **203**, 291–298, (1965).

84. R.G. Baker and J. Nutting, J.I.S.I., **193**, 257–265, (1965).

85. J. Myers, Metals Technology, 5, 391–396, (1978).

86. R.W. Bailey, Journal Junior Inst. Eng., 46, (1), 1–19, (1935).

87. J. Glen and J.D. Murray, I.S.I. Special Report No. 69, 40–53, (1961).
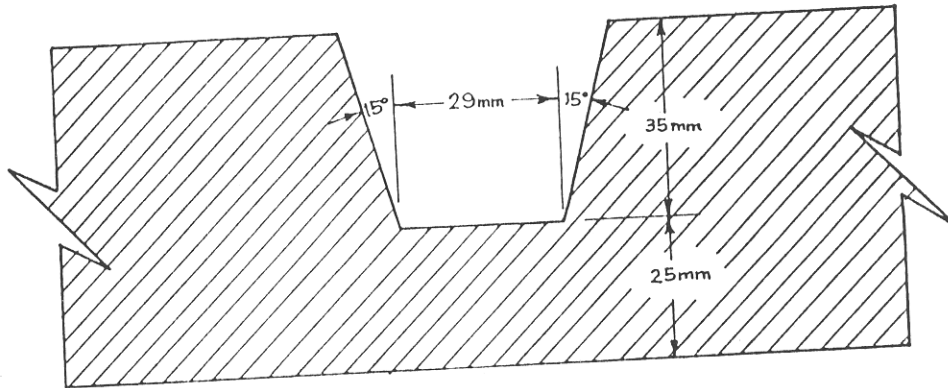
Figure 5.1: The weld preparation of the experimental multipass weld studied in this work.
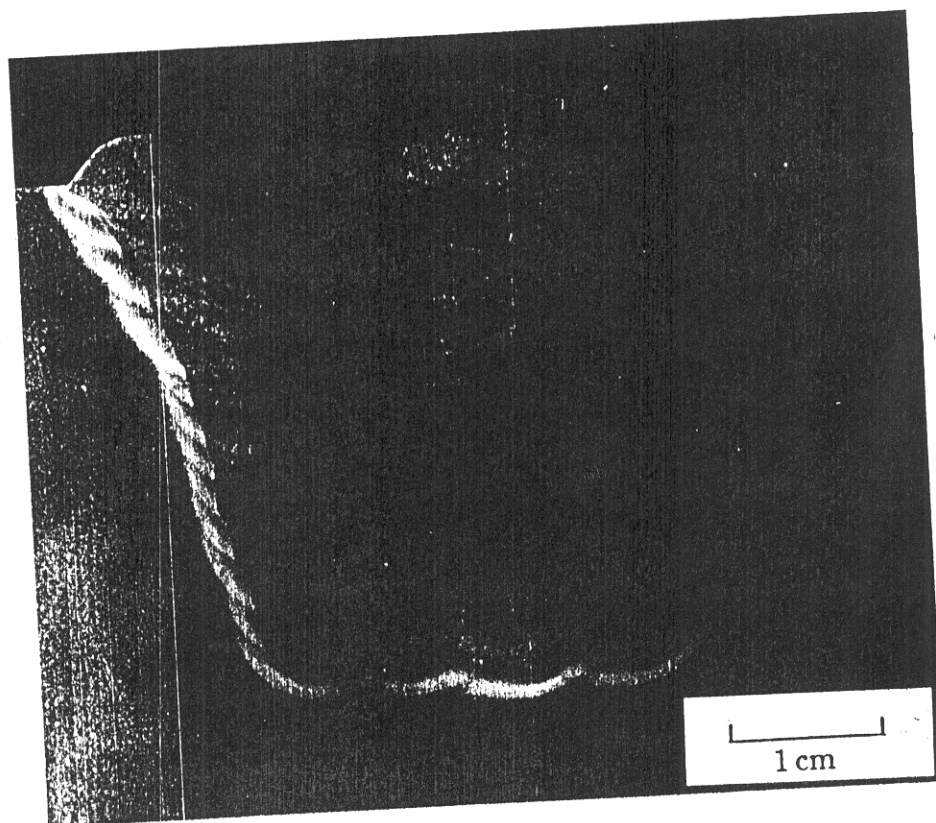
Figure 5.2: Optical macrograph of multipass weld. Etchant: 2% nital.

3000 μm
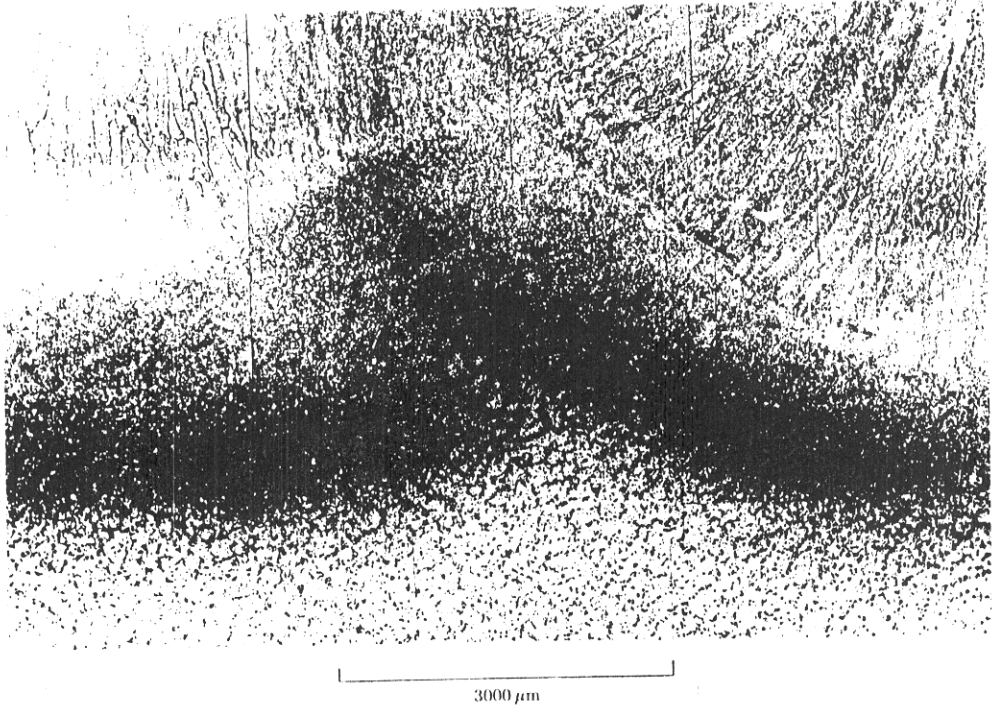
Figure 5.3: Optical macrograph of the HAZ near the root of the multipass weld.

3000 μm
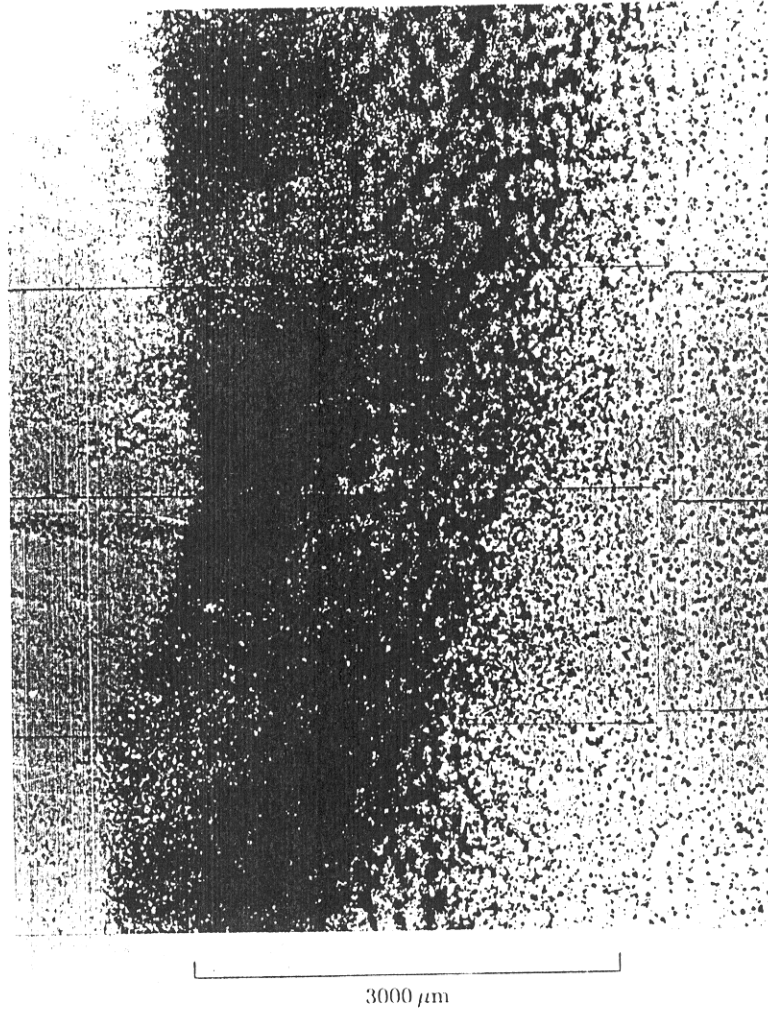
Figure 5.4: Optical macrograph of the HAZ near the vertical face of the multipass weld.

1 cm
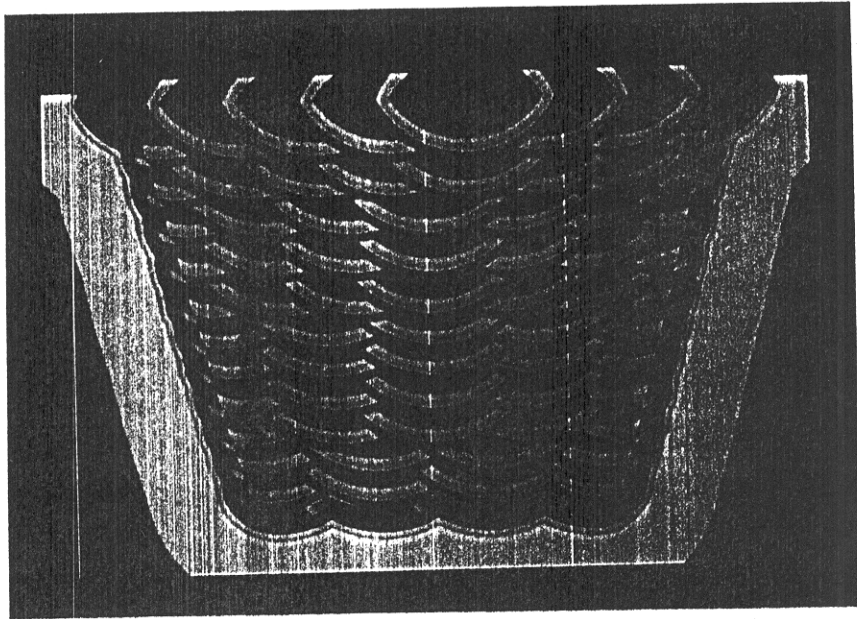
Figure 5.5: The experimental weld as modelled using the computer model developed in chapter three of this dissertation.
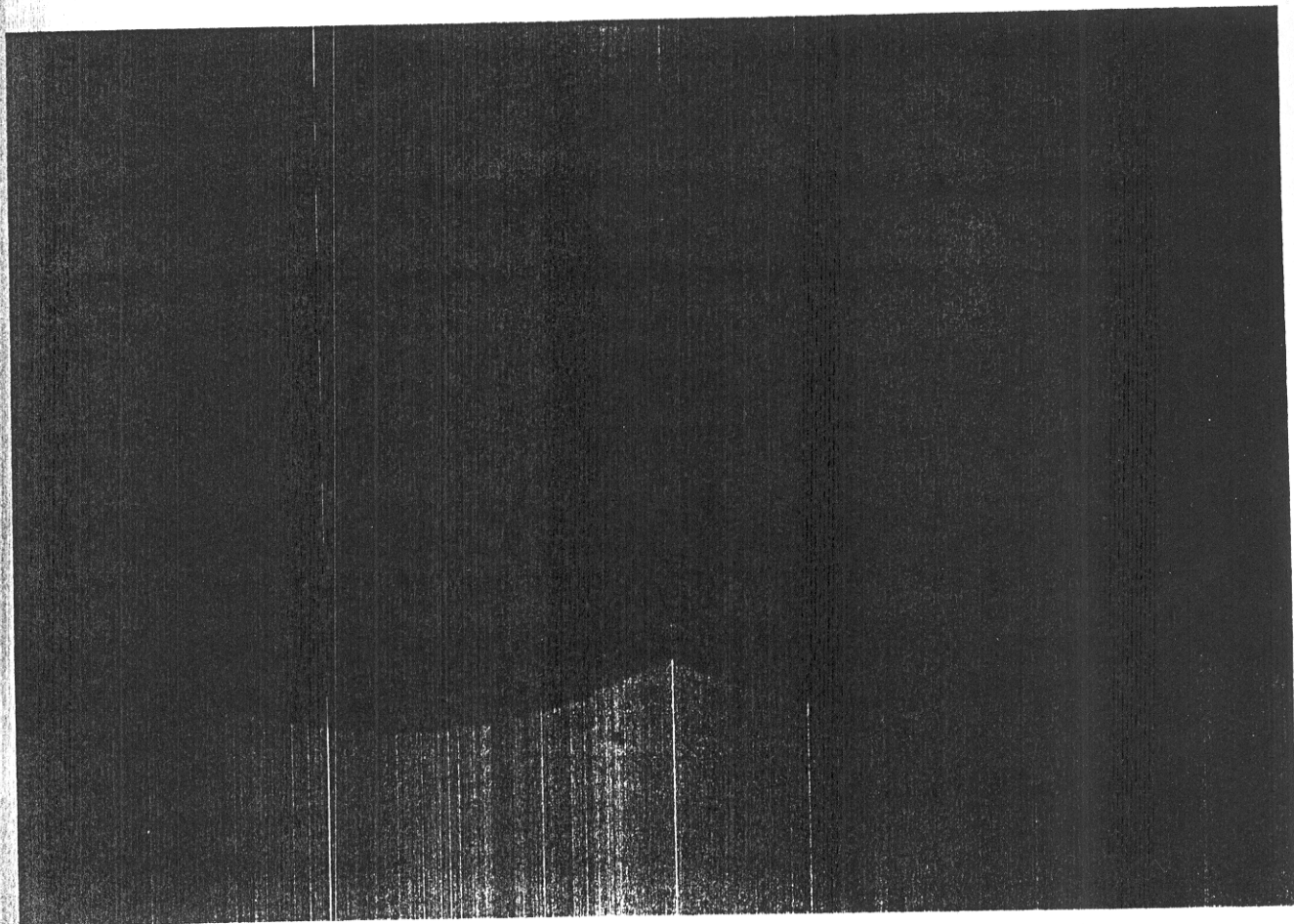
5 mm

Figure 5.6: Graphical output generated from the computer model, of the HAZ near the root of the multipass weld.

5 mm
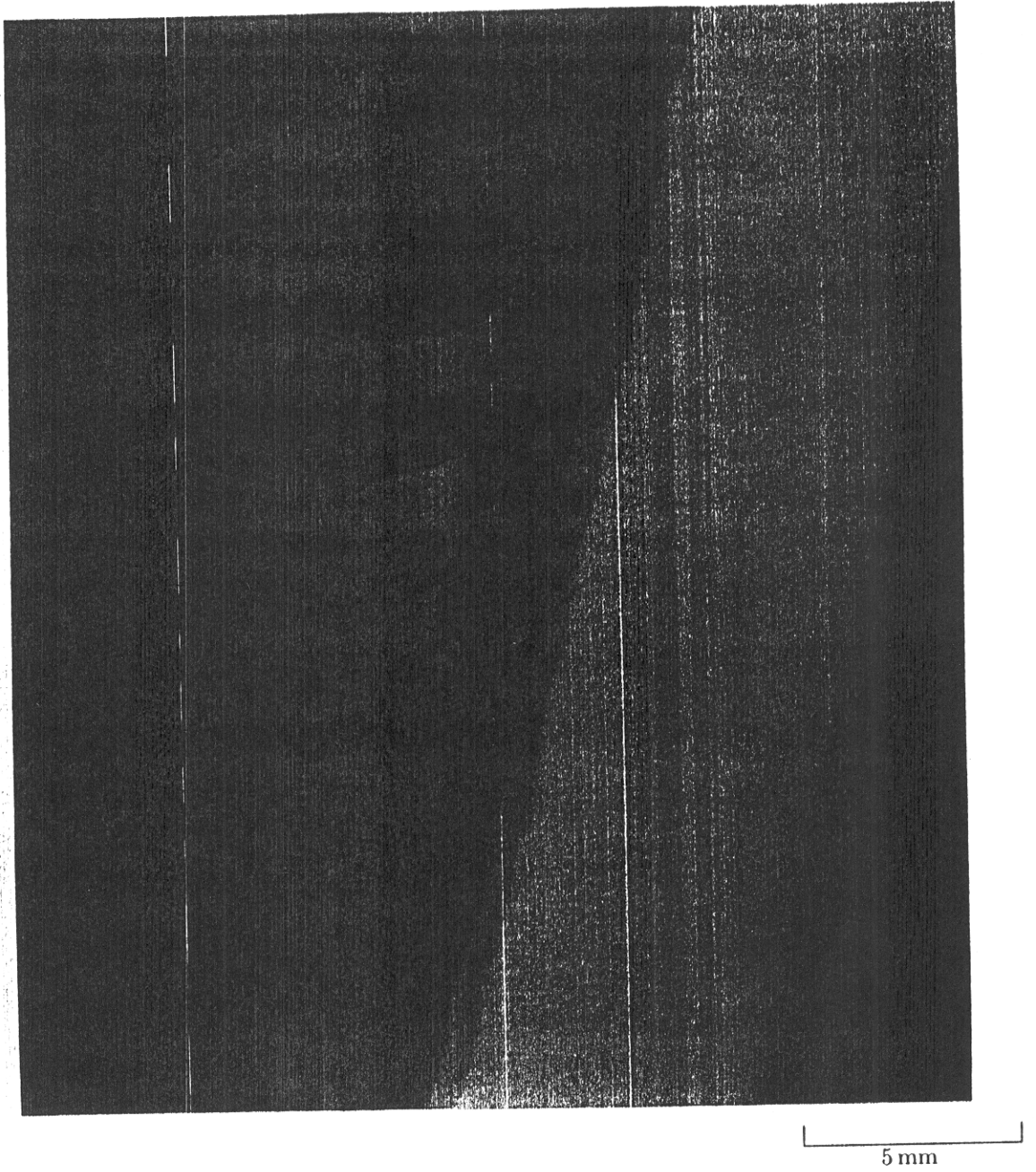
Figure 5.7: Graphical output generated from the computer model, of the HAZ near the vertical face of the multipass weld.
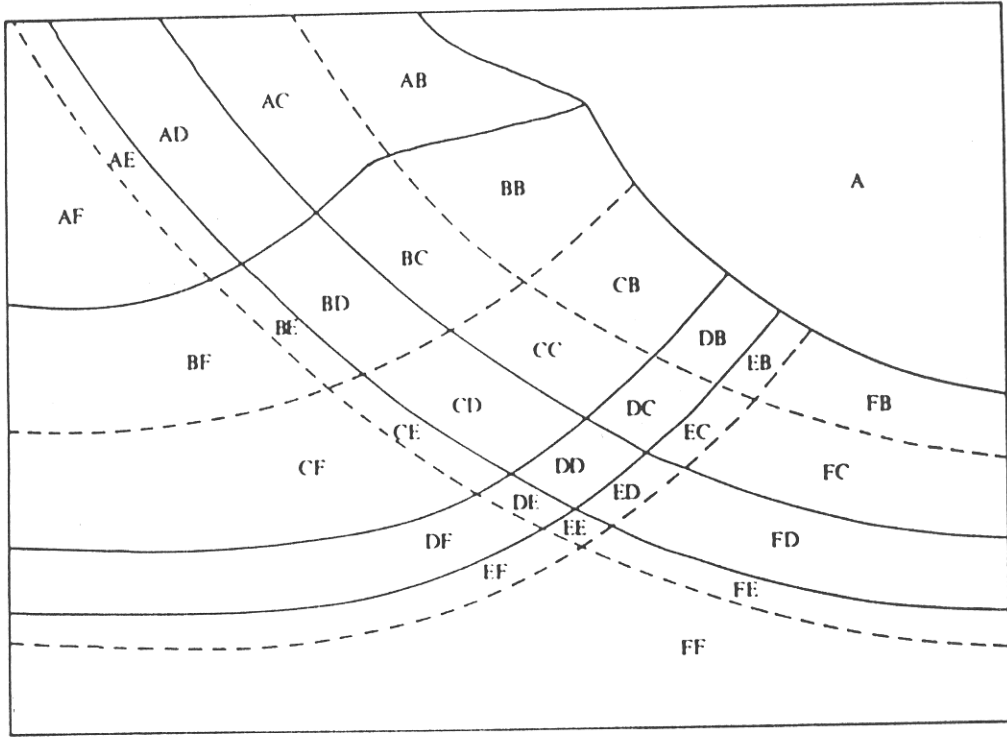
Figure 5.8: Interpretation of figure 5.3, in terms of the terminology of figure 3.10, and with the aid of the computer model (figure 5.6).
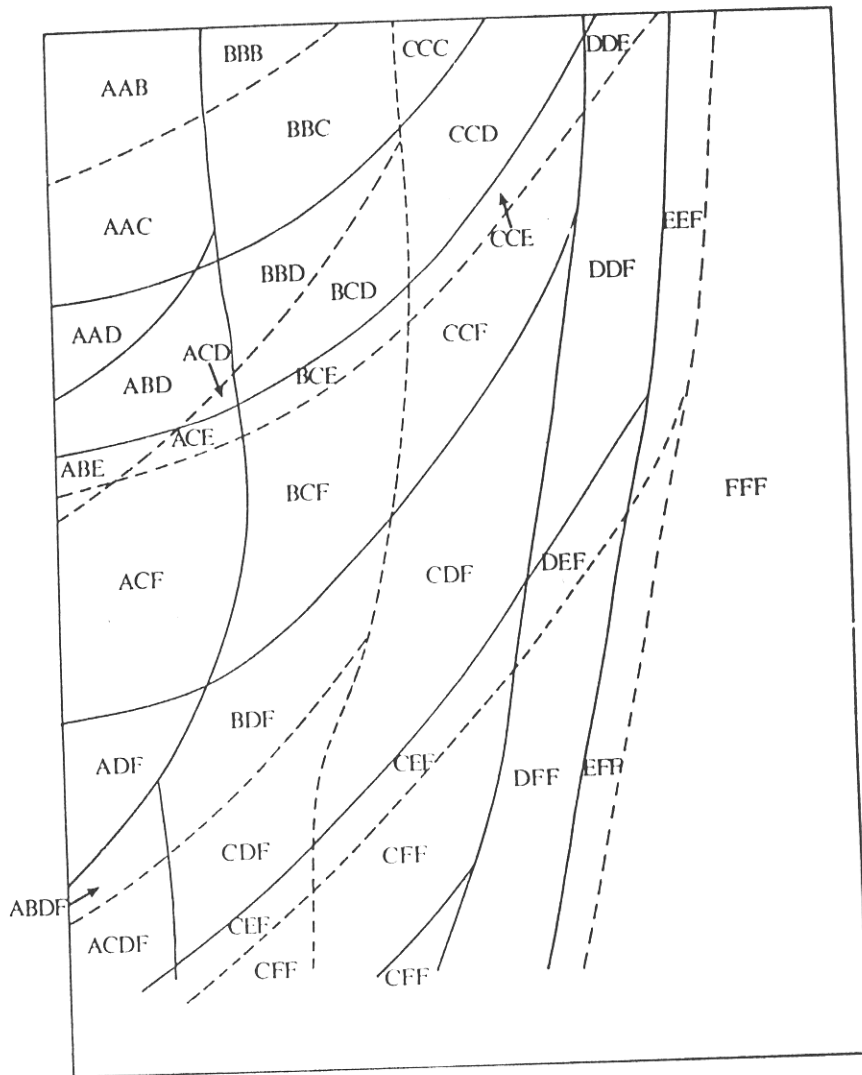
Figure 5.9: Interpretation of figure 5.4, in terms of the terminology of figure 3.10, and with the aid of the computer model (figure 5.7).
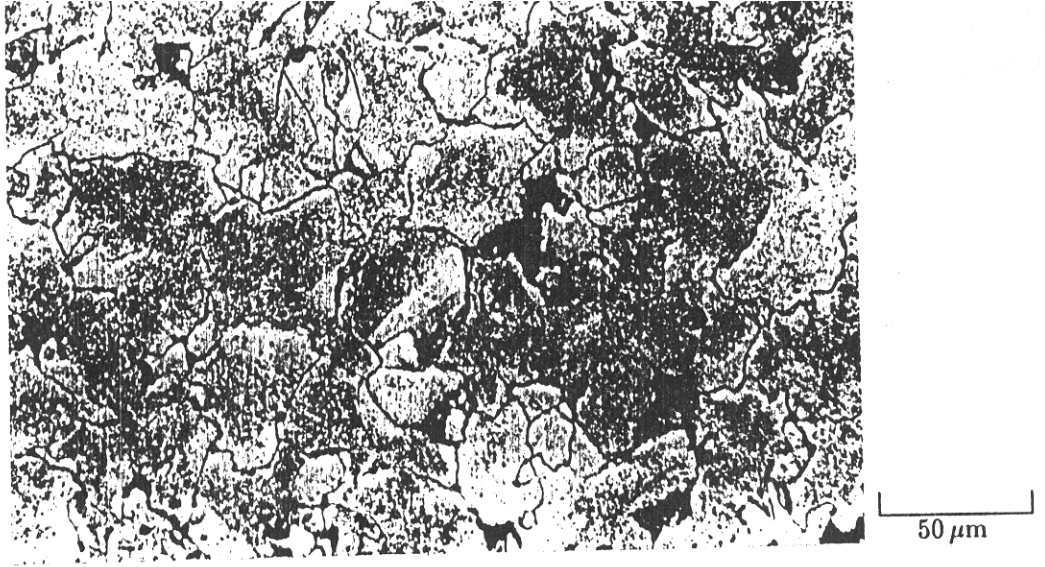
Figure 5.10: Optical micrograph of the baseplate of the multipass weld.
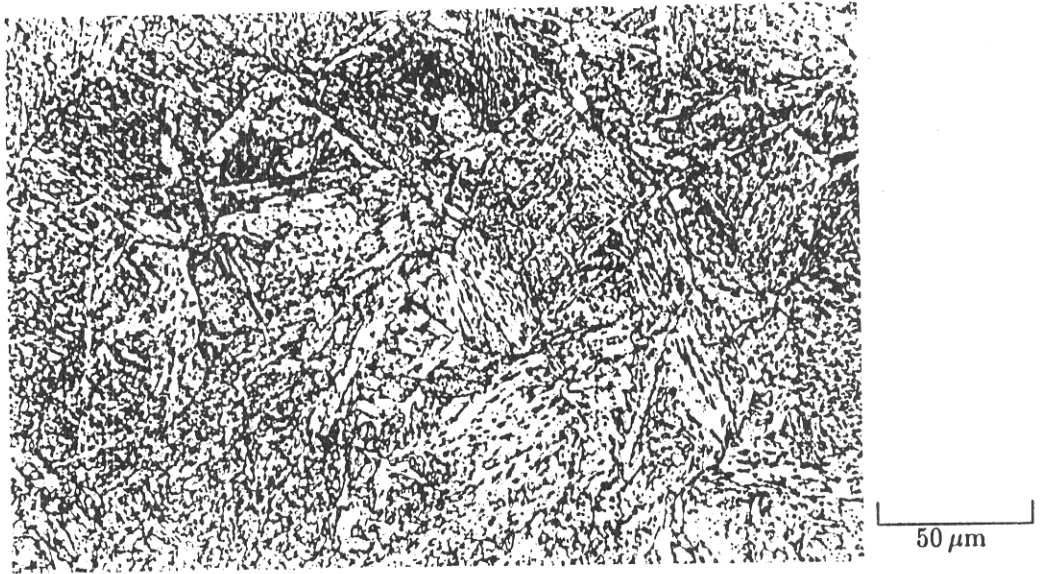
Figure 5.11: Coarse bainitic structure near the fusion boundary, characterised by large prior γ-grains (∼50 μm). Thermal cycles FBE or FBF.
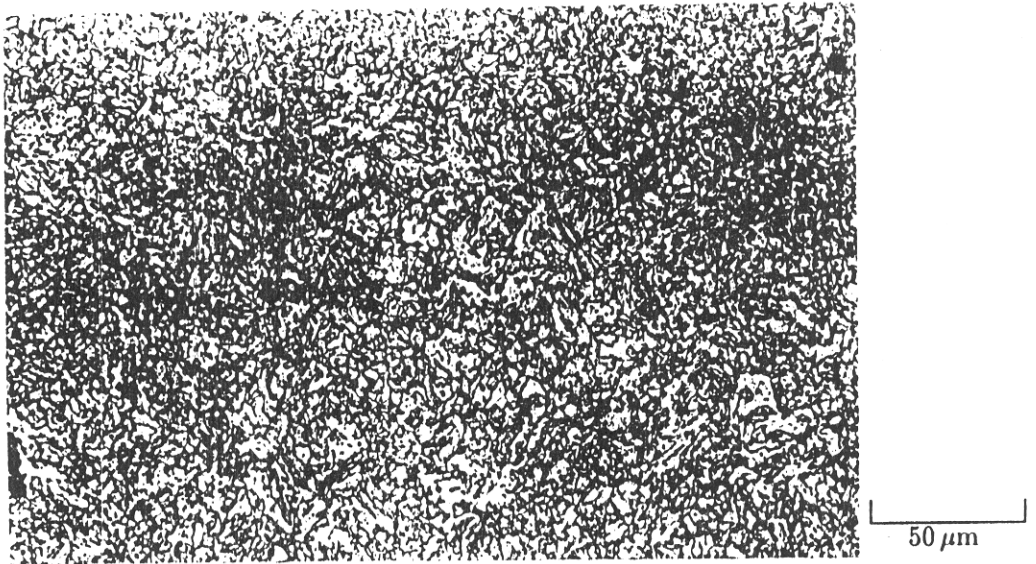
Figure 5.12: Further from the fusion boundary, the prior γ-grains are rather smaller (∼10 μm), but the microstructure is still bainitic. Thermal cycles FCE or FCF.
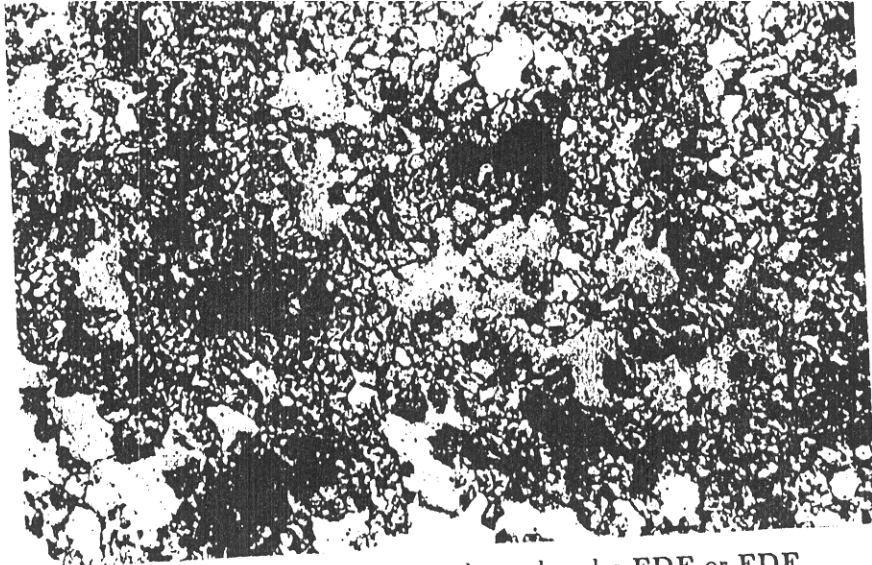
Figure 5.13: Partially reaustenitised microstructure, thermal cycles **FDE** or **FDF**.
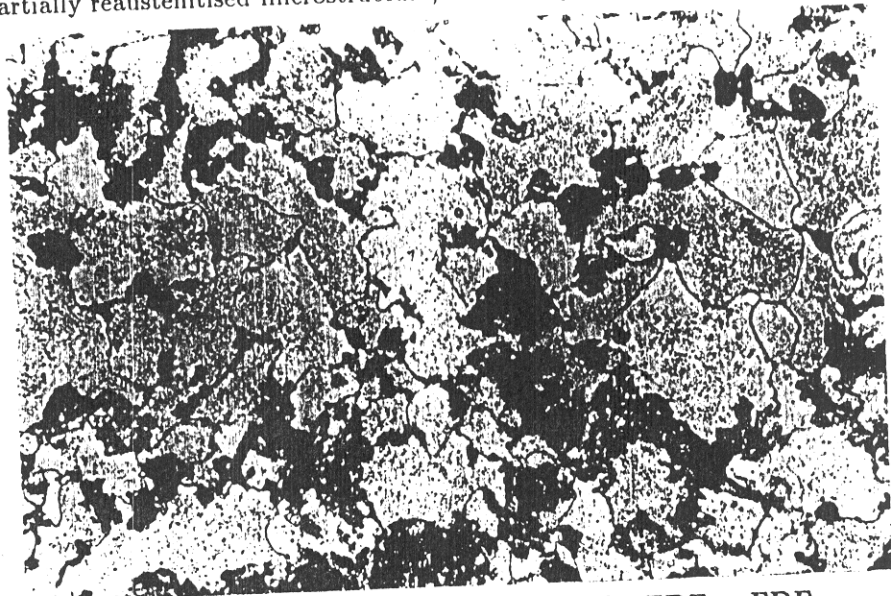
Figure 5.14: Partially reaustenitised microstructure, thermal cycles **FDE** or **FDF**.
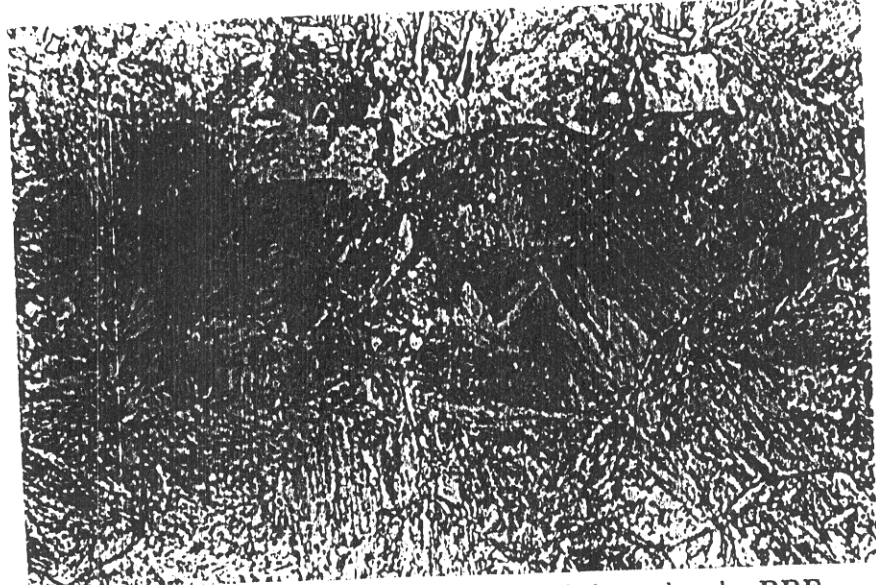
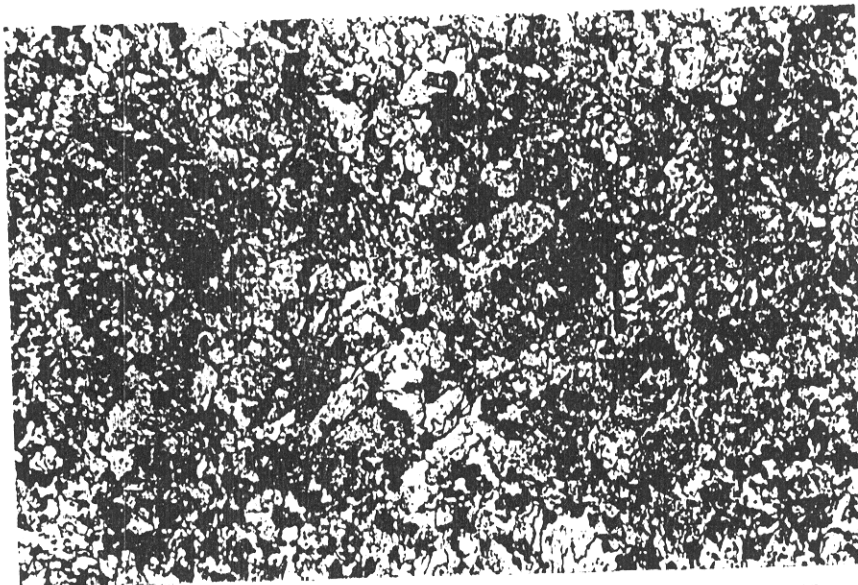Figure 5.15: Microstructure developed due to the series of weld thermal cycles **BBF**.
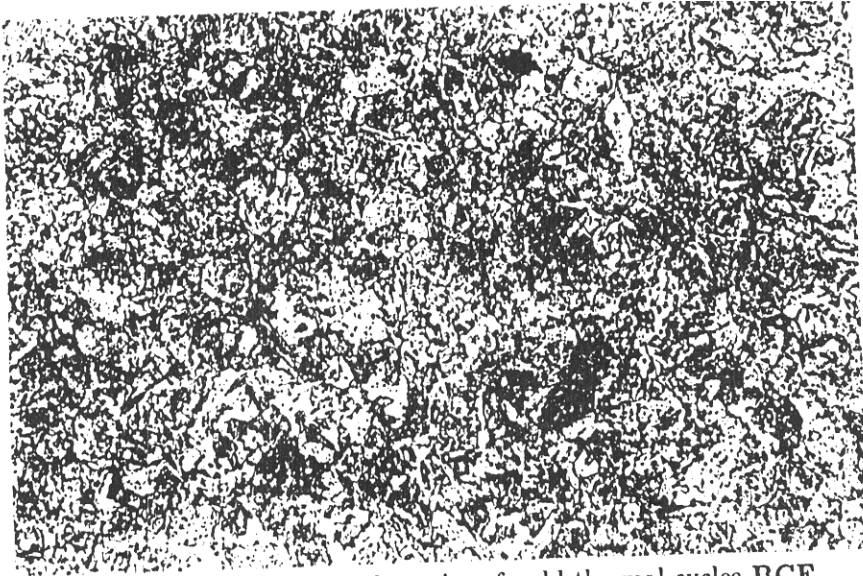
50 μm

Figure 5.16: Microstructure developed due to the series of weld thermal cycles **BCF**.
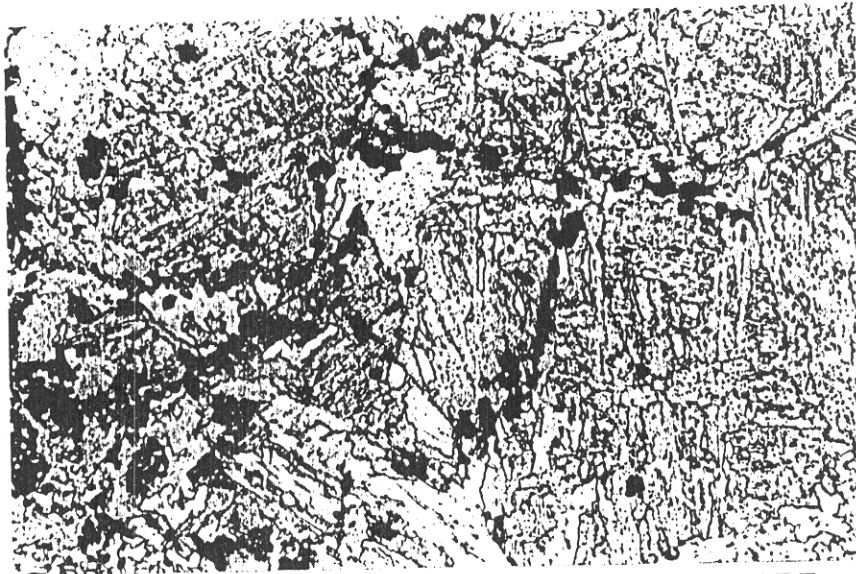
50 μm

Figure 5.17: Microstructure developed due to the series of weld thermal cycles **BDF**.

50 μm

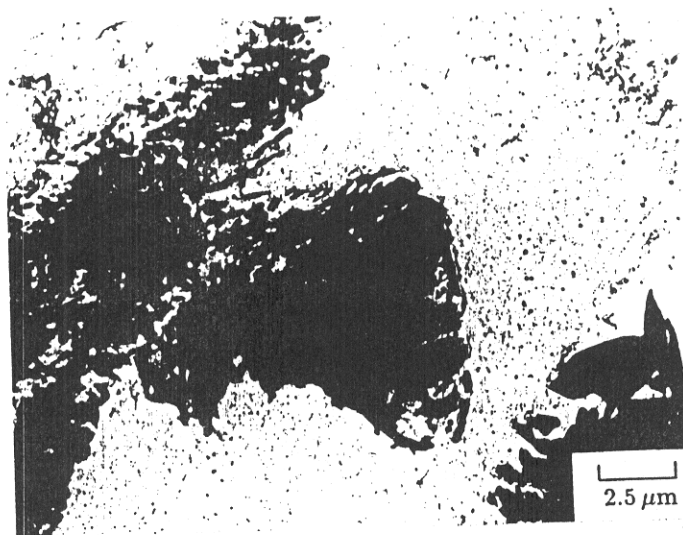Figure 5.18: Microstructure developed due to the series of weld thermal cycles **CDF**.

Figure 5.19: TEM micrograph of a carbon replica specimen from the baseplate of the multipass weld.
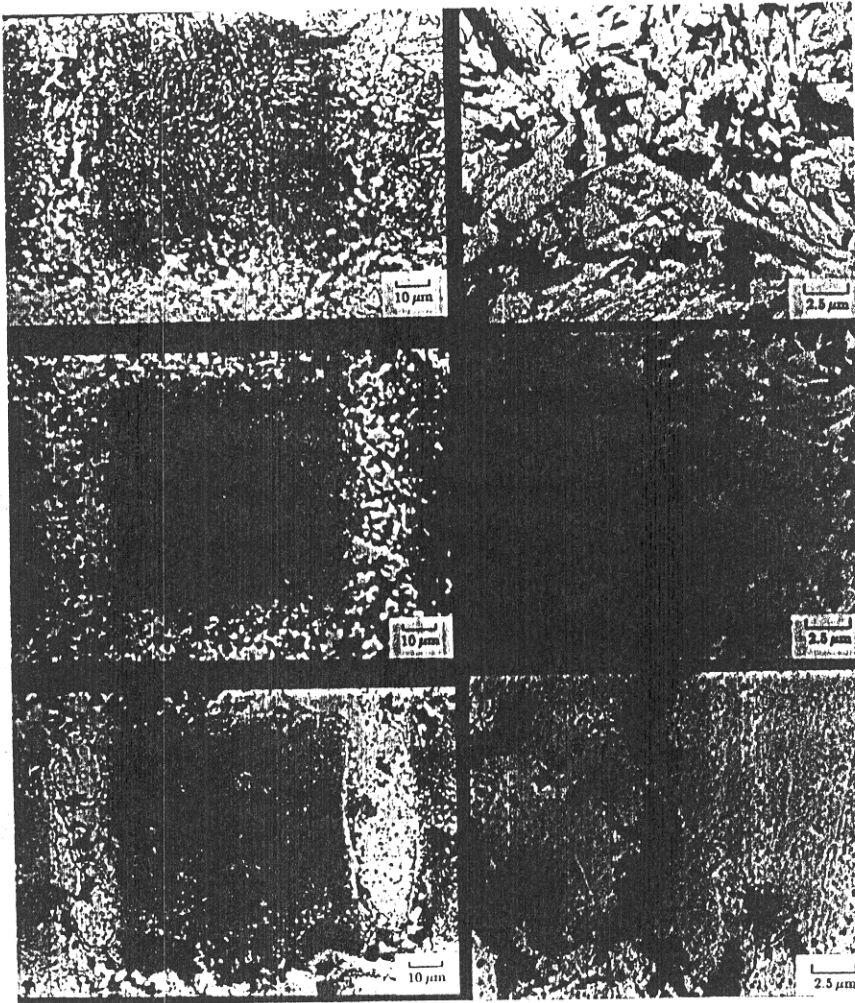
Figure 5.20a,b (top) 5.21a,b (middle) and 5.22a,b (bottom): Optical and TEM micrographs of carbon replica specimens from the HAZ.

x_{Fe}	mole fraction of iron
x_C	mole fraction of carbon
x_X	mole fraction of substitutional solute
y_{Fe}	fraction of substitutional sites occupied by iron
y_C	fraction of interstitial sites occupied by carbon
y_X	fraction of substitutional sites occupied by solute X
Γ_{Fe}	activity coefficient of iron
Γ_C	activity coefficient of carbon
Γ_X	activity coefficient of substitutional solute
ϵ_{CC}	carbon-carbon Wagner interaction parameter
$\epsilon_{XC} = \epsilon_{CX}$	carbon-substitutional solute Wagner interaction parameter
ϵ_{XX}	substitutional solute-substitutional solute Wagner interaction parameter
μ_{Fe}	chemical potential of iron
μ_C	chemical potential of carbon
μ_X	chemical potential of substitutional solute X
$^0\mu_{Fe}$	chemical potential of pure iron
$^0\mu_C$	chemical potential of pure carbon
$^0\mu_X$	chemical potential of pure substitutional solute X
ω_C	in McLellan-Dunn model, the carbon-carbon interaction energy

NB superscripts γ and α refer to the austenite and ferrite phases respectively; α,nuc refers to the critical ferrite nucleus.

6.1 Introduction

As noted in chapter three, the kinetic strength of the weld thermal cycle can be sufficient to partially or fully reaustenitise the underlying weld or HAZ metal. During cooling to ambient temperature, this austenite can transform to a variety of ferrite microstructures, of which allotriomorphic ferrite, Widmanstätten ferrite, bainite or martensite are the most common. The exact volume fractions depend upon the chemical composition of the steel concerned, as well as the cooling curve, which determines the extent to which each of the transformation mechanisms can operate. It is the volume fractions of these constituents, together with their morphologies and compositions, which control ultimately the mechanical properties of the weldment.

A successful model for multipass welds must be able to predict accurately the volume fractions of these constituents from an input of the steel composition, and the weld variables only. To be satisfactory, the phase transformation mechanisms should be modelled in a fundamental way; ultimately this must lead to greater generality and hence wide applicability. Despite much concerted research in the past fifty years, and with the advent of fast computational techniques, this goal has still to be achieved. One could argue that until this has been done, our understanding of ferrous phase transformations is not advanced.

In the proceeding two chapters existing theory is collated and developed in an attempt to model the kinetics of one of these phase transformations: the austenite to allotriomorphic ferrite transformation in low-alloy steel. Allotriomorphic ferrite [88,89,90,91] is the form of ferrite which grows at low undercoolings below the Ae3 temperature, nucleating at prior austenite grain boundaries, and growing along them at a rate faster than along a direction normal to the boundary plane. Thus, although this form of ferrite is crystalline in internal structure, its outward form does not reflect this; the term 'allotriomorphic' acknowledges this fact.

Towards the goal of modelling the transformation kinetics, a thermodynamic model for low-alloy multicomponent steels is developed in this chapter. Such a model is needed because the maximum possible extent of reaction is given by the phase diagram, and because austenite and ferrite are often assumed to be in local equilibrium at the interface, so that multicomponent tie-lines need to be calculated readily. The available thermodynamic models are first reviewed, before a suitable choice of model is made.

6.2 Comparison of Available Thermodynamic Models

6.2.1 Hillert-Staffanson Regular Solution Model

Although originally developed as a description of ionic melts or interstitial solutions, the Hillert-Staffanson model [92] has been used widely [e.g. 93,94] for ternary and higher order systems, and especially steels. Two lattices, one substitutional and one interstitial, are recognised and distinguished from each other; although the two lattices interpenetrate, occupancy is assumed to be restricted to only one of the two lattices, for each type of atom.

Instead of referring to mole fractions, the concentrations are written as molar ratios, i.e. fractions of the appropriate sites occupied. For the ternary steel Fe–C–X, where X represents a substitutional solute, the molar ratios y_{Fe}, y_C and y_X of iron, carbon and X respectively, are then defined by the equations (6.1)

$$y_{Fe} = x_{Fe}/(1 - x_C)$$ (6.2)

$$y_C = x_C/[c(1 - x_C)]$$ (6.3)

$$y_X = x_X/(1 - x_C)$$

where x_{Fe}, x_C and x_X are the mole fractions of iron, carbon and X respectively, and c is the ratio of interstitial to substitutional sites available; thus c takes a value of one for austenite, and three for ferrite.

Assuming a regular solution type model, the expression usually used for the Gibbs free energy per mole of lattice sites G_m is (6.4)

$$G_m = y_{Fe}{}^0\mu_{Fe} + y_C{}^0\mu_C + y_X{}^0\mu_X + y_X y_C \Delta G_X - TS_m^{ideal} + {}^E G_m$$

where ${}^0\mu_{Fe}$, ${}^0\mu_C$ and ${}^0\mu_X$ are the chemical potentials of the pure components. The term T is the absolute temperature, S_m^{ideal} is the ideal molar entropy of mixing and ${}^E G_m$ is the molar excess Gibbs free energy. The term ${}^0\mu_C$ has little meaning, since in this model carbon is an interstitially dissolved element; however, it is possible to define artificial standard states for carbon in iron, and carbon in X [92]. The term ΔG_X represents the difference between the molar Gibbs free energies in these artificial standard states, and may be regarded [95] as representing the interaction between carbon and X. The ideal molar entropy of mixing is given by (6.5

$$S_m^{ideal} = -R\left[y_{Fe}\ln\{y_{Fe}\} + cy_C\ln\{y_C\} + c(1 - y_C)\ln\{1 - y_C\} + y_X\ln\{y_X\}\right]$$

The excess molar Gibbs free energy represents the deviation from ideality. Usually this expression contains adjustable parameters, which are chosen to obtain good agreement with experimental information. In the original Hillert and Staffanson paper, ${}^E G_m$ took the form (6.

$${}^E G_m = y_{Fe} y_X \left[y_C L_{FeX}^C + (1 - y_C)L_{FeX}^V\right] + y_C(1 - y_C)\left[y_{Fe}L_{CV}^{Fe} + y_X L_{CV}^X\right]$$

where the L's are interaction parameters. For example, L_{CV}^{Fe} represents the carbon–vacancy interact parameter, when all the substitutional sites are filled with iron; L_{CV}^X is the carbon–vacancy interact parameter, when all the substitutional sites are filled with solute X. The advantage in using an express such as (6.6) for ${}^E G_m$ is that the model can be readily extended to describe higher order systems with

134

changing the description of the lower ones. To illustrate this point, equation 6.6 describes the excess energy of a binary system when any one of the x's vanishes. In the original regular solution model, the L-parameters were assumed constant. However, in order to match experimental information, it is usually necessary to allow a temperature dependence. In this case, a general (empirical) parameter L can be written [95]

$$L = a + bT + CT\ln\{T\} + dT^2 + eT^3 \dots\dots \tag{6.7}$$

where a, b, c, d, e are constants chosen so that the model matches experimental information.

The chemical potentials are obtained from the free energy diagram by constructing a tangent to the free energy curve, and reading the intersections with the component axes. In the present model, the following expressions perform such an operation [92]

$$\mu_{Fe} = G_m + (1 - y_{Fe})\frac{\partial G_m}{\partial y_{Fe}} - y_C\frac{\partial G_m}{\partial y_C} \tag{6.8}$$

$$\mu_C = \frac{\partial G_m}{\partial y_C} \tag{6.9}$$

$$\mu_X = G_m + (1 - y_X)\frac{\partial G_m}{\partial y_X} - y_C\frac{\partial G_m}{\partial y_C} \tag{6.10}$$

and they yield

$$\mu_{Fe} = {}^0\mu_{Fe} + RT\ln\{y_{Fe}\} + cRT\ln\{1 - y_C\} + {}^EG_{Fe} \tag{6.11}$$

$$\mu_C = {}^0\mu_C + RT\ln\{y_C/(1 - y_C)\} + {}^EG_C \tag{6.12}$$

$$\mu_X = {}^0\mu_X + RT\ln\{y_X\} + cRT\ln\{1 - y_C\} + {}^EG_X \tag{6.13}$$

where ${}^EG_{Fe}$, ${}^EG_C$ and ${}^EG_X$ are excess free energies, given by

$$
\begin{aligned}
{}^EG_{Fe} = &-y_X y_C \left[\Delta G_X + L^C_{FeX} - L^V_{FeX} + L^X_{CV} - L^{Fe}_{CV}\right] \\
&+y_X^2 \left[L^V_{FeX}\right] \\
&+y_C^2 \left[L^{Fe}_{CV}\right] \\
&+2y_X^2 y_C \left[L^C_{FeX} - L^V_{FeX}\right] \\
&+2y_X y_C^2 \left[(L^X_{CV} - L^{Fe}_{CV}\right]
\end{aligned}
\tag{6.14}
$$

$$
\begin{aligned}
c^EG_C = &-2y_C \left[L^{Fe}_{CV}\right] \\
&+y_X \left[\Delta G_X + L^C_{FeX} - L^V_{FeX} + L^X_{CV} - L^{Fe}_{CV}\right] \\
&+2y_X y_C \left[L^{Fe}_{CV} - L^X_{CV}\right] \\
&+y_X^2 \left[L^V_{FeX} - L^C_{FeX}\right]
\end{aligned}
\tag{6.15}
$$

$$
\begin{aligned}
{}^EG_X = &\, y_{Fe} y_C \left[\Delta G_X + L^V_{FeX} - L^C_{FeX} + L^X_{CV} - L^{Fe}_{CV}\right] \\
&+y_{Fe}^2 \left[L^V_{FeX}\right] \\
&+y_C^2 \left[L^X_{CV}\right] \\
&+2y_{Fe}^2 y_C \left[L^C_{FeX} - L^V_{FeX}\right] \\
&+2y_{Fe} y_C^2 \left[(L^{Fe}_{CV} - L^X_{CV}\right]
\end{aligned}
\tag{6.16}
$$

The Gibbs free energies of austenite and of ferrite, are then given by the expressions

$$G^\gamma = x^\gamma_{Fe}\mu^\gamma_{Fe} + x^\gamma_C\mu^\gamma_C + x^\gamma_X\mu^\gamma_X \tag{6.17}$$

$$G^\alpha = x^\alpha_{Fe}\mu^\alpha_{Fe} + x^\alpha_C\mu^\alpha_C + x^\alpha_X\mu^\alpha_X \tag{6.18}$$

135

and the total Gibbs energy of the two phase system by

$$G = x_\gamma G^\gamma + x_\alpha G^\alpha \tag{6.19}$$

where x_γ and x_α are the fractions of austenite and ferrite present in the two phase mixture.

The variables x_{Fe}^γ, x_C^γ, x_X^γ, x_{Fe}^α, x_C^α and x_X^α are then found by the minimisation of G, subject to the condition that the total content of Fe, C and X in the system is fixed. Some sort of a hill-climbing technique is usually employed, in which initial guess values for the x's are made, and a particular strategy for their variation chosen. This minimum value of G for the $(\alpha + \gamma)$ two phase field corresponds to the equilibrium condition

$$\left. \begin{aligned} \mu_{Fe}^\gamma &= \mu_{Fe}^\alpha \\ \mu_C^\gamma &= \mu_C^\alpha \\ \mu_X^\gamma &= \mu_X^\alpha \end{aligned} \right\} \tag{6.20}$$

Sometimes the minimisation process is subject to other auxiliary conditions. For example, when austenite decomposes at temperatures far below the eutectoid temperature, it appears that substitutional alloying elements do not exhibit the mobility necessary to partition during transformation; subject to this kinetic constraint (which has become known as *paraequilibrium* [96]) the chemical potentials of carbon in austenite and ferrite at the advancing interface are equal. Mathematically, paraequilibrium can be expressed by

$$\left. \begin{aligned} \mu_C^\gamma &= \mu_C^\alpha, \\ x_{Fe}^\gamma(\mu_{Fe}^\gamma - \mu_{Fe}^\alpha) &= -x_X^\gamma(\mu_X^\gamma - \mu_X^\alpha) \end{aligned} \right\} \tag{6.21}$$

and these expressions represent a constraint on the process of minimisation.

6.2.2 Hillert-Staffanson Sub-Regular Solution Model

In order to describe deviations from the regular solution model, a concentration dependence of the L-parameters is sometimes introduced. The most common method is to replace the L's with truncated series expansions [95]. In the model presented by Uhrenius [94], the series is truncated after the first power term, so that the dependence upon substitutional alloy content is linear. In such cases, we obtain what is commonly referred to as a sub-regular solution model [95], with:

$$L_{FeX}^C = {}^0L_{FeX}^C + {}^1L_{FeX}^C(y_{Fe} - y_X) \tag{6.22}$$

$$L_{FeX}^V = {}^0L_{FeX}^V + {}^1L_{FeX}^V(y_{Fe} - y_X) \tag{6.23}$$

The expression for the free energy per mole of metal atoms is again given by equation 6.4, but the excess free energies are now given by

$$\begin{aligned} {}^EG_{Fe} = &-y_X y_C \left[\Delta G_X + {}^0L_{FeX}^C - {}^0L_{FeX}^V + L_{CV}^X - L_{CV}^{Fe} + (1 - 2y_X)({}^1L_{FeX}^C - {}^1L_{FeX}^V) \right] \\ &+ y_X^2 \left[{}^0L_{FeX}^V + (3 - 4y_X){}^1L_{FeX}^V \right] \\ &+ y_C^2 \left[L_{CV}^{Fe} \right] \\ &+ 2y_X^2 y_C \left[{}^0L_{FeX}^C - {}^0L_{FeX}^V + (2 - 3y_X)({}^1L_{FeX}^C - {}^1L_{FeX}^V) \right] \\ &+ 2y_X y_C^2 \left[(L_{CV}^X - L_{CV}^{Fe}) \right] \end{aligned} \tag{6.24}$$

$$\begin{aligned} c^EG_C = &-2y_C \left[L_{CV}^{Fe} \right] \\ &+ y_X \left[\Delta G_X + {}^0L_{FeX}^C - {}^0L_{FeX}^V + L_{CV}^X - L_{CV}^{Fe} \right] \\ &+ 2y_X y_C \left[L_{CV}^{Fe} - L_{CV}^X \right] \\ &+ y_X^2 \left[{}^0L_{FeX}^V - {}^0L_{FeX}^C \right] \end{aligned} \tag{6.25}$$

136

$$^E G_X = y_{Fe} y_C \left[\Delta G_X + {}^0 L_{FeX}^V - {}^0 L_{FeX}^C + L_{CV}^X - L_{CV}^{Fe} + (1 - 2y_X)({}^1 L_{FeX}^V - {}^1 L_{FeX}^C) \right]$$
$$+ y_{Fe}^2 \left[{}^0 L_{FeX}^V + (1 - 4y_X){}^1 L_{FeX}^V) \right]$$
$$+ y_C^2 \left[L_{CV}^X \right]$$
$$+ 2 y_{Fe}^2 y_C \left[{}^0 L_{FeX}^C - {}^0 L_{FeX}^V + (1 - 3y_X)({}^1 L_{FeX}^C - {}^1 L_{FeX}^V) \right]$$
$$+ 2 y_{Fe} y_C^2 \left[(L_{CV}^{Fe} - L_{CV}^X \right] \tag{6.26}$$

The first line of equation 6.24 corrects one error of sign in the original reference. The methodology for solution is identical to that in the regular solution case.

6.2.3 Quasichemical Models

Whilst the regular or sub-regular solution models successfully reproduce the experimentally determined phase diagrams and activity data, they are unsatisfactory in the sense that the empirical parameters within the excess Gibbs free energy terms are not physically meaningful. When describing a multicomponent system, the number of these parameters can become very large, so that it is not surprising that such models successfully reproduce the experimental data. In addition, the regular solution models assume an ideal entropy of solution; whilst this is likely to be a reasonable approximation for substitutional solutions, it is not surprising to find that interstitial solid solutions show large departures from such behaviour. Perhaps the most serious difficulty arises when it becomes necessary to extrapolate phase boundaries into regions where the phases themselves are metastable. Extrapolation of the $\gamma/(\gamma + \alpha)$ and $\alpha/(\gamma + \alpha)$ phase boundaries past the eutectoid temperature is an obvious necessity when considering the bainite, or martensite transformations, for example.

The so-called *quasi-chemical* models represent attempts to model departures from an ideal entropy of mixing [96]. Therefore, whilst it is still necessary to establish best fit parameters by considering experimental activity data, the number of adjustable parameters is reduced. It is then possible to extrapolate phase boundaries into metastable regions with more confidence. First-order quasichemical models have been applied widely; in these models, the carbon atoms are assumed to interact only with the first-nearest iron atoms and with other carbon atoms. The carbon-carbon interaction is characterised by a relatively small interaction energy; this has the consequence that the configurational entropy is non-ideal and the partial energy of solution is almost independent of temperature, but strongly dependent on composition.

In their re-examination of the thermodynamics of the Fe–C system, Shiflet *et al.* [98] compared two first-order quasichemical models. They found that the models of Lacher [99] Fowler & Guggenheim [100], and McLellan & Dunn [101] yielded similar values of x_C^γ; moreover the two expressions for the activity of iron were shown to be mathematically equivalent. As far as those functions are concerned, it therefore seems that it makes no difference which of the two models is adopted. However, Shiflet *et al.* pointed out that the McLellan & Dunn's model yields the correct expression for the activity of carbon in austenite in the limit of an infinite pairwise carbon interaction energy ω_C^γ, *i.e.* in the limit of complete blocking of neighbouring sites. This model is therefore adopted in this work; the expression for the activity of carbon in austenite is then [101]

$$\ln\{a_C^\gamma\} = 11 \ln \left\{ \frac{1 - 2x_C^\gamma}{x_C^\gamma} \right\} + \frac{6\omega_C^\gamma}{RT}$$
$$+ 6 \ln \left\{ \left[1 - 2\left(1 + 2J_C^\gamma\right) x_C^\gamma + (1 + 8J_C^\gamma) x_C^{\gamma\,2} \right]^{1/2} - 1 + (1 + 2J_C^\gamma) x_C^\gamma \right\}$$
$$- 6 \ln \left\{ \left[1 - 2\left(1 + 2J_C^\gamma\right) x_C^\gamma + (1 + 8J_C^\gamma) x_C^{\gamma\,2} \right]^{1/2} - 1 + 2J_C^\gamma + (1 - 4J_C^\gamma) x_C^\gamma \right\}$$
$$+ \frac{\Delta \overline{H}_C^\gamma - T \left[{}^E \Delta \overline{S}_C^\gamma \right]}{RT} \tag{6.27}$$

137

and for the activity of iron in austenite

$$\ln\{a_{Fe}^\gamma\} = 5\ln\left\{\frac{1-x_C^\gamma}{1-2x_C^\gamma}\right\}$$
$$+ 6\ln\left\{1 - 2J_C^\gamma + (4J_C^\gamma - 1)\,x_C^\gamma - \left[1 - 2\,(1+2J_C^\gamma)\,x_C^\gamma + (1+8J_C^\gamma)\,x_C^{\gamma\,2}\right]^{1/2}\right\}$$
$$- 6\ln\left\{2J_C^\gamma\,(2x_C^\gamma - 1)\right\} \qquad (6.28)$$

where
$$J_C^\gamma = 1 - \exp\left\{\frac{-\omega_C^\gamma}{RT}\right\} \qquad (6.29)$$

where $\Delta\overline{H}_C^\gamma$ and $^E\Delta\overline{S}_C^\gamma$ are the relative partial enthalpy and non-configurational entropy of carbon, with respect to pure iron at infinite dilution. The term J_C^γ represents the probability of the nearest neighbouring site being excluded from occupancy.

By considering the Ban-ya, Elliot & Chipman's [102,103] data for the activity of carbon in austenite measured relative to solid graphite, Shiflet et $al.$ secured $\omega_C^\gamma = 8054\,\mathrm{J\,mol^{-1}}$, $\Delta\overline{H}_C^\gamma = 38,565\,\mathrm{J\,mol^{-1}}$ and $^E\Delta\overline{S}_C^\gamma = 13.48\,\mathrm{J\,mol^{-1}}$. The positive value for ω_C^γ corresponds to a $repulsive$ interaction between carbon atoms. These values are adopted throughout this work.

Application of quasi-chemical models to carbon in ferrite has proved more difficult. Shiflet et $al.$ were unable to determine a temperature independent pairwise interaction energy between carbon atoms in ferrite; however, Bhadeshia [104] has shown that Shiflet et $al.$'s derivation of the McLellan & Dunn expression for the activity of carbon in ferrite is incorrect. The correct expression is

$$\ln\{a_C^\alpha\} = 3\ln\left\{\frac{3-4x_C^\alpha}{x_C^\alpha}\right\} + \frac{2\omega_C^\alpha}{RT}$$
$$+ 2\ln\left\{\left[9 - 6\,(3+2J_C^\alpha)\,x_C^\alpha + (9+16J_C^\alpha)\,x_C^{\alpha\,2}\right]^{1/2} - 3 + x_C^\alpha\,(3+2J_C^\alpha)\right\}$$
$$- 2\ln\left\{\left[9 - 6\,(3+2J_C^\alpha)\,x_C^\alpha + (9+16J_C^\alpha)\,x_C^{\alpha\,2}\right]^{1/2} - 3 + 6J_C^\alpha + x_C^\alpha\,(3-8J_C^\alpha)\right\}$$
$$+ \frac{\Delta\overline{H}_C^\alpha - T\left[^E\Delta\overline{S}_C^\alpha\right]}{RT} \qquad (6.30)$$

where
$$J_C^\alpha = 1 - \exp\left\{\frac{-\omega_C^\alpha}{RT}\right\} \qquad (6.31)$$

To a good approximation, since the carbon concentration of carbon in ferrite is so small, the activity of iron in ferrite is calculated from the expression

$$\ln\{a_{Fe}^\alpha\} = \ln\{1 - x_C^\alpha\} \qquad (6.32)$$

By considering Lobo & Geiger's [105] data for the activity of carbon in ferrite, measured relative to solid graphite, Bhadeshia [104] used regression analysis to find $\omega_C^\alpha = 132400\,\mathrm{J\,mol^{-1}}$, $\Delta\overline{H}_C^\alpha = 105150\,\mathrm{J\,mol^{-1}}$ and $^E\Delta\overline{S}_C^\alpha = 35.5\,\mathrm{J\,mol^{-1}}$. These values are adopted throughout this work. The positive value for ω_C^α corresponds to a repulsive interaction between carbon atoms, as in austenite.

Recently, Mou & Aaronson [106] have cast doubt on the repulsive nature of the carbon-carbon interaction energy in ferrite. They found that values of a_{Fe}^γ at only two of the eight temperatures investigated by Lobo and Geiger fulfilled the requirements for performance which they imposed on their regression analysis. However, at these two temperatures they found $\omega_C^\alpha < 0$, corresponding to an attractive interaction, for the McLellan-Dunn and Lacher-Fowler-Guggenheim models. At the other six temperatures a unique best-fit value for ω_C^α could not be chosen. For $\omega_C^\alpha > 100\,\mathrm{kJ/mol}$ oscillatory

behaviour was reported, implying that the expression for the activity of carbon in ferrite (equations 6.30 & 6.31) is not well-behaved as ω_C^α approaches infinity. Bhadeshia [107] experienced similar problems with these equations.

In the author's experience, great care needs to be taken in evaluating equation 6.30, as ω_C^α is increased beyond $100\,\mathrm{kJ\,mol^{-1}}$. This can be seen by noting that as $\omega_C^\alpha \to \infty$

$$\left[9 - 6\left(3 + 2J_C^\alpha\right) x_C^\alpha + \left(9 + 16 J_C^\alpha\right) x_C^{\alpha 2} \right]^{1/2} \sim \left[3 - x_C^\alpha \left(3 + 2 J_C^\alpha \right) \right] \tag{6.33}$$

so that rounding errors are quickly accumulated during evaluation of the second line of equation 6.30. The authors recommend that the terms within equation 6.30 are held to an accuracy of 32 figures during calculation.

Finally, it should be noted that since the concentration of carbon in ferrite is so small in the temperature range of interest, it does not significantly influence the kinetics of diffusion-controlled growth of ferrite from austenite. In this respect, the exact magnitudes of x_C^α and hence ω_C^α are unimportant.

6.2.4 Wagner Formalism

In the regular or sub-regular solution models, it is common to use polynomials to represent the partial molar excess properties. For dilute solutions, the use of these polynomials is justified theoretically, provided the logarithm of the activity coefficient can be expressed as a Taylor series in the mole fractions of solutes present. Expanded at the point of infinite dilution (figure 6.1), the series may be written in terms of the mole fractions as [108]

$$\ln\{\Gamma_i\} = \ln\{\Gamma_i^\infty\} + \sum_{j=1}^{n} \left(\frac{\partial \ln\{\Gamma_i\}}{\partial x_j} \right)_{x_{Fe}\to 1} x_j + \sum_{j=1}^{n} \frac{1}{2} \left(\frac{\partial^2 \ln\{\Gamma_i\}}{\partial x_j^2} \right)_{x_{Fe}\to 1} x_j^2$$

$$+ \sum_{j=2}^{n-1} \sum_{k>j}^{n} \left(\frac{\partial^2 \ln\{\Gamma_i\}}{\partial x_j \partial x_k} \right)_{x_{Fe}\to 1} x_j x_k + \ldots \tag{6.34}$$

Such an expression applies for all the solutes present, as well as for the solvent. If the solution is sufficiently dilute, then all the second order terms can be neglected, and equation 6.34 becomes

$$\ln\{\Gamma_i\} = \ln\{\Gamma_i^\infty\} + \sum_{j=1}^{n} \epsilon_{ij} x_j \tag{6.35}$$

where ϵ_{ij} is a matrix of *Wagner interaction coefficients* [109] given by

$$\epsilon_{ij} = \left(\frac{\partial \ln\{\Gamma_i\}}{\partial x_j} \right)_{x_{Fe}\to 1} \tag{6.36}$$

Therefore, even if the total number of solutes is very large, the activity coefficient of i can be calculated as summation of terms which are derived from ternary systems only. The convenience of this result has made the use of this Wagner formalism widespread [e.g. 110].

In this work, we concentrate on the thermodynamics of low-alloy steels, and make the assumption that the interactions between substitutional atoms of different components are negligible. For iron, carbon and each of the substitutionals, an equation such as 6.35 can then be written. Taking the standard state of carbon and the substitutionals as an infinitely dilute solution in iron as solvent, so that $\Gamma_C^\infty = 1$ and $\Gamma_X^\infty = 1$ [109] (figure 6.1), we have

$$\ln\{\Gamma_C\} = \epsilon_{CC} x_C + \sum_{X=1}^{N} \epsilon_{CX} x_X \tag{6.37}$$

139

for the logarithm of the activity coefficient of carbon, and

$$\ln\{\Gamma_X\} = +\epsilon_{XC}x_C + \epsilon_{XX}x_X \qquad (6.38)$$

for that of each of the substitutional alloying elements X. The logarithm of the activity coefficient of iron can be deduced by applying the Gibbs-Duhem equation [108]

$$\ln\{\Gamma_{Fe}\} = -\frac{1}{2}\epsilon_{CC}x_C x_C - \frac{1}{2}\sum_{X=1}^{N}\epsilon_{XX}x_X x_X - \sum_{X=1}^{N}\epsilon_{CX}x_C x_X \qquad (6.39)$$

As discussed by Pelton & Bale [126] it is a thermodynamic necessity that the matrix of Wagner interaction parameters ϵ_{ij} is symmetrical. They also point out that at finite concentrations equations 6.37–6.39 are inconsistent with the Gibbs-Duhem equation; they can be made consistent by adding the term $\ln\{\Gamma_{Fe}\}$ to the right hand side of equations 6.37 and 6.38. However, since equation 6.39 contains only quadratic terms in the x's, whereas 6.37 & 6.38 contains linear terms, the effect of this correction is small. For this reason, and because the correction complicates the location of the equilibrium tie-lines, equations 6.37 & 6.38 are used throughout this work.

6.3 The Model

In the following part of this chapter, a model to describe the iron-rich corner of the multicomponent phase diagram is developed. The model is based upon the Fe–C binary phase diagram, calculated using the quasichemical model, so that extrapolation to temperatures below the eutectoid temperature can be attempted. To accommodate the addition of substitutional solutes, the Wagner interaction parameter formalism is employed. This introduces a degree of error because the expressions for the logarithms of the activity coefficients are then first order approximations. However the overall aim here is to model the *kinetics* of the transformation, and as will be seen in chapter seven of this dissertation, the Wagner interaction parameters are related to the cross-terms in the diffusivity matrix, which must be evaluated if the velocity of the interface is to be calculated under local equilibrium. For this reason, the Wagner formalism is preferred.

The accuracy of all thermodynamic models depends ultimately upon the the reliability of the experimental data used to calibrate it, as well as the type of model. For this reason it is important to examine and evaluate the available data before making a suitable choice.

6.3.1 Thermodynamic Functions of Pure Iron

Since this work is concerned with the thermodynamics and kinetics of low-alloy steels, it is particularly important to have a reliable knowledge of the Gibbs free energy change for the $\alpha \rightarrow \gamma$ transformation in pure iron, $\Delta^0 G_{Fe}^{\alpha \rightarrow \gamma}$. It is to be expected that this term will be dominant in all calculations which follow, since the additions of carbon and substitutionals will be relatively small.

Values of $\Delta^0 G_{Fe}^{\alpha \rightarrow \gamma}$ have been deduced by several investigators. The tabulations due to Orr and Chipman [111], and Kaufman, Clougherty and Weiss [112] are often referred to. More recent evaluations (*e.g.* Hillert and Jahl [113], Agren [114]) have been based upon 'optimising' the existing data. It should be noted that all these data seem to successfully reproduce the well-established Fe–C phase diagram, in the regimes where experimental data are accessible.

The data and functions due to Kaufman, Clougherty & Weiss (corrected by Kaufman & Bernstein [115]), Orr & Chipman and Agren are plotted in figure 6.2, and figure 6.3. It is evident, that between 750 & 950°C the data are consistent within ~20 J mol^{-1}. However, below 50°C the Kaufman *et al.* data diverge from that of Orr & Chipman and Agren; at 400°C they differ by over 300 J mol^{-1}.

In a review of the available thermodynamic data, Bhadeshia [116] came to the conclusion that the results obtained by Kaufman *et al.* are well established, reliable, and accurate for low temperature applications. This tabulation is used in all the calculations which follow.

6.3.2 Thermodynamic Functions of Carbon

As has already been stated, solutions of carbon in austenite or ferrite show large departures from Henrian behaviour even at low carbon concentrations, so that care needs to be taken in the evaluation of the terms $\Delta^0 G_C^{\alpha \to \gamma}$, ϵ_{CC}^γ and ϵ_{CC}^α.

The binary Fe–C phase diagram has already been constructed, using the quasichemical model of McLellan and Dunn for the calculation of the activities of carbon in austenite and ferrite. It should be noted, that these activities are measured relative to solid graphite as standard. In this work, it is necessary to refer the activity data to infinite dilution of iron for consistency.

For the binary Fe–C system, we have from the condition of equipotential for carbon at equilibrium:

$$^0\mu_{Fe}^\gamma + RT \ln \{x_{Fe}^\gamma \Gamma_{Fe}^\gamma\} = {}^0\mu_{Fe}^\alpha + RT \ln \{x_{Fe}^\alpha \Gamma_{Fe}^\alpha\} \tag{6.40}$$

$$^0\mu_C^\gamma + RT \ln \{x_C^\gamma \Gamma_C^\gamma\} = {}^0\mu_C^\alpha + RT \ln \{x_C^\alpha \Gamma_C^\alpha\} \tag{6.41}$$

where the expressions is now written relative to infinite dilution of iron. Upon rearranging, we have

$$\Delta^0 G_{Fe}^{\alpha \to \gamma} = {}^0\mu_{Fe}^\gamma - {}^0\mu_{Fe}^\alpha = RT \ln \left\{ \frac{x_{Fe}^\alpha \Gamma_{Fe}^\alpha}{x_{Fe}^\gamma \Gamma_{Fe}^\gamma} \right\} \tag{6.42}$$

$$\Delta^0 G_C^{\alpha \to \gamma} = {}^0\mu_C^\gamma - {}^0\mu_C^\alpha = RT \ln \left\{ \frac{x_C^\alpha \Gamma_C^\alpha}{x_C^\gamma \Gamma_C^\gamma} \right\} \tag{6.43}$$

The activity coefficients for the binary Fe–C system, written in terms of the Wagner interaction parameters, are given by the expressions

$$\ln \{\Gamma_{Fe}^\gamma\} = -\frac{1}{2} \epsilon_{CC}^\gamma x_C^\gamma x_C^\gamma \tag{6.44}$$

$$\ln \{\Gamma_{Fe}^\alpha\} = -\frac{1}{2} \epsilon_{CC}^\alpha x_C^\alpha x_C^\alpha \tag{6.45}$$

$$\ln \{\Gamma_C^\gamma\} = \epsilon_{CC}^\gamma x_C^\gamma \tag{6.46}$$

$$\ln \{\Gamma_C^\alpha\} = \epsilon_{CC}^\alpha x_C^\alpha \tag{6.47}$$

For calibration against the binary Fe–C phase diagram calculated using the quasichemical model, the unknowns are $\Delta^0 G_C^{\alpha \to \gamma}$, and the Wagner interaction parameters ϵ_{CC}^γ and ϵ_{CC}^α. To evaluate $\Delta^0 G_C^{\alpha \to \gamma}$, the linear function used by Kirkaldy *et al.* [117] is employed; the two carbon-carbon Wagner interaction parameters can therefore be calculated by combining equations 6.42–6.47, to arrive at the expressions

$$\epsilon_{CC}^\gamma = \frac{2}{(x_C^\gamma - x_C^\alpha) x_C^\gamma} \left[\frac{\Delta^0 G_{Fe}^{\alpha \to \gamma}}{RT} - \ln \left\{ \frac{x_{Fe}^\alpha}{x_{Fe}^\gamma} \right\} \right] + \frac{x_C^\alpha}{(x_C^\gamma - x_C^\alpha) x_C^\gamma} \left[\frac{\Delta^0 G_C^{\alpha \to \gamma}}{RT} - \ln \left\{ \frac{x_C^\alpha}{x_C^\gamma} \right\} \right] \tag{6.48}$$

$$\epsilon_{CC}^\alpha = \frac{2}{(x_C^\gamma - x_C^\alpha) x_C^\alpha} \left[\frac{\Delta^0 G_{Fe}^{\alpha \to \gamma}}{RT} - \ln \left\{ \frac{x_{Fe}^\alpha}{x_{Fe}^\gamma} \right\} \right] + \frac{x_C^\gamma}{(x_C^\gamma - x_C^\alpha) x_C^\alpha} \left[\frac{\Delta^0 G_C^{\alpha \to \gamma}}{RT} - \ln \left\{ \frac{x_C^\alpha}{x_C^\gamma} \right\} \right] \tag{6.49}$$

This procedure ensures that the binary Fe–C phase diagram is equivalent to that calculated from the quasichemical model. Figure 6.4 shows the values of the Wagner interaction parameters calculated using this procedure. It is evident that extrapolations of $\Delta^0 G_C^{\alpha \to \gamma}$ and the carbon-carbon Wagner interaction parameters to low temperatures based upon published data will lead to errors.

It is now possible to calculate the $\gamma/(\gamma + \alpha)$ and $\alpha/(\gamma + \alpha)$ phase boundaries for the binary Fe–C system, by equating the chemical potentials of iron and carbon, in austenite and ferrite. Figure 6.5 shows these phase boundaries calculated in this way.

6.3.3 Thermodynamic Functions of Substitutional Alloying Elements

The effect of an alloying element X on the relative stability of austenite and ferrite can be expressed by the term [118]:

$$\Delta^0 G_X^{\alpha \to \gamma} = [\mu_X^\gamma - \mu_X^\alpha]_{x_X^\gamma = x_X^\alpha} \tag{6.50}$$

which represents the free energy of reaction for the transfer of one mole of solute X from ferrite, of composition x_X to austenite, of the same composition. All terms in x are omitted, because the free energy of reaction is defined with respect to an infinitely dilute solution, *i.e.* pure iron.

In terms of the Hillert-Staffansson sub-regular solution model, as expressed by Uhrenius, $\Delta^0 G_X^{\alpha \to \gamma}$ is given by the expression

$$\Delta^0 G_X^{\alpha \to \gamma} = {}^0 \mu_X^\gamma - {}^0 \mu_X^\alpha + {}^0 L_{FeX}^{V,\gamma} + {}^1 L_{FeX}^{V,\gamma} + {}^0 L_{FeX}^{V,\alpha} + {}^1 L_{FeX}^{V,\alpha} \tag{6.51}$$

The terms $\Delta^0 G_X^{\alpha \to \gamma}$ were therefore evaluated for the elements considered by Uhrenius. The results are presented in table 6.1. Also tabulated are functions for cobalt [119] and niobium [120].

ELEMENT	GIBBS FREE ENERGY, $\Delta^0 G_X^{\alpha \to \gamma}$ / Jmol^{-1}
Mn	$-20520 + 4.086T + 1500({}^0 S_{Fe}^\alpha)_{Mag}$
Si	$7087 - 4.127T$
Ni	$-12950 + 5.02T + 383({}^0 S_{Fe}^\alpha)_{Mag}$
Cr	$-1534 - 19.472T + 2.747T \ln T$
Mo	$310 - 0.284T + 400({}^0 S_{Fe}^\alpha)_{Mag}$
Cu	$-11966 + 1.602T + 1000({}^0 S_{Fe}^\alpha)_{Mag}$
V	$7650 - 2.694T$
Nb	$5700 - 0.044T$
W	$5439 - 1.255T$
Co	$6464 + 1.2979T - 1050({}^0 S_{Fe}^\alpha)_{Mag}$

Table 6.1: Gibbs Free Energy change per mole of substitutional solute passing from $\alpha \to \gamma$, at infinite dilution of iron.

The term $({}^0 S_{Fe}^\alpha)_{Mag}$ is the magnetic contribution to the Gibbs free energy change of pure iron. The use of this function in thermodynamic work has arisen because of a suggestion by Zener [121], who first suggested the possibility of dividing the free energy of pure iron into a magnetic, and a non-magnetic term. He proposed that a small alloying addition Δx, which changes the Curie temperature of α-iron by ΔT will displace the magnetic part of the free energy function by the same amount ΔT.

Weiss and Tauer [122] showed that $({}^0 S_{Fe}^\alpha)_{Mag}$ has a sigmoidal form as a function of temperature, reaching the theoretical value of $R \ln \{2s + 1\}$, where s is the unpaired spin per atom, at the melting point. Figure 6.6 compares Weiss and Tauer's original evaluation with that due to Kaufman, Clougherty & Weiss [112]. The latter is used in this work, for the sake of consistency, because the tabulation due to these workers has been chosen for $\Delta^0 G_{Fe}^{\alpha \to \gamma}$.

Figure 6.7 shows a plot of $\Delta^0 G_X^{\alpha \to \gamma}$ for the ten substitutional elements considered, between 600 and 1000°C. As first noted by Zener [123], the elements show the classical division into γ- and α-stabilisers.

6.3.4 Calculation of Wagner Interaction Parameters from Sub-Regular Solution Excess Free Energy

Equations 6.8–6.10 can be re-written in the form

$$\mu_{Fe} = {}^0 \mu_{Fe} + RT \ln \{x_{Fe}\} + RT \ln \{\Gamma_{Fe}\} \tag{6.52}$$

$$\mu_C = {}^0 \mu_C + RT \ln \{x_C\} + RT \ln \{\Gamma_C\} \tag{6.53}$$

$$\mu_X = {}^0 \mu_X + RT \ln \{x_X\} + RT \ln \{\Gamma_X\} \tag{6.54}$$

where

$$\ln \{\Gamma_C\} = -\ln \{-x_C + c(1 - x_C)\} + {}^E G_C / RT \tag{6.55}$$

$$\ln \{\Gamma_X\} = -\ln \{1 - x_C\} + c \ln \{1 - x_C / [c(1 - x_C)]\} + {}^E G_X / RT \tag{6.56}$$

By the definition of the Wagner interaction parameter, we have

$$\epsilon_{CC} = \left(\frac{\partial \ln\{\Gamma_C\}}{\partial x_C} \right)_{x_{Fe} \to 1} \tag{6.57}$$

$$\epsilon_{CX} = \left(\frac{\partial \ln\{\Gamma_C\}}{\partial x_X} \right)_{x_{Fe} \to 1} \tag{6.58}$$

$$\epsilon_{XC} = \left(\frac{\partial \ln\{\Gamma_X\}}{\partial x_C} \right)_{x_{Fe} \to 1} \tag{6.59}$$

$$\epsilon_{XX} = \left(\frac{\partial \ln\{\Gamma_X\}}{\partial x_X} \right)_{x_{Fe} \to 1} \tag{6.60}$$

from which it is possible to arrive at the equations

$$\epsilon_{CC} = \frac{c+1}{c} + \frac{1}{RT} \frac{\partial^E G_C}{\partial x_C} \tag{6.61}$$

$$\epsilon_{CX} = \frac{1}{RT} \frac{\partial^E G_C}{\partial x_X} \tag{6.62}$$

$$\epsilon_{XC} = \frac{1}{RT} \frac{\partial^E G_X}{\partial x_C} \tag{6.63}$$

$$\epsilon_{XX} = \frac{1}{RT} \frac{\partial^E G_X}{\partial x_X} \tag{6.64}$$

It is therefore possible [124] to calculate values of the Wagner interaction parameters from the Hillert-Staffanson regular, or sub-regular solution model by considering equations 6.57–6.60 and appropriate expressions for the excess free energies. The appropriate expressions are

$$\epsilon_{CC}^{\gamma} = 2 - \frac{2}{RT} L_{CV}^{Fe,\gamma} \tag{6.65}$$

$$\epsilon_{CC}^{\alpha} = \frac{4}{3} - \frac{2}{9RT} L_{CV}^{Fe,\alpha} \tag{6.66}$$

$$\epsilon_{XX}^{\gamma} = -\frac{2}{RT} \left[{}^0 L_{FeX}^{V,\gamma} + 3^1 L_{FeX}^{V,\gamma} \right] \tag{6.67}$$

$$\epsilon_{XX}^{\alpha} = -\frac{2}{RT} \left[{}^0 L_{FeX}^{V,\alpha} + 3^1 L_{FeX}^{V,\alpha} \right] \tag{6.68}$$

$$\epsilon_{XC}^{\gamma} = \frac{1}{RT} \left[\Delta G_X^{\gamma} - {}^0 L_{FeX}^{V,\gamma} + {}^0 L_{FeX}^{C,\gamma} + L_{CV}^{X,\gamma} - L_{CV}^{Fe,\gamma} - {}^1 L_{FeX}^{V,\gamma} + {}^1 L_{FeX}^{C,\gamma} \right] \tag{6.69}$$

$$\epsilon_{XC}^{\alpha} = \frac{1}{3RT} \left[\Delta G_X^{\alpha} - {}^0 L_{FeX}^{V,\alpha} + {}^0 L_{FeX}^{C,\alpha} + L_{CV}^{X,\alpha} - L_{CV}^{Fe,\alpha} - {}^1 L_{FeX}^{V,\alpha} + {}^1 L_{FeX}^{C,\alpha} \right] \tag{6.70}$$

$$\epsilon_{CX}^{\gamma} = \frac{1}{RT} \left[\Delta G_X^{\gamma} - {}^0 L_{FeX}^{V,\gamma} + {}^0 L_{FeX}^{C,\gamma} + L_{CV}^{X,\gamma} - L_{CV}^{Fe,\gamma} \right] \tag{6.71}$$

$$\epsilon_{CX}^{\alpha} = \frac{1}{3RT} \left[\Delta G_X^{\alpha} - {}^0 L_{FeX}^{V,\alpha} + {}^0 L_{FeX}^{C,\alpha} + L_{CV}^{X,\alpha} - L_{CV}^{Fe,\alpha} \right] \tag{6.72}$$

A comparison of equations 6.65–6.68 reveals that the sub-regular solution model, as presented by Uhrenius, obeys the essential [125,126] thermodynamic condition, $\epsilon_{XC} = \epsilon_{CX}$ only when ${}^1 L_{FeX}^V = {}^1 L_{FeX}^C$. On examination of the data presented by Uhrenius, it is noted that for the eight substitutional elements considered, this equality holds. The expressions for the Wagner interaction parameters calculated in this way are presented in table 6.2. In addition, values for $\epsilon_{CoCo}, \epsilon_{CoC}, \epsilon_{NbNb}$ and ϵ_{NbC} are taken from the tabulation by Kirkaldy, Thomson and Baganis [127].

However, it is evident from equations 6.14–6.16 that the excess Gibbs Free energy terms depend upon both composition and temperature in a more complicated manner than the Wagner formalism; in this case a linear dependence towards the activity coefficient is predicted. As is well known, the Wagner formalism should therefore only be applied to the solvent-rich region of the multicomponent phase

ELEMENT	ϵ^γ_{XX}	ϵ^α_{XX}	ϵ^γ_{XC}	ϵ^α_{XC}
Mn	$2.406 - 175.6/T$	$3.082 - 4679/T + 360.8(^0S^\alpha_{Fe})_{Mag}/T$	$-4811/T$	$-5834/T$
Si	$26048/T$	$-16.35 + 44829/T$	$14795/T$	$16205/T$
Ni	$-2839/T$	$2.013 - 4595/T + 92.1(^0S^\alpha_{Fe})_{Mag}/T$	$5533/T$	$5533/T$
Cr	$7.655 - 3154/T - 0.661\ln\{T\}$	$2.819 - 6039/T$	$14.19 - 30210/T$	$1.558 - 6160/T$
Mo	$-2330/T$	$-0.219 - 4772/T + 96.2(^0S^\alpha_{Fe})_{Mag}/T$	$-10714/T$	$-10714/T$
Cu	$-1.376 - 5766/T$	$0.634 - 11269.7/T + 240.6(^0S^\alpha_{Fe})_{Mag}/T$	$6.62 - 5533/T$	$6.62 - 5533/T$
V	$11.37 - 3524/T$	$9.863 - 3849/T$	$-21650/T$	$-21650/T$
Nb	0	0	$-28770/T$	$-28770/T$
W	$0.453 - 7851/T$	$-9058/T$	$-3447/T$	$-3447/T$
Co	0	0	$2800/T$	$2800/T$

Table 6.2: Expressions derived for the Wagner interaction parameters.

diagram. However, in order to check to what level of the alloying additions the first-order formalism is valid, the excess energies calculated from equations 6.15–6.16 have been plotted against carbon additions in the range 0.000–0.036 mole fraction, and for substitutional additions in the range 0.00–0.05 mole fraction over a range of temperatures. Figures 6.8–6.11 represent typical results, at the arbitrarily chosen temperature of 1000 K. It appears that the excess Gibbs free energy terms show a linear dependence on the mole fractions, at least in these composition ranges, so that a model based on the Wagner formalism, and a model based upon a regular solution model, should yield identical results.

6.4 Method of Solution

6.4.1 Equilibrium

At equilibrium, the chemical potential of each element in ferrite is equal to that in austenite, and equation 6.20 applies. This condition can be written in the present context as

$$x^\alpha_C \exp\{\epsilon^\alpha_{CC} x^\alpha_C\} = x^\gamma_C \exp\left\{\frac{\Delta^0 G^{\alpha\to\gamma}_C}{RT} + \epsilon^\gamma_{CC} x^\gamma_C\right\} \left[\frac{\exp\left\{\sum_{X=1}^N \epsilon^\gamma_{CX} x^\gamma_X\right\}}{\exp\left\{\sum_{X=1}^N \epsilon^\alpha_{CX} x^\alpha_X\right\}}\right] \tag{6.73}$$

for carbon,

$$x^\alpha_X \exp\{\epsilon^\alpha_{XX} x^\alpha_X\} = x^\gamma_X \exp\left\{\frac{\Delta^0 G^{\alpha\to\gamma}_X}{RT} + \epsilon^\gamma_{XC} x^\gamma_C - \epsilon^\alpha_{XC} x^\alpha_C\right\} \exp\{\epsilon^\gamma_{XX} x^\gamma_X\} \tag{6.74}$$

for each of the substitutional alloying elements, and

$$x^\alpha_{Fe} \exp\left\{-\frac{1}{2}\epsilon^\alpha_{CC} x^\alpha_C x^\alpha_C\right\} \exp\left\{-\frac{1}{2}\sum_{X=1}^N \epsilon^\alpha_{XX} x^\alpha_X x^\alpha_X\right\} \exp\left\{-x^\alpha_C \sum_{X=1}^N \epsilon^\alpha_{XC} x^\alpha_X\right\}$$

$$= x^\gamma_{Fe} \exp\left\{\frac{\Delta^0 G^{\alpha\to\gamma}_{Fe}}{RT} - \frac{1}{2}\epsilon^\gamma_{CC} x^\gamma_C x^\gamma_C\right\} \exp\left\{-\frac{1}{2}\sum_{X=1}^N \epsilon^\gamma_{XX} x^\gamma_X x^\gamma_X\right\} \exp\left\{-x^\gamma_C \sum_{X=1}^N \epsilon^\gamma_{XC} x^\gamma_X\right\} \tag{6.75}$$

for iron.

At the Ae3 temperature, the composition of austenite is equivalent to the mean alloy composition. The independent variables are then T_{Ae3}, x^α_C and x^α_X ($X = 1, N$), and the set of $N + 2$ equations can be solved to yield values for these variables.

However, at temperatures below Ae3 (in the $\alpha + \gamma$ phase-field) it is not possible to define a unique tie-line for systems with three or more components. In this case, it is necessary to choose which of the infinite number of tie-lines is the one of interest. This could be the tie-line passing through the mean alloy composition (and thus defining the compositions of austenite and ferrite at equilibrium), or the tie-line which governs the interface compositions during diffusion-controlled growth under the assumption

of local equilibrium. As chapter seven of this dissertation shows, this tie-line is defined by considering Fick's laws and by acknowledging that the mass of each solute is conserved during growth.

For example, in the case of the tie-line passing through the mean alloy composition, we can specify

$$\frac{x_X^\gamma - \bar{x}_X}{x_X^\gamma - x_X^\alpha} = \frac{x_C^\gamma - \bar{x}_C}{x_C^\gamma - x_C^\alpha} \qquad \text{for } X = 1, N \tag{6.76}$$

This gives $2N + 2$ equations which can be solved to yield the $2N + 2$ compositional variables x_C^γ, x_C^α, x_X^γ ($X = 1, N$) and x_X^α ($X = 1, N$).

6.4.2 Paraequilibrium

The paraequilibrium mode of transformation refers to the state of constrained equilibrium between austenite and ferrite, in which the two phases have the same substitutional to iron atom ratios. Subject to this constraint, carbon comes to local equilibrium at the α/γ interface. This mode of transformation has been envisaged for phase changes which occur so rapidly that the slower diffusers (here the substitutional solutes) do not have the mobility to redistribute between the two phases in the time available for transformation.

The constrained equilibrium between austenite and ferrite is represented by

$$x_{Fe}^\gamma(\mu_{Fe}^\gamma - \mu_{Fe}^\alpha) + \sum_{X=1}^{N} x_X^\gamma(\mu_X^\gamma - \mu_X^\alpha) = 0 \tag{6.77}$$

where the chemical potentials are evaluated using equations 6.52–6.54 and 6.37–6.39. The condition of equipotential of carbon in austenite and ferrite, i.e. $\mu_C^\gamma = \mu_C^\alpha$, given by equation 6.73, applies once again. Finally, the non-redistribution of substitutional solutes is represented mathematically by

$$\frac{x_X^\gamma}{x_{Fe}^\gamma} = \frac{x_X^\alpha}{x_{Fe}^\alpha} = \frac{\bar{x}_X}{\bar{x}_{Fe}} \qquad \text{for } X = 1, N \tag{6.78}$$

As before this gives $2N + 2$ equations which can be solved to yield the $2N + 2$ compositional variables x_C^γ, x_C^α, x_X^γ ($X = 1, N$) and x_X^α ($X = 1, N$). It should be noted that as a consequence of the paraequilibrium constraint, the choice of tie-line is restricted to just one.

6.4.3 Composition of the Ferrite Nucleus, Using the Parallel Tangent Construction

When applying classical nucleation theory, it is often necessary to calculate the composition and driving force ΔG^{nuc} associated with the formation of a critical nucleus of ferrite, at finite undercoolings below Ae3. Because of capillarity, the composition of this nucleus differs from the equilibrium composition of ferrite, i.e. that given by drawing a tangent to the ferrite & austenite free energy curves. Assuming that the partial molar volumes of iron, carbon and substitutionals are equal, the parallel tangent construction takes account of this effect. The driving force calculated in this way (ΔG_{max}^{nuc}) corresponds to the *maximum* value of ΔG^{nuc}. Enomoto & Aaronson [128] have taken account of the partial molar volumes rigorously; they found that ΔG^{nuc} differed only very slightly from ΔG_{max}^{nuc}. The parallel tangent construction is therefore used throughout this work.

Assuming that substitutional solutes as well as carbon can partition during nucleation, the composition of the ferrite nucleus is given by solving the equations

$$\mu_{Fe}^\gamma - \mu_{Fe}^{\alpha,nuc} = \mu_C^\gamma - \mu_C^{\alpha,nuc} = \mu_X^\gamma - \mu_X^{\alpha,nuc} \qquad \text{for } X = 1, N \tag{6.79}$$

where $\mu_{Fe}^{\alpha,nuc}$, $\mu_C^{\alpha,nuc}$ and $\mu_X^{\alpha,nuc}$ refer to the chemical potentials of iron, carbon and substitutional X in the ferrite nucleus. This gives $N + 1$ equations which can be solved to yield the $N + 1$ unknown compositions, $x_C^{\alpha,nuc}$ and $x_X^{\alpha,nuc}$ ($X = 1, N$), the nucleus mole fractions of carbon and substitutional solutes respectively.

If the substitutional solutes are assumed not to partition during nucleation, i.e. nucleation is assumed to occur under paraequilibrium conditions, the nucleus composition is given by solving the equations

$$x_{Fe}^{\gamma}(\mu_{Fe}^{\gamma} - \mu_{Fe}^{\alpha,nuc}) + \sum_{X=1}^{N} x_{X}^{\gamma}(\mu_{X}^{\gamma} - \mu_{X}^{\alpha,nuc}) = x_{C}^{\gamma}(\mu_{C}^{\gamma} - \mu_{C}^{\alpha,nuc}) \tag{6.80}$$

together with equation 6.78. This again gives $N+1$ equations which can be used to calculate the $N+1$ independent nucleus mole fractions.

For both the equilibrium as well as the paraequilibrium mode of transformation, the driving force associated with the formation of the critical nucleus is given by

$$\Delta G_{max} = x_{Fe}^{\gamma}(\mu_{Fe}^{\alpha,nuc} - \mu_{Fe}^{\gamma}) + x_{C}^{\gamma}(\mu_{C}^{\alpha,nuc} - \mu_{C}^{\gamma}) + \sum_{X=1}^{N} x_{X}^{\gamma}(\mu_{X}^{\alpha,nuc} - \mu_{X}^{\gamma}) \tag{6.81}$$

Equations 6.73–6.78 are non-linear in the x's, and therefore have to be solved iteratively. In the present work, the method developed by Hashiguchi et al. [124] is adopted, with additional iterations to improve the accuracy with which the compositions are determined. The errors which arise during the location of the solutions are likely to be small. More serious inaccuracies arise at high solute concentrations, when substitutional elements interact with each other, and when the first-order Wagner formalism breaks down.

6.5 Testing of the Model

6.5.1 Ae3 Temperatures

As has been carried out in the past [123,124,127,129] the model developed in this paper is tested against a large number of experimental data for the Ae3 temperatures of commercial alloys. Here, the experimental data points are taken from the Atlas of Isothermal Transformation Diagrams published by ASM [130], a similar volume published by BISRA [131] and the experimental data published by Grange [132].

Figures 6.12–6.14 compare the experimental and predicted Ae3 temperatures. As noticed before [123,124,127,129], the observed Ae3 temperatures tend to be somewhat larger than the calculated values. It is possible that this is due to the fact that much of the data is obtained using dilatometry, rather than metallographic assessment. This observation is supported by the somewhat better agreement obtained from Grange's data, and that in the case of data extracted from the BISRA Atlas, the calculated Ae3 temperatures are, without exception, higher than the temperature to which the ferrite start C-curve tends.

6.5.2 Phase Boundaries

The model developed here has been tested against calculations performed with the National Physical Laboratory's MTDATA database for metallurgical thermochemistry [133]. For ternary alloys of composition Fe-0.20%C-1.00%X (wt%) and Fe-0.40%C-1.00%X (wt%) (where X represents Mn, Si, Cr, Ni, Mo & V, the elements for which the author can currently perform calculations with MTDATA) the compositions of ferrite and austenite governed by the tie-line passing through the mean alloy composition, have been calculated between 600°C and the respective Ae3 temperature. This has been done using the model developed here, as well as using MTDATA.

A reasonable level of agreement between the two models has been found; figures 6.15–6.19 illustrate the level of agreement found. It should be stressed that the compositions of carbon and X in austenite and ferrite calculated here correspond to the compositions at the very end of transformation from austenite to ferrite. As will be seen in chapter seven of this work, the tie-line governing the interface compositions during reconstructive growth of ferrite from austenite does not in general pass through the mean alloy

composition. In this case, the thermodynamic and kinetic theory are *coupled*, and the choice of tie-line becomes important in determining how quickly the interface can advance.

6.6 Summary

A thermodynamic model capable of describing the system Fe-C-X_1-X_2-X_3 *etc.* in the iron-rich corner of the multicomponent phase diagram has been developed. The model can cope with significant additions of Mn, Si, Ni, Cr, Mo, Cu, V, Nb, W and Co. The phase diagram of the Fe–C binary system is calculated using the quasichemical model of McLellan & Dunn [101], the parameters for which have been derived by Shiflet *et al.* [98] and Bhadeshia [104]. Such quasichemical models allow extrapolation of the $\gamma/(\gamma + \alpha)$ and $\alpha/(\gamma + \alpha)$ phase boundaries with a reasonable degree of confidence.

To account for the deviation from the Fe–C diagram caused by the addition of substitutional alloying elements, the Wagner interaction parameter formalism is chosen, because this allows the extension to a full multicomponent system to be achieved easily. There is also the advantage that the Wagner interaction parameters relate readily to the cross-terms in the diffusivity matrix, provided that the solution is dilute. When considering the kinetics of the diffusion-controlled decomposition of austenite, as in chapter seven of this dissertation, this fact must be exploited. Expressions for the Wagner interaction parameters [108,109,110] have been derived from the Hillert-Staffanson sub-regular solution model [92,93], the parameters for which are (mostly) taken from a recent tabulation by Uhrenius [94].

The model has been tested against a large amount of experimental data, including the the National Physical Laboratory's database [133]. The program allows the calculation of equilibrium and paraequilibrium phase boundaries, Gibbs free energy differences between ferrite & austenite during nucleation, and Ae3, Ae3′ temperatures. This work provides a basis for an attempt to model the kinetics of the reconstructive decomposition of austenite to ferrite, and this is now attempted in chapter seven of this dissertation.

REFERENCES

88. H.I. Aaronson, C. Laird and K.R. Kinsman, Phase Transformations, p.313, ASM, Metals Park, Ohio (1970).

89. R.W.K. Honeycombe, Metall. Trans., **7A**, 915–936, (1976).

90. R.T. De Hoff, Proc. Int. Conf. on Solid→Solid Phase Transformations, 503–520, TMS–AIME, Warrendale, Pennsylvania, (1981).

91. H.K.D.H. Bhadeshia, Progress in Materials Science, **29**, 321–386, (1985).

92. M. Hillert and L.-I. Staffanson, Acta Chem. Scand., **24**, 3618–3626, (1970).

93. M. Hillert and M. Waldenstrom, Metall. Trans., **8A**, 5–13, (1977).

94. B. Uhrenius, in 'Hardenability Concepts with Applications to Steel', ed., D.V. Doane and J.S Kirkaldy, AIME, 28–81, (1978).

95. M. Hillert, in 'Hardenability Concepts with Applications to Steel', ed., D.V. Doane and J.S Kirkaldy, AIME, 5–27, (1978).

96. G.R. Purdy, D.H. Weichert and J.S. Kirkaldy, TMS-AIME, **230**, 1025–1034, (1964).

97. J.W. Christian, 'The Theory of Phase Transformations In Metals and Alloys', Part I, 2nd Edition, Pergamon Press, (1975).

98. G.J. Shiflet, J.R. Bradley and H.I. Aaronson, Metall. Trans., **7A**, 1347–1364, (1978).

99. J.R. Lacher, Proc. Cambridge Phil. Soc., **33**, 518–523, (1937).

100. R.H. Fowler and E.A. Guggenheim, Statistical Thermodynamics, Cambridge University Press, New York (1939).

101. R.B. McLellan and W.W. Dunn, J. Phys. Chem. Solids, **30**, 2631–2637, (1969).

102. S. Ban-ya, J.F. Elliot and J. Chipman, TMS-AIME, **245**, 1199–1206, (1969).

103. S. Ban-ya, J.F. Elliot and J. Chipman, Metall. Trans., **1**, 1313–1320, (1970).

104. H.K.D.H. Bhadeshia, Metal Science, **16**, 167–169, (1982).

105. J.A. Lobo and G.H. Geiger, Metall. Trans., **7A**, 1347–1364, (1976).

106. Y. Mou and H.I. Aaronson, Acta Metall., **37**, 757–765, (1989).

107. H.K.D.H. Bhadeshia, Metal Science, **14**, 230–232, (1980).

108. C.H.P. Lupis, 'Chemical Thermodynamics of Materials', Elsevier Science Publishing Co., New York, (1983).

109. C. Wagner, 'Thermodynamics of Alloys', Addison-Wesley, Reading MA, 47–53, (1952).

110. J. Chipman, J.I.S.I., **180**, 97–106, (1955).

111. R.L. Orr and J, Chipman, TMS–AIME, **239**, 630–633, (1967).

112. L. Kaufman, E.V. Clougherty and R.J. Weiss, Acta Metall., **11**, 323–335, (1963).

113. M. Hillert and M. Jarl, CALPHAD, **2**, 227–238, (1978).

114. J. Agren, Metall. Trans., **10A**, 1847–2065, (1979).

115. L. Kaufman, H. Bernstein, in 'Computer Calculation of Phase Diagrams; with special reference to Refractory Metals', (Refractory Materials, Vol. 4, 1970), Academic Press, New York.

116. H.K.D.H. Bhadeshia, Materials Science and Technology, **1**, 497–504, (1985).

117. J.S. Kirkaldy and E.A. Baganis, Metall. Trans., **9A**, 495–501, (1978).

118. M. Hillert, T. Wada and H. Wada, J.I.S.I., **205**, 539–546, (1967).

119. H. Harvig, G. Kirchner and M. Hillert, Metall. Trans., **3**, 329–332, (1972).

120. H. Ohtani, M. Hasebe and T. Nishizawa, CALPHAD, **13**, 183–204, (1989).

121. C. Zener, Trans. AIME., **203**, 619–630, (1955).

122. R.J. Weiss and K.J. Tauer, Phys. Rev., **102**, 1490–1495, (1956).

123. C. Zener, Trans. AIME., **167**, 513–534, (1946).

124. K. Hashiguchi, J.S. Kirkaldy, T. Fukuzumi and V. Pavasker, CALPHAD, **8**, 173–186, (1984).

125. L.S. Darken, TMS–AIME, **239**, 90–96, (1967).

126. A.D. Pelton and C.W. Bale, Metall. Trans., **17A**, 1211–1215, (1986).

127. J.S. Kirkaldy, B.A. Thomson and E.A. Baganis, in 'Hardenability Concepts with Applications to Steel', ed., D.V. Doane and J.S. Kirkaldy, AIME, 82–125, (1978).

128. M. Enomoto and H.I. Aaronson, Metall. Trans., **17A**, 1381–1384, (1986).

129. A.A.B. Sugden and H.K.D.H. Bhadeshia, Materials Science and Technology, **5**, 977–984, (1989).

130. Atlas of Isothermal Transformation and Cooling Transformation Diagrams, ASM, Metals Park, Ohio, USA, (1977).

131. BISRA Atlas of Isothermal Transformation Diagrams of BS En Steels, Special Report No.56, 2nd Edition, The Iron and Steel Institute, London, (1956).

132. R.A. Grange, Metal Progress, **70**, 73–75, (1961).

133. MTDATA, the National Physical Laboratory metallurgical and thermochemical databank, Teddington, Middlesex.
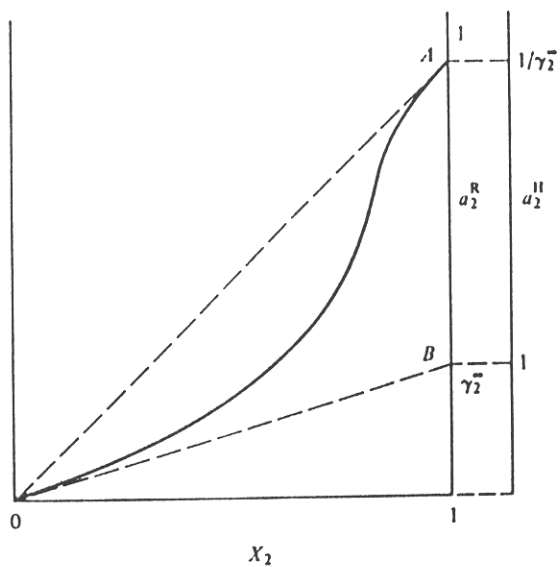
Figure 6.1: The Henrian standard state is defined as the hypothetical state obtained by extrapolating the Henrian behaviour of 2 (in this work carbon and substitutional solutes) to the concentration where 2 is pure. Thus, Henry's law is assumed to apply not only at infinite dilution, but across the composition range to the point where $X_2 = 1$. The activity of component 2 is unity at $X_2 = 1$, and the activity coefficient of 2 is unity at infinite dilution of solvent (iron). After Lupis [108].
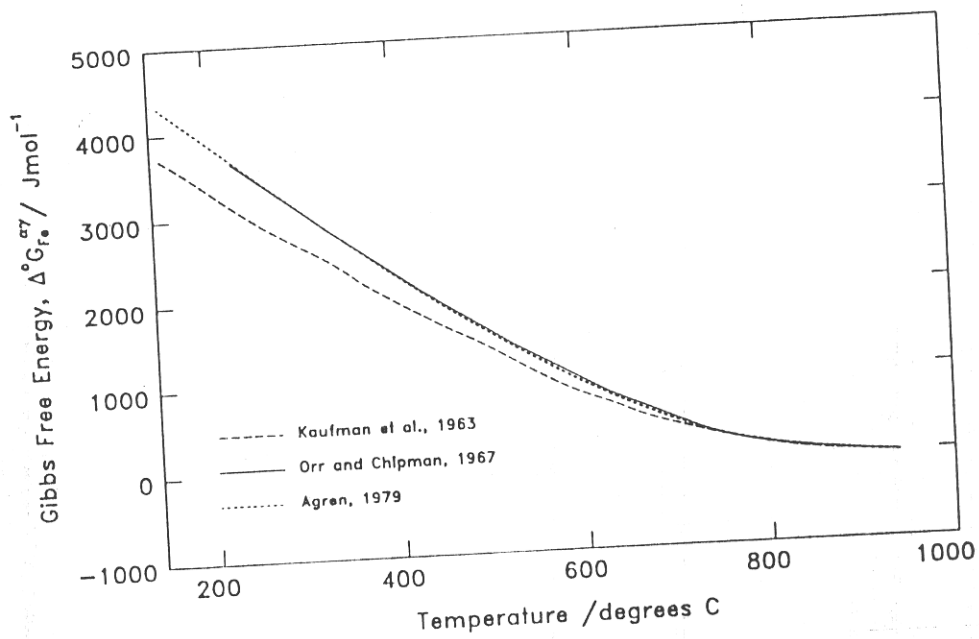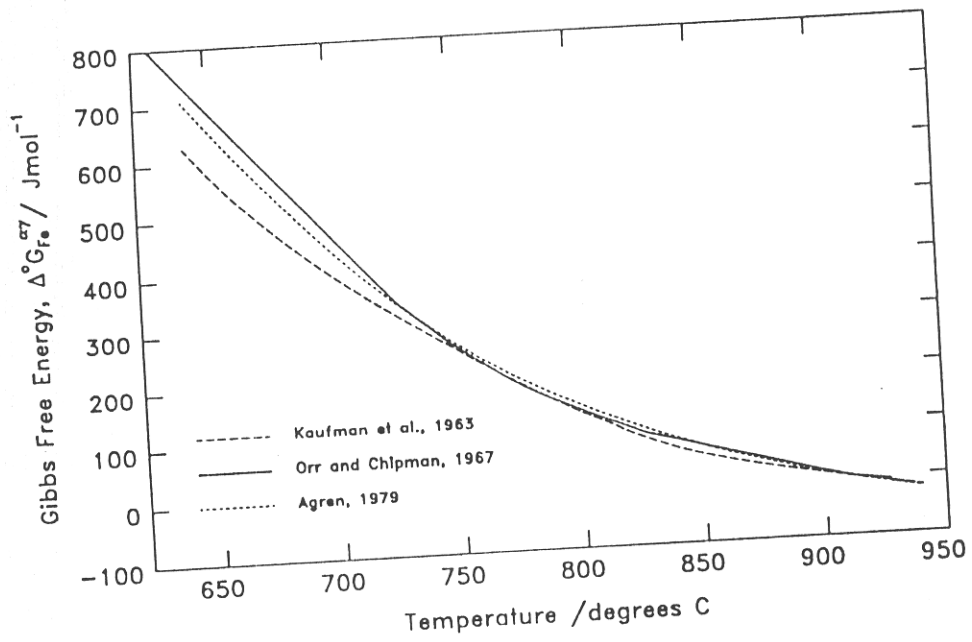
Figures 6.2 & 6.3: The difference in Gibbs free energy of iron between ferrite and austenite, $\Delta^0 G_{Fe}^{\alpha \to \gamma}$, as a function of temperature.
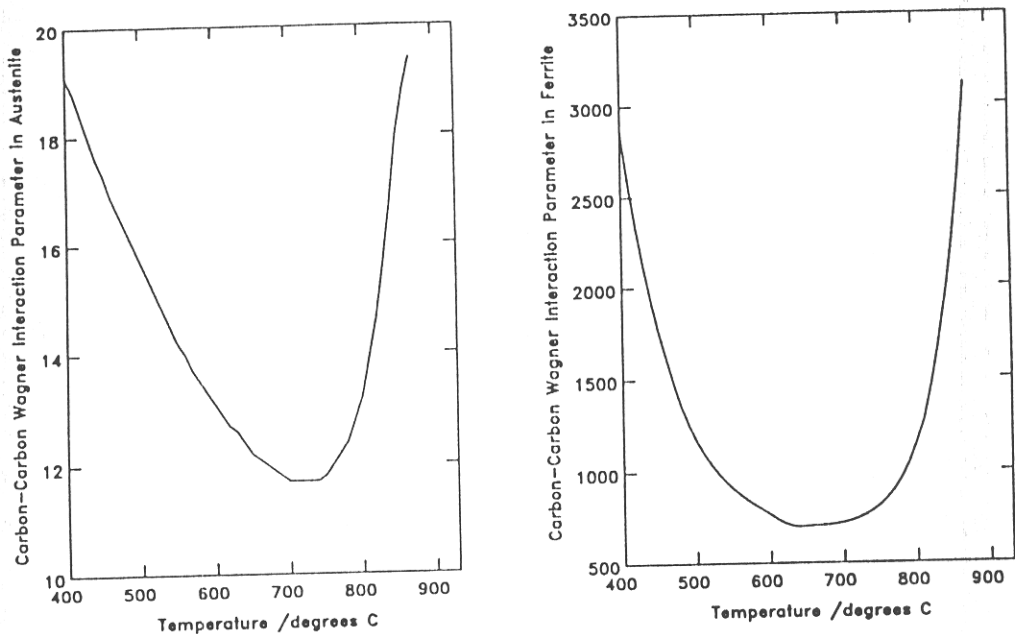
Figure 6.4: The carbon–carbon interaction parameters calculated from the quasichemical model of McLellan & Dunn [101].
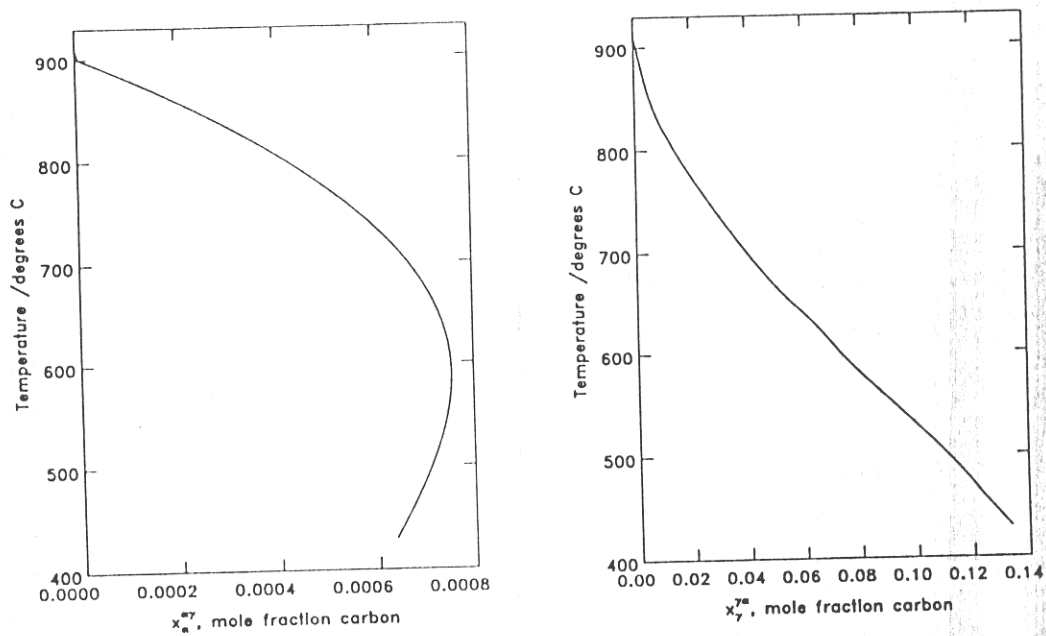
Figure 6.5: The binary Fe–C phase diagram, calculated using the quasichemical model [101], extrapolated past the equilibrium eutectoid temperature.
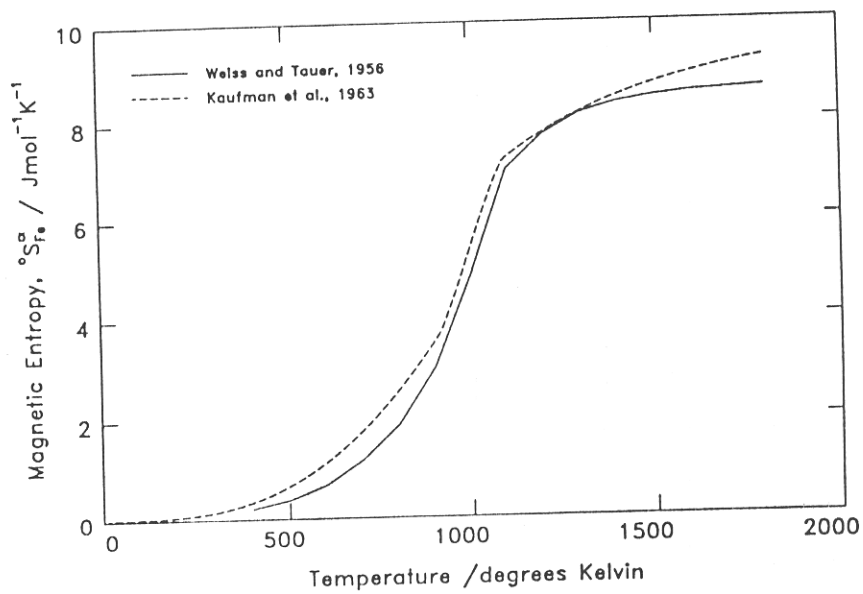
Figure 6.6: The magnetic contribution to the Gibbs free energy change of pure iron, $(^0S_{Fe}^{\alpha})_{Mag}$, calculated according to Weiss & Tauer [122] and Kaufman *et al.* [112].
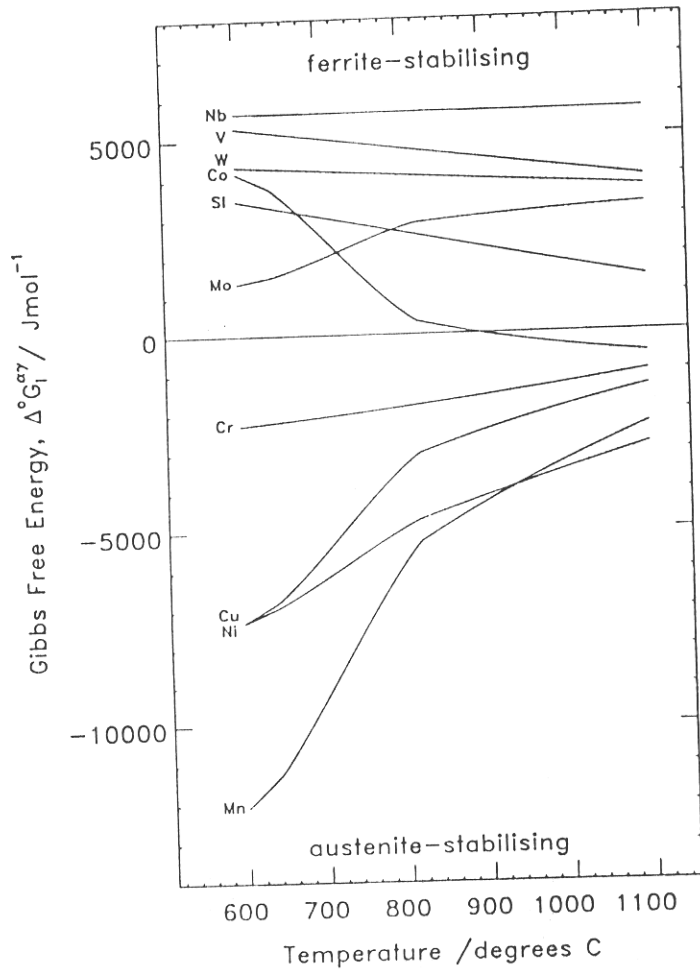
Figure 6.7: The free energy change for the transfer of one mole of solute X from ferrite to austenite, $\Delta^0 G_X^{\alpha \to \gamma}$, as a function of temperature. The elements divide into $\gamma-$ and $\alpha-$stabilisers.

AUSTENITE, TEMPERATURE = 1000 K
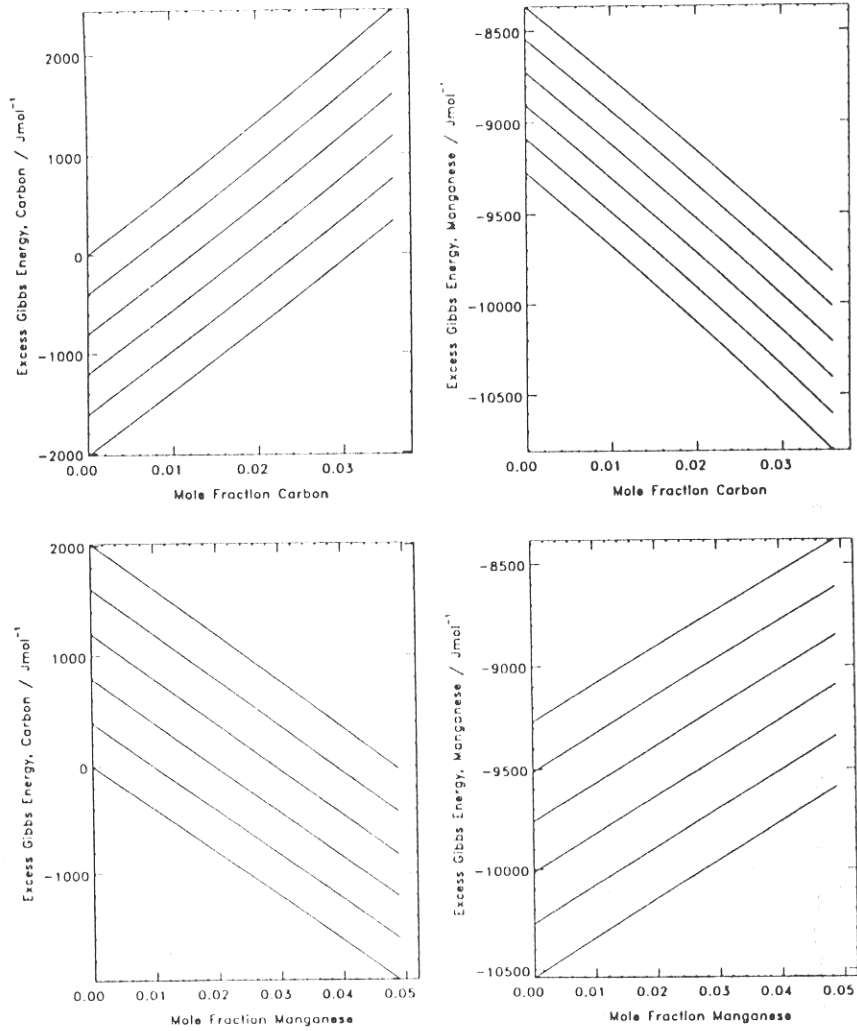
Figure 6.8: The rate of change of excess Gibbs free energy of manganese, with carbon and manganese mole fractions, in austenite at 1000 K. Carbon additions are in the range 0.000–0.036, and manganese in the range 0.00–0.05.

FERRITE, TEMPERATURE = 1000 K
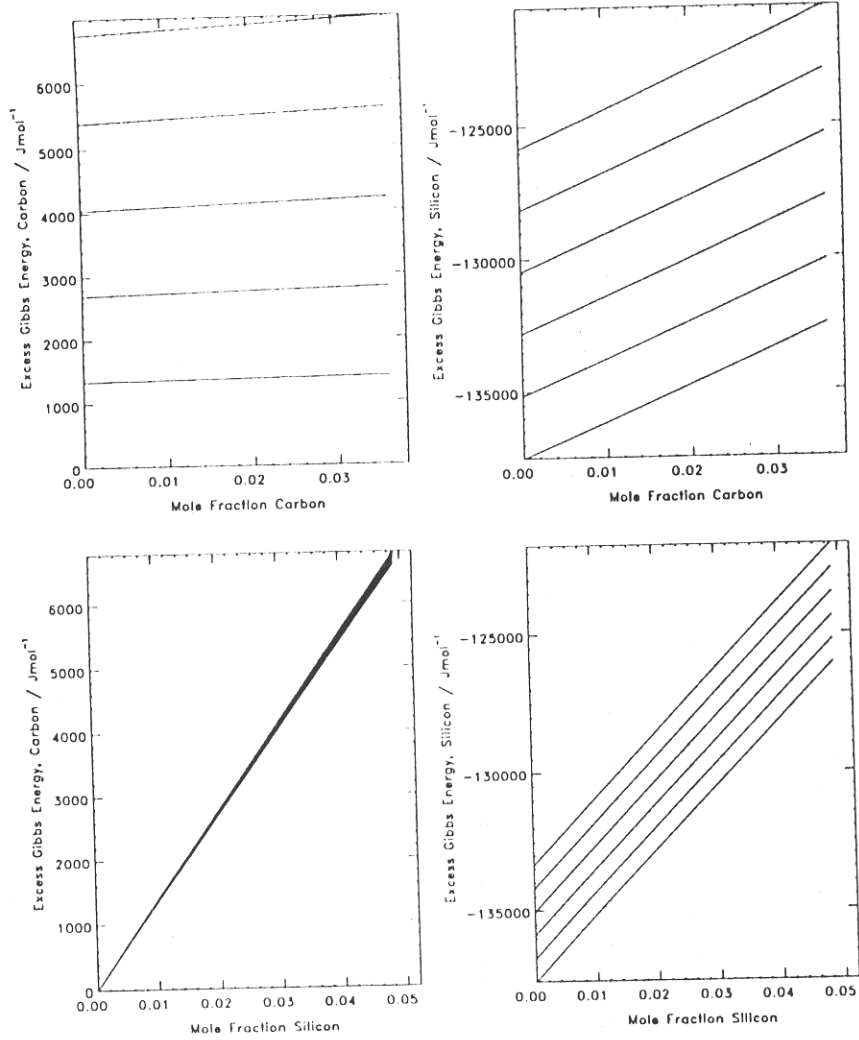
Figure 6.9: The rate of change of excess Gibbs free energy of silicon, with carbon and silicon mole fractions, in ferrite at 1000 K. Carbon additions are in the range 0.000–0.036, and silicon in the range 0.00–0.05.

FERRITE, TEMPERATURE = 1000 K
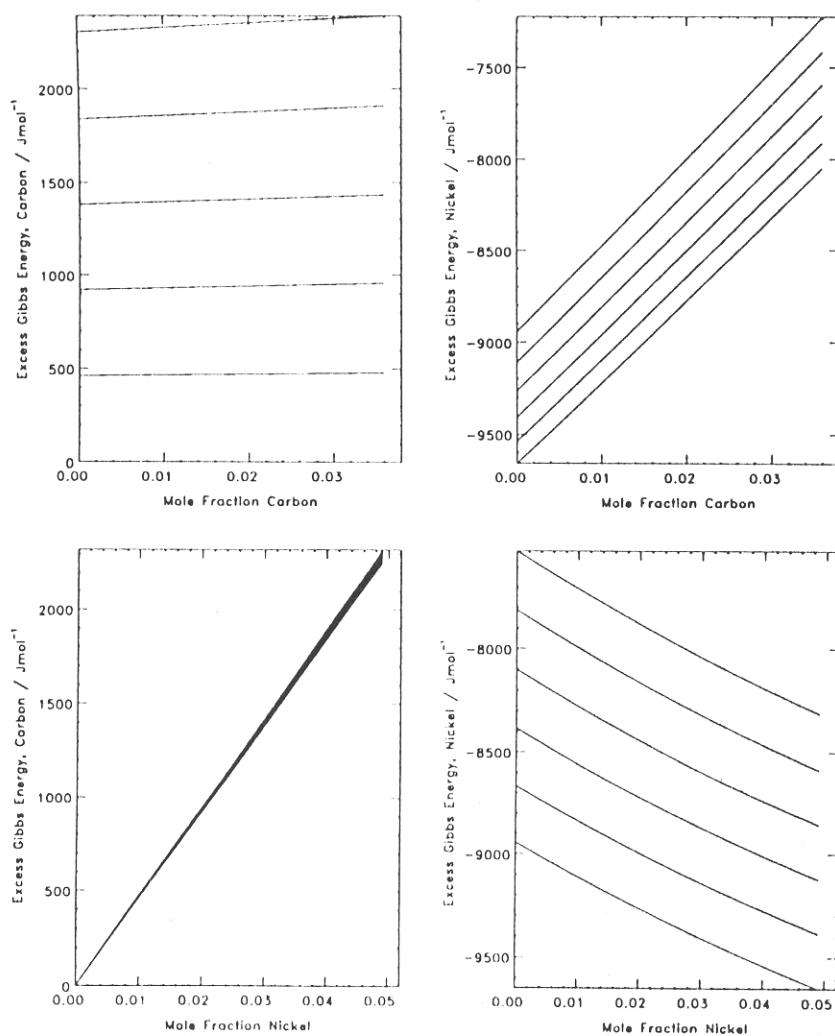
Figure 6.10: The rate of change of excess Gibbs free energy of nickel, with carbon and nickel mole fractions, in ferrite at 1000 K. Carbon additions are in the range 0.000–0.036, and nickel in the range 0.00–0.05.

FERRITE, TEMPERATURE = 1000 K
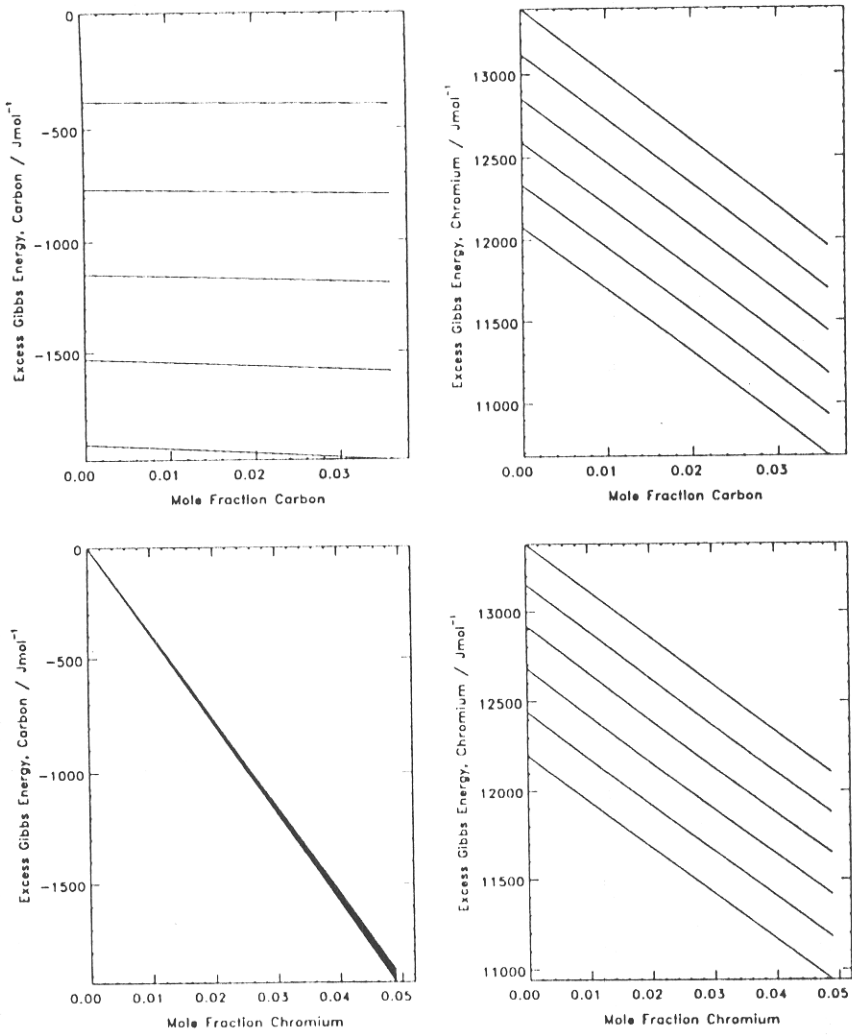
Figure 6.11: The rate of change of excess Gibbs free energy of chromium with carbon and chromium mole fractions, in ferrite at 1000 K. Carbon additions are in the range 0.000–0.036, and chromium in the range 0.00–0.05.
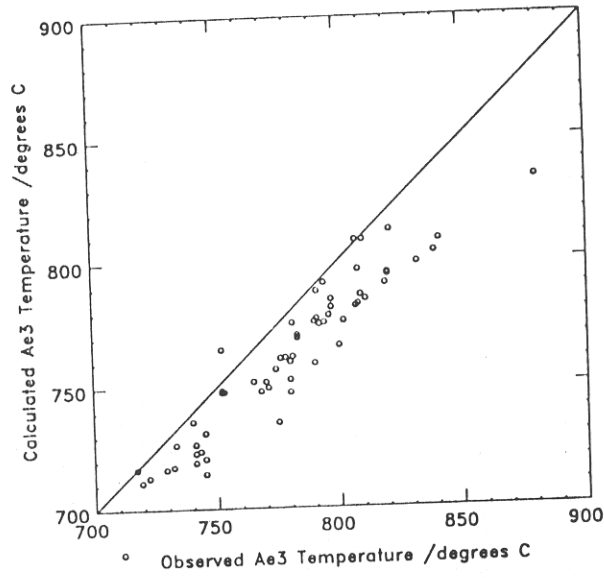
Figure 6.12: Observed and calculated Ae3 temperatures for steels in the ASM steel atlas [130].
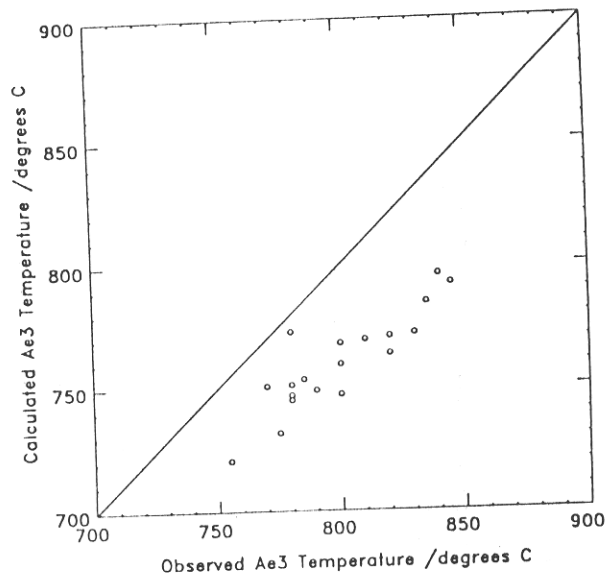
Figure 6.13: Observed and calculated Ae3 temperatures for steels in the BISRA atlas [131].
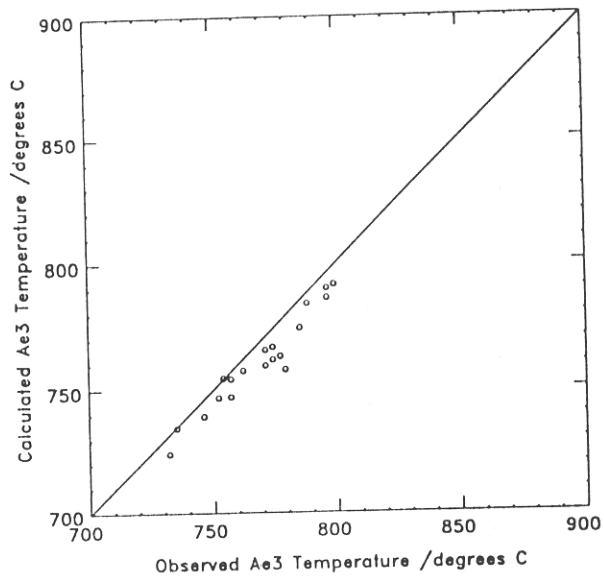
Figure 6.14: Observed and calculated Ae3 temperatures, data from Grange [132].
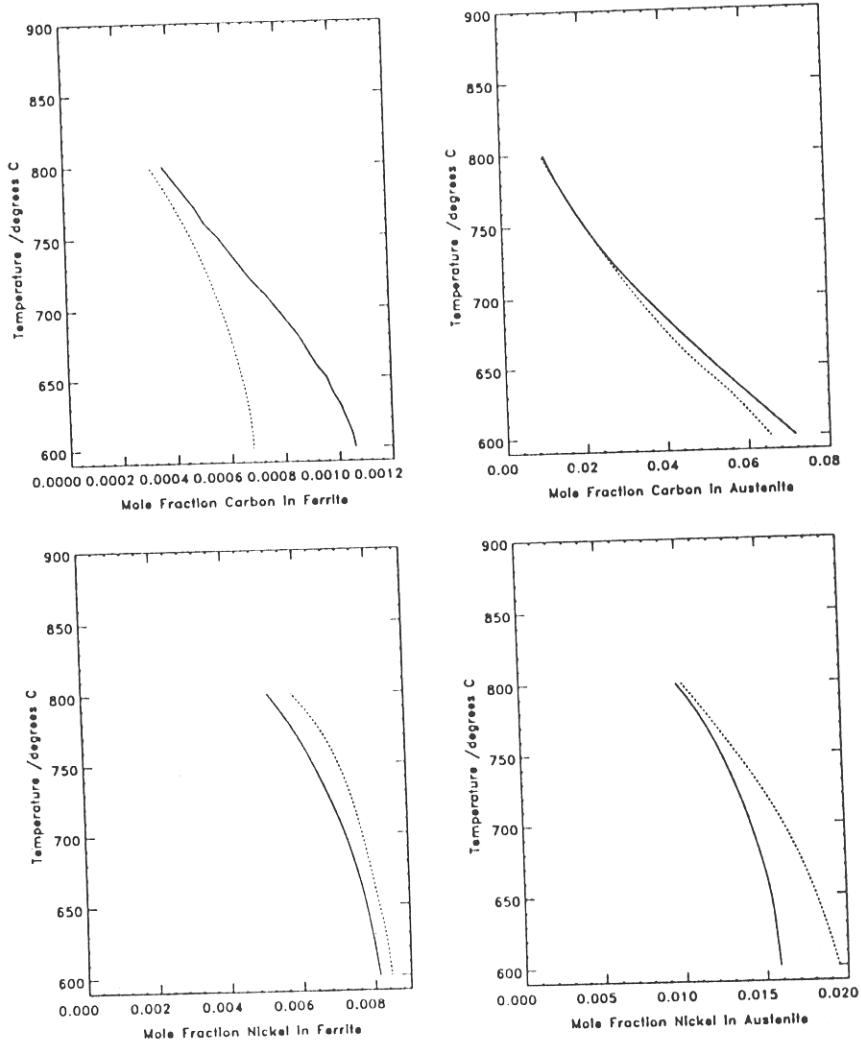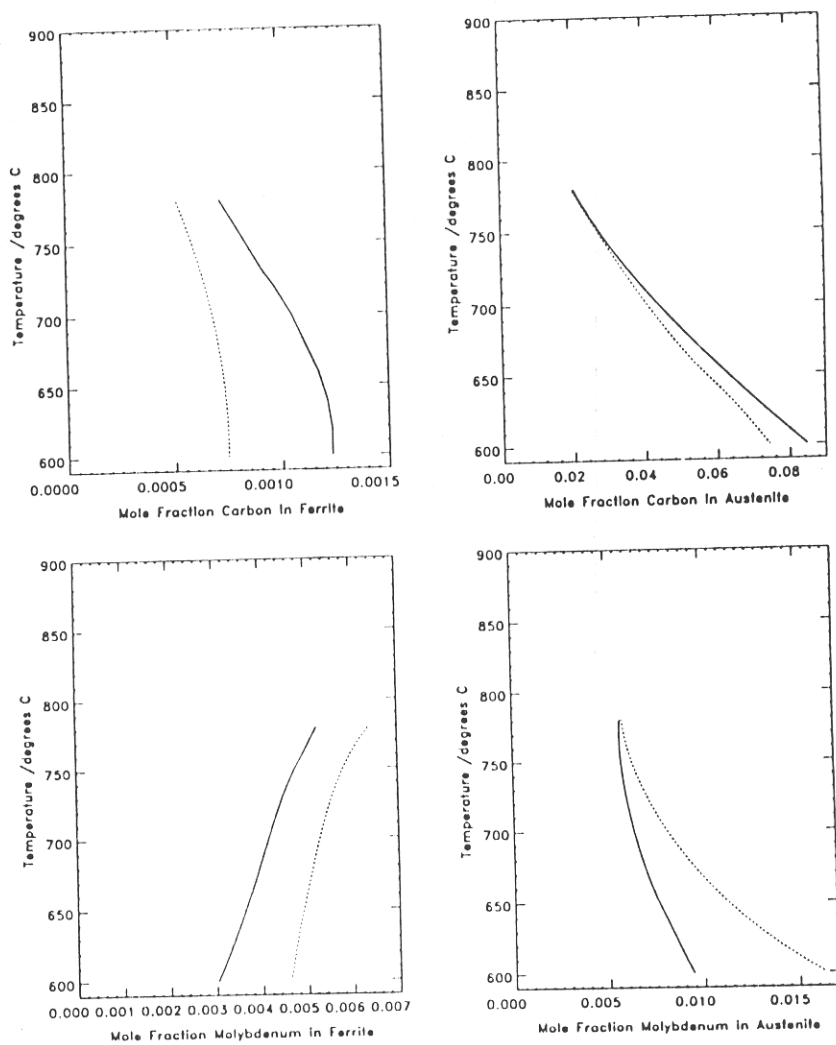
Fe-1.0Mn-0.2C weight per cent
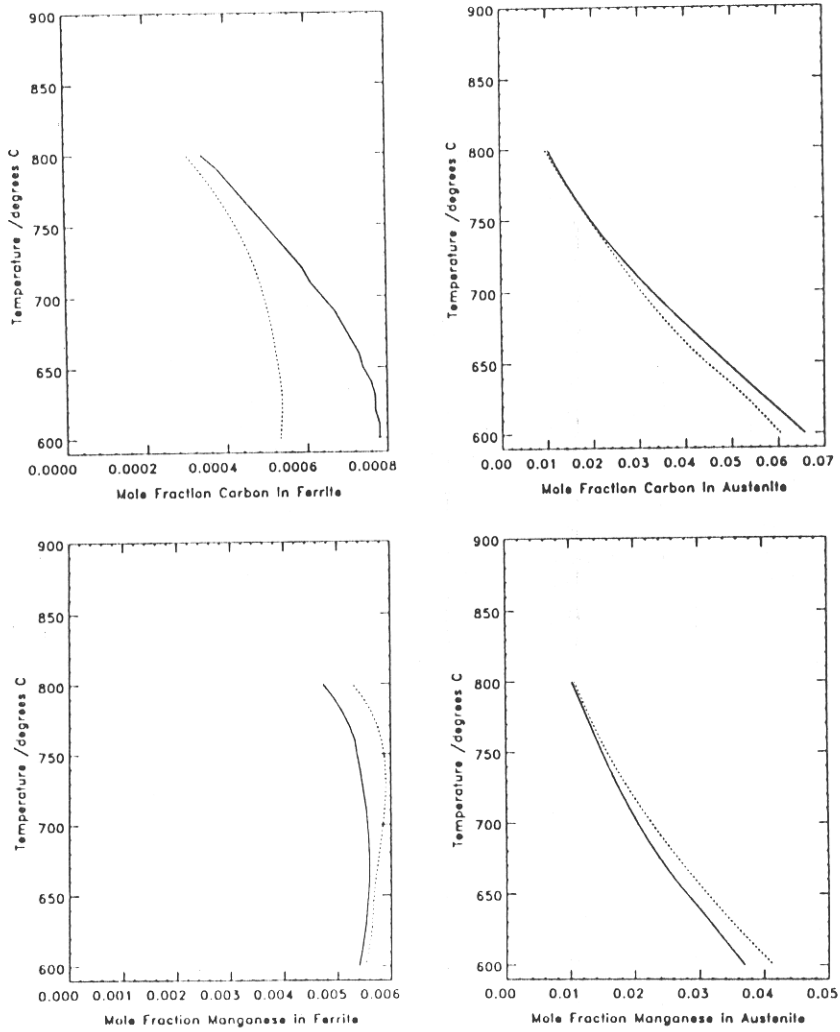
Figure 6.15: Phase boundaries for the Fe–Mn–C ternary system. The phase boundaries are constructed from the tie-line passing through the mean alloy composition.
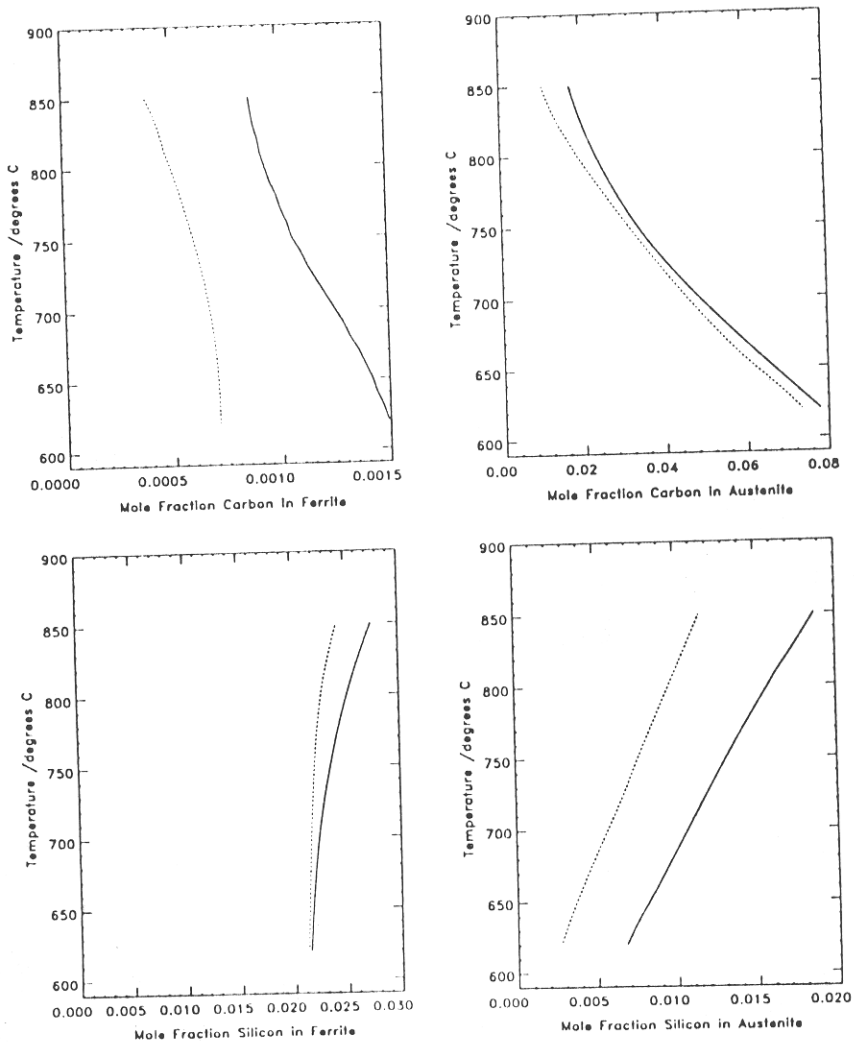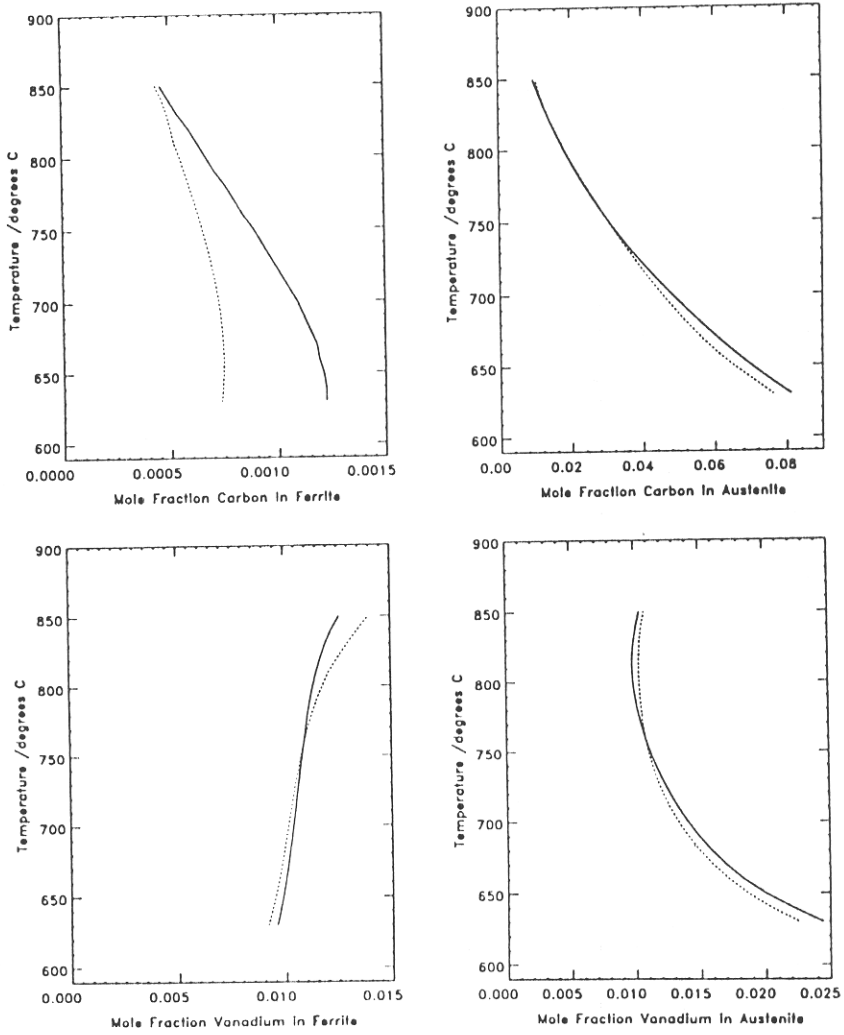
Figure 6.16: Phase boundaries for the Fe–Si–C ternary system. The phase boundaries are constructed from the tie-line passing through the mean alloy composition.

Fe−1.0Ni−0.2C weight per cent

Figure 6.17: Phase boundaries for the Fe–Ni–C ternary system. The phase boundaries are constructed from the tie-line passing through the mean alloy composition.

Fe-1.0Mo-0.4C weight per cent

Figure 6.18: Phase boundaries for the Fe–Mo–C ternary system. The phase boundaries are constructed from the tie-line passing through the mean alloy composition.

Fe−1.0V−0.2C weight per cent

Figure 6.19: Phase boundaries for the Fe–V–C ternary system. The phase boundaries are constructed from the tie-line passing through the mean alloy composition.

R	gas constant
S_V	austenite grain boundary area per unit volume
t	time
T	absolute temperature
V	total volume of system
V_α	volume of ferrite
V_α^e	extended volume of ferrite
W	number of nearest-neighbour octahedral interstitial sites surrounding a given octahedral interstice in γ
x_i	mole fraction of component i
$\overline{x}_i$	average mole fraction of i in alloy, also taken to be the concentration in the matrix at infinity
$x_i^{\gamma\alpha}$	mole fraction of i in γ which is in equilibrium with α
$x_i^{\alpha\gamma}$	mole fraction of i in α which is in equilibrium with γ
y	distance of plane O_b from austenite grain boundary
z	co-ordinate normal to interface plane
Z	position of interface along co-ordinate z
α	allotriomorphic ferrite
α_1	parabolic thickening constant for one-dimensional growth
γ	austenite
Γ_m	activity coefficient arising in absolute reaction rate theory
ζ	extent of reaction; volume fraction of ferrite, divided by the equilibrium volume
η	function of carbon concentration in γ (equation 7.15); also the aspect ratio of ferrite allotriomorphs
θ	interstitial to substitutional atom ratio $x_1/(1-x_1)$; also the ratio y/q
λ	spacing of $\{002\}_\gamma$ planes
ϕ	ensemble average interstitial site exclusion parameter
σ	interfacial energy per unit area
τ	incubation time for allotriomorph
ϕ	equilibrium volume fraction of ferrite
ω_γ	nearest-neighbour carbon-carbon interaction energy in austenite

7.1 Introduction

In the past thirty years or so, there has been remarkable progress in the collection and assessment of thermodynamic data for metals and alloys. Such work is near fruition, since there are now available a number of software systems [e.g. 133,134] capable of estimating the phase diagram as a function of pressure, temperature and the combined effect of numerous alloying elements, given a starting set of possible phases.

The ability to predict phase diagrams in this way is of obvious necessity in the design of new alloys. However, in many applications, metastable phases are present, often because they offer advantageous properties. Indeed, many large scale processes are now tending towards conditions of high supercooling, since it is in those circumstances that ultrafine-grained microstructures, phases with non-equilibrium solute-concentrations etc. can be produced. It follows that detailed understanding of the *kinetics* of phase transformations in metals and alloys is becoming of overriding importance in a co-ordinated search for alloys with improved, and novel properties.

This chapter represents an ambitious attempt to model the decomposition of austenite to allotrio-morphic ferrite, so that the part of the time-temperature-transformation (TTT) diagram which is due

7.3 Growth Kinetics

7.3.1 The Ternary Fe-C-X System

Kirkaldy [135] was the first to obtain general solutions to the multicomponent diffusion equations for planar, cylindrical and spherical precipitates. These equations have been applied [136–140] to the ternary system Fe-C-X and a reasonable level of agreement between theory and experiment has been found.

For the ternary system 0-1-2 in which 0 is the solvent (Fe), 1 is an interstitial solute (C) and 2 is a substitutional solute (X) the appropriate diffusion equations for planar growth are [137,138]

$$\frac{\partial c_1}{\partial t} = D_{11}\frac{\partial^2 c_1}{\partial z^2} + D_{12}\frac{\partial^2 c_2}{\partial z^2} \tag{7.1}$$

and

$$\frac{\partial c_2}{\partial t} = D_{21}\frac{\partial^2 c_1}{\partial z^2} + D_{22}\frac{\partial^2 c_2}{\partial z^2} \tag{7.2}$$

where D_{ij} are chemical diffusion coefficients (assumed concentration independent), the c_j are concentrations in moles per unit volume, z is the co-ordinate normal to the interface, along which ferrite is growing, and t refers to the time measured from the start of precipitate growth.

Because components 1 and 2 diffuse interstitially and by a vacancy mechanism respectively, it follows that

$$D_{11} \gg D_{22} \tag{7.3}$$

moreover, for dilute solutions, it has been demonstrated [144,145] that

$$D_{11} \gg D_{12} \quad \text{and} \quad D_{22} \gg D_{21} \tag{7.4}$$

The above conditions indicate that equations 7.1 & 7.2 can be approximated by

$$\frac{\partial c_1}{\partial t} = D_{11}\frac{\partial^2 c_1}{\partial z^2} + D_{12}\frac{\partial^2 c_2}{\partial z^2} \tag{7.5}$$

and

$$\frac{\partial c_2}{\partial t} = D_{22}\frac{\partial^2 c_2}{\partial z^2} \tag{7.6}$$

so that the distribution of carbon in austenite can be assumed to have a negligible effect on the flux of X ahead of the α/γ interface.

Coates [137,138] wrote down the solutions to equations 7.5 & 7.6 corresponding to the diffusion-controlled growth of ferrite, by setting $D_{21} = 0$ in Kirkaldy's general solutions [135] for the ternary system. The solutions can be written

$$c_1 = \bar{c}_1 + \left[\frac{D_{12}\left(c_2^{\gamma\alpha} - \bar{c}_2\right)}{D_{11} - D_{22}} + c_1^{\gamma\alpha} - \bar{c}_1\right]\frac{\text{erfc}\left\{z/2\sqrt{D_{11}t}\right\}}{\text{erfc}\left\{\alpha_1/2\sqrt{D_{11}}\right\}}$$
$$- \left[\frac{D_{12}\left(c_2^{\gamma\alpha} - \bar{c}_2\right)}{D_{11} - D_{22}}\right]\frac{\text{erfc}\left\{z/2\sqrt{D_{22}t}\right\}}{\text{erfc}\left\{\alpha_1/2\sqrt{D_{22}}\right\}} \tag{7.7}$$

$$c_2 = \bar{c}_2 + \left(c_2^{\gamma\alpha} - \bar{c}_2\right)\frac{\text{erfc}\left\{z/2\sqrt{D_{22}t}\right\}}{\text{erfc}\left\{\alpha_1/2\sqrt{D_{22}}\right\}} \tag{7.8}$$

where $\bar{c}_i$ and $c_i^{\gamma\alpha}$ are the concentrations of component i in the alloy or bulk austenite, and in the austenite at the austenite/ferrite interface respectively. The position of the interface, $z = Z$ is given by

$$Z = \alpha_1 t^{1/2} \tag{7.9}$$

where α_1 is known as the one-dimensional *parabolic rate constant* or *parabolic thickening constant*.

The interface mass conservation conditions for components 1 and 2 are respectively,

$$(c_1^{\alpha\gamma} - c_1^{\gamma\alpha}) \frac{\alpha_1}{2\sqrt{t}} = D_{11} \left.\frac{\partial c_1}{\partial z}\right|_{z=Z} + D_{12} \left.\frac{\partial c_2}{\partial z}\right|_{z=Z} \tag{7.10}$$

and

$$(c_2^{\alpha\gamma} - c_2^{\gamma\alpha}) \frac{\alpha_1}{2\sqrt{t}} = D_{22} \left.\frac{\partial c_2}{\partial z}\right|_{z=Z} \tag{7.11}$$

where $c_i^{\alpha\gamma}$ is the concentration of component i in ferrite at the interface. Differentiation of equations 7.7 & 7.8 with respect to z, combining with equation 7.9 and substitution into equations 7.10 & 7.11 yields

$$f_1 = H_1\{D_{11}\} - \left[\frac{B_1 D_{12}}{D_{11} - D_{22}}\right][H_1\{D_{22}\} - H_1\{D_{11}\}] \tag{7.12a}$$

$$f_2 = H_1\{D_{22}\} \tag{7.12b}$$

where

$$H_1\{D_{ii}\} = \left(\frac{\pi}{4D_{ii}}\right)^{1/2} \text{erfc}\left\{\frac{\alpha_1}{2D_{ii}^{1/2}}\right\} \exp\left\{\frac{\alpha_1^2}{4D_{ii}}\right\} \tag{7.12c}$$

$$B_2 = \frac{c_2^{\gamma\alpha} - c_2^{\alpha\gamma}}{c_1^{\gamma\alpha} - c_1^{\alpha\gamma}} \tag{7.12d}$$

and f_1 and f_2 are fractional supersaturations, given by

$$f_i = \frac{\bar{c}_i - c_i^{\gamma\alpha}}{c_i^{\alpha\gamma} - c_i^{\gamma\alpha}} \qquad \text{for } i = 1, 2 \tag{7.13}$$

The term B_2 represents the slope of the α/γ interface tie-line, provided that on orthogonal ternary isotherms, components 2 and 1 are the ordinate and abscissa respectively.

Under the assumption of local equilibrium at the interface, only one of $c_1^{\gamma\alpha}$, $c_1^{\alpha\gamma}$, $c_2^{\gamma\alpha}$ and $c_2^{\alpha\gamma}$ are independent, since they are all linked by a tie-line of the equilibrium phase diagram. Equation 7.12 therefore contain two unknowns, and thus can be solved simultaneously to determine the growth velocity and the tie-line governing interface compositions during growth.

The above theory is based upon the assumption that the diffusion coefficients are concentration independent. Whilst this is probably a reasonable assumption for substitutional elements, the diffusivity of carbon is known to be strongly concentration dependent [146,147], and in diffusion-controlled reactions it is imperative to account for this effect [91]. Trivedi & Pound [148] have demonstrated that for most purposes, a weighted average diffusivity $\overline{D}_{11}$, given by

$$\overline{D}_{11}\{x_1, T\} = \int_{x_1^{\gamma\alpha}}^{\bar{x}_1} \frac{D_{11}\{x_1, T\}}{\bar{x}_1 - x_1^{\gamma\alpha}} \, dx_1 \tag{7.14}$$

can adequately represent the effective diffusivity of carbon in austenite. The term x_1 is the mole fraction of carbon in austenite, $x_1^{\gamma\alpha}$ is the mole fraction of carbon in austenite at the interface, and $\bar{x}_1$ is the mole fraction of carbon in austenite far from the interface. Even though this expression is strictly only valid for steady-state growth, Coates [140] has suggested that it should be a reasonable approximation for parabolic growth as well. Throughout this work, $\overline{D}_{11}$, is used in place of D_{11} in equation 7.12.

While there are many empirical expressions for $\overline{D}_{11}\{x_1, T\}$, the theoretical representation due to Siller and McLellan [149,150] respects the kinetic and thermodynamic behaviour of carbon in austenite. The model takes account of the concentration dependence of the activity of carbon in austenite, and the existence of a finite repulsive interaction between nearest neighbouring carbon atoms situated in octahedral sites [151]. The diffusivity is represented by

$$D_{11}\{x_1, T\} = (kT/h)(\exp\{-\Delta G^*/kT\})(\lambda^2/3\Gamma_m)\, \eta\{\theta\} \tag{7.15a}$$

CHAPTER SEVEN
The Reconstructive Austenite–Ferrite Transformation In Low-Alloy Steels
Part II– Kinetics

Nomenclature

a	interatomic spacing
a_i^α	activity of i in phase α
ASTM	ASTM grain size of austenite
B_i	constant referring to i (equations 7.12 & 7.23)
c_i	concentration of component i, moles per unit volume, also taken to be the concentration in the matrix at infinity
$\bar{c}_i$	average concentration of i in alloy, moles per unit volume
$c_i^{\gamma\alpha}$	concentration of i in γ which is in equilibrium with α, moles per unit volume
$c_i^{\alpha\gamma}$	concentration of i in α which is equilibrium with γ, moles per unit volume
D_{ik}	chemical or interdiffusion coefficient
$\overline{D}_{11}$	weighted average diffusivity of carbon in austenite
ϵ_{ik}	Wagner interaction parameter
f	function arising in nucleation and growth theory
f_i	fractional supersaturation of i
ΔG^*	molar Gibbs activation free energy
ΔG_c^{F}	critical activation free energy per atom for ferrite nucleation on faces
ΔG_c^{E}	critical activation free energy per atom for ferrite nucleation on edges
ΔG_c^{C}	critical activation free energy per atom for ferrite nucleation on corners
ΔG_V	free energy accompanying nucleation of ferrite, calculated using the parallel tangent construction
h	Planck's constant
H_1	function arising in diffusion-controlled growth theory (equations 7.12 & 7.24)
i	subscript identifying element
I_B	austenite grain boundary nucleation rate, per unit area per unit time
k	Boltzmann's constant
K_1^{F}	fraction of face sites supporting nucleation
K_1^{E}	fraction of edge sites supporting nucleation
K_1^{C}	fraction of corner sites supporting nucleation
K_2^{F}	shape factor for nucleation on faces
K_2^{E}	shape factor for nucleation on edges
K_2^{C}	shape factor for nucleation on corners
N_{F}	number of face sites per unit area of boundary supporting nucleation
N_{E}	number of edge sites per unit edge of boundary supporting nucleation
N_{C}	fraction of corner sites supporting nucleation
O_b	area of plane surface, parallel to a particular γ-grain boundary (equation 7.27)
O_B	total austenite grain boundary area
O_α	area of ferrite which intersects the area O_b
O_α^e	extended area of ferrite which intersects the area O_b
q	half-thickness of ferrite allotriomorph
Q	activation free energy per atom, for atoms crossing the austenite/ferrite nucleus interface

where

$$\eta\{\theta\}/a_1^\gamma = 1 + [W(1+\theta)/(1-(0.5W+1)\theta+(0.25W^2+0.5W)(1-\phi)\theta^2)]$$
$$+ (1/a_1^\gamma)(1+\theta)\frac{\partial a_1^\gamma}{\partial\theta} \tag{7.15b}$$

where k and h are the Boltzmann and Planck constants respectively, W is the number of octahedral interstices around a single such interstice (equal to 12 in austenite), ΔG^* is an activation free energy, Γ_m is an activity coefficient, λ is the distance between $\{002\}$ austenite planes and a_1^γ the activity of carbon in austenite. The term ϕ is given by $\phi = 1 - \exp\{-\omega_\gamma/kT\}$, ω_γ is the nearest neighbour carbon-carbon interaction energy, taken to be 8250 J/mole [152], and θ is the ratio of the number of carbon atoms to the total number of solvent atoms, given by $\theta = x_1/(1-x_1)$. Bhadeshia [157] found $\Delta G^*/k = 21230$ K and $\ln\{\Gamma_m/\lambda^2\} = 31.84$. Substitutional alloying elements alter the carbon-carbon interaction energy ω_γ, and therefore influence D_{11}. The method adopted here to account for this effect follows Bhadeshia [158].

The on-diagonal diffusion coefficients D_{ii} for substitutional elements can be evaluated from the compilation due to Fridberg, Torndahl and Hillert [159]. Provided the solution is dilute, the cross-terms D_{1i} can be expressed [145] in terms of the Wagner interaction parameters ϵ_{ij}:

$$D_{1i}/D_{11} = \frac{\epsilon_{1i}x_1}{1+\epsilon_{11}x_1} \tag{7.16}$$

The ratio D_{1i}/D_{11} is also concentration dependent, but numerical calculations [160] suggest that the use of a constant D_{1i}/D_{11}, evaluated at the interface composition $x_1^{\gamma\alpha}$ gives an adequate approximation to the problem [140].

7.3.2 Extension to Multicomponent System

The kinetic theory developed by Kirkaldy, Coates and others applies to ternary systems of the form Fe-C-X, and testing of the theory has always been carried out against 'model' ternary alloys. There is obviously a great desire to develop such kinetic theory for multicomponent steels, because it is these which are important both practically and commercially. The above analysis will now be extended to multicomponent steels, in which a number of substitutional components have been added to the Fe-C binary.

In order to do this it is necessary to adopt further assumptions, which make the problem of tie-line choice easier. In the following analysis, it is implicit that substitutional-substitutional terms D_{jk} $(j,k>1)$ in the diffusivity matrix are negligible. This amounts to the assumption that the flux of one substitutional element is not influenced by the presence of a (possibly large) concentration gradient of a second. Whilst this may be a major assumption, in many cases experimental measurements of the cross-terms in the diffusivity matrix have not been carried out.

By analogy with equations 7.5 & 7.6, the multicomponent diffusion equations considered here are

$$\frac{\partial c_1}{\partial t} = \sum_{i=1}^n D_{1i}\frac{\partial^2 c_i}{\partial z^2} \tag{7.17}$$

and

$$\frac{\partial c_i}{\partial t} = D_{ii}\frac{\partial^2 c_i}{\partial z^2} \qquad \text{for } i = 2, n \tag{7.18}$$

It is possible to demonstrate by substitution that the solutions to equations 7.17 & 7.18 are

$$c_1 = \bar{c}_1 + \left[\sum_{i=2}^n \left[\frac{D_{1i}(c_i^{\gamma\alpha}-\bar{c}_i)}{D_{11}-D_{ii}}\right] + c_1^{\gamma\alpha} - \bar{c}_1\right]\frac{\text{erfc}\{z/2\sqrt{D_{11}t}\}}{\text{erfc}\{\alpha_1/2\sqrt{D_{11}}\}}$$
$$- \sum_{i=2}^n \left[\frac{D_{1i}(c_i^{\gamma\alpha}-\bar{c}_i)}{D_{11}-D_{ii}}\right]\frac{\text{erfc}\{z/2\sqrt{D_{ii}t}\}}{\text{erfc}\{\alpha_1/2\sqrt{D_{ii}}\}} \tag{7.19}$$

and

170

$$c_i = \bar{c}_i + (c_i^{\gamma\alpha} - \bar{c}_i) \frac{\text{erfc}\left\{z/2\sqrt{D_{ii}t}\right\}}{\text{erfc}\left\{\alpha_1/2\sqrt{D_{ii}}\right\}} \qquad \text{for } i = 2, n \tag{7.20}$$

The mass conservation conditions are now

$$(c_1^{\alpha\gamma} - c_1^{\gamma\alpha})\frac{\alpha_1}{2\sqrt{t}} = D_{11}\frac{\partial c_1}{\partial z}\bigg|_{z=Z} + \sum_{i=2}^{n} D_{1i}\frac{\partial c_i}{\partial z}\bigg|_{z=Z} \tag{7.21}$$

and

$$(c_i^{\alpha\gamma} - c_i^{\gamma\alpha})\frac{\alpha_1}{2\sqrt{t}} = D_{ii}\frac{\partial c_i}{\partial z}\bigg|_{z=Z} \qquad \text{for } i = 2, n \tag{7.22}$$

where $c_i^{\alpha\gamma}$ is the concentration of component i in ferrite. By differentiating equations 7.19 & 7.20 with respect to z, combining with equation 7.9, and substituting into equations 7.21 & 7.22, the problem of tie-line choice can be expressed by

$$f_1 = H_1\{D_{11}\} - \sum_{i=2}^{n}\left[\frac{B_i D_{1i}}{D_{11} - D_{ii}}\right][H_1\{D_{ii}\} - H_1\{D_{11}\}] \tag{7.23a}$$

$$f_i = H_1\{D_{ii}\} \qquad \text{for } i = 2, n \tag{7.23b}$$

where

$$H_1\{D_{ii}\} = \left(\frac{\pi}{4D_{ii}}\right)^{1/2} \text{erfc}\left\{\frac{\alpha_1}{2D_{ii}^{1/2}}\right\} \exp\left\{\frac{\alpha_1^2}{4D_{ii}}\right\} \tag{7.23c}$$

and

$$B_i = \frac{c_i^{\gamma\alpha} - c_i^{\alpha\gamma}}{c_1^{\gamma\alpha} - c_1^{\alpha\gamma}} \qquad \text{for } i = 2, n \tag{7.23d}$$

In all the calculations which follow, the terms D_{1i} are evaluated according to equation 7.16. Although this equation was derived [144,145] for the ternary system, the assumptions implicit in writing equation 7.18 mean that no further assumptions are introduced if this equation is adopted.

7.3.3 Paraequilibrium

There are some difficulties with the above theory. With decreasing temperature, the local equilibrium assumption predicts [137] that the width of the solute 'spike' rapidly approaches the width of the interface itself. Even before the concentration gradient reaches such an unfeasable magnitude, it is not clear whether the substitutional atoms possess the atomic mobility necessary to partition ahead of the interface.

The concept of *paraequilibrium* has been introduced [161,162,163] to describe the kinetically constrained equilibrium in which, subject to the constraint that substitutional alloying elements do not redistribute during transformation, the carbon atoms at the interface are in local equilibrium. In this case, it is then implicit that the chemical potentials of iron and the substitutional elements change abruptly at the α/γ interface.

Under the assumption of paraequilibrium, there is only one possible tie-line for the interface to choose at constant temperature, because the ratio of the concentration of iron to that of each of the substitutionals is constant. It is therefore necessary to determine only $c_1^{\gamma\alpha}$ and $c_1^{\alpha\gamma}$ as a function of temperature. In this case, the kinetic theory is once again decoupled from the thermodynamic theory; the one-dimensional parabolic thickening rate can then be determined from the equation

$$f_1 = H_1\{\overline{D}_{11}\} \tag{7.24}$$

where $\overline{D}_{11}$ is the weighted average diffusivity, given by equation 7.14.

Finally it should be noted that the lack of bulk partitioning of substitutional alloying elements is insufficient to distinguish between the NP-LE and the paraequilibrium modes of transformation; the

substitutional alloying composition in austenite needs to be measured at the α/γ interface. As will be seen in the calculations which follow, the difference between the interface velocities calculated under the local equilibrium and paraequilibrium modes becomes very small at high undercoolings too.

7.4 Calculation of the Parabolic Thickening Rate

If the $\alpha/(\alpha+\gamma)$ and $\gamma/(\gamma+\alpha)$ surfaces are known as a function of alloy chemistry, the above equations can be solved to yield a value for the one-dimensional thickening constant α_1 for the multicomponent system. It is therefore necessary to couple the thermodynamic model to the kinetic model, because the multicomponent tie-lines need to be known. The calculations must necessarily involve iterative processes, since the equations are non-linear. In the following calculations, we make one further assumption, that

$$f_i = \frac{\bar{c}_i - c_i^{\gamma\alpha}}{c_i^{\alpha\gamma} - c_i^{\gamma\alpha}} \simeq \frac{\bar{x}_i - x_i^{\gamma\alpha}}{x_i^{\alpha\gamma} - x_i^{\gamma\alpha}} \qquad \text{for } i = 1, n \tag{7.25}$$

so that the supersaturations in equations 7.23 and 7.24 are calculated using concentrations expressed as mole fractions. This is equivalent to the assumption that the densities of austenite and ferrite are equal.

To illustrate the behaviour predicted by the theory, calculations have been carried out on three alloys, namely a ternary alloy Fe-0.33C-1.00Mn (wt%), as well as En16 & En19 [131], the last two being multicomponent steels. The rate constants calculated under the local equilibrium, and paraequilibrium assumptions are presented in figures 7.1, 7.2 and 7.3 respectively, together with the values of the supersaturations, as given by equation 7.13.

The predicted behaviour can be summarised as follows. Under P-LE, the supersaturations of the substitutional solutes increase with decreasing temperature, finally becoming very nearly equal to unity on entry into the NP-LE regime; at this temperature, α_1 increases dramatically. At lower temperatures, α_1 decreases in magnitude, reflecting the decreasing diffusivities. At temperatures below Ae3' α_1 calculated under the paraequilibrium assumption is larger than that calculated under local equilibrium. However, at temperatures within the NP-LE field, the difference is only marginal. This effect occurs because at low temperatures, the substitutional-substitutional diffusional interaction has little influence on the growth kinetics, because the carbon distribution becomes too steep to respond to the X distribution [138]. In this case, equation 7.23a approximates to

$$f_1 = H_1\{D_{11}\} - \sum_{i=2}^{n} \left[\frac{B_i D_{1i}}{D_{11} - D_{ii}}\right] [H_1\{D_{ii}\} - H_1\{D_{11}\}] \simeq H_1\{D_{11}\} \tag{7.26}$$

The results are in qualitative agreement with the recent calculations of Enomoto [164], although this analysis was limited to ternary systems.

7.5 Nucleation and Growth Theory

Recently, Bhadeshia et al. [165] presented a theory capable of handling the nucleation and growth of allotriomorphic ferrite. The allotriomorphs, prior to site saturation, are modelled as discs with their faces parallel to the austenite grain boundary plane (figure 7.4). The discs are assumed to grow radially, with the half thickness q and radius ηq varying parabolically with time, through the equation $q = \alpha_1 t^{1/2}$. The aspect ratio η of the allotriomorphs is considered constant because in reality, the lengthening and thickening processes are coupled; consistent with the experimental evidence [166] η is taken as 3.0.

The theory is as follows. Consider a plane surface of total area O_b parallel to a particular boundary; the extended area O_α^e is defined as the sum of the areas of intersection of the discs with this plane. It follows that the small change δO_α^e in O_α^e due to a disc nucleated between $t = \tau$ and $t = \tau + \delta\tau$ is

$$\delta O_\alpha^e = \begin{cases} \pi O_b I_B \left[(\eta\alpha_1)^2 (t - \tau)\right] \delta\tau & \text{if } \alpha_1(t-\tau)^{1/2} > y \\ 0 & \text{if } \alpha_1(t-\tau)^{1/2} < y \end{cases} \tag{7.27}$$

172

where I_B is the grain boundary nucleation rate per unit area of boundary. The term τ is the incubation time for the nucleation of one particle. Only allotriomorphs nucleated for $\tau > (y/\alpha_1)^2$ can contribute to the extended area intersected by the plane at y; if τ takes a value less than $(y/\alpha_1)^2$ then the allotriomorph has not had enough time to grow the distance y to the arbitrary plane. It follows that the whole extended area is then given by

$$O_\alpha^e = \int_0^{t-(y/\alpha_1)^2} (\eta\alpha_1)^2 \pi O_b I_B(t-\tau)\, d\tau$$

$$= \tfrac{1}{2}\pi O_b I_B (\eta\alpha_1)^2 t^2 \left[1 - \theta^4\right] \tag{7.28}$$

where $\theta = y/(\alpha_1 t^{1/2})$, corresponding to the ratio between the distance to the arbitrary plane, and the half-thickness of the allotriomorph at time t.

The actual area O_α which intersects the plane O_b will be somewhat smaller than the extended area, because the extended area includes a fraction $(1 - [O_\alpha/O_b])$ of 'phantom' area which has already transformed to ferrite. The relationship between the extended area and the actual area O_α is then given by [167,168]

$$O_\alpha^e/O_b = \ln\left\{1 - [O_\alpha/O_b]\right\} \tag{7.29}$$

Assuming that there is no interference with allotriomorphs from other boundaries, the total volume V_b of material originating from this grain boundary is given by integrating y between negative and positive infinity; in terms of θ this gives

$$V_b = 2\int_0^1 O_b\, \alpha_1 t^{1/2} \left[1 - \exp\left\{-O_\alpha^e/O_b\right\}\right]\, d\theta$$

$$= 2\int_0^1 O_b\, \alpha_1 t^{1/2} \left[1 - \exp\left\{-0.5\pi I_B(\eta\alpha_1)^2 t^2 \left[1 - \theta^4\right]\right\}\right]\, d\theta \tag{7.30}$$

$$= 2 O_b\, \alpha_1 t^{1/2} f\left\{\eta\alpha_1,\, I_B,\, t\right\}$$

where

$$f\left\{\eta\alpha_1,\, I_B,\, t\right\} = \int_0^1 1 - \exp\left\{-0.5\pi I_B(\eta\alpha_1)^2 t^2 \left[1 - \theta^4\right]\right\}\, d\theta \tag{7.31}$$

If the total grain boundary area is $O_B = \Sigma O_b$, then by substituting O_B for O_b in the above equation the total extended volume V_α^e of material is found; this is an extended volume because allowance was not made for impingement of discs originating from different boundaries.

Thus

$$V_\alpha^e = 2 O_B\, \alpha_1 t^{1/2} f\left\{\eta\alpha_1,\, I_B,\, t\right\} \tag{7.32}$$

and if V is the total volume, and S_V the γ grain surface area per unit volume, then

$$V_\alpha^e/V = 2 S_V\, \alpha_1 t^{1/2} f\left\{\eta\alpha_1,\, I_B,\, t\right\} \tag{7.33}$$

This can be converted into the actual volume V_α using the equation (related to equation 7.29)

$$V_\alpha/(V\phi) = 1 - \exp\left\{-V_\alpha^e/(V\phi)\right\} \tag{7.34}$$

where ϕ is the equilibrium volume fraction of ferrite, so that $V\phi$ is the volume of ferrite in the austenite matrix. The term ϕ can be estimated from the phase diagram, by calculation of the tie-line passing through the mean alloy composition:

$$\phi = \frac{\bar{c}_i - c_i^{\gamma\alpha}}{c_i^{\alpha\gamma} - c_i^{\gamma\alpha}} \tag{7.35}$$

173

Since the tie-line under consideration passes through the overall alloy composition, ϕ can be evaluated using the c's of any of the components in the system. It should be noted that in the paraequilibrium mode of transformation, ϕ equals f_1, independent of the volume fraction transformed. Under local equilibrium, ϕ does not equal any of the f_i until the end of the transformation, when austenite and ferrite reach their equilibrium volume fractions.

It follows that

$$-\ln\{1 - \zeta\} = 2\,(S_V/\phi)\,\alpha_1 t^{1/2}\,f\,\{\eta\alpha_1, I_B, t\} \qquad (7.36)$$

where $\zeta = V_\alpha/(V\phi)$ is often referred to as the *extent of reaction*. It corresponds to the volume of α divided by its equilibrium volume.

The value of the integral f tends to unity as I_B increases or time increases, since site saturation occurs. In the limit as the integral tends to unity, equation 7.36 simplifies to one dimensional thickening governed by the equation

$$-\ln\{1 - \zeta\} = 2\,(S_V/\phi)\,\alpha_1 t^{1/2} \qquad (7.37)$$

Bhadeshia *et al.* [4] used equation 7.37 to model the growth of allotriomorphic ferrite in low-alloy weld deposits, after nucleation. In that work, the incubation time for the first detectable amount of transformation was determined semi-empirically [169] from a form of a general expression derived by Russell [170]. Bhadeshia *et al.*'s method *underpredicts* the experimental volume fraction of α found in low-alloy weld deposits by a factor of approximately two.

In summary, the theory takes account of hard impingement between allotriomorphs growing from the same, or adjacent austenite grain boundaries. It should be noted however, that soft impingement (the overlap of diffusion fields) between neighbouring allotriomorphs is ignored.

7.6 Classical Nucleation Theory

In order to use the above theory to estimate the time-temperature-transformation (TTT) curves for the decomposition of austenite to allotriomorphic ferrite, it is necessary to find a function which describes the process of nucleation. Following classical nucleation theory [e.g. 97] I_B^F, the rate of nucleation on grain boundary faces per unit area of boundary is given by:

$$I_B^F = N_F\,\frac{kT}{h}\,\exp\left\{\frac{-(\Delta G_c^F + Q)}{kT}\right\} \qquad (7.38)$$

where N_F is the number of face sites per unit area of boundary supporting nucleation, k is the Boltzmann constant, h the Planck constant, T the absolute temperature, ΔG_c^F the critical activation free energy per atom for nucleation on faces and Q an activation free energy per atom, for atoms crossing the austenite/ferrite nucleus interface. The term kT/h is in effect a frequency factor for atomic vibrations in the crystal lattice.

In the calculations which follow, N_F is defined through the equation

$$N_F = \frac{K_1^F}{a^2} \qquad (7.39)$$

where K_1^F is the fraction of face sites supporting nucleation, and a is the inter-atomic spacing, taken as $0.25\,\text{nm}$. The term K_1^F allows for the poisoning of possible nucleation sites on the boundary.

There are many expressions available for the critical activation energy, ΔG_c^F. If the strain energy associated with the nucleus is ignored, common expressions are of the form [e.g. 171,172]

$$\Delta G_c^F = \frac{\sigma^3}{\Delta G_V^2}\,K_2^F \qquad (7.40)$$

174

where ΔG_V is the free energy per unit volume for ferrite nucleation from supersaturated austenite, calculated here using the parallel tangent construction as discussed in chapter six, and σ is the austenite/ferrite nucleus interfacial energy, which is taken as $0.2\,\mathrm{Jm}^{-2}$, and is assumed not to vary with interface orientation, or alloy chemistry. The multiplicative factor K_2^{F} takes account of non-spherical nucleus shape [e.g. 172].

Nucleation is also possible on grain boundary edges and corners. For these situations, different site densities and activation energies apply; for nucleation on edges we adopt the expression

$$I_B^{\mathrm{E}} = \frac{N_{\mathrm{E}}}{a}\,\frac{kT}{h}\,\exp\left\{\frac{-(\Delta G_c^{\mathrm{E}} + Q)}{kT}\right\} \tag{7.41}$$

for I_B^{E}, the rate of nucleation on grain boundary faces per unit area of boundary, N_{E} is the number of edge sites per unit edge of boundary supporting nucleation, and ΔG_c^{E} the critical activation free energy per atom for nucleation on grain edges. The term N_{E} is defined through the equation

$$N_{\mathrm{E}} = \frac{K_1^{\mathrm{E}}}{a} \tag{7.42}$$

where K_1^{E} is the fraction of edge sites supporting nucleation, and ΔG_c^{E} is given by

$$\Delta G_c^{\mathrm{E}} = \frac{\sigma^3}{\Delta G_V^2}\,K_2^{\mathrm{E}} \tag{7.43}$$

where K_2^{E} is a constant taking account of the shape of the critical nucleus.

For nucleation on corners, the expressions considered are

$$I_B^{\mathrm{C}} = \frac{N_{\mathrm{C}}}{a^2}\,\frac{kT}{h}\,\exp\left\{\frac{-(\Delta G_c^{\mathrm{C}} + Q)}{kT}\right\} \tag{7.44}$$

where I_B^{C} is the rate of nucleation on grain boundary corners per unit area of boundary, and $N_{\mathrm{C}} = K_1^{\mathrm{C}}$ represents the fraction of corner sites supporting nucleation. The term ΔG_c^{C} is given by

$$\Delta G_c^{\mathrm{C}} = \frac{\sigma^3}{\Delta G_V^2}\,K_2^{\mathrm{C}} \tag{7.45}$$

where K_2^{C} is the shape factor for corner nucleation.

Summing the contributions from faces, edges and corners, the total nucleation rate (to be used in equation 7.36) is given by the expression

$$I_B = I_B^{\mathrm{F}} + I_B^{\mathrm{E}} + I_B^{\mathrm{C}} \tag{7.46}$$

As discussed by Cahn [168] and Christian [97] we expect $K_2^{\mathrm{F}} > K_2^{\mathrm{E}} > K_2^{\mathrm{C}}$ so that $\Delta G_c^{\mathrm{F}} > \Delta G_c^{\mathrm{E}} > \Delta G_c^{\mathrm{C}}$. However, the relative nucleation rates do not necessarily increase in the same order as the activation energies for nucleation decrease [97], since the density of sites also decreases as the mode of nucleation changes from faces, to edges and finally to grain boundary corners. It is to be expected that $N_{\mathrm{F}} > N_{\mathrm{E}}/a > N_{\mathrm{C}}/a^2$. This means that with decreasing temperature corners, edges and finally faces make the greatest contribution to the nucleation rate.

It is possible to make approximations to equations 7.38, 7.41 & 7.44. For example, at temperatures well below Ae3, nucleation at faces is likely to dominate; moreover, the activation free energy for nucleation becomes relatively small, and the diffusion of atoms across the austenite/ferrite nucleus is the rate-controlling step; equation 7.38 then approximates to

$$I_B^{\mathrm{F}} \simeq N_{\mathrm{F}}\,\frac{kT}{h}\,\exp\left\{\frac{-Q}{kT}\right\} \tag{7.47}$$

At slightly higher temperatures, nucleation is dominated by a large ΔG_c^F, which is in turn dependent upon the driving force for transformation, and the interfacial energy; equation 7.38 then approximates to

$$I_B^F \simeq N_F \frac{kT}{h} \exp\left\{\frac{-\Delta G_c^F}{kT}\right\} \tag{7.48}$$

7.7 Method of Fit to Experimental Data

The experimental data chosen for analysis are contained in BISRA's 'Atlas of Isothermal Transformation Diagrams of BS En Steels' [131], one of the more meticulously determined sets of TTT curves. Since it is necessary to distinguish between parts of the C-curves which are due to the formation of allotriomorphic ferrite by reconstructive diffusion, and displacive reactions (such as Widmanstätten ferrite or bainite), only those diagrams whose component curves could be distinguished readily were used in the following analysis. The analysis is also restricted to steels which are sufficiently dilute for the thermodynamic model to be applicable; following Kirkaldy & Baganis [117] the total substitutional alloying content of the steels analysed is less than 6wt%. The steels selected, together with the chemical compositions and ASTM grain sizes, are given in table 7.1. Also tabulated are Ae3 & Ae3' temperatures calculated using the thermodynamic model.

REF	COMPOSITION/wt%						Ae3 /°C	Ae3' /°C	ASTM Grain Size
	C	Si	Mn	Ni	Mo	Cr			
En13	0.19	0.14	1.37	0.56	0.31	0.20	792	774	7
En16	0.33	0.18	1.48	0.26	0.27	0.16	770	748	8
En17	0.38	0.25	1.49	0.24	0.41	0.14	764	740	8
En18	0.48	0.25	0.86	0.18	0.04	0.98	753	734	5.5
En19	0.41	0.23	0.67	0.20	0.23	1.01	768	753	8
En20	0.27	0.13	0.60	0.19	0.55	0.74	796	786	8
En20	0.41	0.28	0.58	0.15	0.74	1.39	773	757	7.5
En24	0.38	0.20	0.69	1.58	0.26	0.95	749	725	7
En100	0.40	0.21	1.34	1.03	0.22	0.53	745	715	6
En110	0.39	0.23	0.62	1.44	0.18	1.11	751	728	7
En354	0.19	0.21	0.90	1.87	0.18	1.08	772	746	8
En355	0.20	0.23	0.61	2.00	0.19	1.65	771	746	8

Table 7.1: Chemical compositions of steels analysed in this work.

The term S_V required in equation 7.36 has been calculated from the ASTM grain sizes presented in the BISRA atlas using the equation [173]

$$S_V = 2000 \times 10^{(ASTM+3.298)/6.6457} \tag{7.49}$$

where ASTM is the ASTM grain size, and S_V (m^{-1}) is the γ-grain boundary area per unit volume.

In principle, the model developed is capable of calculating the experimental C-curves, before the onset of soft impingement. However, the constants K_1^F, K_1^E, K_1^C, K_2^F, K_2^E, K_2^C and Q remain unknown. The method adopted here involves determining the values of these constants, by fitting against the experimental C-curves. The values chosen could then be regarded as universal constants which should be applicable to all low-alloy steels. In this way it would then be possible to extrapolate with confidence between steels of different compositions.

Thus, the nucleation rate I_B necessary to reproduce the experimentally determined C-curves has been calculated as a function of temperature. Because soft impingement must eventually occur, only the 0%, 10% and 50% C-curves in the BISRA atlas are considered, and for the purposes of calculation the 0% curve is taken as corresponding to 0.1% transformation.

From equation 7.47, a plot of $(\log_{10}\{I_B\} - \log_{10}\{kT/h\})$ vs. $(1/T)$ should yield a straight line of gradient Q and intercept N_F at low temperatures. From equations 7.41, 7.44 and 7.48, a plot of $(\log_{10}\{I_B\} - \log_{10}\{kT/h\} + Q/(kT))$ vs. $(1/(T\Delta G_V^2))$ should yield three straight lines, with decreasing

intercepts N_F, N_E/a and N_C/a^2, and decreasing (negative) intercepts $\sigma^3 K_2^F/k$, $\sigma^3 K_2^E/k$ and $\sigma^3 K_2^C/k$ as the temperature rises; these lines correspond to the regimes in which face, edge and finally corner nucleation dominate.

However, as will be seen, the scatter associated with the experimental data means that it is difficult to determine the boundaries between these regimes with precision. After some trial and error, for the equilibrium mechanism equation 7.47 is applied for $T < 640°C$, equation 7.48 for $1/(T\Delta G_V^2) < 2 \times 10^{-18} K^{-1}(J\,atom^{-1})^{-2}$, equation 7.41 for $2 \times 10^{-18}K^{-1}(J\,atom^{-1})^{-2} < 1/(T\Delta G_V^2) < 6.75 \times 10^{-18}K^{-1}(J\,atom^{-1})^{-2}$, and equation 7.44 for $1/(T\Delta G_V^2) > 6.75 \times 10^{-18}K^{-1}(J\,atom^{-1})^{-2}$.

For the paraequilibrium mechanism, equation 7.47 is applied for $T < 640°C$, equation 7.48 for $1/(T\Delta G_V^2) < 5 \times 10^{-18}K^{-1}(J\,atom^{-1})^{-2}$, equation 7.41 for $5 \times 10^{-18}K^{-1}(J\,atom^{-1})^{-2} < 1/(T\Delta G_V^2) < 3 \times 10^{-17}K^{-1}(J\,atom^{-1})^{-2}$, and equation 7.44 for $1/(T\Delta G_V^2) > 3 \times 10^{-17}K^{-1}(J\,atom^{-1})^{-2}$.

7.8 Results

Figures 7.5 and 7.6 (for equilibrium and paraequilibrium respectively) illustrate the extent to which the data fall on straight lines. Linear regression analysis was used to determine the best-fit lines through the data points; from these lines the constants necessary to define the nucleation function were calculated. The values are tabulated in tables 7.2 & 7.3, together with errors based upon the standard errors in the gradients and intercepts of the best-fit lines in the figures.

Figure 7.5a	$K_1^F = 1 \times 10^{21}$,	5×10^{12}–2×10^{29}	$Q = (1.3 \pm 0.2) \times 10^{-18}\,J\,atom^{-1}$
Figure 7.5b	$K_1^F = 1.9 \times 10^{21}$,	7.4×10^{20}–4.4×10^{21}	$K_2^F = (4.0 \pm 2.0) \times 10^{-3}$
Figure 7.5c	$K_1^E = 4.9 \times 10^{20}$,	1.8×10^{20}–1.3×10^{21}	$K_2^E = (2.3 \pm 0.6) \times 10^{-3}$
Figure 7.5d	$K_1^C = 3.3 \times 10^{17}$,	1.1×10^{17}–1.0×10^{18}	$K_2^C = (4.2 \pm 2.2) \times 10^{-5}$

Table 7.2: Values of the nucleation constants, assuming nucleation and growth by the equilibrium mode of transformation. The value of K_1^F derived from figure 7.6b is used throughout the rest of this work.

Figure 7.6a	$K_1^F = 4 \times 10^{-8}$,	1×10^{-12}–1×10^{-3}	$Q = (5.9 \pm 1.3) \times 10^{-19}\,J\,atom^{-1}$
Figure 7.6b	$K_1^F = 6.9 \times 10^{-8}$,	3.1×10^{-8}–1.5×10^{-7}	$K_2^F = (2.7 \pm 0.6) \times 10^{-3}$
Figure 7.6c	$K_1^E = 1.3 \times 10^{-8}$,	1.8×10^{-9}–8.9×10^{-8}	$K_2^E = (1.0 \pm 0.3) \times 10^{-3}$
Figure 7.6d	$K_1^C = 1.2 \times 10^{-10}$,	2.1×10^{-11}–7.0×10^{-10}	$K_2^C = (3.3 \pm 0.5) \times 10^{-3}$

Table 7.3: Values of the nucleation constants, assuming nucleation and growth by the paraequilibrium mode of transformation. The value of K_1^F derived from figure 7.6b is used throughout the rest of this work.

The values of Q correspond to $800\,kJ\,mol^{-1}$ (equilibrium) and $350\,kJ\,mol^{-1}$ (paraequilibrium). It seems intuitively reasonable to expect that Q should be comparable to the activation energy for self-diffusion in iron, which is close to $250\,kJ\,mol^{-1}$ [159].

Figures 7.7 and 7.8 illustrate the level of agreement between the experimentally observed C-curves, and those calculated using the model developed here.

7.9 Discussion

It is apparent that the kinetic model developed here is capable of reproducing the C-curve of the TTT diagram due to the formation of allotriomorphic ferrite. However, the values of the constants K_1^F, K_1^E and K_1^C determined assuming local equilibrium during nucleation & growth are physically unreasonable; in addition the shapes of the computed C-curves reflect the large increase in the interface velocity predicted when the temperature falls into the NP-LE regime. This is not detected in practice.

On the other hand, the values of K_1^F, K_1^E and K_1^C determined assuming paraequilibrium are physically reasonable, as are the shapes of the calculated C-curves. For this reason this work suggests that at temperatures below Ae3′ austenite decomposes to allotriomorphic ferrite by the paraequilibrium mode of transformation, in which iron and substitutional alloying elements are configurationally frozen, and

so do not redistribute during transformation. Of course, at temperatures between Ae3' & Ae3 growth under PLE becomes a thermodynamic necessity.

7.10 Summary

The thermodynamic model developed in chapter six has been coupled with simplified kinetic theory, so that subject to a variety of assumptions, the one-dimensional parabolic thickening constant α_1 for allotriomorphic ferrite can be estimated as a function of temperature, and composition. To do this, kinetic theory for ternary Fe-C-X systems (where X represents a substitutional alloying element) has been extended to multicomponent alloys. Values of α_1 calculated assuming local equilibrium and paraequilibrium have been compared. Consistent with recent calculations [164], the slope of the α_1 vs. temperature plot changes abruptly on entry into the NP-LE regime, consistent with an increase in the interface velocity. As noted by Coates [138], at very high supersaturations the effect of the cross-terms in the diffusivity matrix appears to be small. Only in this case do the approximations used by DeHoff [141] become reasonable. At temperatures below Ae3' α_1 calculated assuming local equilibrium is smaller than that calculated assuming paraequilibrium.

Classical nucleation theory has been used to model the growth of allotriomorphs as discs growing from prior γ-grain boundaries. It has been demonstrated that the model developed here is capable of reproducing the C-curve behaviour typical of the parts of the time-temperature-transformation (TTT) diagrams which are due to allotriomorphic ferrite, provided the paraequilibrium mode of transformation is assumed to be operative. The work therefore suggests that in multicomponent alloys, the state of true local equilibrium does not exist at the advancing interface.

REFERENCES

134. 'THERMOCALC' databank, see for example B. Sundman, report D53, 'Summary of the Modules in Thermocalc', The Royal Institute of Technology, Stockholm, Sweden, (1984).
135. J.S. Kirkaldy, Canadian Journal of Physics, 36, 907–916, (1958).
136. G.R. Purdy, D.H. Weichert and J.S. Kirkaldy, Trans. TMS-AIME, 230, 1025–1034, (1964).
137. D.E. Coates, Metall. Trans., 3, 1203–1212, (1972).
138. D.E. Coates, Metall. Trans., 4, 395–396, (1973).
139. D.E. Coates, Metall. Trans., 4, 1077–1086, (1973).
140. D.E. Coates, Metall. Trans., 4, 2313–2325, (1973).
141. R.T. DeHoff, Proc. Int. Conf. on Solid→Solid Phase Transformations, 503–520, TMS-AIME, Warrendale, Pennsylvania, (1981).
142. J.R. Bradley and H.I. Aaronson, Metall. Trans., 12A, 1729–1741, (1981).
143. H.I. Aaronson and J.R. Bradley, TMS-AIME, 236, 781–796, (1966).
144. J.S. Kirkaldy and G.R. Purdy, Canadian Journal of Physics, 40, 208–217, (1962).
145. L.C. Brown and J.S. Kirkaldy, TMS-AIME, 230, 223–226, (1964).
146. C. Wells, W. Batz and R.F. Mehl, TMS-AIME, 188, 533–, (1950).
147. R.P. Smith, Acta Metall., 1, 578–587, (1953).
148. R. Trivedi and G.M. Pound, Journal of Applied Physics, 38, 3569–3576, (1967).
149. R.H. Siller and R.B. McLellan, TMS-AIME, 245, 697–700, (1969).
150. R.H. Siller and R.B. McLellan, Metall. Trans., 1, 985–988, (1970).
155. R.B. McLellan and W. Dunn, J. Phys. Chem. Solids., 30, 2631–2637, (1970).
156. W. Dunn and R.B. McLellan, Metall. Trans., 1, 1263–1265, (1970).
157. H.K.D.H. Bhadeshia, Metal Science, 15, 477–479, (1981).
158. H.K.D.H. Bhadeshia, Metal Science, 15, 178–180, (1981).
159. J. Fridberg, L. Torndahl and M. Hillert, Jernkontorets Ann., 153, 263–276, (1969).

160. G. Bolze, D.E. Coates and J.S. Kirkaldy, Trans. ASM, **62**, 794–803, (1969).

161. A. Hultgren, Jernkontorets Ann., **135**, 403–483, (1951).

162. M. Hillert, Jernkontorets Ann., **136**, 25–37, (1952).

163. H.I. Aaronson, II.A. Domian and G.M. Pound, TMS-AIME, **236**, 768–781, (1966).

164. M. Enomoto, Transactions I.S.I.J., **28**, 826–835, (1988).

165. H.K.D.H. Bhadeshia, L.-E. Svensson and B. Gretoft, in 'Proceedings of an International Conference on Welding Metallurgy of Structural Steels, The Metallurgical Society of AIME, Warrendale, Pennsylvania. Edited by J.Y. Koo, (1987).

166. J.R. Bradley, J.M. Rigsbee and II.I. Aaronson, Metall. Trans., **6A**, 911–919, (1977).

167. M. Avrami, J. Chem. Phys., **7**, 1103–, (1939).

168. J.W. Cahn, Acta Metall., **4**, 449–459, (1956).

169. H.K.D.II. Bhadeshia, Metal Science, **16**, 159–165, (1982).

170. K.C. Russell, Acta Metall., **17**, 1123–1131, (1969).

171. W.C. Johnson, C.L. White, P.E. Marth *et al.*, Metall. Trans., **6A**, 911–919, (1975).

172. W.F. Lange, M. Enomoto and II.I.Aaronson, Metall. Trans., **19A**, 427–440, (1988).

173. G.F. Vander Voort, 'Metallography: Principles and Practices', McGraw-IIill Inc., New York, (1984).

Fe−0.33C−1.00Mn weight per cent
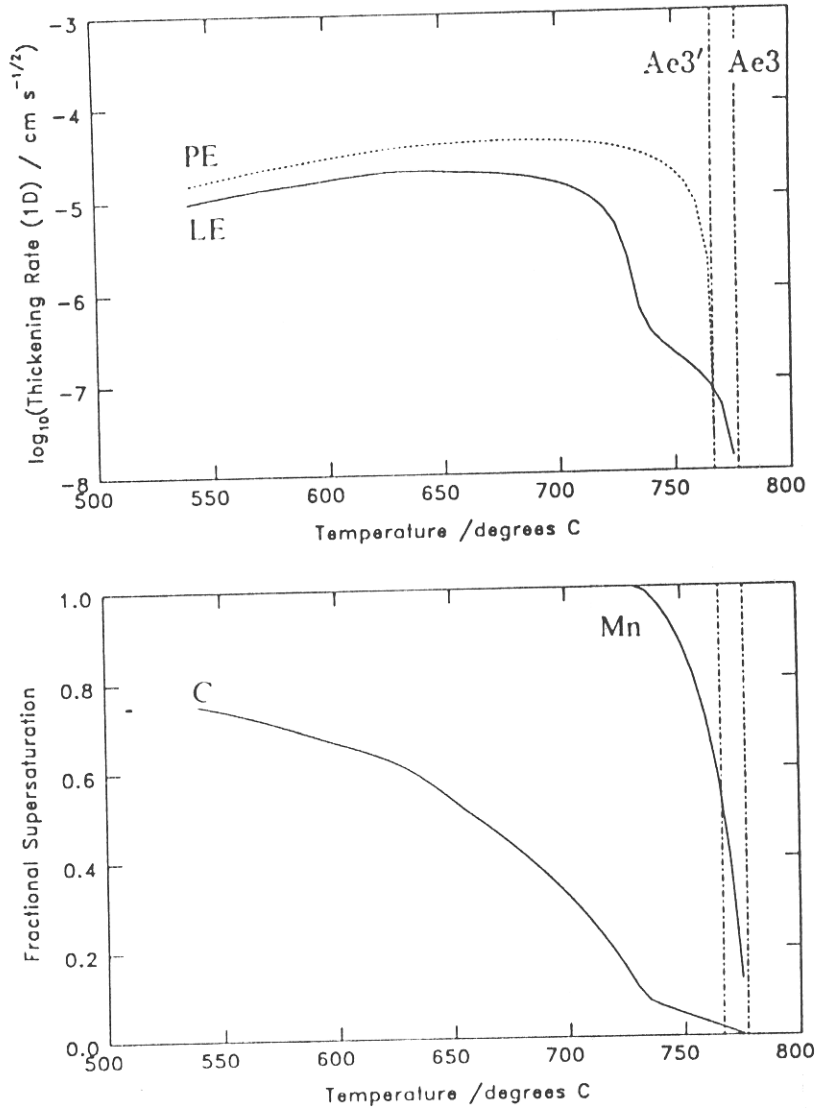
Figure 7.1: Top, one-dimensional thickening constant α_1 evaluated under the local equilibrium (LE) and the paraequilibrium (PE) assumptions, for a Fe-0.33C-1.00Mn (wt%) alloy, as a function of temperature. Bottom, the associated fractional supersaturations.
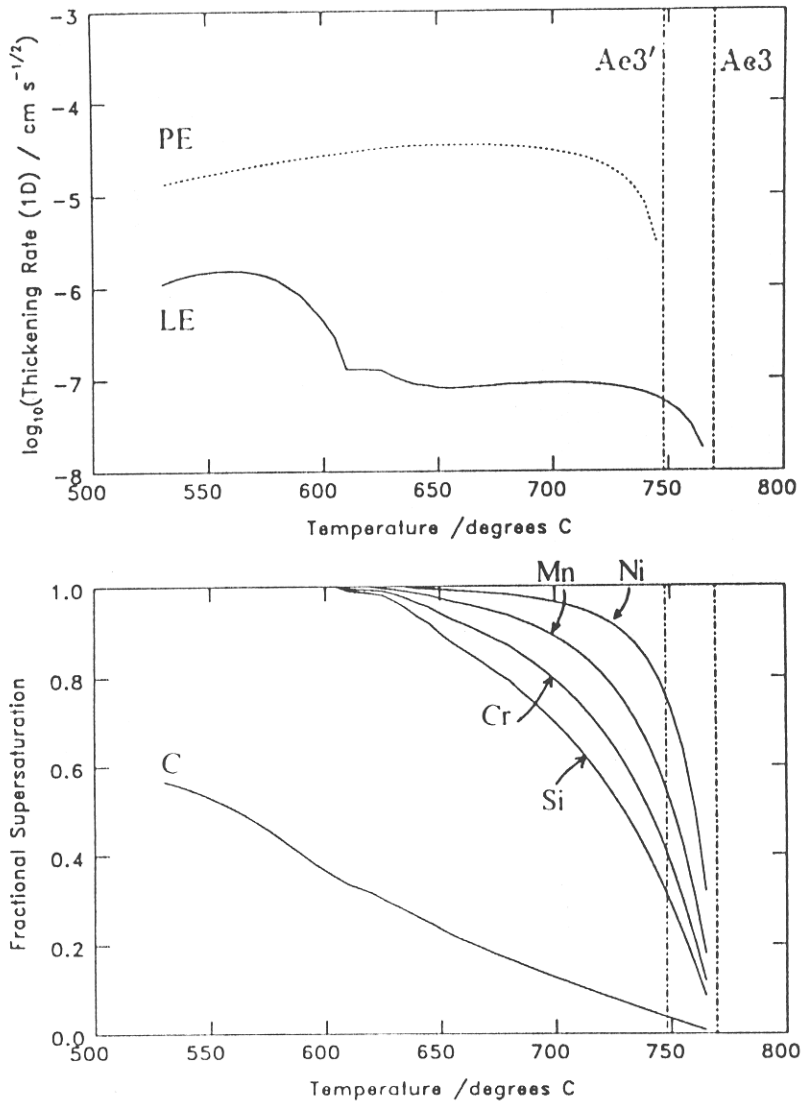
Figure 7.2: Top, one-dimensional thickening constant α_1 evaluated under the local equilibrium (LE) and the paraequilibrium (PE) assumptions, for En16, as a function of temperature. Bottom, the associated fractional supersaturations.
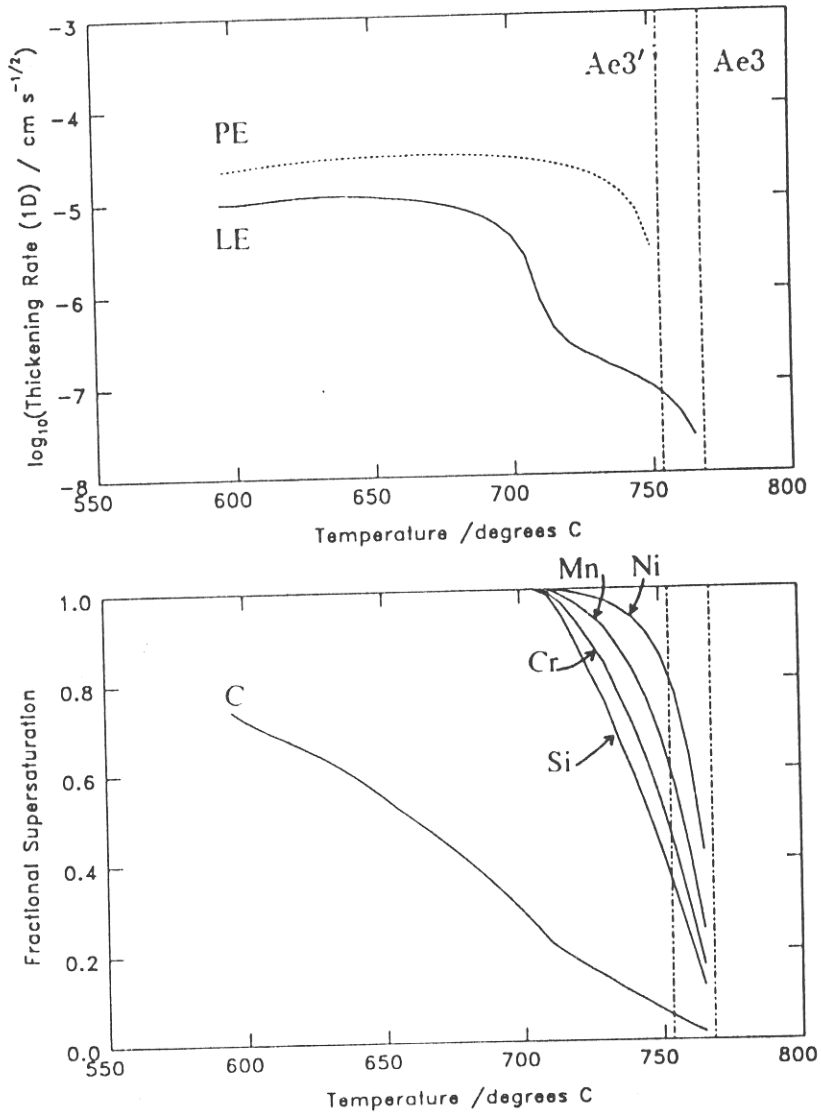
Figure 7.3: Top, one-dimensional thickening constant α_1 evaluated under the local equilibrium (LE) and the paraequilibrium (PE) assumptions, for En19, as a function of temperature. Bottom, the associated fractional supersaturations.

Plane surface of area O_b parallel to γ-grain boundary

Allotriomorphs of half-thickness q, radius $3q$

γ-grain boundary

y
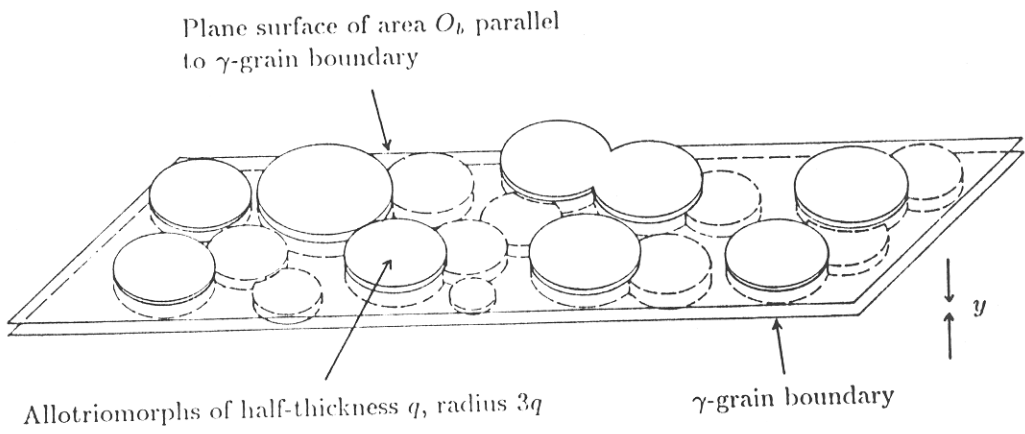
Figure 7.4: Model for the nucleation and growth of allotriomorphic ferrite. The allotriomorphs are modelled as discs of half-thickness q and radius $3q$, such that their faces lie parallel to the austenite grain boundary.
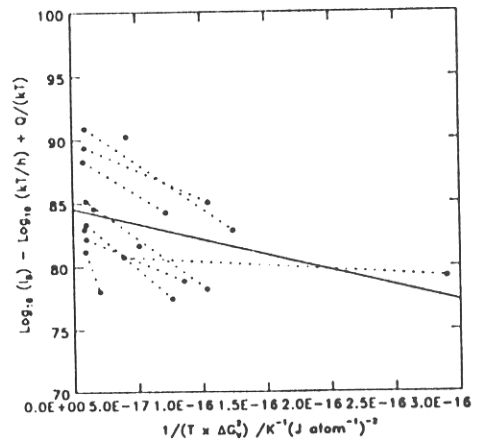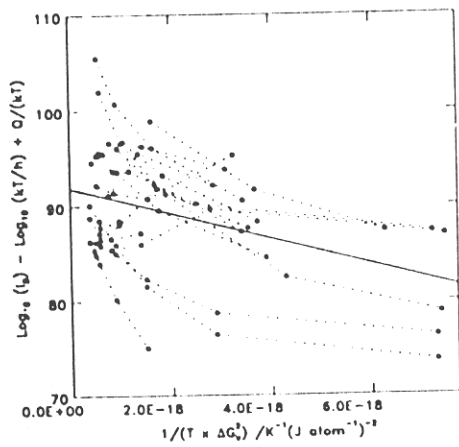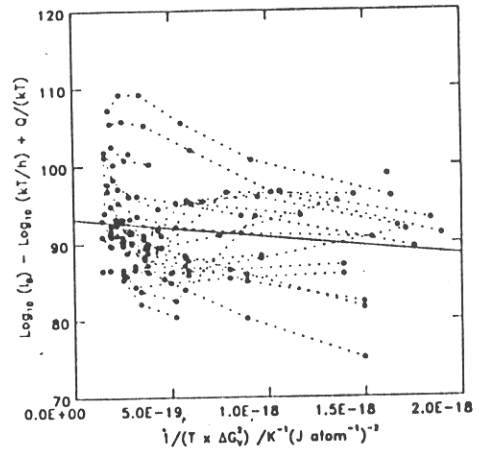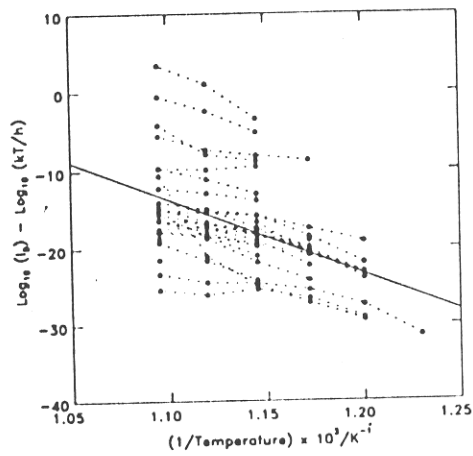
Figure 7.5: Determination of the constants for nucleation, assuming the equilibrium mode for nucleation and growth. Top left, figure 7.5a, for equation 7.47; top right, figure 7.5b, for equation 7.48; bottom left, figure 7.5c, for equation 7.41; bottom right, figure 7.5d, for equation 7.44.
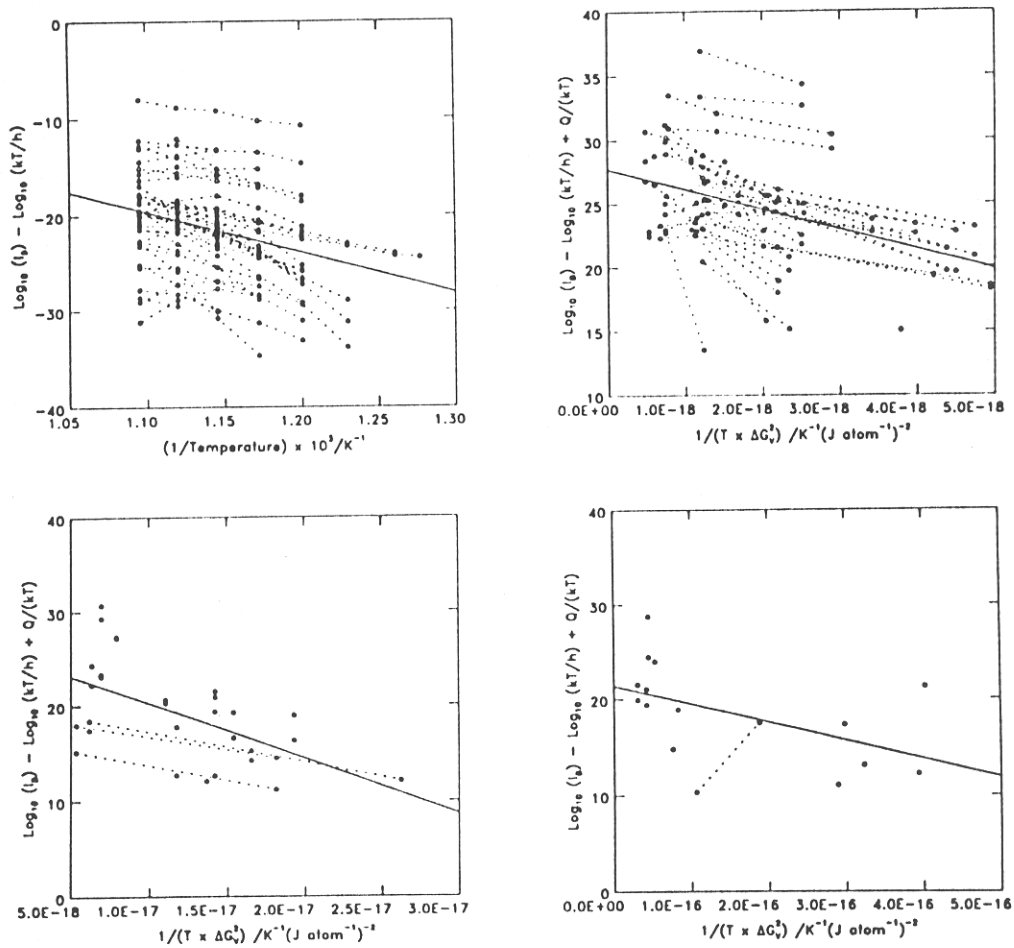
Figure 7.6: Determination of the constants for nucleation, assuming the paraequilibrium mode for nucleation and growth. Top left, figure 7.6a, for equation 7.47; top right, figure 7.6b, for equation 7.48; bottom left, figure 7.6c, for equation 7.41; bottom right, figure 7.6d, for equation 7.44.
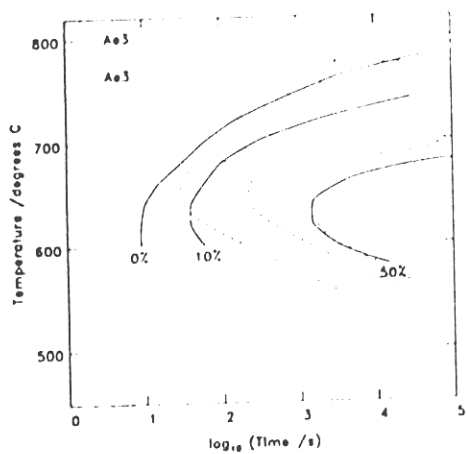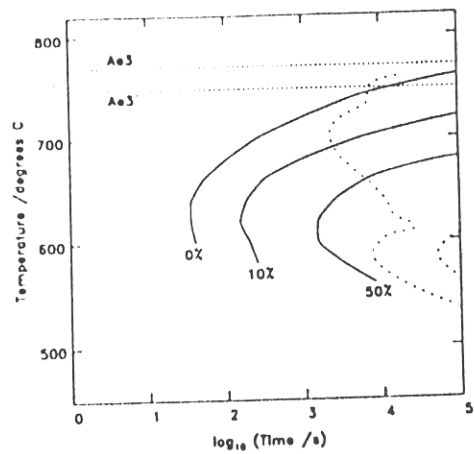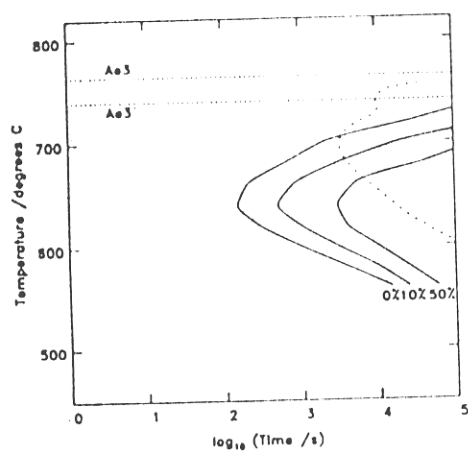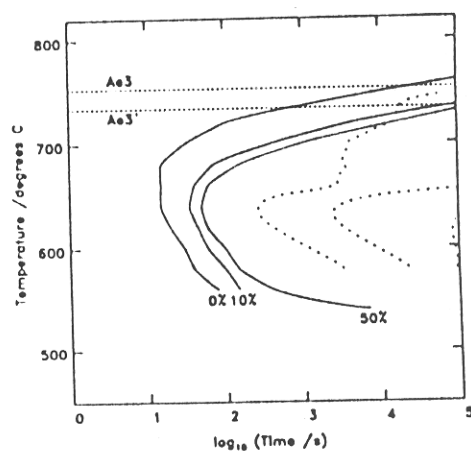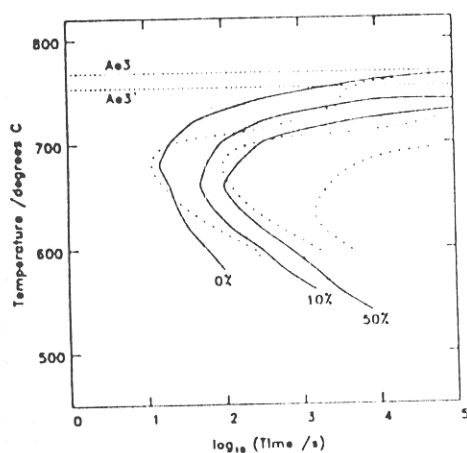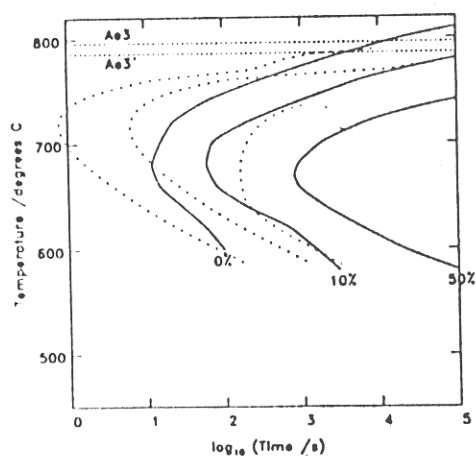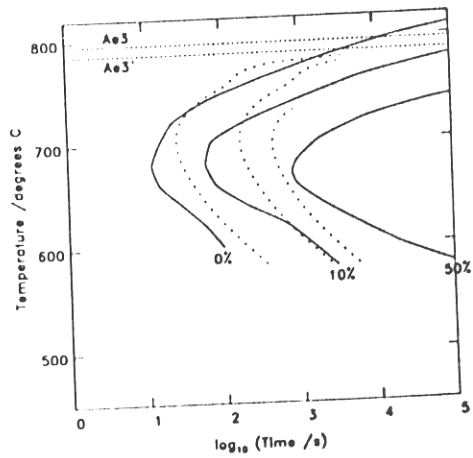
Figure 7.7: Observed (solid lines) and calculated (dashed lines) C-curves for the steels analysed in this work. Calculations performed assuming an equilibrium mode of transformation.
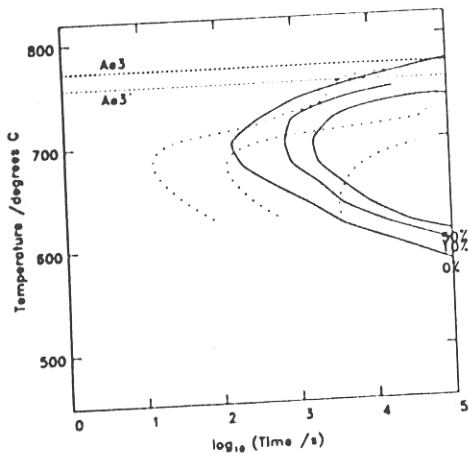
En20 Fe-0.41C-0.28Si-0.58Mn-0.15Ni-0.74Mo-1.39Cr wt%

En24 Fe-0.38C-0.20Si-0.69Mn-1.58Ni-0.26Mo-0.95Cr wt%

En100 Fe-0.40C-0.21Si-1.34Mn-1.03Ni-0.22Mo-0.53Cr wt%

En110 Fe-0.39C-0.23Si-0.62Mn-1.44Ni-0.18Mo-1.11Cr wt%

En354 Fe-0.19C-0.21Si-0.90Mn-1.87Ni-0.18Mo-1.08Cr wt%

En355 Fe-0.20C-0.23Si-0.61Mn-2.00Ni-0.19Mo-1.65Cr wt%

Figure 7.7 (cont.)

187
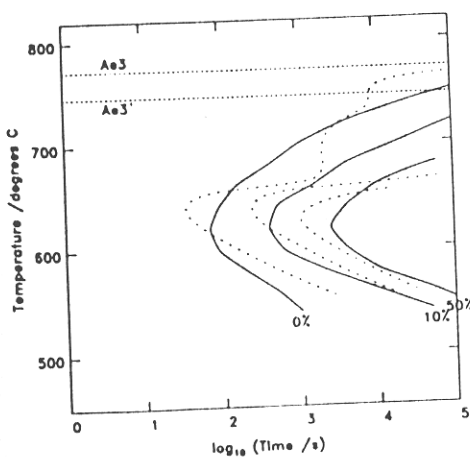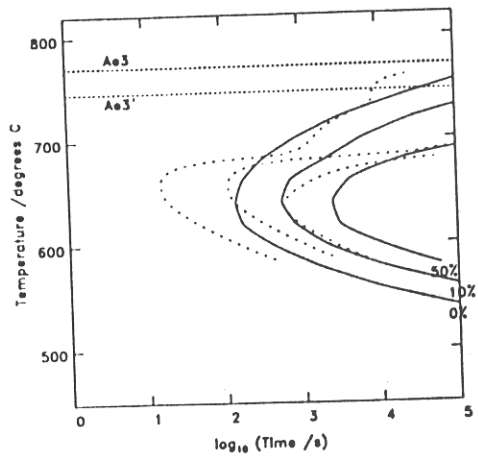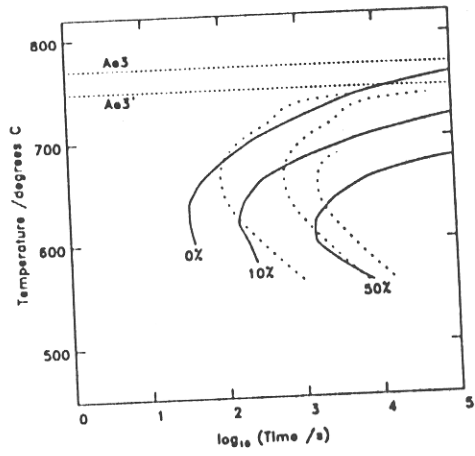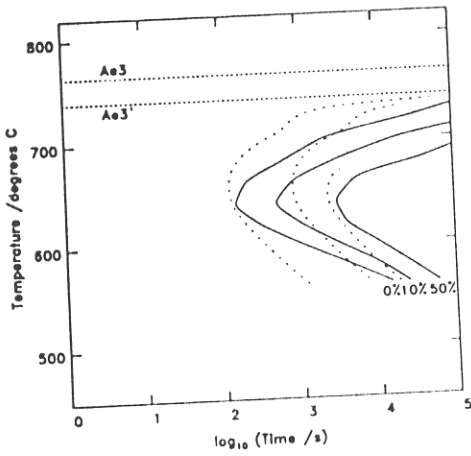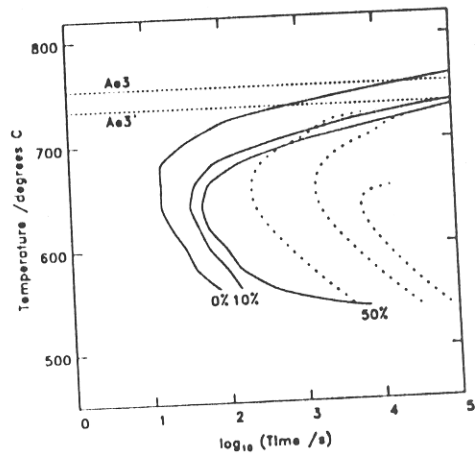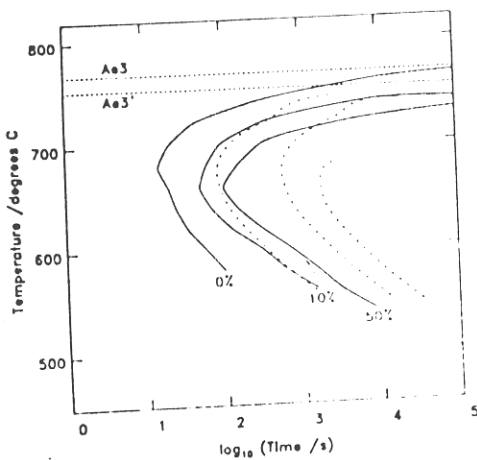
Figure 7.8: Observed (solid lines) and calculated (dashed lines) C-curves for the steels analysed in this work. Calculations performed assuming a paraequilibrium mode of transformation.
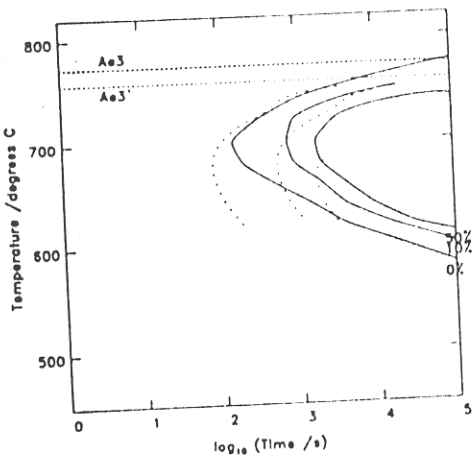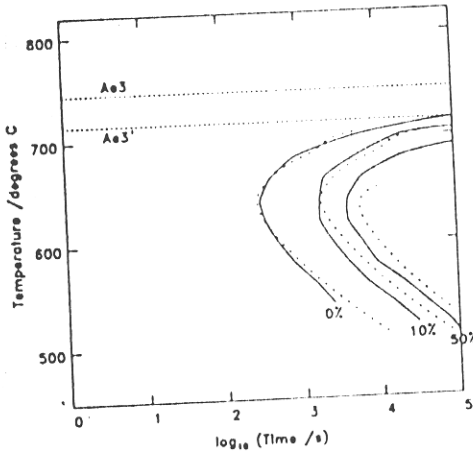
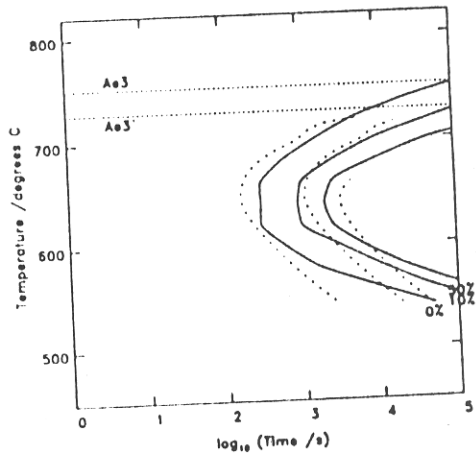En20 Fe-0.41C-0.28SI-0.58Mn-0.15NI-0.74Mo-1.39Cr wt%
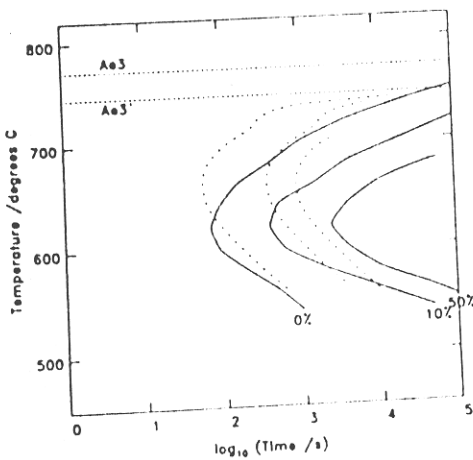
En24 Fe-0.38C-0.20SI-0.69Mn-1.58NI-0.26Mo-0.95Cr wt%
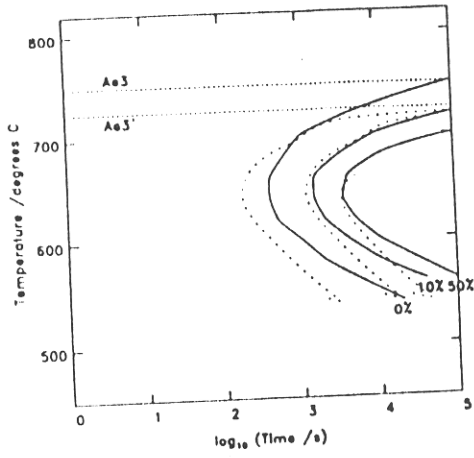
En100 Fe-0.40C-0.21SI-1.34Mn-1.03NI-0.22Mo-0.53Cr wt%

En110 Fe-0.39C-0.23SI-0.62Mn-1.44NI-0.18Mo-1.11Cr wt%

En354 Fe-0.19C-0.21SI-0.90Mn-1.87NI-0.18Mo-1.08Cr wt%

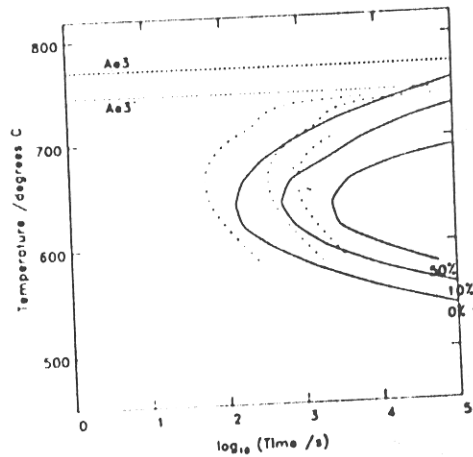En355 Fe-0.20C-0.23SI-0.61Mn-2.00NI-0.19Mo-1.65Cr wt%

Figure 7.8 (cont.)

189

CHAPTER EIGHT
Conclusions and Further Work

This work has been concerned with the development of a computer model capable of determining the microstructure of multipass steel welds, from an input of the weld variables and steel composition only. Although significant advances have been made in a number of areas, this objective has not been achieved, and was, in retrospect, probably a little ambitious for a three-year research programme.

Nevertheless, the groundwork for much future research in this area has been laid. In particular, the heat-flow model which is described in chapter three represents the backbone of what is ultimately required, since the weld thermal cycles are computed for each point within the multipass weld. The challenge now facing future researchers is to relate these thermal cycles to the microstructure they produce, by employing existing thermodynamic models and by developing theory to describe the phase transformations which occur. The kinetic theory developed in chapter seven, for the allotriomorphic ferrite transformation, is typical of what is required. It should be noted that adequate theory for the pearlite, Widmanstätten ferrite, bainite and martensite transformations is not available at present. Ultimately, these models must be capable of estimating the volume fractions of phases accurately. It has not yet been demonstrated that the model developed in chapter seven is capable of estimating the volume fraction of allotriomorphic ferrite; this must be attempted in the future. It should be possible to extend the theory to account for arbitrary cooling curves, and in principle, to allow a prediction of the mean allotriomorphic ferrite grain size, since the nucleation rate is known.

Throughout this work it has sometimes proved necessary to make seemingly gross assumptions in the development of the models. For example, in the heat-flow model developed in chapter three, no account was taken of the re-melting of weld beads within each weld layer. It would have been possible to take this effect into account, but only at the expense of considerable time spent developing and testing the programs. The assumptions made in the development of this model were justified, given that the heat-flow equations employed are analytical, and therefore approximate. In the author's opinion further effort was better rewarded in developing the phase transformation theory in chapter seven. As discussed above, such theory seems to be lacking at present. Thus this work has demonstrated that during the development of such large-scale models, it is necessary to make rather crude assumptions so that program development is not halted. It should be remembered that such programs, if structured correctly, can be made more complex at a later stage, if this is deemed necessary.

There is another problem which must be overcome in the development of such computer models. It is becoming increasingly clear that programs such as that attempted here cannot be written by one researcher. Thus, as the amount of computer code becomes large, there is a problem in ensuring that the code is self-consistent, so that subroutines can interact freely. To give an example, in the present context it is obviously very desirable to couple the heat-flow model developed in chapter three, the thermodynamic model in chapter six and the kinetic model developed in chapter seven. When the amount of code generated becomes large the program as a whole must become immensely powerful.

As the amount of code generated becomes large, it will become necessary to use faster computers. Much of the computation necessary for this work was carried out using standard Fortran on an IBM mainframe. It is clear that in many cases the use of such mainframes is an outdated concept, and in the future the use of dedicated workstations should be contemplated.

A long-term aim is the development of fundamental structure/property relationships, in particular the yield stress, fracture toughness and creep properties as a function of weld variables and chemistry. A more immediate aim is to model the build-up of stress during the welding process, and the subsequent relaxation during stress-relief heat-treatment. However, the ultimate goal is to produce software which is friendly to the engineer, so that it can be used to ensure good welding practice. In this case, such

models could be incorporated into design procedures so that computer-aided design (CAD) rather than merely computer-aided modelling (CAM) is possible.